

Investigations of the atmospheric OH, HO₂ and RO₂ radical chemical budgets and their impact on tropospheric ozone formation in a rural area in West-Germany in the JULIAC 2019 campaign

Changmin Cho

Energie & Umwelt / Energy & Environment

Band / Volume 575

ISBN 978-3-95806-625-0

Forschungszentrum Jülich GmbH
Institut für Energie- und Klimaforschung
Troposphäre (IEK-8)

Investigations of the atmospheric OH, HO₂ and RO₂ radical chemical budgets and their impact on tropospheric ozone formation in a rural area in West-Germany in the JULIAC 2019 campaign

Changmin Cho

Schriften des Forschungszentrums Jülich
Reihe Energie & Umwelt / Energy & Environment

Band / Volume 575

ISSN 1866-1793

ISBN 978-3-95806-625-0

Bibliografische Information der Deutschen Nationalbibliothek.
Die Deutsche Nationalbibliothek verzeichnet diese Publikation in der
Deutschen Nationalbibliografie; detaillierte Bibliografische Daten
sind im Internet über <http://dnb.d-nb.de> abrufbar.

Herausgeber und Vertrieb: Forschungszentrum Jülich GmbH
Zentralbibliothek, Verlag
52425 Jülich
Tel.: +49 2461 61-5368
Fax: +49 2461 61-6103
zb-publikation@fz-juelich.de
www.fz-juelich.de/zb

Umschlaggestaltung: Grafische Medien, Forschungszentrum Jülich GmbH

Druck: Grafische Medien, Forschungszentrum Jülich GmbH

Copyright: Forschungszentrum Jülich 2022

Schriften des Forschungszentrums Jülich
Reihe Energie & Umwelt / Energy & Environment, Band / Volume 575

D 468 (Diss. Wuppertal, Univ., 2022)

ISSN 1866-1793
ISBN 978-3-95806-625-0

Vollständig frei verfügbar über das Publikationsportal des Forschungszentrums Jülich (JuSER)
unter www.fz-juelich.de/zb/openaccess.



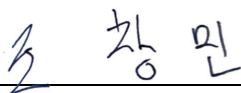
This is an Open Access publication distributed under the terms of the [Creative Commons Attribution License 4.0](https://creativecommons.org/licenses/by/4.0/), which permits unrestricted use, distribution, and reproduction in any medium, provided the original work is properly cited.

Declaration of Authorship

I, Changmin Cho, declare that this thesis titled, “Investigations of the atmospheric OH, HO₂ and RO₂ radical chemical budgets and their impact on tropospheric ozone formation in a rural area in West-Germany in the JULIAC 2019 campaign” and the work presented in it are my own. I confirm that:

- This work was done wholly or mainly while in candidature for a research degree at this University.
- Where any part of this thesis has previously been submitted for a degree or any other qualification at this University or any other institution, this has been clearly stated.
- Where I have consulted the published work of others, this is always clearly attributed.
- Where I have quoted from the work of others, the source is always given. With the exception of such quotations, this thesis is entirely my own work.
- I have acknowledged all main sources of help.
- Where the thesis is based on work done by myself jointly with others, I have made clear exactly what was done by others and what I have contributed myself.

Signed:

 Changmin

Date:

08.11.2021

Acknowledgements

There are many people who helped me over the period of my doctoral degree. Therefore, I would like to thank the following people for supporting this research project.

First of all, I thank Prof. Dr. Peter Wiesen for accepting the supervision of this thesis as ‘Doktorvater’ at the Bergische Universität Wuppertal. Furthermore, I would like to thank my committee members: for accepting and reviewing my thesis.

I would like to show my sincere gratitude to my scientific supervisor Dr. Anna Novelli for the dedicated support throughout the duration of my Ph.D. with her patience, motivation, and knowledge. I also want to thank PD. Dr. Andreas Hofzumahaus and PD. Dr. Hendrik Fuchs for co-supervision. They always provided me a lot of motivations and useful discussions. Without them, I do not think I could not complete this project successfully.

I thank all the members of the LIF group for providing valuable comments and technical helps for the LIF instrument.

I send special thanks to Dr. Doreen Niether and Dr. Hans-Peter Dorn who provided great material for the analysis of net ozone production rate and DOAS measurements, respectively.

I gratefully appreciate the directors Prof. Dr. Andreas Wahner and Prof. Dr. Astrid Kiendler-Scharr of the IEK-8, Forschungszentrum Jülich for enriching Ph.D. life in the institute.

Although I did not mention here, many colleagues in JULIAC team and IEK-8 helped my project. I would like to express my deepest gratitude for their supporting.

Abstract

Hydroxyl radicals (OH) are the main daytime oxidant, which determine the tropospheric oxidation capacity of an environment by limiting the chemical lifetime of most trace gases including volatile organic compounds (VOCs) and nitrogen oxides ($\text{NO}_x = \text{NO} + \text{NO}_2$). In the oxidation process of VOCs by OH, hydroperoxy (HO_2), and organic peroxy (RO_2) radicals are produced and they can regenerate OH through reactions with nitric oxide (NO). This RO_x (= the sum of OH, HO_2 , RO_2) cycle play a key role in converting primary emissions to secondary air pollutants such as ozone and secondary organic aerosols (SOA) (Levy, 1971; Carslaw et al., 2010; Li et al., 2019). Therefore, understanding the production and destruction of atmospheric RO_x radicals is essential to develop strategies for efficiently mitigating secondary air pollutants.

Measurements of atmospheric RO_x radicals require highly selective and sensitive techniques because their atmospheric concentrations are very low with typical daytime values for OH of $10^5 - 10^7 \text{ cm}^{-3}$, and for HO_2 and RO_2 of $10^7 - 10^9 \text{ cm}^{-3}$. Over the last decades, various instruments for the detection of radicals have been developed and used in various field campaigns and chamber experiments. However, recent studies showed that some of the instruments used extensively to investigate the chemistry of radicals in the atmosphere may suffer from interferences (Fuchs et al., 2011; Novelli et al., 2014a; Fuchs et al., 2016; Hofzumahaus and Heard, 2016). For the accurate investigation of radical chemistry, quantifying and correcting for these interferences are necessary.

In this study, investigations of the atmospheric OH, HO_2 , RO_2 and RO_x radical chemistry and their impacts on the tropospheric ozone formation were performed for data obtained during the Jülich Atmospheric Chemistry project Campaign (JULIAC) performed in the atmospheric simulation chamber SAPHIR at Forschungszentrum Jülich (FZJ), Germany. Ambient air was continuously drawn into the chamber through a 50 m high inlet line for one month in each season throughout 2019. As the location is surrounded by a mixed deciduous forest and is located close to a small-size city (Jülich), the sampled air was influenced by both anthropogenic and biogenic emissions. The dataset allowed to investigate the diurnal and seasonal variations of tropospheric trace gas concentrations to quantify how chemical processes affect the production of ozone at different levels of nitrogen oxides. This helps improving the understanding of tropospheric chemical mechanisms for conditions representative for a rural environment.

To achieve accurate OH measurements, a chemical modulation reactor (CMR) used in the laser-induced fluorescence (LIF) instrument of Forschungszentrum Jülich was implemented and characterized in this work. The characterization included laboratory tests and chamber experiments. Besides dedicated experiments in synthetic air, the new technique was extensively tested in the JULIAC campaign. Measurements of OH radicals using the CMR-LIF technique are compared to measurements by Differential Optical Absorption Spectroscopy (DOAS) in synthetic and ambient air in the atmospheric simulation chamber SAPHIR in chamber experiments and in the JULIAC campaign. The latter allowed the investigation of possible interference signals for a range of chemical and meteorological conditions in a rural environment. During the JULIAC campaign, good agreement was obtained between OH radical measurements performed with the new CMR-LIF instrument and a reference instrument. All observed interferences by the CMR-LIF could be fully explained by the well-characterized interference from ozone. No evidence for unexpected interferences was found. This demonstrates that the new chemical modulation system of the FZJ-LIF instrument is suitable for measurements of interference-free OH

concentrations for conditions encountered in the JULIAC campaign. Furthermore, a chemical model of the CMR system was developed in this work and applied to account for potential changes of the OH transmission and scavenging efficiency of the CMR system, if specific mixtures of reactive atmospheric trace gases are sampled.

Using the accurate radical measurements and measurements of various trace gases detected by state-of-art instruments, OH, HO₂, RO₂ and RO_x radical production and destruction rates were analyzed for the spring and summer periods of the JULIAC campaign. For NO mixing ratios below 2 ppbv, a significant OH sources with a rate of up to 3.5 ppbv h⁻¹ was required to balance the OH destruction rate. This missing OH source could be explained by a combination of a missing primary radical source and missing conversion reactions of peroxy radicals to OH. For NO mixing ratios higher than 2 ppbv, OH production and destruction rates were balanced, but missing HO₂ production and RO₂ loss pathways with rates of up to 6 ppbv h⁻¹ and 12 ppbv h⁻¹, respectively, were needed to balance production and destruction rates. In addition, imbalances in the RO_x radical budget indicated a missing primary RO_x source with a rate of up to 3 ppbv h⁻¹. However, uncertainties in the discrepancies were high, when they were highest, because measured HO₂ and RO₂ concentrations were close to the limit of detection in these air masses with high NO mixing ratios of more than 4 ppbv.

The photochemical net ozone production rate was investigated in the JULIAC campaign. By considering the JULIAC-SAPHIR system as a large photochemical flow reactor, the measured O_x (O₃ + NO₂) production rates in the chamber could be determined from the differences between the measured NO₂ and O₃ concentrations in the SAPHIR chamber and in the air that is flowed into the chamber. The comparison between this O_x production rate and the O_x production rate calculated from the NO₂ production from the reactions of peroxy radicals (HO₂ and RO₂) with NO and O_x destruction reactions using measured radical and trace gas concentrations showed good agreement within the uncertainties (13 %) of the methods. This indicates that the reaction of peroxy radicals (RO₂ and HO₂) with NO is the main contributor to the net O_x formation and the reaction of OH with NO₂ is the main O_x loss. It also demonstrates a high reliability of the measurements of HO₂ and RO₂ radical concentrations by the LIF instrument. Results confirm our current chemical understanding of tropospheric ozone formation for chemical conditions in a rural environment.

Contents

Declaration of Authorship	3
Abstract	6
Chapter 1 Introduction	18
1.1 Tropospheric OH, HO ₂ , and RO ₂ radical chemistry	18
1.2 Detection of atmospheric OH, HO ₂ and RO ₂	22
1.3 Measurement-model comparisons of ambient radical concentrations measured in field campaigns in various environments	25
1.4 Calculation and measurement of ozone production rates in field campaigns.....	27
1.5 Outline of the work	29
Chapter 2. The Jülich Atmospheric Chemistry Project (JULIAC): Investigation of photochemistry in rural air using the atmospheric simulation chamber SAPHIR	32
2.1 The atmospheric simulation chamber SAPHIR.....	32
2.2 The JULIAC campaign	34
2.3 Instrumentation during the JULIAC campaign	36
2.4 Characterization of the SAPHIR chamber with the JULIAC inlet system for ambient air sampling.....	39
2.5 Evolution of trace gas concentrations and determination of net chemical production rates	40
Chapter 3. Radical detection by laser induced fluorescence and characterization of a chemical modulation reactor (CMR) for the measurement of atmospheric concentrations of hydroxyl radicals...	43

3.1	The Forschungszentrum Jülich LIF instrument for OH, HO₂ and RO₂ radical concentration measurements	43
3.2	Potential interferences in radical concentration measurements by the LIF instrument.....	50
3.2.1	Potential interferences in the OH concentration measurement.....	50
3.2.2	Potential interferences in HO₂ concentration measurements	52
3.2.3	Potential interference and limitation in RO₂ concentration measurement	53
3.2.4	Corrections of background signals in HO₂ and RO₂ concentration measurements in the JULIAC campaign	54
3.3	The Forschungszentrum Jülich LIF OH instrument with the chemical modulation reactor (FZJ-LIF-CMR)	55
3.4	Characterization and test of the CMR system for clean air conditions.....	58
3.4.1	OH transmission of the CMR without OH scavenger	58
3.4.2	Scavenging efficiency in the CMR	61
3.4.3	Scavenging of OH in the fluorescence detection cell.....	64
3.4.4	Performance of the LIF-CMR system in experiments with clean air in the SAPHIR chamber	65
3.4.5	Test of the CMR for known interferences	67
3.4.5.1	Interference from ozone photolysis	67
3.4.5.2	Interference from NO₃.....	68
3.5	OH concentration measurements in ambient air applying chemical modulation	69
3.5.1	Sensitivity study of the influence of ambient conditions on the performance of the chemical modulation	69
3.5.1.1	Model description of the impact of ambient conditions on the OH transmission efficiency	69
3.5.1.2	Modelling the scavenging assuming homogeneous mixing of the scavenger	71
3.5.1.3	Modelling of the scavenging assuming inhomogeneous mixing of the scavenger ..	73
3.5.1.4	Model description of the OH transmission	74
3.5.2	Atmospheric OH radical measurements with the FZJ-LIF-CMR instrument during the JULIAC campaign	75
3.5.2.1	Influence of ambient conditions.....	76

3.5.2.2	Comparison of OH concentrations measured in the JULIAC campaign	79
3.5.2.3	OH interferences determined by the CMR system during the JULIAC campaign	81
3.6	Comparison of the CMR system of the FZJ-LIF instrument with systems of other LIF instruments and challenges of the application in specific environments	83

Chapter 4. Measurements of radical and trace gas concentrations and experimental chemical budgets of OH, HO₂ and RO₂ radicals in the JULIAC campaign..... 88

4.1	Measurements of radical and trace gas concentrations during the JULIAC campaign	88
4.1.1	Meteorological and chemical conditions during the JULIAC campaign	88
4.1.2	OH, HO ₂ , and RO ₂ radical concentrations and OH reactivity during the JULIAC campaign.....	93
4.1.3	Nighttime observation of OH concentrations during the JULIAC	101
4.1.4	Data quality check of radical measurements.....	102
4.2	Chemical budget calculations	103
4.2.1	OH radical chemical budget.....	103
4.2.2	HO ₂ radical chemical budget	105
4.2.3	RO ₂ radical chemical budget.....	106
4.2.4	RO _x radical chemical budget.....	107
4.2.5	Uncertainty of the calculated production and destruction rates	108
4.3	Results of the OH, HO ₂ , RO ₂ and RO _x radical chemical budgets	108
4.3.1	Results of Case #1: Chemical radical budgets for conditions with different NO mixing ratios.....	112
4.3.2	Results of Case #2: Chemical radical budgets for conditions with low NO mixing ratios and medium temperature	115
4.3.3	Results of Case #3: Chemical radical budgets for conditions with low NO mixing ratios and high temperature	117
4.4	Discussion of the chemical budget analysis	120
4.4.1	Discussion of discrepancies in the radical budgets.....	120
4.4.2	Comparisons with other field campaigns investigating the radical budgets	122

Chapter 5. Investigation of tropospheric ozone formation in a rural area in West-Germany in the JULIAC 2019 campaign	126
5.1 Determination of the net odd oxygen (O_x) production rate from ozone and NO_2 concentration measurements	126
5.2 Calculation of the net odd oxygen (O_x) production rate from turnover rates of single reactions	127
5.3 Results of the calculations of the net odd oxygen (O_x) production for measurements in the JULIAC campaign	130
5.4 Discussion of the net odd oxygen production for measurements in the JULIAC campaign.....	133
5.4.1 Comparison of results from the different methods for determining the net O_x production rate.....	133
5.4.2 Potential impact of additional O_x production or destruction reactions on the net O_x production rate.....	136
5.4.3 Potential simplification of the calculation of the net O_x production rate by using peroxy radical production rates determined from the measured OH reactivity	140
5.4.4 NO dependency of the net O_x production rates	142
Chapter 6. Summary and conclusions	145
Appendix	151
Bibliography.....	162

List of Table

Table 2. 1: Specification of instruments that performed measurements in the JULIAC campaign in the SAPHIR chamber.....	33
Table 2. 2: Experiment days in each intensive period of the JULIAC campaign 2019	36
Table 2. 3: List of VOC species measured in the JULIAC campaign.	38
Table 3. 1: Characteristics of chemical modulation reactors developed for OH LIF instruments from different groups worldwide	51
Table 3. 2: HO ₂ and RO ₂ background signals used in the evaluation of HO ₂ and RO ₂ measurements in the JULIC campaign	54
Table 3. 3: Transmission and wall-loss rate coefficients for OH and HO ₂ in the CMR	60
Table 3. 4: Operational conditions of the CMR during the JULIAC campaigns	63
Table 3. 5: Summary of meteorological conditions and trace gas concentrations during daytime of the JULIAC campaign	77
Table 3. 6: Summary of meteorological conditions and trace gas concentrations during nighttime of the JULIAC campaign	78
Table 4. 1: Chemical reactions with rate constants and their uncertainty used for the chemical radical budget analysis.....	104
Table 4. 2: Summary of trace gas concentrations and temperatures for each case study given as daytime mean values with 1σ standard deviations.....	112
Table 5. 1: Chemical reactions with rate constants and their uncertainties used for the calculation of O _x production rates.....	129
Table 5. 2: Rate constants of the reaction of organic compounds with chlorine used for the calculation of the Cl reactivity.....	139
Table A 1: Specification of the FZJ-LIF-CMR instrument used in this study.....	151

List of Figures

Figure 1. 1: Schematics of the tropospheric OH, HO ₂ , and RO ₂ radical reaction chain.	22
Figure 1. 2: Mean O _x production rates calculated from modelled and measured RO _x concentrations during the AIRPRO campaign in Beijing, China.....	29
Figure 2. 1: Picture of the SAPHIR chamber.....	32
Figure 2. 2: Schematics of the JULIAC-SAPHIR flow system.	34
Figure 2. 3: Schematics of the Jülich laser flash photolysis and laser-induced fluorescence instrument (LP-LIF) for the measurement of the OH reactivity.	37
Figure 2. 4: Time series of mixing ratios of CO ₂ in the incoming ambient air and in the chamber, and exponential decay of the measured CO ₂ mixing ratios in the chamber	39
Figure 2. 5: Concentrations of CH ₄ measured in the inlet and in the chamber and expected in the chamber	41
Figure 2. 6: Concentrations of CO ₂ measured in the inlet and in the chamber and expected in the chamber	42
Figure 3. 1: Schematic of the FZJ-LIF instrument used at the SAPHIR chamber for the detection of OH, HO ₂ and RO ₂ radicals.	44
Figure 3. 2: Schematics of a fluorescence cell in the FZJ-LIF instrument	45
Figure 3. 3: Excitation spectrum of OH showing rovibrational absorption lines around 308 nm.	45
Figure 3. 4: Schematic of the RO _x -LIF system for measurements of RO ₂ radical concentrations.....	46
Figure 3. 5: Schematic of the radical source used to calibrate the sensitivity of the FZJ-LIF instrument. .	48
Figure 3. 6: Schematic drawing of the chemical modulation reactor (CMR) that is mounted on top of the OH LIF detection cell	56
Figure 3. 7: Total OH radical transmission for varying the flow rate in the CMR.	59
Figure 3. 8: Measured and modelled (homogeneous or inhomogeneous mixing) residual factor of OH in the CMR for humidified synthetic air, and measured removal of OH inside the OH detection cell by OH scavenging.....	62
Figure 3. 9: Time series of OH concentrations measured by DOAS and LIF (with CMR) instruments in an experiment with humidified synthetic air in the SAPHIR chamber.....	66
Figure 3. 10: OH interference from the laser photolysis of ozone in humidified synthetic air for a range of concentrations of ozone, water vapor and laser power	68
Figure 3. 11: Correlation between the measured OH interference and the NO ₃ concentration measured during an experiment in the SAPHIR chamber.....	69
Figure 3. 12: Theoretical dependence of the residual factor and transmission on the OH reactivity in the sampled air (homogeneous mixing). The bias in the determination of the ambient OH signal and interference signal, if the k _{OH} dependence of the residual factor is not taken into account.	72
Figure 3. 13: Calculated dependence of the residual factor and ratio of the evaluated ambient OH signals on the OH reactivity in the sampled air using a model that takes inhomogeneous mixing of the scavenger into account.	74

Figure 3. 14: The median ratio of dark to total atmospheric OH production rates during the four periods of the JULIAC campaign.	77
Figure 3. 15: Modelled dependence of the CMR properties on the OH reactivity for the chemical conditions during the different seasons 2019 in the JULIAC campaign.....	79
Figure 3. 16: Time series of OH concentrations measured by LIF-CMR and DOAS instrument and the interference signal of the LIF instrument determined from the CMR during the summer period of the JULIAC campaign	80
Figure 3. 17: Correlation plot between OH concentrations measured by the FZJ-LIF-CMR and the DOAS instruments during the summer period of the JULIAC campaign.	81
Figure 3. 18: Measured OH concentrations and OH interference signals by the LIF instrument with the CMR system and DOAS instrument during the JULIAC campaign in the winter, spring and autumn periods.....	82
Figure 3. 19: Averaged OH interference measured during all periods of the JULIAC campaign compared to calculations of the expected ozone interference	83
Figure 4. 1: Time series of temperature and trace gas concentrations during the winter period of the JULIAC campaign	89
Figure 4. 2: Time series of temperature and trace gas concentrations during the spring period of the JULIAC campaign	90
Figure 4. 3: Time series of temperature and trace gas concentrations during the summer period of the JULIAC campaign	91
Figure 4. 4: Time series of temperature and trace gas concentrations during the autumn period of the JULIAC campaign	92
Figure 4. 5: Time series of OH, HO ₂ , and RO ₂ concentration measured by the FZJ-LIF-CMR instrument and OH reactivity (k _{OH}) measured by the FZJ-LP-LIF instrument during the winter period of the JULIAC.	95
Figure 4. 6: Time series of OH, HO ₂ , and RO ₂ concentration measured by the FZJ-LIF-CMR instrument and OH reactivity (k _{OH}) measured by the FZJ-LP-LIF instrument during the spring period of the JULIAC campaign.....	96
Figure 4. 7: Time series of OH, HO ₂ , and RO ₂ concentration measured by the FZJ-LIF-CMR instrument and OH reactivity (k _{OH}) measured by the FZJ-LP-LIF instrument during the summer period of the JULIAC campaign	97
Figure 4. 8: Time series of OH, HO ₂ , and RO ₂ concentration measured by the FZJ-LIF-CMR instrument and OH reactivity (k _{OH}) measured by the FZJ-LP-LIF instrument during the autumn period of the JULIAC campaign	98
Figure 4. 9: Median values of the diurnal profiles of OH, HO ₂ , RO ₂ , concentrations, OH reactivity, j(O ¹ D), NO, O ₃ mixing ratios measured during spring and summer periods of the JULIAC campaign.	99
Figure 4. 10: Median values of the diurnal profiles of OH, HO ₂ , RO ₂ concentrations, OH reactivity, j(O ¹ D), NO, O ₃ mixing ratios measured during winter and autumn periods of the JULIAC campaign. ..	100
Figure 4. 11: Correlation plot between OH concentrations measured by the FZJ-LIF-CMR instrument and the photolysis frequency of ozone leading to O(¹ D) during the JULIAC campaign	101
Figure 4. 12: Time series of total production and destruction rates of OH, HO ₂ , RO ₂ , and RO _x radicals during the spring period of the JULIAC campaign.....	110

Figure 4. 13: Time series of total production and destruction rates of OH, HO ₂ , RO ₂ , and RO _x during the summer period of the JULIAC campaign	111
Figure 4. 14: Production and destruction rates of OH, HO ₂ , and RO ₂ radicals for the period of Case #1.	113
Figure 4. 15: Production and destruction rates of RO _x radicals for the period of Case #1.....	114
Figure 4. 16: Median values of production and destruction rates of OH, HO ₂ , and RO ₂ radicals for the period of Case #2	116
Figure 4. 17: Median values of production and destruction rates of RO _x radicals for the period of Case #2	117
Figure 4. 18: Median values of production and destruction rates of OH, HO ₂ , and RO ₂ radicals for the period of Case #3	118
Figure 4. 19: Median values of production and destruction rates of RO _x radicals for the period of Case #3	119
Figure 5. 1: Concentrations of O _x measured in the inlet and the chamber and expected in the chamber.	126
Figure 5. 2: Time series of O _x production rates calculated from NO ₂ and O ₃ measurements in the incoming air and in the chamber during the spring period of the JULIAC campaign	131
Figure 5. 3: Time series of O _x production rates calculated from NO ₂ and O ₃ measurements in the incoming air and in the chamber during the summer period of the JULIAC campaign	131
Figure 5. 4: Median diel profiles of turnover rates of reactions contributing to the O _x production and destruction for the spring period and the summer period of the JULIAC campaign.	132
Figure 5. 5: Time series of the net O _x production rate calculated from either NO ₂ and O ₃ measurements or turnover rates of reactions for the spring and summer periods of the JULIAC campaign.....	134
Figure 5. 6: Median diel profiles of the net O _x production rates calculated from either NO ₂ and O ₃ measurements or turnover rates of reactions using the base chemistry or the extended chemistry during the spring and summer periods of the JULIAC campaign	135
Figure 5. 7: Correlations between the net O _x production rates calculated from either NO ₂ and O ₃ measurements or turnover rates of reactions using the base chemistry or the extended chemistry during the spring and summer periods of the JULIAC campaign	135
Figure 5. 8: Median diel profiles of turnover rates of reactions contributing to the O _x production and destruction for the spring period and the summer period of the JULIAC campaign	137
Figure 5. 9: Chlorine radical reactivity calculated from measured reactant concentrations for the period from 5 August to 8 August of the JULIAC campaign.	138
Figure 5. 10: Time series of O _x production rates either calculated from NO ₂ and O ₃ measurements or from turnover rates of reactions using peroxy radical production rates calculated from OH reactivity measurements for the period from 19 April to 24 April and from 23 August to 29 August of the JULIAC campaign.....	140
Figure 5. 11: Median diel profiles of the net O _x production rate calculated from either NO ₂ and O ₃ measurements or turnover rates of reactions using peroxy radical production rates calculated from OH reactivity measurements for the spring and summer periods of the JULIAC campaign	141
Figure 5. 12: NO dependence of median O _x production rates derived from the different methods during the spring and summer periods of the JULIAC campaign	143

Figure A. 1: Chemical budgets for OH, HO ₂ , and RO ₂ radicals (Case #1 period) using the high limits for the concentration of alkene species that contribute to radical production by ozonolysis reactions	154
Figure A. 2: Chemical budget for the sum of OH, HO ₂ , and RO ₂ radicals (Case #2 period) using the high limits of alkene concentrations contributing to radical production by ozonolysis reactions	155
Figure A. 3: Chemical budget for the sum of OH, HO ₂ , and RO ₂ radicals (Case #3 period) using the high limit of alkene concentrations contributing to radical production by ozonolysis reactions.....	156
Figure A. 4: Chemical budgets for OH, HO ₂ , and RO ₂ radicals using the upper limit of the RO ₂ background signal	157
Figure A. 5: Chemical budgets for OH, HO ₂ , and RO ₂ radicals in the spring period, when NO concentrations were low, using the low limit of the reaction rate coefficient of the reaction of RO ₂ with NO, $1.1 \times 10^{-12} \text{ cm}^3 \text{ s}^{-1}$ to calculate the turnover rate of this reaction.	158
Figure A. 6: Chemical budgets for OH, HO ₂ , and RO ₂ radicals (Case #2 period) using the low limit of the reaction rate coefficient of the reaction of RO ₂ with NO, $7.7 \times 10^{-12} \text{ cm}^3 \text{ s}^{-1}$ to calculate the turnover rate of this reaction.....	159
Figure A. 7: Timeseries of calculated O _x production rates using different methods.....	160

Chapter 1 Introduction

1.1 Tropospheric OH, HO₂, and RO₂ radical chemistry

The troposphere is the lowest layer of the atmosphere of the Earth where we live. The composition of the ambient air is influenced by the emissions from human activities and natural processes, which impact both the quality of the air we breathe and the Earth's climate. During the last few centuries, the chemical composition of the troposphere has been drastically impacted by human activities, which caused, among others, photochemical smog, acidic rain, and affected the climate (Finlayson-Pitts, 2000). The World Health Organization (WHO (2016)) reported that air pollution contributes to approximately 7 million premature deaths per year, and about 92 % of the worldwide population is exposed to toxic air. In total, 0.6 million children die every year from air pollution making it the most frequent cause of death of children (WHO (2018)). The severe impacts of air pollution on human life and the planet have drawn an interest to investigate atmospheric chemistry and establish efficient air pollution regulatory policies.

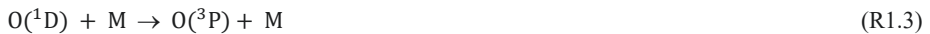
Air pollution is caused not only by the emission of primary pollutants, but also by secondary pollutants generated through the oxidation process of the primary pollutants in the atmosphere. The investigation of the radical mechanism is essential to study the degradation process of atmospheric trace gases and develop air pollution control strategies.

The hydroxyl radical, OH, is a highly reactive oxidant and therefore it has typically a sub-second chemical lifetime in the atmosphere. Due to its high reactivity, OH is the most active daytime atmospheric oxidant making it responsible for the chemical transformation of most trace gases (Finlayson-Pitts, 2000).

In the troposphere, OH is primarily produced via the photolysis of O₃ (Reaction R1.1) at short wavelengths ($\lambda < 340$ nm) (Takahashi et al., 2002) and the subsequent reaction of an electronically excited oxygen atom, O(¹D), with water vapor (Reaction R1.2).



O(¹D) can also be quenched via collisions with other molecules (M: N₂ and O₂) yielding an oxygen atom in the ground state, O(³P), that reacts with O₂ and regenerate O₃ (Reaction R1.3 and R1.4).



As the OH formation rate depends on the water vapor mixing ratio, the OH production rate by the photolysis of O₃ can be calculated as:

$$P_{\text{OH},\text{O}_3+h\nu} = 2 j(\text{O}^1\text{D}) \times [\text{O}_3] \times \varphi_{\text{OH}} \quad (\text{Eq. 1.1})$$

where $j(O^1D)$ is the photolysis frequency for the formation of $O(^1D)$ and φ_{OH} is the branching ratio of the reaction of $O(^1D)$ with H_2O (Reaction R1.2) and $O(^1D)$ taking quenching by N_2 and O_2 into account:

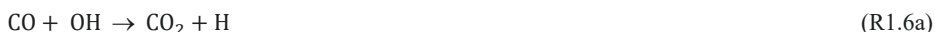
$$\varphi_{OH} = \frac{k_{R1.2}[H_2O]}{k_{R1.2}[H_2O] + k_{R1.3}[N_2] + k_{R1.3}[O_2]} \quad (\text{Eq. 1.2})$$

k_i is the reaction rate coefficients for the given reactions (Atkinson et al., 2004). The photolysis of nitrous acid (HONO) (Reaction R1.5) can also be an important primary OH source (Alicke et al., 2003; Kleffmann et al., 2005; Li et al., 2014):



In addition, OH can be primarily produced from the photolysis of oxygenated VOCs such as unsaturated hydroperoxyl aldehyde (HPALD) (Peeters and Müller, 2010; Wolfe et al., 2012; Liu et al., 2017) and methanol (Atkinson et al., 2006) and from the ozonolysis reaction of alkenes (Jenkin et al., 2019).

The produced OH radical initiates the oxidation of inorganic and organic compounds. In the case of carbon monoxide (CO) (Reaction R1.6) and volatile organic compounds (VOCs) (Reaction R1.7), hydroperoxy radicals (HO_2) and organic peroxy radicals (RO_2) are produced in a radical chain reaction (Figure 1.1):



In the atmosphere, there are more than $10^4 - 10^5$ of inorganic and organic compounds that react with OH. All atmospheric reactants (X_i) are summarized in the total OH reactivity (k_{OH}) that is the inverse of the chemical OH lifetime (τ_{OH}):

$$k_{OH} = \frac{1}{\tau_{OH}} = \sum_i k_{OH+X_i} [X_i] \quad (\text{Eq. 1.3})$$

Here, k_{OH+X_i} represents the rate coefficient for the reaction of OH with X_i .

In the presence of NO, the formed RO_2 reacts with NO to produce alkoxy radicals (RO) and NO_2 (Reaction R1.8). The alkoxy radicals can undergo three different competing reaction pathways: 1) they can react with O_2 to yield HO_2 and a carbonyl compound (Reaction R1.9), 2) they can undergo unimolecular isomerization, which yields a hydroxy-substituted alkoxy radical, 3) or they can undergo unimolecular decomposition to generate an alkyl fragment (R'') and a carbonyl compound (Reaction R1.10) (Orlando et al., 2003).





A minor fraction (5 – 20 % depending on the organic moiety (Jenkin et al., 2019)) of the reaction of RO_2 with NO produces alkylnitrate compounds (RONO_2) (Reaction R1.11).



HO_2 also reacts with NO regenerating an OH radical (Reaction R1.12).



Due to this efficient radical regeneration process, OH concentrations on the order of 10^6 cm^{-3} can be sustained even in environments where the OH reactivity is high. NO_2 produced in the reaction of peroxy radicals (HO_2 and RO_2) with NO can photolyze back to NO producing O_3 (Reaction R1.13 and R1.4).



This net ozone production is the most important source of tropospheric ozone. As the produced NO quickly reacts with O_3 yielding NO_2 again (Reaction R1.14), NO , NO_2 and O_3 reach a photo-stationary state in the troposphere.



Reactions of OH with NO_2 can terminate the radical propagation by producing nitric acid (HNO_3) (Reaction R1.15).



Also, HO_2 and RO_2 react with NO_2 (Reaction R1.16 and R1.17) to produce peroxy-nitric acid (HO_2NO_2) and peroxy-alkyl nitrates (RO_2NO_2) that can act as radical reservoir species.



However, HO_2NO_2 and RO_2NO_2 are thermally labile and can quickly decompose back to peroxy radicals and NO_2 . Therefore, concentrations are in a thermal equilibrium.

In environments with low NO concentrations, HO_2 and RO_2 radical recombination reactions (Reaction R1.18 – 1.20) can become competitive with the reaction of peroxy radicals with NO and can therefore play an important role in the termination of the RO_x cycle.



In addition, RO₂ can undergo unimolecular H-shift reactions (Vereecken and Nozière, 2020). Subsequent decomposition of the products could produce OH and HO₂ radicals. The reaction rate coefficient highly depends on the structure of organic moiety. The most widely known example of unimolecular H-shift reactions of RO₂ is the isomerization of RO₂, which are produced from the isoprene oxidation by OH (Peeters et al., 2009; Peeters and Müller, 2010; Crouse et al., 2011; Peeters et al., 2014). Recently, theoretical calculations of the reactions in the photo-oxidation of isoprene (Leuven Isoprene Mechanism, LIM) revealed specific RO₂ isomers formed in the reaction of isoprene with OH can undergo fast H-shift reactions (Peeters et al., 2014). An HO₂ radical together with an hydroperoxy-aldehyde (HPALD) are formed, which can rapidly produce OH by its photolysis. The impact of the isomerization reaction of the specific RO₂ isomers is enhanced, because several RO₂ isomers can rapidly interconvert. Because these H-shift reactions are unimolecular reactions, they increase in importance, if concentrations of reactants of competing bi-molecular RO₂ reactions such as NO are small as it is typically observed in forested environments. Radical production from RO₂ isomerization reaction has also been found for one of the most important organic products of isoprene, methacrolein (Crouse et al., 2012, Fuchs et al., 2018). Furthermore, some RO₂ produced from the aromatic and monoterpene oxidations by OH or ozone can undergo H-shift reactions with the subsequent addition of O₂ to the alkyl position and form highly oxidized RO₂, which can contribute to the formation of highly oxidized molecules (HOMs).

Recent studies (George et al., 2007; Taketani et al., 2008, 2009; George et al., 2013; Lakey et al., 2015; Song et al., 2020) found that HO₂ uptake onto aerosol surfaces could be another significant radical-termination process.

Stable products of radical termination reactions (Reaction R1.11 and R1.18 – 1.21), for example, HNO₃, ROOH, RONO₂ and ROOR, can be often removed out of the atmosphere by washout by precipitation. They can also be deposited on aerosol and thereby contribute to the formation of secondary organic aerosol (SOA).

Secondary products from the oxidation of VOCs, for example formaldehyde (HCHO), can be important sources of HO₂ for example from photolysis reactions (Reaction R1.21 – 1.24) and the reaction with OH (Reaction R1.25).



In addition, as for the OH radicals, HO₂ and RO₂ are produced from the ozonolysis of alkenes.

Recent studies (Young et al., 2014; Bannan et al., 2015; Le Breton et al., 2018; Sommariva et al., 2021) showed that the oxidation of VOCs by chlorine atom (Cl), which can be for example produced by the photolysis of nitryl chloride (ClNO₂) that accumulates during the night can be a source of RO₂

radicals in particular in the early morning. Finally, the nitrate radical (NO_3) produces RO_2 radicals after its reaction with VOCs in particular during nighttime (Sillman et al., 2002; Lu et al., 2014; Stone et al., 2014).

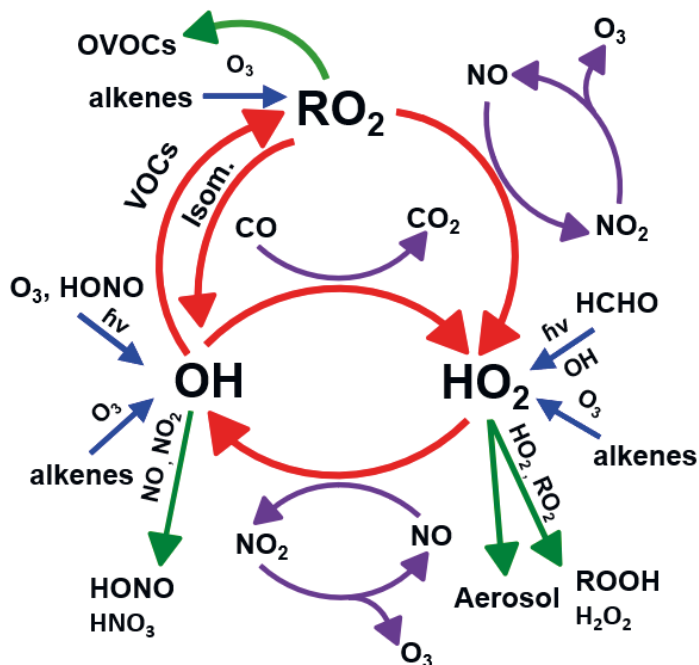


Figure 1. 1: Schematics of the tropospheric OH , HO_2 , and RO_2 radical reaction chain. Red arrows represent inter-radical conversion reactions. Blue and green arrows show radical initiation and radical termination reactions, respectively.

1.2 Detection of atmospheric OH , HO_2 and RO_2

OH , HO_2 and RO_2 radical concentrations are typically small in the troposphere. This makes their detection in ambient air very challenging as it requires a high detection sensitivity and low radical loss during sampling. Calibration methods are needed, in which a known concentration of radicals is produced, because it is not possible to store radicals in a calibration standard gas mixture like done for other trace gases. So far, several methods have been used for the measurements of OH , HO_2 and RO_2 radicals in ambient air, including laser-induced fluorescence (LIF), chemical ionization mass spectrometry (CIMS), peroxy radical chemical amplification (PERCA), differential optical absorption spectrometry (DOAS) and matrix isolation electron spin resonance spectroscopy (MIESR).

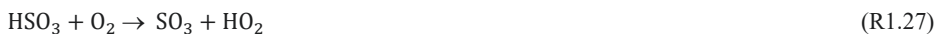
The laser-induced fluorescence (LIF) technique is the most commonly used method for the detection of atmospheric OH radicals. The atmospheric OH radical measurement by LIF was

pioneered in 1975 using pulsed laser excitation of OH at an absorption line at 282nm ($A(v' = 1) - X(v'' = 0)$ vibronic transition) (Baardsen and Terhune, 1972; Wang and Davis, 1974; Hard et al., 1984). The excited OH molecules emit fluorescence at longer wavelengths ($\lambda = 311-307$ nm), and the emitted photons can be collected by a photomultiplier tube (PMT). Although this method can discriminate scattered laser light from fluorescence with an optical filter, the excitation at 282nm has the disadvantage that high concentrations of artificial OH is concurrently produced by the efficient photolysis of ozone in the detection cell (Smith and Crosley, 1990). To reduce this interference, OH excitation at an absorption line at 308nm ($A(v' = 0) - X(v'' = 0)$ vibronic transition) is used in current LIF instruments for the detection of OH, since the absorption cross section for ozone is a factor of 30 lower at 308 nm compared to 282nm. The 308 nm excitation wavelength also increases the OH detection sensitivity by a factor of 4 because of the high OH absorption cross section. Since the fluorescence photons are collected at a similar wavelength range between 311–307nm, a time delayed gated photon detection and counting system is used (Stevens et al., 1994; Holland et al., 1995; Heard and Pilling, 2003). A short laser pulse (10 – 40 ns) with a high repetition rate (5 – 10 kHz) is applied to separate the OH fluorescence that lasts for several 100ns at low pressure from the laser-scattered light (Hofzumahaus and Heard, 2016). To minimize physical and chemical loss of OH and to increase the fluorescence lifetime of OH by reducing collisional quenching, ambient air is sampled into a low pressure (~4 hPa) detection cell through a critical orifice (Fluorescence Assay by Gas Expansion, FAGE).

With the LIF technique, also HO₂ radicals can be indirectly measured by its chemical conversion to OH in the reaction with NO (Reaction R1.12), which is injected in the detection cell. The converted OH is subsequently measured with the same detection set-up as for OH giving total HO_x (OH + HO₂) concentrations. The HO₂ concentration is obtained by subtracting the contribution of the signal from ambient OH. Recently, some LIF instruments have been extended to measure RO₂ concentrations. This can be achieved by the addition of a chemical converter, in which RO₂ radicals are converted to HO₂ by NO (Reaction R1.8 and R1.9) on top of the fluorescence cell (Fuchs et al., 2008; Whalley et al., 2013; Lahib, 2019). Excess CO is added in the converter to convert OH that is formed in the reaction of HO₂ with NO back to HO₂ (Reaction R1.6), because OH has a higher wall loss rate compared to HO₂. Consequently, only HO₂ radicals are present at the end of converter. Downstream of the converter, the formed HO₂ is sampled into the detection cell, in which it is further converted to OH by the reaction with excess NO (Reaction R1.12). The RO₂ concentration is obtained by subtracting the contribution of the ambient HO_x concentrations. A detailed description on the OH, HO₂ and RO₂ radical measurements by the FZJ-LIF instrument used in this work can be found in Chapter 2.

The chemical ionization mass spectrometry (CIMS) technique has also been widely used for field measurements of OH and peroxy radicals, especially in pristine and forested environments (Berresheim et al., 2000; Handisides et al., 2003; Sanchez et al., 2018; Lew et al., 2020). With the CIMS instrument, OH radicals are indirectly measured by the chemical conversion of isotopically labelled ³⁴SO₂ to sulfuric acid (H₂³⁴SO₄) and subsequent detection of H³⁴SO₄⁻ (Reaction R1.26-28) by mass spectrometry (Eisele and Tanner, 1991; Tanner et al., 1997; Berresheim et al., 2000).





Although the CIMS technique has the lowest detection limit for the measurement of OH radicals ($1 - 3 \times 10^5 \text{ cm}^{-3}$) (Tanner et al., 1997; Heard and Pilling, 2003), it can suffer from interferences in polluted environments where the ambient NO_x level is higher than 2 ppbv because of the OH regeneration from the reaction of NO and HO_2 (Tanner et al., 1997).

HO_2 and RO_2 radicals can be measured by the CIMS instrument by conversion to OH with NO in the inlet. In contrast to the LIF instruments, the concentration of the measured species, H_2SO_4 , is amplified, because a reaction cycle is established in the inlet system (Reaction R1.12, R1.26-28), in which several H_2SO_4 molecules per sampled RO_x molecule are formed, before the air enters the mass spectrometer (typical chain length of 10 - 15) (Cantrell et al., 2003; Edwards et al., 2003; Ren et al., 2005; Hornbrook et al., 2011). Recently, a direct measurement of HO_2 using the CIMS method has been developed. In these instruments, HO_2 is detected as an ion cluster (HO_2Br^-) (Sanchez et al., 2016; Albrecht et al., 2019).

Another indirect technique for the measurement of peroxy radicals is the peroxy radical chemical amplification (PERCA). With this technique, the sum of HO_2 and RO_2 radicals concentrations is obtained. The initial radical concentration is amplified as NO_2 in a reaction cycle that is established by the injection of NO and CO in the inlet of the instrument (Reaction R1.6, R1.8, R1.12, chain length 50 to 100). NO_2 is then measured by a Luminol detector, laser-induced fluorescence, cavity ring-down spectroscopy (CRDS) or cavity enhanced-absorption spectroscopy (CEAS) (Hernández et al., 2001; Edwards et al., 2003; Sadanaga et al., 2004; Green et al., 2006; Liu and Zhang, 2014).

While LIF and CIMS instruments require calibration of the sensitivity by applying a radical source that produces a known amount of OH, HO_2 and RO_2 radical concentration, the differential optical absorption spectrometry (DOAS) is an absolute method for the detection of OH radicals as it relies only on the molecular differential absorption cross-section of OH and the optical path length. The DOAS measures ambient OH concentrations based on the wavelength-dependent absorption. A picosecond long laser pulse is passed through the air and the transmitted light intensity is spectrally analyzed by an Echelle grating spectrograph coupled to a linear photodiode array detector. Lambert-Beers law cannot be directly applied because the light intensity without absorber is not concurrently measured. Therefore, a polynomial function that is fitted to the light intensity as a function of the wavelength is subtracted from the measured transmitted intensity. The polynomial function describes the wavelength dependent initial light intensity that is reduced by scattering of the light and the part of the absorption by trace gases, which has a weak wavelength dependence. After the subtraction, only narrow absorption lines of trace gases are left in the signal. Lambert-Beers law can be then applied by replacing the initial light intensity by the polynomial fit function and the absorption cross section by the differential absorption cross section that needs to be experimentally determined. If several absorbers are present, a superposition of the differential absorptions of the single compounds is optimized to describe the total signal. The DOAS instrument is the most accurate instrument for the measurement of OH concentrations with an 1σ accuracy of 6.5% because it is only limited by the knowledge of the differential absorption cross section and the optical path length (Hausmann et al., 1997). Therefore, it is used as a reference for OH measurements (Hofzumahaus and Heard, 2016).

The only currently available DOAS instrument for the measurement of atmospheric OH radicals is permanently mounted in the atmospheric simulation chamber SAPHIR (Simulation of Atmospheric Photochemistry In a large Reaction Chamber) at Forschungszentrum Jülich, Germany (Dorn et al., 1996; Hausmann et al., 1997; Schlosser et al., 2007; Schlosser et al., 2009)

Concentrations of HO₂, RO₂, and CH₃CO₃ radicals have also been measured by matrix isolation electron spin resonance spectroscopy (MIESR) (Mihelcic et al., 1985; Mihelcic et al., 1990; Mihelcic et al., 2003). Briefly, the radicals in the air are sampled through a nozzle and trapped in an ice matrix at a temperature of 77 K. Radical concentrations are measurement by electron spin resonance (ESR) spectroscopy in the laboratory. Due to the similar electronic structure of most RO₂ radicals, this method cannot distinguish between different RO₂ radicals except for CH₃CO₃. Although this technique does not require calibration, it has a few critical limitations. First, a long sampling time is required to trap a sufficient number of radicals and the analysis of one sample takes approximately 8 hours, which results in a very low time resolution, and it is very demanding for the operators. Second, it requires maintaining the sample at very low temperature between sampling and analysis, which is difficult to achieve during field campaigns especially in remote locations. Consequently, this technique has not been employed since 2005.

1.3 Measurement-model comparisons of ambient radical concentrations measured in field campaigns in various environments

Measurements of OH, HO₂ and more recently RO₂ radicals have been performed in various field campaigns from a small number of groups worldwide. Results are often used to test the current understanding of OH, HO₂ and RO₂ radical concentrations by comparing measured concentrations to calculations using numerical chemical box models, in which radical precursors and OH reactants are constrained to measurements.

In forested environments characterized by low NO_x (NO + NO₂) levels and emissions of biogenic VOCs (BVOCs) like isoprene and monoterpenes, discrepancies between simulated and observed OH and HO₂ radical concentration were largely diverse. In isoprene-rich forests such as tropical forests, there was a tendency for models to underestimate OH radical concentrations up to a factor of 10 whilst HO₂ concentrations were relatively well predicted (Tan et al., 2001; Lelieveld et al., 2008; Kubistin et al., 2010; Whalley et al., 2011). The missing OH source was attributed to a regeneration reaction of OH in oxidation process of isoprene. Theoretically postulated (Peeters et al., 2009; da Silva et al., 2010; Peeters and Müller, 2010; Peeters et al., 2014; Wang et al., 2018) and experimentally confirmed (Crouse et al., 2011; Berndt, 2012; Crouse et al., 2012; Wolfe et al., 2012; Fuchs et al., 2013; Fuchs et al., 2014; Teng et al., 2017; Fuchs et al., 2018; Novelli et al., 2020) RO₂ isomerization reactions in the oxidation of isoprene could partly explain the field observations. In forests, where monoterpenes dominate hydrocarbon, such as boreal forests, both of OH and HO₂ were significantly underpredicted by simulations (Wolfe et al., 2011; Kim et al., 2013; Hens et al., 2014; Wolfe et al., 2014; Griffith et al., 2016). The data analysis showed that an unknown, additional HO₂ source was missing in the models. Consequently, the predicted HO₂ concentration and the OH production from the reaction of HO₂ with NO were underestimated, causing also an underprediction

of OH. Consistent with field observations, theoretical (Vereecken et al., 2007; Vereecken and Peeters, 2012; Møller et al., 2020) and chamber (Kubistin et al., 2010; Rolletter et al., 2019) studies also conclude that HO₂ is more efficiently regenerated in the oxidation of monoterpenes than is currently explained by models.

For field campaigns in polluted urban region, where radical propagation is often dominated by the reaction of peroxy radicals with NO, OH radical concentrations predicted by box model calculations could often reproduce the observation within 50%, if NO mixing ratios were high (> 1 ppbv), while calculated HO₂ concentrations were substantially underpredicted by up to a factor of 3. This discrepancy had an increasing tendency for increasing NO_x concentrations (Ren et al., 2006; Dusanter et al., 2009; Chen et al., 2010; Ren et al., 2013; Brune et al., 2016; Griffith et al., 2016; Chen et al., 2017; Tan et al., 2018; Whalley et al., 2018; Slater et al., 2020; Whalley et al., 2020). Similar as for HO₂ radicals, simulated RO₂ concentrations showed significant discrepancies compared to observations for NO levels higher than 1 ppbv. These discrepancies cause a large underestimation of net ozone production rates in models for high NO_x conditions (Tan et al., 2018; Whalley et al., 2018; Slater et al., 2020; Whalley et al., 2021).

In semi-polluted suburban and rural regions, where a wide range of VOC and NO_x conditions can be encountered by the transport of plumes from nearby cities or forests, diverse results from the comparison of modelled and measured OH and HO₂ radical concentrations were found. In the BERLIOZ (BERLIner Ozone experiment, 1998) campaign performed in the small town Pabstthum, Germany, it was found that the model could reproduce the observed OH, HO₂ and RO₂ concentrations also at high NO_x mixing ratios (>5 ppbv), when the air masses were transported from the city of Berlin, but the model overpredicted the radical concentrations by a factor of 1.5 to 2 even at low NO_x conditions in most cases (Konrad et al., 2003; Mihelcic et al., 2003). On the other hand, in field campaigns in the Pearl River Delta, China (Hofzumahaus et al., 2009; Lou et al., 2010; Lu et al., 2012), and in Michigan, USA (Sillman et al., 2002), as well as in Wangdu, China (Tan et al., 2017), observed OH concentrations were higher than the model results by a factor of 3-5 at NO levels below 1 ppbv. In contrast, measured HO₂ concentrations were well described by the simulation (within 30%), suggesting that additional OH regeneration from RO₂ and/or the presence of additional primary radical source were needed to explain the observations. The study by Tan et al. (2017) in particular found a good agreement between modelled and observed RO₂ concentrations at low NO (<0.3ppbv), but the simulation showed a significant underestimation of RO₂ by a factor of 3 to 5 when the NO mixing ratio exceeded 1 ppbv. Another study performed in Jülich, Germany, (Kanaya et al. (2012)) found that model results could reproduce the observed OH concentrations, but the modelled HO₂ concentrations overestimated significantly by a factor of 1.9 the measured HO₂ radical concentrations over a range of NO mixing ratios from 0.1 to 10 ppbv.

The level of agreement between simulated and observed radical concentrations in various environments shows the degree of understanding of the underlying radical chemical mechanisms. Even though good agreement was found in some cases, there were significant unexplained discrepancies between modelled and observed concentrations of OH in isoprene-rich forested regions (Tan et al., 2001; Lelieveld et al., 2008; Kubistin et al., 2010; Whalley et al., 2011) and of HO₂ and RO₂ in both of monoterpene-rich forested (Wolfe et al., 2011; Kim et al., 2013; Hens et al., 2014; Wolfe et al., 2014; Griffith et al., 2016) and polluted areas (Tan et al., 2018; Whalley et al., 2018;

Slater et al., 2020; Whalley et al., 2021), while different results were found depending on the abundance of NO in rural environments (Konrad et al., 2003; Mihelcic et al., 2003; Kanaya et al., 2007; Hofzumahaus et al., 2009; Lou et al., 2010; Lu et al., 2012; Tan et al., 2017).

A chemical budget analysis using measured OH, HO₂ and RO₂ radical concentrations is an alternative method to assess the strength of different radical production and loss paths. This allows to identify possible missing chemical processes. The experimental budget is performed by comparing the total production and destruction rates for the different radicals. This requires that radical concentrations are in a steady state, but this assumption is typically justified due to their short chemical lifetime. As a large number of measurements needs to be available (e.g., k_{OH}, OH, peroxy radicals), there have been only few studies focusing on the analysis of the experimental budget for OH radicals so far (Handisides et al., 2003; Hofzumahaus et al., 2009; Brune et al., 2016; Whalley et al., 2018; Tan et al., 2019; Whalley et al., 2021).

In field campaigns in China, a larger OH radical destruction rate compared to the production rate was observed in the afternoon pointing to a missing OH radical source, especially, when NO mixing ratios are low (< 2 ppbv) (Hofzumahaus et al., 2009; Tan et al., 2019; Whalley et al., 2021). On the other hand, studies in the USA and Europe showed no significant gap between the OH production and destruction rates (Handisides et al., 2003; Brune et al., 2016; Whalley et al., 2018). Recently, radical measurements including RO₂ enabled the investigation of HO₂, RO₂ and RO_x production and destruction rates in field campaigns in China (Tan et al., 2019; Whalley et al., 2021). Tan et al. (2019) showed that a missing RO₂ loss process was required to balance production and destruction rates in Wangdu in summer, while HO₂ production and destruction rates were balanced. This suggests a missing conversion process of RO₂ radicals to OH in addition to the reaction of peroxy radicals with NO. Whalley et al. (2021) found large imbalances in the peroxy radical budgets for measurements in Beijing, indicating a substantially slower propagation of RO₂ radicals to HO₂.

1.4 Calculation and measurement of ozone production rates in field campaigns

Tropospheric ozone is a hazardous air pollutant that affects the environment and human health in multiple ways. In addition, ozone is as a greenhouse gas that contributes to the climate warming. In addition to its direct radiative forcing, ozone can have a warming effect due to its negative impact on vegetation resulting in a decreased CO₂ consumption by plants (Simpson et al., 2014). Due to its strong damaging effect on plants, ozone decreases crop yields, so that high ozone concentrations can be a threat for global food security and ecosystem functions (Ainsworth et al., 2012; Bisbis et al., 2018; Mills et al., 2018). The highest concern, however, is the impact on human health. Ozone has been linked to cardiorespiratory diseases and to an increased infant mortality (Requia et al., 2017; Schraufnagel et al., 2019). It is estimated that increased ground ozone concentrations cause a million of premature deaths per a year (Cohen et al., 2017). Therefore, efficient regulatory strategies for ozone are essential to improve air quality.

Tropospheric ozone is nearly exclusively produced by the reactions of peroxy radicals (HO₂ and RO₂) with NO (Reaction R1.8, R1.12). In the troposphere, ozone is in a photochemical equilibrium

with NO₂ which acts as a reservoir for ozone (Section 1.1). Therefore, the production of O_X (the sum of O₂ and NO₂), P(O_X), can be interpreted as an ozone production potential. This approach is only valid, if there are no direct emissions of NO₂ as it is the case for example for vehicle emissions. The major O_X loss is the reaction of NO₂ with OH to form HNO₃ (Reaction R1.15). Therefore, the net instantaneous O_X production rate (P_{O_X}) can be calculated as (Martinez et al., 2003; Kanaya et al., 2007; Ren et al., 2013; Brune et al., 2016):

$$P_{O_X} = k_{NO+HO_2}[NO][HO_2] + k_{NO+RO_2}[NO][RO_2] - L_{O_X}, \quad (\text{Eq. 1.4})$$

where L_{O_X} represents the O_X loss rate including the reaction of NO₂ with OH and other O₃ and NO₂ loss pathways.

The calculation of the ozone production rate using Eq. 1.4 requires OH, HO₂ and RO₂ radical concentrations either from measurements or model calculations. Therefore, discrepancies between radical concentrations from models and measurements not only question our knowledge of chemical mechanisms, but also strongly affect the ability of atmospheric models to correctly predict ozone concentrations. Previous studies have calculated the O_X production rates based on modelled and measured HO_X (OH + HO₂) radical concentrations in urban areas (Martinez et al., 2003; Kanaya et al., 2007; Ren et al., 2013; Brune et al., 2016). As these studies found that box model calculations could reproduce HO₂ concentrations for ambient NO concentration below a few ppbv, O_X production can be expected to be well predicted for these conditions. For high NO concentration, however, the O_X production rate using modelled HO₂ has been found to be smaller compared to using measured HO₂ due to the inability of the model to correctly predict HO₂ concentrations (Brune et al., 2016). In addition, the lack of measured RO₂ radical concentrations limited the analysis. Recently, Whalley et al. (2021) showed a comparison of the O_X production rates from model and measurement of RO_X in the center of Beijing using measurements from their newly developed RO_X-LIF system. This study also found a large discrepancy between O_X production rates calculated using either modelled or measured radical concentrations due to the large underestimation of modelled HO₂ and RO₂ concentrations compared to measurements (Figure 1.2).

In the last ten years, several instruments have been built to directly measure the ozone production rate in ambient air. This measurement was pioneered by Cazorla and Brune (2010) with the Measurement of Ozone Production Sensor (MOPS). This method relies on the comparative measurement of ozone evolving in two flow reactors (volume of 10 – 30 L). One reactor is kept in the dark (reference chamber), while the other is exposed to sunlight (irradiated chamber). The residence times of the sampled air in the reactors is on the order of 5 min. Photochemical ozone production can occur only in the irradiated chamber and other processes impacting the ozone concentration occur in both chambers in the same way. The net O₃ production rate can then be calculated from the difference of the measured O₃ concentrations in both chambers. The method applied by the MOPS instrument has several limitations for example due to the high uncertainty of wall effects such as heterogeneous NO₂ loss that can vary with relative humidity (Cazorla et al., 2012) and HONO production from Teflon surfaces in the irradiated chamber (Baier et al., 2015).

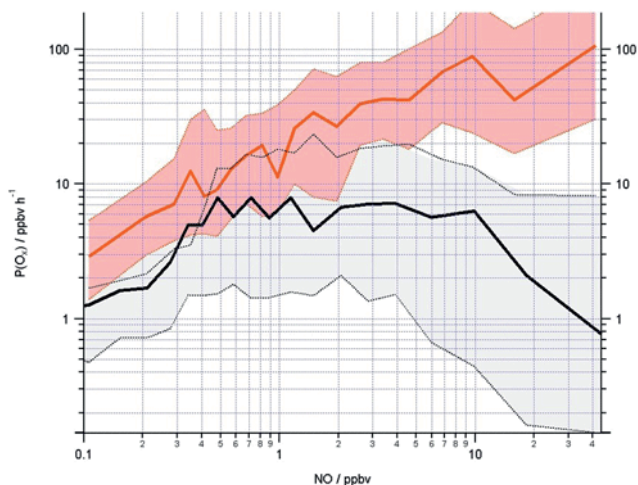


Figure 1. 2: Mean O_X production rates calculated from modelled (black line) and measured (red line) RO_X concentrations during the AIRPRO campaign in Beijing, China. Coloured areas represent 25th and 75th percentile confidence limits. Adapted from the open access publication Whalley et al. (2021), under the CC BY 4.0 license (<https://creativecommons.org/licenses/by/4.0>).

More recently, ozone production rate (OPR) systems were further developed in different groups using a similar measurement principle (Sadanaga et al., 2017; Sklaveniti et al., 2018). The major differences of the OPR instrument compared to the MOPS instrument is the use of a quartz flow tubes instead of Teflon tubes. However, O_3 and NO_2 losses can become very significant in the instruments, so that only a high detection limit is achieved (6 ppbv hr^{-1}), which does not allow to measure typical daytime O_3 production rates in remote and forested environments. Therefore, the current OPR and MOPS instruments face many challenges to produce reliable O_3 production rate measurements in ambient air (Sklaveniti et al., 2018).

1.5 Outline of the work

In the following, the experimental procedures and instruments used in this study for the measurement of trace gases and aerosol property in the atmospheric simulation chamber SAPHIR during the Jülich Atmospheric Chemistry Project (JULIAC) campaign are described (Chapter 2).

In Chapter 3, the Forschungszentrum Jülich LIF instrument for the measurements of OH, HO_2 and RO_2 radical concentrations in use at the SAPHIR and its calibration method are described in detail.

Furthermore, the implantation and characterization of the chemical modulation reactor (CMR) used as part of the LIF instrument at Forschungszentrum Jülich for the detection of radicals is described. The characterization includes laboratory tests and chamber experiments. Furthermore, a model is developed to provide estimates of the influence of various conditions that could be experienced in different on the chemical modulation efficiency. Measurements of OH radicals using the CMR LIF method are compared to measurements by Differential Optical Absorption Spectroscopy (DOAS) in synthetic and ambient air in the atmospheric simulation chamber SAPHIR. The latter allowed the investigation of possible interference signals for a range of chemical conditions in a rural environment. This work was published by the author of this thesis in the journal *Atmos. Meas. Techn.* (Cho et al., 2021).

In Chapter 4, ambient measurements of OH, HO₂, and RO₂ radical concentrations as well as of OH reactivity during the JULIAC campaign are presented. The dataset allows investigating the diurnal and seasonal variation of tropospheric trace gas concentrations and aerosol properties in order to quantify how local chemical processes affect the degradation of VOCs at different levels of NO_x. Results improve the understanding of tropospheric chemical mechanisms for conditions that are typical in central Europe. To explore missing radical sources and/or sinks, a chemical budget analysis of OH, HO₂, RO₂ radicals, and their sum (RO_x) is performed using measured species and well-established chemical mechanisms.

Lastly, Chapter 5 describes the photochemical net ozone production rate in the JULIAC campaign. By considering the JULIAC-SAPHIR system as a large photochemical flow reactor, the O_x production rate in the chamber can be determined from measured NO₂ and O₃ concentrations in the incoming flow and in the SAPHIR chamber. In addition, this chapter shows the comparison of these O_x production rate values with calculations using turnover rates of O_x production and destruction reactions by using measured peroxy radical and trace gases concentrations.

Chapter 2. The Jülich Atmospheric Chemistry Project (JULIAC): Investigation of photochemistry in rural air using the atmospheric simulation chamber SAPHIR

2.1 The atmospheric simulation chamber SAPHIR

The atmospheric simulation chamber SAPHIR (Simulation of Atmospheric PHotochemistry In a large Reaction chamber) is built for the investigation of photochemical and nighttime chemical processes of trace gases and aerosols under tropospheric conditions in a controlled system (Figure 2.1). The air in the chamber is well mixed and there are no unaccounted sources or losses of traces gases, so that processes can be investigated without the influence of transport and segregation. The SAPHIR chamber is located on the campus of Forschungszentrum Jülich, Germany. With the instrumentation summarized in Table 2.1, the chemical conditions in the chamber can be well characterized.



Figure 2. 1: Picture of the SAPHIR chamber. At the right side, the tower is seen at which the inlet line for ambient air was mounted in the JULIAC campaign. Copyright to: “Forschungszentrum Jülich / Sascha Kreklau“

The chamber has a cylindrical shape (length: 18 m, diameter: 5 m, volume: 270 m³) and is made of a double Teflon (FEP) film, which has a light transmission higher than 0.8 over the complete solar spectral range (Bohn and Zilken, 2005). A slight overpressure is maintained inside the chamber and clean nitrogen is used to flush the volume between the inner and outer FEP films to prevent contaminations from outside the chamber. A replenishment flow of synthetic air is continuously injected to compensate for leakages and air consumption of instruments, which dilutes trace gases at a rate of approximately 6 % h⁻¹ (equivalent to a lifetime of 16 hours). Two fans are mounted inside the chamber to ensure a homogeneous mixing of trace gases. A shutter system allows to operate the chamber in light or dark conditions. Previous investigations of atmospheric chemistry in the chamber show that chamber specific processes are well characterized (Bohn and Zilken, 2005; Rohrer et al., 2005; Novelli et al., 2018) and are adequately considered in the evaluation of experiments. Due to the

use of the Teflon film, the chamber has photolytic sources of nitrous acid (HONO) and formaldehyde (HCHO) with typical source strengths of 0.3 – 0.7 ppbv hr⁻¹ and 0.07 – 0.5 ppbv hr⁻¹, respectively, for typical ambient conditions (Karl et al., 2004; Rohrer et al., 2005).

Table 2. 1: Specification of instruments that performed measurements in the JULIAC campaign in the SAPHIR chamber.

Species	Measurement technique	Instrument	Time resolution	Limit of detection (1 σ)	1 σ accuracy
Measurements in the SAPHIR chamber					
OH	CMR-LIF	^a	270 s	$0.7 \times 10^6 \text{ cm}^{-3}$	18 %
OH	DOAS	^a	134 s	$0.8 \times 10^6 \text{ cm}^{-3}$	6.5 %
HO ₂	LIF	^a	47 s	$0.8 \times 10^7 \text{ cm}^{-3}$	18 %
RO ₂	LIF	^a	47s	$2.0 \times 10^7 \text{ cm}^{-3}$	18 %
OH reactivity (k _{OH})	LP-LIF	^a	180 s	0.3 s ⁻¹	18 %
Photolysis frequencies	Spectroradiometer	^a	60 s	^b	18 %
O ₃	UV photometry	ESA 42e TS 49i AN 41m	60 s	0.5 ppbv	2 %
NO _x (NO+NO ₂)	Chemiluminescence	Eco Physics TR780	60 s	NO: 20 pptv NO ₂ : 30 pptv	NO: 5 % NO ₂ : 7 %
CO, CO ₂ , CH ₄ , H ₂ O	Cavity ring-down spectroscopy	Picarro G2401	60 s	CO and CH ₄ : 1 ppbv CO ₂ : 25 ppbv H ₂ O: 0.1 %	5 %
HONO	LOPAP	^a	180 s	5 pptv	10 %
HCHO	Cavity ring-down spectroscopy	Picarro G2307	300 s	0.1 ppbv	10 %
ClNO ₂	Mass spectrometry	I-CIMS	60 s	ClNO ₂ : 2.1 pptv	27 %
VOCs	PTR-TOF-MS		30 s	15 pptv	14 %
	VOCUS		30 s		
	GC-FID		30 min		
Total aerosol surface area	SMPS		7 min	10nm – 1 μ m	N/A
Measurements in the JULIAC inlet					
O ₃	UV photometry	Eco Physics CraNO _x	68 s	1 ppbv	2 %
NO _x (NO+NO ₂)	Chemiluminescence	Eco Physics CraNO _x	68 s	NO: 20 pptv NO ₂ : 30 pptv	NO: 5 % NO ₂ : 7 %
CO, CO ₂ , CH ₄ , H ₂ O	Cavity ring-down spectroscopy	Picarro G2401	60 s	CO and CH ₄ : 1 ppbv CO ₂ : 25 ppbv H ₂ O: 0.1 %	5 %

^a Custom-built instrument.

^b Several orders of magnitude lower than the maximum value at noon.

2.2 The JULIAC campaign

The Jülich Atmospheric Chemistry Project (JULIAC) was conducted at Forschungszentrum Jülich (FZJ, 50.908° N, 6.412° E), Germany, and included one-month long intensive measurement periods in each season throughout 2019 (Table 2.2). The campus is surrounded by a deciduous forest and is located near a small city, Jülich. There are several large cities, Cologne, Aachen, Düren and Düsseldorf within distances of approximately 40 km. Therefore, the sampled ambient air was influenced by both biogenic and anthropogenic emissions.

Figure 2.2 shows a schematic drawing of the JULIAC inlet system and the connection to the SAPHIR chamber. Ambient air was sampled from 50m height through a SilcoNert® coated inlet tube (104 mm i.d.) with a flow rate of $660 \text{ m}^3 \text{ h}^{-1}$ using a blower (Aerzener Maschinenfabrik, AERZEN Turbo G3 Typ: TB 50-0.6 S). The transit times from the top of the JULIAC tower to the ground and further to the SAPHIR chamber were 3.1 s and 1.2 s, respectively. Several sensors were mounted on top and along the inlet line to monitor ambient pressure, temperature, and relative humidity. In addition, an ultrasonic anemometer for 3D-wind data was mounted on top of the tower. The temperature in the inlet line was controlled to be slightly higher than ambient temperature (+1 to 2 °C) to avoid water vapor condensation in the line. Approximately 50% and 90% of coarse particles with diameters of 2 – 3 μm and 6 – 10 μm , respectively, were removed by a cyclone (LTG, ZSB-6). A 3/2-way valve controlled the sampled flow of the ambient air directed to the chamber. Close to the valve a sampling line was installed for the measurement of the chemical composition (e.g., NO_x , VOCs and O_3) of the air that is flowed into the chamber. The flow rate into the chamber was $250 \text{ m}^3 \text{ h}^{-1}$ resulting in a residence time of the air in the chamber of approximately one hour.

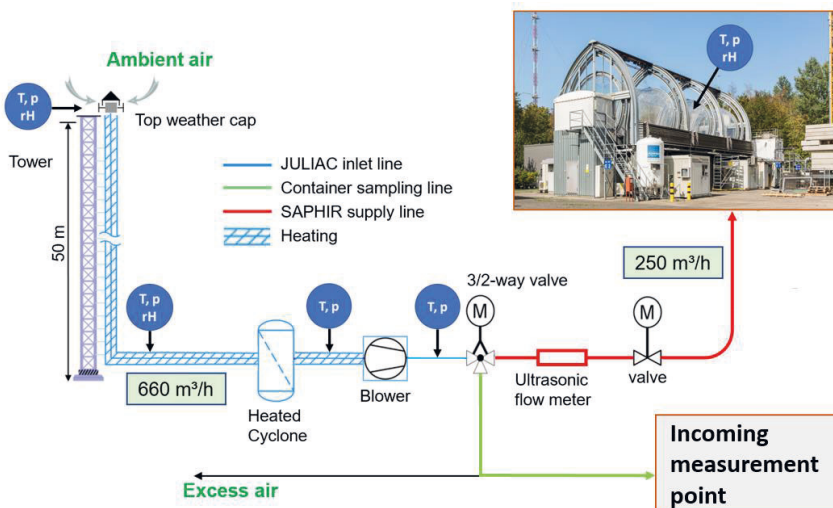


Figure 2. 2: Schematics of the JULIAC-SAPHIR flow system.

Although the design of the JULIAC campaign intended to investigate ambient air, chemical and physical conditions were also influenced by the chamber.

First, while the sampled ambient air is transferred to the chamber, the air composition could be changed by wall losses. At least part of the atmospheric radicals are expected to be lost in the inlet system. However, this loss does not impact radical concentrations in the SAPHIR chamber, because radicals are rapidly achieving again steady state concentrations for conditions in the SAPHIR chamber. Wall losses of other trace gases are assumed to be negligible. The assumption was checked by several comparisons of the measurements of OH reactivity at several positions in the inlet system like before the cyclone and after the blower where most significant wall losses of trace gases are expected. The differences in the OH reactivity measured at these positions is small ((2 ± 5) %) indicating no significant losses of trace gases.

Second, due to the transmission through the Teflon film and shading of construction elements of the chamber, the absolute actinic flux density is 20 to 40 % smaller than outside of the chamber. It is worth noting, however, that the relative spectral distribution of the solar radiation does not change (Bohn and Zilken, 2005).

HONO and HCHO are emitted from the chamber film when it is exposed to solar radiation (Section 2.1). These sources significantly change the concentrations of HONO and HCHO in the chamber.

Lastly, there is an aluminum plate underneath the chamber that can be raised in order to walk inside the chamber. Although this plate does not have direct contact with the Teflon film during the experiments, it is heated by solar radiation. As a result, the air temperature in the chamber at daytime is usually a few (during winter and autumn) to several (during spring and summer) degrees higher than the ambient temperature outside the chamber.

During each intensive measurement period of the campaign, the shutter system of the chamber was open at nearly all times and measurements were continuously performed except for breaks for calibration measurements of instruments which was done approximately every 7 days for one day. The chamber roof was occasionally closed for the entire day to protect the chamber film from strong wind gusts and/or precipitation. Reference experiments with clean synthetic air were performed before and after the intensive periods to investigate possible changes in the strength of HONO and HCHO emissions of the Teflon film and to check for instrumental backgrounds. Few specific experiments were performed, in which chemical species (e.g., NO₂, O₃, Cl₂) were injected in addition to the ambient air. In some experiments, the high flow of ambient air was stopped in the morning, in order to observe the evolution of trace gas concentrations under perturbed conditions.

Table 2. 2: Experiment days in each intensive period of the JULIAC campaign 2019. Special experiments were for example experiments with zero, addition of trace or experiments, in which the high flow of ambient air through the chamber was stopped.

	Intensive period	Calibration or shutter system closed	Special experiments
Winter (JULIAC-I)	14. Jan. – 10. Feb.	Jan.: 17, 22, 23, 26, 27, 28, 30, 31 Feb.: 02, 03, 09	12. Feb.
Spring (JULIAC-II)	09. Apr. – 06. May	Apr.: 11, 17, 24, 27, 28, 30 May: 04, 05	08. Apr., 09. May., 10. May, 02. May – 03. May
Summer (JULIAC-III)	04. Aug. – 02. Sep.	Aug.: 09, 10, 15, 17, 18, 21, 29	01. Aug., 02.Sep., 22. Aug. – 23. Aug.
Autumn (JULIAC-IV)	28. Oct. – 24. Nov.	Oct.: 26, 27, 30, 31 Nov.: 02, 03, 04, 12, 18	31. Oct., 29. Nov., 19. Nov. 20. Nov.

2.3 Instrumentation during the JULIAC campaign

A large suite of instruments was available for the experimental studies in the SAPHIR chamber during the JULIAC campaign. Measurements used for the analysis in this work are listed in Table 2.1 together with the measurement technique, time resolution, 1σ accuracy and precision.

The concentrations of OH, HO₂ and RO₂ radicals were measured by the FZJ laser-induced fluorescence (LIF) instrument. The principle of the LIF technique is described in Section 1.2 and details of the specific FZJ-LIF instrument in Section 3.1.

The calibration-free differential optical absorption spectroscopy (DOAS) instrument, which is permanently installed in the chamber simultaneously measured OH, HCHO, SO₂ and naphthalene. It provides an absolute reference for OH radical measurements with a 1σ accuracy of 6.5 % (Hausmann et al., 1997; Schlosser et al., 2007; Schlosser et al., 2009). Broad-band UV radiation at 308.04 nm is emitted by a dye laser operated at a repetition rate of 82.2 MHz. Two mirrors are mounted at the ends of the chamber in a distance of 20 m. The laser light is multiple times reflected in a White cell configuration resulting in a long absorption path length of 2.2 km. The absorption signal is detected by a high-resolution Echelle spectrometer coupled to a photodiode array detector.

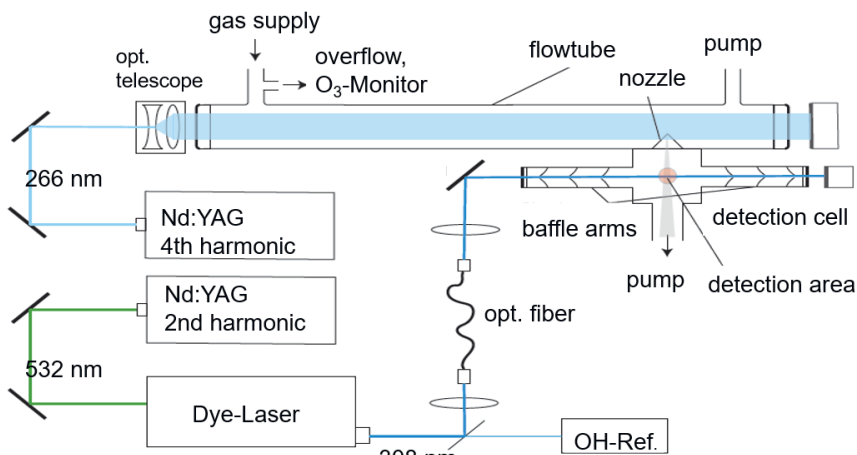


Figure 2. 3: Schematics of the Jülich laser flash photolysis and laser-induced fluorescence instrument (LP-LIF) for the measurement of the OH reactivity.

In addition to the measurement of radical concentrations, the total OH reactivity (k_{OH}), which is the inverse of the chemical OH lifetime (τ_{OH} , Eq. 1.3), was measured by combining a flow tube, through which ambient air is flowed (flow rate 10 to 20 slpm), and a time-resolved measurement of the OH radical concentration by LIF (Figure 2.3) (Fuchs et al., 2017). In the flow tube, a large amount of OH (up to $1 \times 10^{10} \text{ cm}^{-3}$) is artificially generated by a laser flash photolysis (266 nm, 1 Hz repetition rate) of ozone in a humid air (Reaction R2.1 and R2.2).



Part of the air (3 L slpm) is further sampled to a fluorescence detection cell to detect OH radicals. The OH decay measured at a high time resolution of 1 ms follows a pseudo first-order loss (Eq. 2.1), so that an exponential fit gives directly the OH reactivity:

$$[\text{OH}]_t = [\text{OH}]_0 e^{-k_{\text{OH}}t} \quad (\text{Eq. 2.1})$$

An instrumental zero loss rate in the flow tube likely due to the wall loss and diffusion of OH is checked and by sampling synthetic air at least once per a day. All measurements are corrected for the zero value. Typical values were 1 to 2 s^{-1} during the JULIAC campaign. At the chamber, the air from the chamber is sampled through a stainless-steel inlet line with a SilcoNert[®] coating (i.d.: 10mm, length: approximately 5 m), minimizing the loss of OH reactants.

Photolysis frequencies were calculated from spectral actinic flux densities measured by a spectroradiometer outside the chamber. Calculations take into account the transmission of the chamber film and shading of the structure of the chamber (Bohn et al., 2005; Bohn and Zilken, 2005).

In the chamber, NO_3 radical concentrations were monitored by a custom-built cavity ring-down spectroscopy (FZJ-CRDS) instrument that is similar to the instrument described in Wagner et al.

(2011); nitrous acid (HONO) by a custom-built long-path absorption photometer (LOPAP) (Kleffmann et al., 2006; Li et al., 2014); CO, CO₂, CH₄, and H₂O by a cavity ring-down spectroscopy instrument (CRDS, Picarro); nitric oxide (NO) and nitrogen dioxide (NO₂) by a chemiluminescence instrument with a photolytic converter (CL, Eco Physics); and O₃ by UV absorption instruments (Ansyco and Thermo scientific). Measurements by different instruments agreed within 5%. Furthermore, concentrations of O₃, NO_x, CH₄, CO₂, CO and water vapor were additionally measured in the inlet system before the air entered the SAPHIR chamber by combined monitors (CraNOX, Eco Physics; CRDS, Picarro).

VOCs were detected by a gas chromatography – flame ionization instrument (GC-FID, Gerstel), a proton-transfer-reaction time-of-flight mass spectrometer (PTR-TOF-MS, Ionicon) (Jordan et al., 2009) and a VOCUS PTR-TOF instrument (Aerodyne). Although three different instruments were used to identify various VOC species, the three instruments measured only concurrently on 28 days out of 112 days. The VOC species that were detected in the JULIAC campaign are listed in Table 2.3. In the summer and autumn periods, ClNO₂ was observed by a chemical ionization mass spectrometer applying ionization with iodine (I-CIMS) (Sommariva et al., 2018). Aerosol total surface area was measured by a scanning mobility particle sizer (SMPS).

Table 2. 3: List of VOC species measured in the JULIAC campaign.

	Species	Instrument
alkenes	pentene, hexene	VOCUS
alkanes	hexane, heptane, decane, nonane	GC-MS
aromatics	toluene, xylene, benzene, phenol, furan, styrol, cresol	PTR-TOF-MS
BVOCs	isoprene, monoterpenes, sesquiterpenes	VOCUS
OVOCs	acetaldehyde, acetone, acetonitrile, acrolein, adipinic acid, benzaldehyde, butanone, cyclohexanone, formic acid, glycolaldehyde, glycolic acid, hydroxyacetone, methylglyoxal, methyl vinyl ketone, methacrolein, nopinone, pentanone, pinonaldehyde, succinic acid	VOCUS

2.4 Characterization of the SAPHIR chamber with the JULIAC inlet system for ambient air sampling

In the JULIAC campaign, the SAPHIR chamber was operated as a continuously stirred photochemical flow reactor, through which ambient air was flowed, (Section 2.2, Fig. 2.2). The residence time of air in the chamber for the operational conditions (flow rate of $250 \text{ m}^3 \text{ h}^{-1}$) during the JULIAC campaign was characterized in a separate experiment on 23 April (Fig. 2.4). A high concentration of the non-reactive tracer (CO_2) was injected into the chamber, while ambient air was flowed through the chamber, and the decay of its concentration was observed. The fraction of the measured CO_2 concentration that was due to the CO_2 in the ambient air flowed into the chamber was calculated from the CO_2 measured in the incoming air at JULIAC inlet system described in Section 2.5. Figure 2.4(b) shows the total CO_2 concentrations and the contribution from ambient CO_2 . The excellent fit of the experimental data to an exponential decay function over four orders of magnitude shows that the air in the chamber is homogeneously mixed. The residence time of the air inside the chamber (chamber volume $V = (277 \pm 3) \text{ m}^3$) is determined from the measured decay to be $\tau = (1.13 \pm 0.01) \text{ h}$ for a volumetric flow rate of the air flowing into the chamber of $250 \text{ m}^3 \text{ h}^{-1}$. For further calculations in this work, the actual residence time of air in the chamber, τ , is calculated from the measured volume flow rate \dot{V} of the incoming air:

$$\tau = \frac{V}{\dot{V}} = k_{\text{air}}^{-1} \quad (\text{Eq. 2.2})$$

k_{air} , the inverse of the residence time, is the air exchange rate. This calculation assumes that the chamber volume V is constant.

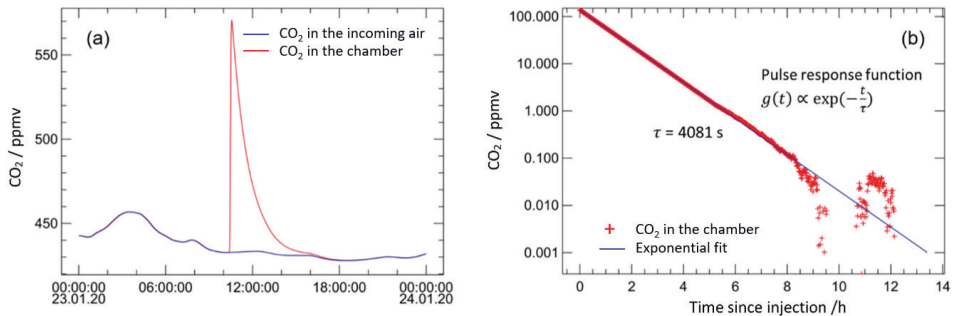


Figure 2. 4: (a) Time series of mixing ratios of CO_2 in the incoming ambient air and in the chamber, when CO_2 was injected in the chamber. (b) Exponential decay of the measured CO_2 mixing ratios in the chamber after subtracting the contribution from ambient CO_2 . The limit of detection of the instrument detecting CO_2 was 0.025 ppmv. A fit to the pulse response function ($g(t)$) gives the residence time (τ) of air in the chamber.

2.5 Evolution of trace gas concentrations and determination of net chemical production rates

The observed concentration of a trace gas in the chamber ($[X]$) is determined by its concentration in the ambient air flowing into the chamber ($[X]_{\text{inlet}}$), the air exchange rate (k_{air}) and its chemical production (P) and destruction rate (D).

$$\frac{d[X]}{dt} = k_{\text{air}} \cdot [X]_{\text{inlet}} - k_{\text{air}} \cdot [X] + P - D \quad (\text{Eq. 2.3a})$$

The differential equation can be written for further numerical calculations using discrete values with a time step Δt :

$$\frac{[X](t_i) - [X](t_{i-1})}{\Delta t} = k_{\text{air}} \cdot [X]_{\text{inlet}}(t_{i-1}) - k_{\text{air}} \cdot [X](t_{i-1}) + P(t_i) - D(t_i) \quad (\text{Eq. 2.3b})$$

If there is no chemical production or destruction on the time scale of the residence time of air in the chamber ($P = D = 0$), the concentration of the species in the chamber is only due to its concentration in the air transported into the chamber ($[X]_{\text{trans}}$). In this case, the concentration in the chamber can be iteratively calculated from the time series of concentrations measured in the inlet line using Eq. 2.3b:

$$[X]_{\text{trans}}(t_i) = \Delta t \cdot k_{\text{air}} \cdot [X]_{\text{inlet}}(t_{i-1}) + (1 - \Delta t \cdot k_{\text{air}}) \cdot [X](t_{i-1}) \quad (\text{Eq. 2.4})$$

Equation 2.4 can also be used to calculate the concentration of a trace gas that would be expected, if there was no chemical production and destruction on the time scale of residence time of air in the chamber. Differences to the actual concentration measurement in the chamber indicate that there was chemical production or destruction.

The rate of the net chemical production and destruction rate ($P(t_i) - D(t_i)$) of a species X can be iteratively calculated from Eq. 2.3b, if concentrations are measured in the inlet line and in the chamber:

$$P(t_i) - D(t_i) = \frac{[X](t_i) - [X](t_{i-1})}{\Delta t} + k_{\text{air}}(t_i) \cdot ([X](t_i) - [X]_{\text{inlet}}(t_i)) \quad (\text{Eq. 2.5})$$

To test the predictability of the concentration of a trace gas in the without chemical production and destruction chamber from the concentration in the inflowing air ($[X]_{\text{trans}}$), the measurements of CH_4 and CO_2 were used, because concentrations of these species were both measured in the JULIAC inlet and there is no significant chemical production and destruction within the residence time of air inside the chamber. Figure 2.5(a) shows the comparison of the CH_4 concentrations measured in the inlet, measured in the SAPHIR chamber and expected in the chamber from calculations using Eq. 2.4. The differences between calculated and measured concentration in the chamber were insignificant (0.4 %, maximum difference 10 ppbv). Maximum differences are within the accuracy of measurements that are limited by the instrumental offsets that were determined from comparisons of measurements, when both instruments sampled the same air mass. The average offsets between instruments were (3±6) to (6±9) ppbv. In addition, for the whole JULIAC campaign, the average deviation between measured and calculated methane concentrations in the chamber was less than 14 ppbv or 0.7% relative to the average measured CH_4 concentration. Similarly, deviations between

measured and calculated CO_2 concentrations in the chamber were less than 0.5% (Fig. 2.5). The excellent agreement between calculated and measured concentrations for long-lived species demonstrates that the flow system of the JULIAC-SAPHIR system is well understood and characterized.

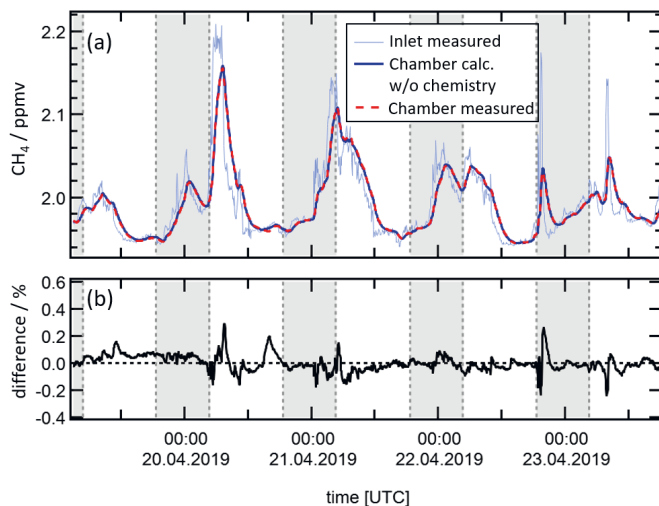


Figure 2. 5: (a) Concentrations of CH_4 measured in the inlet, in the chamber and expected in the chamber from transportation from the inflowing air. (b) Relative differences between measured and calculated concentrations in the chamber ($[\text{CO}_2]_{\text{chamber}} - [\text{CO}_2]_{\text{trans}}$). Grey areas indicate nighttime (solar zenith angles $> 90^\circ$). Results from the days shown in this figure are representative for the results from the entire campaign.

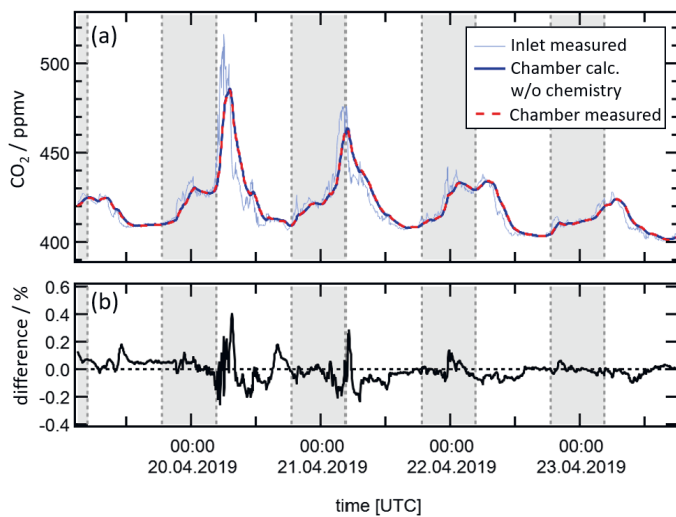


Figure 2. 6: (a) Concentrations of CO₂ measured in the inlet, in the chamber and expected in the chamber from transportation from the inflowing air. (b) Relative difference between measured and calculated concentrations in the chamber ($[\text{CH}_4]_{\text{chamber}} - [\text{CH}_4]_{\text{trans}}$). Grey areas indicate nighttime (solar zenith angles $> 90^\circ$). Results from the days shown in this figure are representative for the results from the entire campaign.

Chapter 3. Radical detection by laser induced fluorescence and characterization of a chemical modulation reactor (CMR) for the measurement of atmospheric concentrations of hydroxyl radicals

The content of this chapter was published in the journal *Atmos. Meas. Techn.* by the author of this thesis as part of the Ph.D. work. Parts of the text and figures in this chapter are adapted from the open access publication Cho et al., 2021, under the CC BY 4.0 license (<https://creativecommons.org/licenses/by/4.0>).

3.1 The Forschungszentrum Jülich LIF instrument for OH, HO₂ and RO₂ radical concentration measurements

In Chapter 1, the principles for the measurement of OH, HO₂ and RO₂ radicals with LIF technique were described. This section focuses on the specific properties of the Forschungszentrum Jülich LIF instrument in use at the atmospheric simulation chamber SAPHIR.

The instrument includes a laser module stored in a container and a measurement module mounted below the SAPHIR chamber (Figure 3.1). A schematic of the fluorescence detection cells in the Forschungszentrum Jülich (FZJ)-LIF instrument is shown in Figure 3.2. The measurement of OH radicals is achieved by sampling air (1.1 slpm = 1 L min⁻¹ at 1 atm, 20 °C) through a 0.4 mm pinhole nozzle into a low-pressure (4 hPa) detection cell. A sheath flow of 800 sccm (1 sccm = 1 cm³ min⁻¹ at 1 atm, 20 °C) N₂ injected downstream of the nozzle avoids accumulation of contaminations from the sampled air. Also baffles arms containing multiple baffles to reduce laser stray light are flushed with a flow of 200 sccm N₂.

The sampled air crosses the single-pass laser beam in the center of the detection cell with a velocity of about 200 m s⁻¹ without having wall contact. The OH radical is resonantly excited by the UV laser pulse (308 nm) produced by a narrow-bandwidth (2.5 pm) tunable dye laser system. The dye laser system is pumped by a frequency doubled Nd:YAG laser, which provides short laser pulses (25 ns) at a repetition rate of 8.5 kHz. The UV power is typically 30 – 40 mW. A reference cell, in which a high concentration of OH radicals is generated by pyrolysis of water vapor by a hot filament, is used to track the OH excitation line and to automatically correct of slow drifts of the laser wavelength.

The OH fluorescence is detected by a micro-channel plate photomultiplier (MCP) connected to a gated photon counting system. To distinguish the OH fluorescence from background signals, the excitation wavelength is modulated on and off the peak of the OH Q₁(3) absorption line (Fig. 3.3) (Hofzumahaus et al., 1996). The photon count rates are integrated over 25 s and 10 s in the on- and off- resonance mode, respectively, in order to acquire a sufficient number of fluorescence photons and to obtain a precise background signal. A complete measurement cycle including times for tuning the laser wavelength takes 45 s.

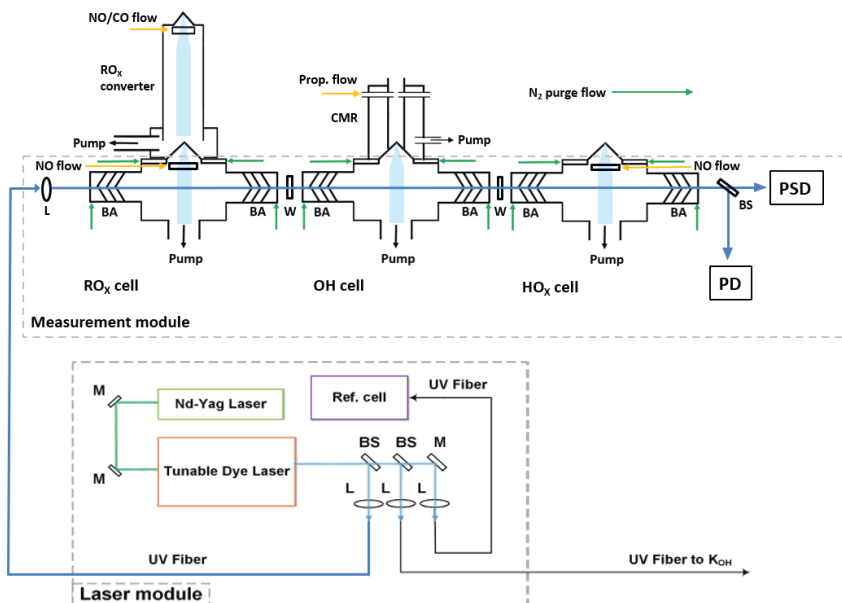


Figure 3. 1: Schematic of the FZJ-LIF instrument used at the SAPHIR chamber for the detection of OH, HO₂ and RO₂ radicals. The laser module is located inside a container. The 308 nm laser light is divided into three optical fibers (BS: beam splitter; L: lens) that guide the light to (1) the measurement module mounted below the SAPHIR chamber, (2) the reference cell and (3) the OH reactivity instrument. Ambient air is sampled into the low-pressure detection cells that are separated by glass windows (W). Reactive gases (NO, CO and propane) are injected into the HO_x and RO_x cells (NO), the RO_x converter (NO and CO) and the chemical modulation reactor (CMR) (propane). Baffle arms (BAs) and detection cells are continuously purged with pure nitrogen. The position and the power of the laser beam are monitored by a photodiode (PD) and a position-sensitive diode (PSD). Adapted from the open access publication by Tan et al. (2017) under the CC BY 4.0 license (<https://creativecommons.org/licenses/by/4.0>).

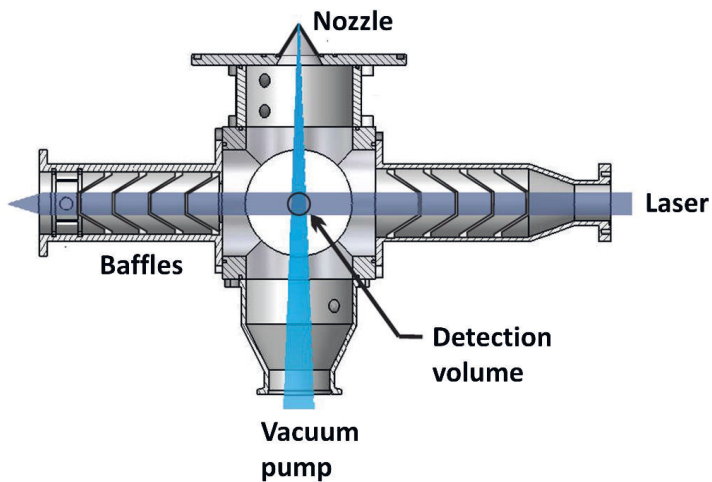


Figure 3. 2: Schematics of a fluorescence cell in the FZJ-LIF instrument. Adapted from (Broch, 2011).

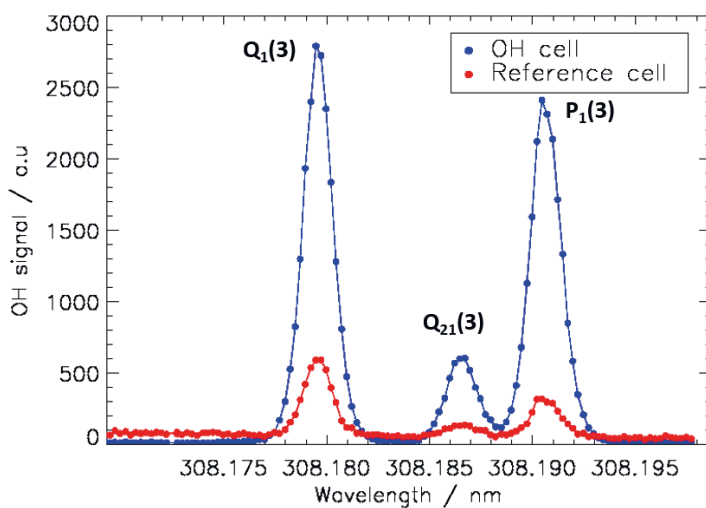


Figure 3. 3: Excitation spectrum of OH showing rovibrational absorption lines around 308 nm. The spectrum was acquired in a laboratory experiment with the calibration source on top of the OH measurement cell. Signals from the OH cell and the reference cell are shown.

The measured OH concentration resulting from the wavelength modulation of the exciting laser is hereafter called $[\text{OH}]_{\text{WAVE}}$ and is calculated as:

$$[\text{OH}]_{\text{WAVE}} = \frac{S_{\text{WAVE}}}{C_{\text{OH}}} = \frac{1}{C_{\text{OH}}} \times (S_{\text{ON}} - S_{\text{OFF}}) \quad (\text{Eq. 3.1})$$

Here, S_{WAVE} is the OH radical fluorescence signal normalized to the UV laser power. It is obtained from the difference between S_{ON} and S_{OFF} , the on- and off-resonance signals, respectively. C_{OH} is the OH radical detection sensitivity, which is obtained from the calibration of the instrument. During the JULIAC campaign, a chemical modulation reactor (CMR) was mounted on the top of the OH cell to measure potential interferences in the OH measurement. Further description of the CMR can be found in the following sections.

The HO_x fluorescence cell, which runs in parallel to the OH cell, is similar to the OH cell. Ambient air is sampled through a small pinhole (0.2 mm) resulting in a flow rate of 0.28 slpm. HO_2 radicals are chemically converted to OH radicals in the reaction with NO (Air Liquid, 1% NO in N_2 , purity > 99.9990 %) that is injected downstream of the inlet nozzle (Fuchs et al., 2011). The NO concentration in the fluorescence cell is $\sim 2.5 \times 10^{13} \text{ cm}^{-3}$, resulting in an HO_2 to OH conversion efficiency of approximately 20 %. By using the small pinhole and small flow rate the residence time of air in the fluorescence cell is shorter compared to the OH cell. This and operating the cell with moderate NO concentrations minimize possible interference from specific RO_2 radicals as shown by Fuchs et al. (2011).

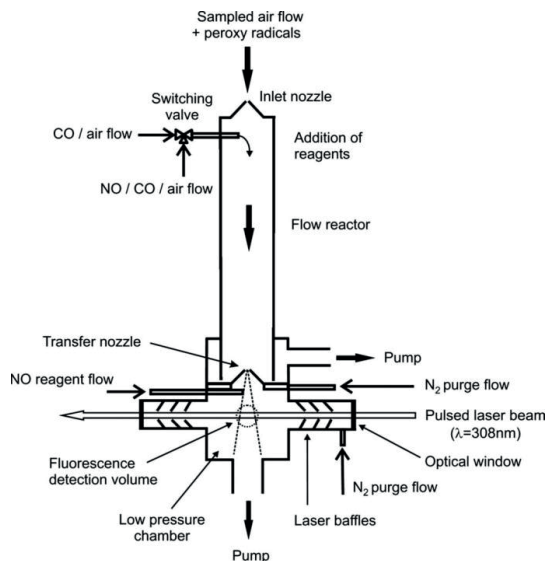


Figure 3. 4: Schematic of the RO_x -LIF system for measurements of RO_2 radical concentrations. Adapted from Fuchs (2007).

In the RO_x cell (Fig. 3.4), which runs in parallel to the OH and HO_x cells, RO₂ radicals are measured using a two-step radical conversion (RO₂ → HO₂ → OH). The RO₂ radicals are sampled with a flow rate of 7 slpm into the RO_x converter (~ 25 hPa), where a mixture of NO (Air Liquide, 500 ppmv NO in N₂, purity > 99.9990 %) and CO (Air Liquide, 10% CO in N₂, purity > 99.9990 %) is injected. The NO converts the RO₂ radicals to HO₂ radicals and the CO converts the OH formed from the reaction of HO₂ radical with NO back to HO₂. Concentrations are chosen, such that the equilibrium concentrations are on the side of HO₂. At the end of the converter, the HO₂ radical are sampled with a flow rate of 3.5 slpm into the fluorescence cell, where radicals are finally converted to OH radicals by injection of excess NO (Linde, 99.9%) (Fuchs et al., 2008). A much higher NO concentration of $1.0 \times 10^{17} \text{cm}^{-3}$ compared to the NO concentration in the HO_x cell is used to maximize the HO₂-to-OH conversion efficiency. After the subtraction of the signals from HO₂ and OH concentrations measured in the other two cells, the total RO₂ concentration from the RO_x signal is obtained.

The sensitivities of the instrument are calibrated with a radical source, which can produce a known amount of OH, HO₂ and RO₂ radicals. In the radical source, OH and HO₂ are produced by the photolysis of water vapor at 185nm in the presence of oxygen (Reaction R3.1 and R3.2). This method is widely used for the calibration of instruments detecting HO_x radicals (J. Creasey et al., 1997; Kanaya et al., 2001; Hard et al., 2002; Holland et al., 2003; Faloona et al., 2004; Hofzumahaus and Heard, 2016).



Figure 3.5 shows a schematic of the calibration source, which is used for the calibration of the FZJ-LIF instrument. Humidified clean synthetic air (flow rate: 20 slpm) is flowed through a quartz glass tube (20 cm length, 18.7 mm i.d. with a frit at the top, Reynolds number Re = 1920). At the end of the flow tube, a known amount of OH and HO₂ is produced by the irradiation with 185 nm radiation from a low-pressure discharge mercury lamp (pen-ray lamp). Equal concentrations of OH and HO₂ are produced and can be calculated as:

$$[\text{OH}] = [\text{HO}_2] = [\text{H}_2\text{O}] \sigma_{\text{H}_2\text{O}} \Phi_{\text{OH}} t_{\text{rad}} I_{185\text{nm}} \quad (\text{Eq. 3.2})$$

Here, $\sigma_{\text{H}_2\text{O}}$ is the absorption cross section of H₂O at 185 nm that has a value of $7.2 \pm 0.2 \times 10^{-20} \text{cm}^2$ (Hofzumahaus et al., 1996; Cantrell et al., 1997; Creasey et al., 2003). Φ_{OH} is the OH quantum yield of the photolysis reaction. The value of the yield is 1.0 (Engel et al., 1992). t_{rad} is the irradiation time, and $I_{185\text{nm}}$ is the lamp intensity from the mercury emission line at 185 nm. Because values are specific for the design of the calibration source, they are experimentally determined by ozone actinometry. As the synthetic air contains oxygen, oxygen is concurrently photolyzed at 185nm and forms ozone (Reaction R3.3, R3.4).



Similar to OH (Equation 3.2), the produced O₃ concentration is calculated as:

$$[O_3] = [O_2] \sigma_{O_2}^{eff} \Phi_{O_3} t_{rad.} I_{185nm} \quad (\text{Eq. 3.3})$$

Unlike the absorption cross section of water, the absorption spectrum of oxygen has a distinct structure around 185 nm (Sedlacek, 2001). Therefore, the effective absorption cross section of oxygen ($\sigma_{O_2}^{eff}$) is specific for the emission of an individual mercury lamp (for example, $\sigma_{O_2}^{eff} = (1.28 \pm 0.05) \times 10^{-20} \text{ cm}^2$ for the calibration source used in this work). The value needs to be determined in laboratory experiments (Hofzumahaus et al., 1996; Creasey et al., 2000). The ozone yield in the photolysis reaction is $\Phi_{O_3} = 2$ derived by stoichiometry.

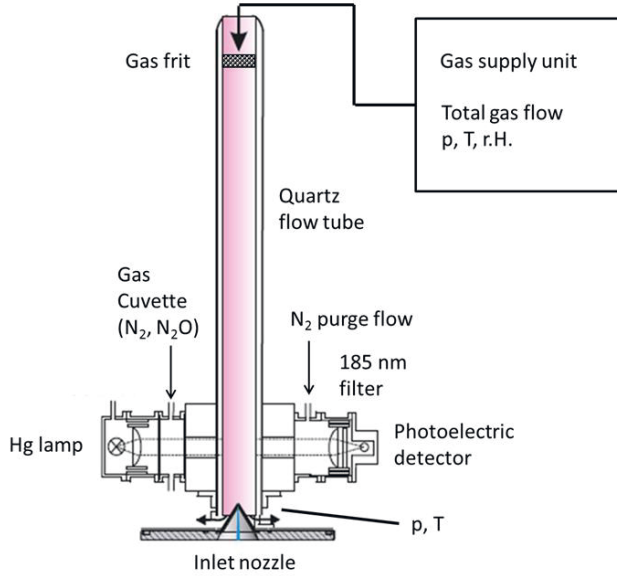


Figure 3. 5: Schematic of the radical source used to calibrate the sensitivity of the FZJ-LIF instrument.

By combining Equations 3.2 and 3.3, the OH and HO₂ concentrations produced by the calibration source are calculated as:

$$[OH] = [HO_2] = [O_3] \frac{[H_2O] \sigma_{H_2O} \Phi_{OH}}{[O_2] \sigma_{O_2}^{eff} \Phi_{O_3}} \quad (\text{Eq. 3.4})$$

The mixing ratio of the produced ozone (several ppbv) is close to the limit of the detection of standard ozone photometers. Therefore, the ozone concentration is related to the intensity of the radiation (I_p) monitored by a phototube. The linear relationship (slope a) between the phototube

signal and the produced ozone concentrations is determined in a separate laboratory experiment, in which the O₃ concentration is detected by a modified chemiluminescence detector (CLD, Eco Physics), which allows to accurately measure O₃ mixing ratios in the low ppbv range. Variations of the residence time of air in the illumination section of the radicals are accounted for by considering the measured volume flow rate of the air (Q_v), so that the ozone concentration produced during the calibration can be calculated as:

$$[\text{O}_3] = \frac{aIp}{Q_v} \quad (\text{Eq. 3.5})$$

The air in the calibration source used in this work flows as a plug flow that ensures a uniform distribution of OH and O₃ in the calibration gas. The uniform distribution was confirmed by ozone measurements with the chemiluminescence detector showing that the ozone concentration in the central flow was the same as the mean ozone concentration in the calibration source within a few percent.

For the calibration of the HO₂ sensitivity of the instrument, 250 ppmv of CO (Air Liquide, 10% CO in N₂, purity > 99.9990 %) is added to the synthetic air in the calibration source in order to convert OH to HO₂ (Reaction R3.5). The doubled HO₂ concentration that is provided.



For the calibration of the RO₂ sensitivity, 0.1 % methane (CH₄) (Air Liquide, purity > 99.9990 %) is added to the calibration gas leading to the production of methylperoxy radicals (CH₃O₂) in the reaction of OH with methane (Reactions R3.6, R3.7):



In this operational mode of the calibration source, the same concentrations of CH₃O₂ and HO₂ are produced. Because the instrument measures the sum of RO₂ and HO₂ concentration, the RO_x system needs to be separately calibrated for HO₂ running the calibration source with CO. From both calibration measurements together, the RO₂ sensitivity can be determined.

Because the rate constants of the reaction of RO₂ with NO and RO decompositions vary for different RO₂ radicals, the RO₂ sensitivity may also differ. Laboratory tests adding different hydrocarbons instead of CH₄ in the calibration source leading to the production of organic peroxy radicals in the reaction with OH showed that RO₂ radicals formed from simple alkanes, alkenes and isoprene can be measured with almost the same detection sensitivity as methylperoxy radicals (Fuchs et al., 2008). Therefore, the instrument is typically only calibrated for methylperoxy radicals, if ambient air containing a complex mixture of different RO₂ species is analyzed.

The 1σ accuracy of the calibration is 10 % from Gaussian error propagation of errors from the parameters used in the calculation of the radical concentrations (Holland et al., 2003). During the JULIAC campaign, calibrations of the FZJ-LIF instrument were performed approximately every 7

days (Section 2.2). Values varied only approximately 15 % demonstrating a good reproducibility of the calibration. The overall 1σ accuracies of the measurement of OH, HO₂ and RO₂ concentrations are calculated to be 18 % (Table 2.2), if the reproducibility of the calibration is additionally taken into account. Details of the calibration of the instrumental sensitivity, if the CMR is applied, is described in Section 3.3 and 3.4.

3.2 Potential interferences in radical concentration measurements by the LIF instrument

3.2.1 Potential interferences in the OH concentration measurement

Previous studies have investigated and reported possible interferences in the detection of ambient OH by LIF instruments, which originate from the formation of OH inside the instrument. OH can be for example formed inside the detection cell from the laser photolysis of ozone in the presence of water (Holland et al., 2003; Ren et al., 2004), from the laser photolysis of acetone (Ren et al., 2004; Fuchs et al., 2016), from the ozonolysis of alkenes (Ren et al., 2004; Novelli et al., 2014b; Fuchs et al., 2016; Rickly and Stevens, 2018), and by unknown reactions of nitrate radicals (NO₃) (Fuchs et al., 2016). Most of these interfering species do not to play a role at ambient concentrations with the exception of ozone photolysis in humid air. This interference is often corrected in ambient air measurements based on laboratory characterization experiments (Holland et al., 2003).

In accordance with a recommendation from the International HO_x workshop 2015 (Hofzumahaus and Heard, 2016), the majority of LIF instruments nowadays applies a chemical modulation method, in order to account for possible interferences. This method is also applied in CIMS instruments detecting OH (Berresheim et al., 2000). Chemical modulation is done by periodically scavenging the ambient OH by addition of a reactant (propane or hexafluoropropene) before the air enters the detection cell. Any remaining OH fluorescence signal can then be attributed to OH produced inside the detection cell (Mao et al., 2012; Novelli et al., 2014a; Tan et al., 2017; Rickly and Stevens, 2018; Tan et al., 2018; Tan et al., 2019; Woodward-Massey et al., 2020) (Table 3.1). The difference between the signal without and with the scavenger provides interference-free ambient OH signals, from which OH radical concentrations are calculated applying a calibration factor. However, no distinct reason for the different behavior of instruments have been identified so far.

After considering interference measured by specific LIF instruments using CMR systems (PSU, MPI, IU, Table 3.1), a significantly improved agreement was found between measured OH concentrations and chemical box model predictions in field campaigns (Mao et al., 2012; Feiner et al., 2016; Mallik et al., 2018; Lew et al., 2020). In these cases, measured interferences contributed 40 - 80 % to the total signal in daytime and 50 -100 % in nighttime in campaigns in forested environments (Mao et al., 2012; Hens et al., 2014; Novelli et al., 2014a; Feiner et al., 2016; Lew et al., 2020). Smaller contributions of 20 - 40 % to the total signal were found in campaigns in coastal (Mallik et al., 2018), rural (Novelli et al., 2014a), and urban (Brune et al., 2016; Griffith et al., 2016) environments

during daytime, but interferences in nighttime were sometimes similar to those found in forested environments.

Table 3. 1: Characteristics of chemical modulation reactors developed for OH LIF instruments from different groups worldwide.

Parameter	FZJ ^a	PKU ^b	MPIC ^c	PSU ^d	IU ^e	UL ^f
Volume flow (slpm)	21	21	150-280	7	3-9	32
Residence time (ms) ^g	18	22 / 18 ^h	not specified	100	not specified	20
Reaction time (ms) ⁱ	11	19 / 11 ^h	2.5-4	25 / 10 ^j	50	20
Scavenger	C ₃ H ₈	C ₃ H ₈	C ₃ H ₈	C ₃ F ₆	C ₃ F ₆	C ₃ H ₈
Scavenger concentration (ppmv) ^k	19	3 - 500	100	150 - 500	400 - 1200	110 or 1100
Scavenger reactivity ^{k, l} (s ⁻¹)	540	70 - 13500	2700	7700 - 26000	20000 - 60000	3000 or 30000
OH scavenging (%) ^m	96 ⁿ	80 - 97 ⁿ	80 - 95 ^o	94 ^o	> 90	> 99 ⁿ
OH transmission (%) ^p	64 ⁿ	70 ⁿ	73 ^q	~ 100 ^j	~ 100	> 95 ^{o, q}
Reference	This study	Tan et al. (2017); (2018)	Novelli et al. (2014a)	Mao et al. (2012)	Rickly and Stevens (2018)	Woodward-Massey et al. (2020)

^a Forschungszentrum Jülich, Germany.

^b Peking University, Beijing, China.

^c Max-Planck-Institute for Chemistry, Mainz, Germany.

^d Pennsylvania State University, PA, USA.

^e Indiana University, IN, USA.

^f University of Leeds, UK.

^g Total transit time.

^h The shorter time applies to the CMR version as used in Tan et al. (2018).

ⁱ Transit time from the injectors to the inlet.

^j The shorter time was used by Feiner et al. (2016).

^k Assuming homogeneous mixing in the CMR flow.

^l The scavenging reactivity was calculated assuming homogeneous mixing. The used rate coefficients for C₃H₈ and C₃F₆ + OH radical are 1.1×10^{-12} and 2.08×10^{-12} cm³ s⁻¹ at 298K, respectively (Dubey et al., 1996; Atkinson et al., 2006).

^m Corresponds to $(1 - \alpha) \times 100\%$.

ⁿ Measured in synthetic air.

^o Measured in ambient air with OH produced photolytically by Hg lamp radiation.

^p Corresponds to $\beta_{N_2} \times 100\%$.

^q Measured in ambient air in the presence of ambient OH concentrations at daytime.

In field campaigns, in which other LIF instruments using chemical modulation (PKU and UL, Table 3.1) for OH concentration measurements, insignificant interferences were observed after the

well-quantified photolytic ozone interference had been subtracted (Tan et al., 2017; Tan et al., 2018; Tan et al., 2019; Woodward-Massey et al., 2020). These field studies were performed under the conditions of rural in Wangdu (Tan et al., 2017), suburban in Per River Delta (Tan et al., 2019) and Beijing (Tan et al., 2018; Woodward-Massey et al., 2020) in China, in which less influences (ozonolysis reaction rates of several ppbv h⁻¹ from simple alkenes, isoprene and monoterpenes) by BVOC emission than in forested environments were present.

Some studies suggest that the observed interferences may be partly caused by the dissociation of stabilized Criegee intermediates (SCIs) that are produced from ozonolysis of alkenes (Novelli et al., 2014b; Novelli et al., 2017; Rickly and Stevens, 2018). However, laboratory and chamber studies (Fuchs et al., 2016; Woodward-Massey et al., 2020) found insignificant interference from the ozonolysis of BVOCs for atmospheric concentrations of reactants. It remains an open question, which chemical species and processes produce OH interferences in some of the LIF instruments and how the technical design and operating conditions of the instruments influence the magnitude of the interferences. Chemical modulation seems to be an appropriate way to account for these measurement artefacts. However, the accurate evaluation of chemical modulation measurements can be challenging and could result in systematic errors in the measured OH concentration, because chemical reactions of atmospheric trace gases can disturb the efficiency of the chemical modulation method. In this study, the chemical modulation method is applied to the OH measurements by the FZJ-LIF instrument. Details of characterization and implementation of this method and discussion about the interferences in the JULIAC campaign are shown in the following sections.

3.2.2 Potential interferences in HO₂ concentration measurements

As the HO₂ radical is detected after it has been converted to OH in the reaction with NO, the OH interference described in the section above could also impact the measurement of HO₂ radicals. However, given the range of ambient HO₂ concentrations, which are typically more than an order of magnitude higher than ambient OH concentrations (Heard and Pilling, 2003), interferences that are highly relevant for OH do often not play a significant role in the HO₂ measurement.

In the presence of NO in the HO₂ detection cell, RO₂ radicals can be converted to HO₂, so that they could cause an interference in the HO₂ measurement (Fuchs et al., 2011; Whalley et al., 2013; Lew et al., 2018). However, for RO₂ radicals from C₁ to C₄ alkane compounds, the RO₂ to HO₂ conversion efficiency in the LIF detection cell is negligible because of the slow reaction rate of H-atom abstraction from the alkoxy radical by O₂ required to produce HO₂ (Reaction R1.9) in the low pressure detection cell (Ren et al., 2004). For example, only less than 5% of methylperoxy radicals (CH₃O₂) converts to HO₂ at the pressure in the detection cell (4 hPa) (Holland et al., 2003).

In contrast, RO₂ originating from the OH oxidation of large alkenes (including isoprene), aromatics and oxidized VOCs can lead to a significant interference with a RO₂ conversion efficiency of up to 80% for operating conditions that are optimized to achieve a high sensitivity for the detection of HO₂ (Fuchs et al., 2011). This RO₂ interference can be substantially reduced by lowering the NO concentration and shortening the residence time of air in the detection cell, both of which reduce the

conversion efficiency for HO₂ and RO₂ radicals. RO₂ conversion to OH requires two reaction steps with NO and HO₂ conversion only one reaction step, so that the RO₂ interferences can be suppressed while sustaining a sufficiently high sensitivity for HO₂.

3.2.3 Potential interference and limitation in RO₂ concentration measurement

OH interferences listed in Section 3.2.1 are typically negligible for the detection of RO₂ radicals. This is again due to the much higher ambient concentrations of RO₂ compared to OH.

The measurement of RO₂ radicals by LIF instruments requires converting RO₂ to HO₂ radicals in a conversion reactor upstream of the fluorescence detection cell (RO_X-LIF, Section 1.2, 3.1). Sampling of ambient air in highly polluted environments could cause perturbations in the radical production and destruction in the converter. Fuchs et al. (2008) showed that impacts on the RO₂ detection sensitivity from ambient NO concentrations between 0.2 ppmv and 1.0 ppmv, which are values that could be observed in highly polluted environments, are small. The sensitivity is changed by 0.04% per 1 ppbv NO. In addition, other species contained in ambient air such as CO, NO₂ and VOCs show a negligible impact on the RO₂ sensitivity of the instrument. Another possible interference could be due to the peroxy radical production from the thermal decomposition of peroxy nitrates such as peroxy acetyl nitrate (PAN), pernitric acid (PNA, HO₂NO₂) and methyl peroxy nitrate (MePN, CH₃O₂NO₂), which are in a thermal equilibrium with peroxy radicals and NO₂ (Reaction R3.8, R3.9).



Fuchs et al. (2008) showed that the interferences from PNA and MePN can be up to 1.7 % and 6 %, respectively, for 10 ppbv of ambient NO₂, while the decomposition of PAN is negligible due to the small decomposition rate for conditions of the conversion reactor ($2.6 \times 10^{-4} \text{ s}^{-1}$ at 25 hPa and 298 K, (Burkholder et al., 2015)). Whalley et al. (2018) also investigated the possible impact of MePN decomposition in the converter by assuming that the measured RO₂ is dominated by CH₃O₂ ($[\text{RO}_2] \approx [\text{CH}_3\text{O}_2]$) for conditions encountered in the Clean air for London project (ClearLo) in summer 2012. The MePN concentration was estimated from the measured RO₂ and NO₂ concentrations resulting in concentrations in the range of 0.3 to $0.5 \times 10^8 \text{ cm}^{-3}$. Correcting for potential MePN decomposition in the conversion reactor improved the agreement between modelled and measured RO₂ concentrations for conditions of high NO mixing ratios (> 2 ppbv). However, as the RO₂ speciation was not unknown, the correction is highly uncertain.

Because RO₂ measurements by the RO_X-LIF instrument rely on the RO₂ conversion to HO₂, RO₂ radicals which do not yield HO₂ after their reaction with NO cannot be detected. Although most RO₂ radicals produced from the reaction of organic compounds with OH radicals yield HO₂, some nitrated-RO₂ radicals formed from the reaction with NO₃ radicals cannot be measured, because some nitrated-alkoxy radicals (nitrate-RO) formed from the reaction of nitrated-RO₂ and NO decompose and form NO₂ instead of HO₂ in the conversion reactor.

Recently, Novelli et al. (2021) and Vereecken et al. (2021) investigated the degradation pathways of nitrated-RO formed from C₂ to C₆ nitrated-RO₂ by combining experimental, theoretical and modeling studies. They found that nitrated-RO₂ radicals from for example the NO₃ oxidation of ethene, propene are detectable, because the reaction of nitrated-RO with O₂ yielding HO₂ is the dominant degradation path. In addition, nitrated-RO₂ radicals from larger parent VOCs such as 1-pentene and trans-2-hexene can be detected, because isomerization and decomposition reactions of nitrated-RO forming HO₂ dominantly. In contrast, the study shows that RO_x-LIF instruments cannot detect most of the nitrated-RO₂ formed from the NO₃ oxidation of cis-2-butene, 2,3-dimethyl-2-butene, and isoprene due to their fast fragmentation to NO₂ and a carbonyl product and epoxidation for nitrated-RO in case of isoprene for conditions of the converter. Therefore, this study emphasized that a careful investigation of the VOC speciation is required in campaigns, in which RO₂ is measured in nighttime.

Table 3. 2: HO₂ and RO₂ background signals used in the evaluation of HO₂ and RO₂ measurements in the JULIC campaign, and upper limits for HO₂ and RO₂ background signals.

	HO ₂ background / 10 ⁷ cm ⁻³	Upper limit HO ₂ background / 10 ⁷ cm ⁻³	RO ₂ background / 10 ⁷ cm ⁻³	Upper limit RO ₂ background / 10 ⁷ cm ⁻³
Winter (JULIAC-I)	0.4±0.6		1.2	0.5±0.2 to 2.8±0.4 ^a
Spring (JULIAC-II)	1.0±0.15		2.0	0.5±0.2
Summer (JULIAC-III)	1.0±0.6		2.1	2.8±0.5
Autumn (JULIAC-IV)	0.0		1.5	0.0

^a Variable RO₂ background concentration was observed; from 14. Jan. to 25. Jan.: (0.5±0.2) × 10⁷ cm⁻³, from 26. Jan. to 06. Feb.: (1.6±0.2) × 10⁷ cm⁻³, from 07. Feb. to 10 Feb.: (2.8±0.4) × 10⁷ cm⁻³.

3.2.4 Corrections of background signals in HO₂ and RO₂ concentration measurements in the JULIAC campaign

A small background signal is observed in the HO_x and RO_x measurements, when NO is injected into the fluorescence cells. This can be quantified, if clean synthetic air without radicals is sampled. A possible explanation for the observed signal is that OH is produced from the laser photolysis of HONO, which could be heterogeneously produced from the conversion of nitrogen oxides on wall surfaces (Künstler, 2020). Typical background signals for HO₂ and RO₂ are equivalent to radical concentrations of less than 1×10⁷ cm⁻³ and 3×10⁷ cm⁻³, respectively. The background is routinely characterized by sampling the clean synthetic air during the calibration procedures or, specifically for

the FZJ-LIF instrument in operation at the SAPHIR chamber, by measuring during clean-air phases of experiments, when the chamber is only filled with synthetic air. This allows to correct measurements for the background.

In the JULIAC campaign, HO₂ and RO₂ background signals were between 0 – 2.1 × 10⁷ cm⁻³ for HO₂ and 0 – 5.4 × 10⁷ cm⁻³ for RO₂ (Table 3.2) determined from reference and laboratory experiments, in which no HO₂ and RO₂ radicals are expected. Only few reference experiments with only synthetic air were performed during each intensive period in the JULIAC campaign. In addition, unlike in previous field campaigns (Tan et al., 2017; Tan et al., 2018; Tan et al., 2019), where calibrations were performed every second or third day, calibrations were only performed once per week in the JULIAC campaign to avoid an artificial perturbation of the air composition in the chamber by venting reactive trace gases from the calibration system into the chamber. HO₂ and RO₂ background signals applied in the evaluation of ambient HO₂ and RO₂ concentrations were taken from the reference experiments, because background signals determined in calibration measurements were highly variable and gave often higher values than the lowest signals observed in the ambient air in the chamber (Table 3.2). Because the NO concentration injected in the HO_x detection cell for the measurement of HO₂ radicals is much lower compared to the NO injected in the RO_x detection cell for the measurement of RO₂ radicals, the background signal in the HO₂ measurements was much lower than that in the RO₂ measurements. The uncertainties from the HO₂ and RO₂ background signals were included in the uncertainty of radical concentrations.

3.3 The Forschungszentrum Jülich LIF OH instrument with the chemical modulation reactor (FZJ-LIF-CMR)

Within this work, a chemical modulation reactor was developed for the FZJ-LIF instrument for interference-free OH measurements (Cho et al., 2021).

Hydroxyl radicals originating not from ambient air but formed in the detection cell are also detected by the LIF instrument, because they can be excited by the laser in the detection volume. To quantify the interference signal from internally generated OH radicals, the majority of LIF instruments now apply chemical modulation in order to correct possible interferences in accordance with a recommendation from the International HO_x Workshop 2015 (Hofzumahaus and Heard, 2016).

A schematic of the CMR system is shown in Figure 3.6 and instrumental characteristics are listed in Table 3.2. The reactor consists of a 79 mm long PTFE Teflon tube with 10 mm inner diameter that is mounted in an aluminum body. Two stainless steel injectors (1/8" o.d. tubes with 50 μm pinhole or 1/16" o.d. tubes) are located 50 mm above the nozzle pinhole of the detection cell pointing to the center of the CMR tube.

A constant flow of 500 sccm nitrogen (N₂, purity > 99.9990 %) or a mixture of nitrogen as carrier gas and the OH scavenger molecule (Air Liquide, propane, purity > 99.95 %, (5.0±0.1) % mixture in nitrogen, purity > 99.999%) controlled by mass flow controllers is injected into the air flow sampled through the CMR. When propane is added, the resulting propane mixing ratio downstream of the

injectors is 19 ppmv for typical operational conditions. This concentration of propane was chosen to efficiently scavenge OH radicals (90 – 95 %) in the CMR but to avoid scavenging OH radicals in the detection cell of the instrument (Section 3.4.3). Propane is used as an OH scavenger because it does not photolyze at the excitation wavelength at 308nm of the laser and it does not react with other oxidants (e.g., NO₃ and O₃), which could produce OH radicals in the CMR. When switching from the mixture of the scavenger in nitrogen to pure nitrogen, the injection lines are flushed for 15 s with a flow rate of 700 sccm to remove any residual scavenger molecule from the lines. The measurement time with addition of propane is 135 s, followed by another period of 135 s without propane injection. A complete cycle therefore takes 270 s.

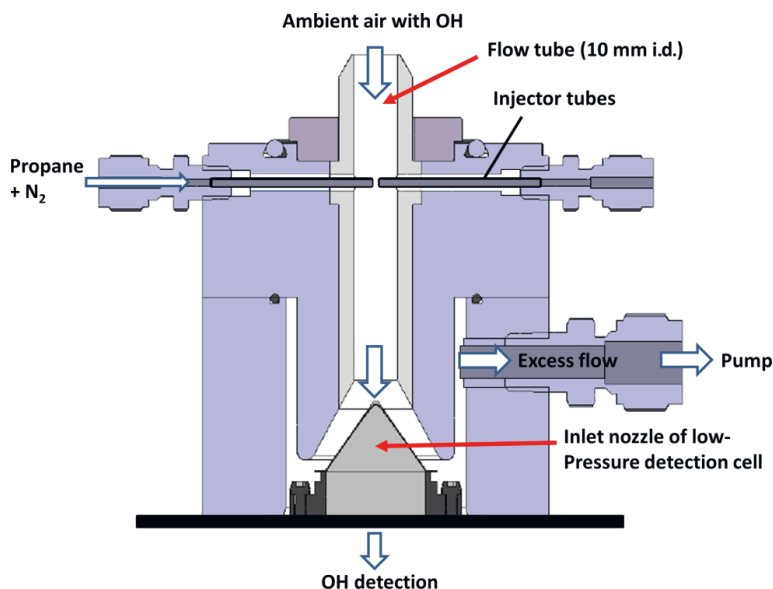


Figure 3. 6: Schematic drawing of the chemical modulation reactor (CMR) that is mounted on top of the OH LIF detection cell. 20 slpm of ambient air is drawn through a PTFE flow tube (79mm length; 10mm inner diameter). Part of the flow (1.1 slpm) is sampled into the low-pressure cell for the OH detection downstream of the CMR, and 20 slpm of excess air is removed by a pump. A nitrogen flow of 0.5 slpm containing 19 ppmv propane as an OH scavenger is added via two 1/8" (o.d.) (50 μm pinhole) or 1/16" (o.d.) injector tubes 50 mm above the nozzle of the detection cell. The distance between the injector tips is less than 1 mm.

For typical measurement conditions, 20 slpm ambient air is sampled. The flow rate downstream of the injectors is increased to 21.1 slpm due to the additional flow. It is controlled by a flow controller (Bronkhorst, model low Δ-p) connected to a membrane pump which removes 20 slpm of

excess air, while the OH measurement cell samples 1.1 slpm, resulting the air residence time of 17.8 ms.

Without added scavenger (N_2 mode of operation), the OH signal obtained from a wavelength modulation (on-off-resonance) measurement cycle (Section 3.1) is

$$S_{OH}^{N_2} = S_{OH} + S_i. \quad (\text{Eq. 3.6})$$

It contains the signal S_{OH} from ambient OH radicals which pass the CMR and reach the inlet nozzle of the detection cell and potentially an interference signal S_i from OH radicals that are produced inside the cell (internal OH). When the scavenger is added (SC mode of operation), a large percentage (typically 96 %) of atmospheric OH radicals is removed by the reaction with propane. The OH signal in the scavenger mode is

$$S_{OH}^{SC} = \alpha S_{OH} + S_i. \quad (\text{Eq. 3.7})$$

It consists of the OH signal from the residual ambient OH, which is reduced by a factor α due to scavenging, and the signal from interferences S_i . The residual factor α has to be determined experimentally (Section 3.4.2), in order to calculate S_{OH} and S_i from a cycle of measurements in the scavenging and nitrogen modes.

$$S_{OH} = \frac{S_{OH}^{N_2} - S_{OH}^{SC}}{1 - \alpha} \quad (\text{Eq. 3.8})$$

$$S_i = \frac{S_{OH}^{SC} - \alpha S_{OH}^{N_2}}{1 - \alpha} \quad (\text{Eq. 3.9})$$

The conversion of S_{OH} into an interference-free ambient OH concentration, $[OH]_{CHEM}$, requires calibration.

$$[OH]_{CHEM} = \frac{1}{C_{OH}\beta_{N_2}} S_{OH} \quad (\text{Eq. 3.10})$$

In addition to the detection sensitivity C_{OH} of the OH detection cell without the CMR, the OH transmission of the CMR in the N_2 mode (β_{N_2}) needs to be known. In the present system, the transmission is reduced due to wall loss reactions and has a typical value of 64 %. The values of the detection sensitivity C_{OH} and transmission β_{N_2} have to be determined either separately or together ($C_{OH} \times \beta_{N_2}$) by calibration measurements (Section 3.4.1).

The interference OH signal S_i can be converted into an equivalent OH concentration in analogy to Eq. (3.5).

$$[OH]_i = \frac{1}{C_{OH}\beta_{N_2}} S_i \quad (\text{Eq. 3.11})$$

It should be noted that the application of the CMR relies on the assumption that interfering chemical species, which produce OH inside the instrument, are not affected by switching between N_2 and scavenger injection in the CMR. Furthermore, it is assumed that internally produced OH is not

scavenged by propane inside the OH detection cell. The latter assumption was confirmed for this instrument (Section 3.4.3).

3.4 Characterization and test of the CMR system for clean air conditions

3.4.1 OH transmission of the CMR without OH scavenger

The loss of OH radicals in the CMR and the scavenging efficiency were determined in laboratory experiments using the radical source, which is also used for absolute calibration of the instrument (Section 3.1). The radical source was operated with a total flow of 24 slpm, which overflowed the inlet of the CMR tube. It is worth to noting that the radical source produces a plug flow that ensures a uniform distribution of OH.

Several tests were performed to characterize potential OH loss on the surfaces in the CMR. Three regions can be distinguished (Figure 3.6): the entrance section above the injectors, the injector tubes, and the reaction section downstream of the injectors. The flow in the entrance section is in the transition regime between laminar and turbulent (Reynolds number, $Re = 2800$), but turbulence is further increased by the injectors, which protrude approximately 4mm into the flow tube. In order to quantify potential OH loss on the surface of the injectors, the stainless-steel injectors were replaced by Teflon tubes of the same geometry to compare the OH loss. Within the measurement precision ($\pm 3\%$), no difference in the transmission of OH was found, when the material of the injectors was changed. Since Teflon and stainless steel have orders of magnitude different surface reaction probabilities for radicals (Rozhenshtein et al., 1985), the result suggests that OH loss on the injector surfaces is negligible regardless of its material because of the overall small surface that is provided by the injectors.

Since the injector tubes do not cause OH losses, the OH transmission in the N_2 mode (β_{N_2}) can be described as the product of transmissions of the entrance section (β^e) and the reaction section ($\beta_{N_2}^r$) (Figure 3.6). Here, the superscripts e and r denote the entrance and reaction sections, respectively.

$$\beta_{N_2} = \beta^e \times \beta_{N_2}^r \quad (\text{Eq. 3.12})$$

The values of the transmissions β^e and $\beta_{N_2}^r$ were experimentally determined using clean air as carrier gas for OH. Parameters determined for clean air conditions without ambient OH reactants (OH reactivity $k_{OH} = 0$) are indicated by the superscript (0) in the following.

The OH transmission of the CMR tube without the injectors was determined by measuring OH from the radical source with and without the CMR mounted on the OH cell. A transmission β_{tube}^0 of 0.81 ± 0.02 was determined for a flow rate of 21.1 slpm. Assuming that the OH loss is caused by only wall loss reactions following first order kinetics, a rate coefficient of $k_w = 11.8 \text{ s}^{-1}$ is calculated from

$$\beta_{\text{tube}}^0 = \exp(-k_w \Delta t) \quad (\text{Eq. 3.13})$$

where Δt is the transit time through the tube. The rate coefficient, k_w , that was obtained can be used to estimate the transmission of the entrance section ($\beta^{e,0}$)

$$\beta^{e,0} = \exp(-k_w^e \Delta t_e) \tag{Eq. 3.14}$$

which has a transit time $\Delta t_e = 6.6$ ms, yielding a transmission $\beta^{e,0} = 0.92$.

With the 1/8" injectors and nitrogen injection, an OH transmission of $\beta_{N_2}^0 = 0.64 \pm 0.03$ was measured for the complete CMR system operated at a flow rate of 21.1 slpm. In addition, the OH radical transmission was investigated for various flow rates between 12 and 21.1 slpm (Figure 3.7). An increasing flow rate has two opposing effects. First, it decreases the residence time in the CMR leading to an increase of the OH transmission from about 60% at 12 slpm to 65% at 15 slpm. Second, an increasing flow rate causes more turbulence and therefore a faster transport of radicals to the wall. The compensating effects are the likely reason for the flattening of the transmission curve at flow rates above 15 slpm (Figure 3.7). Further increase of the flow rate to higher values than 21 slpm does not improve the OH transmission in synthetic air.

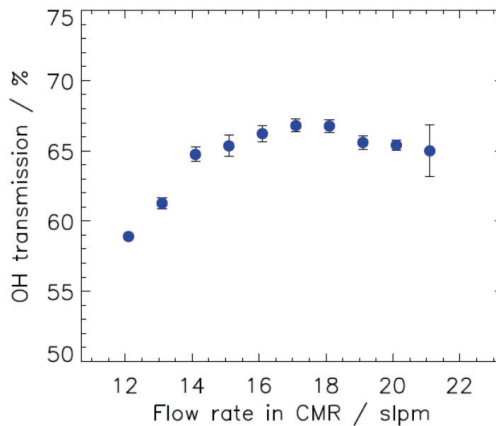


Figure 3. 7: Total OH radical transmission for varying the flow rate in the CMR.

To minimize the possible effect of secondary chemistry, the CMR was operated with the fastest flow rate that could be technically achieved (21.1 slpm), which gives a transmission $\beta_{N_2}^0$ of 0.64. Using the experimental values of $\beta_{N_2}^0$ and $\beta^{e,0}$, the OH transmission of the reaction section in the CMR system for clean air (Eq. 3.12) is $\beta_{N_2}^{r,0} = 0.69$. With a transit time $\Delta t_r = 11.2$ ms, a wall loss rate coefficient $k_w^r = 33$ s⁻¹ is obtained (Table 3.3).

This number can be compared to estimates assuming that there is no resistance for transporting OH to the walls. In this case, the rate coefficient k_s for wall loss due to collisions with a reactive surface can be calculated for a cylindrical tube with radius R by

$$k_s = \gamma \frac{\bar{u}}{2R} \quad (\text{Eq. 3.15})$$

(Zasytkin et al., 1997). For OH with a mean molecular velocity \bar{u} of 610 m/s (298 K) and reaction probability of $\gamma = 2.5 \times 10^{-3}$ for Teflon surfaces (Rozhenshtein et al., 1985), a wall loss rate $k_s = 152 \text{ s}^{-1}$ is obtained. The measured rate coefficients for OH loss (k_w) (Table 3.3) are an order of magnitude smaller, indicating that OH loss in the CMR tube is limited by turbulent transport to the walls. The different loss rates in the regions of the CMR indicates that transportation in the reaction section is approximately three times faster compared to the CMR entrance region.

The same procedure was used to determine also the CMR transmission for HO₂ radicals, which provides information needed to calculate corrections of the OH transmission in polluted air, when OH could be artificially produced by the reaction of HO₂ with NO in the CMR (Section 3.5). For these tests, the calibration source was operated, such that only HO₂ radicals are provided by adding CO (300 ppmv) in order to convert all OH to HO₂ (Fuchs et al., 2011). In order to detect HO₂, the CMR was mounted on the HO_x detection cell of the LIF system. The measured transmissions and wall loss rate coefficients for HO₂ are listed in Table 3.3. The rate coefficients for HO₂ are a factor of two smaller than for OH as could be expected, because HO₂ is less reactive compared to OH. If the wall loss was limited by the reactive collision frequency at the wall surfaces, a larger difference would be expected, because the reaction probability γ on Teflon surfaces is about a factor of ten smaller for HO₂ compared to OH (Rozhenshtein et al., 1985).

Table 3. 3: Transmission (β) and wall-loss rate coefficients (k_w) for OH and HO₂ in the chemical modulation reactor (1/8" injectors) when nitrogen is injected.

	OH		HO ₂	
	k_w / s^{-1}	β	k_w / s^{-1}	β
Entrance section ^a	12.3	0.92	5.5	0.96
Reaction section ^b	33	0.69	14.5	0.85
Total CMR	-	0.64	-	0.82

^a Transit time is 6.6 ms.

^b Transit time is 11.2 ms.

3.4.2 Scavenging efficiency in the CMR

The same radical source operated with clean synthetic air was also used for the characterization of the scavenging efficiency. For this, changes of the chemical composition of air due to chemistry in the reaction section needs to be considered. This changes, when either nitrogen or propane is injected into the CMR. When no propane is injected (N_2 mode), OH is only lost by wall reactions:

$$\beta_{N_2}^{r,0} = \exp(-k_w^r \Delta t_r) \quad (\text{Eq. 3.16})$$

In the scavenger mode, additional OH loss occurs by the gas-phase reaction with propane. The OH transmission is then given by

$$\beta_{sc}^{r,0} = \exp(-[k_w^r + k_{sc}] \Delta t_r). \quad (\text{Eq. 3.17})$$

where k_{sc} is the pseudo first-order rate constant of the reaction between OH and propane.

$$k_{sc} = k_{OH+propane}[propane] \quad (\text{Eq. 3.18})$$

Here, $k_{OH+propane}$ is the bimolecular reaction rate constant of the scavenging reaction, which has a value of $1.1 \times 10^{-12} \text{ cm}^3 \text{ s}^{-1}$ at 298 K for propane (Atkinson et al., 2006).

The fraction α of ambient OH transmitted through the CMR, when the CMR is operated in the scavenging mode, is given by the ratio of transmissions with scavenger β_{sc}^r and without scavenger $\beta_{N_2}^r$.

$$\alpha = \frac{\beta_{sc}^r}{\beta_{N_2}^r} \quad (\text{Eq. 3.19})$$

In the specific case of sampling synthetic air (no ambient OH reactants present, $k_{OH} = 0$), Eq. 3.19 becomes

$$\alpha^0 = \frac{\beta_{sc}^{r,0}}{\beta_{N_2}^{r,0}} = \exp(-k_{sc} \Delta t_r). \quad (\text{Eq. 3.20})$$

The value of α^0 was experimentally determined for OH in synthetic air from experiments with the radical source by calculating the ratio of OH signals measured with and without scavenger. It is worth noting that the value of the residual factor ' α ' is different for ambient air containing OH reactants ($k_{OH} \neq 0$). The residual factor in ambient air is discussed in Section 3.5.

Figure 3.8a and 3.8b show the measured dependence of α^0 on the added amount of propane for different instrumental conditions. For small amounts of propane, the fraction of OH transmitted through the CMR, α^0 , decreases nearly exponentially as expected from Eq. 3.20, when homogenous mixing of the scavenger can be assumed. At higher scavenger concentrations, however, α^0 levels off and decreases slower than expected from an exponential decay. This behavior indicates inhomogeneous mixing of propane in the CMR flow.

Figure 3.8a also shows that the use of 1/8" injectors leads to an improved mixing compared to the use of 1/16" injectors. The likely reason is that the 1/8" injectors produce a larger flow resistance in the CMR tube and produce higher turbulence in the flow because of their larger outer diameter. The disadvantage of the 1/8" injectors is a smaller CMR transmission of $\beta_{N_2}^0 = 0.64$ compared to a value of 0.75 for the 1/16" injectors. Thus, the faster mixing of propane using the 1/8" injectors goes along with a higher OH wall loss.

Figure 3.8b shows that the carrier gas (N_2) flow rate in the injectors has only a minor influence on α^0 , when the injector flow rate is changed between 100 sccm and 500 sccm. In order to ensure fast exchange of the gases in the injector lines, the higher flow rate of 500 sccm was chosen for routine operation. For the majority of the results shown in this study, the 1/8" injectors were used to maximize the mixing in the CMR. The 1/16" injectors were only tested during part of the JULIAC experiments (Table 3.4).

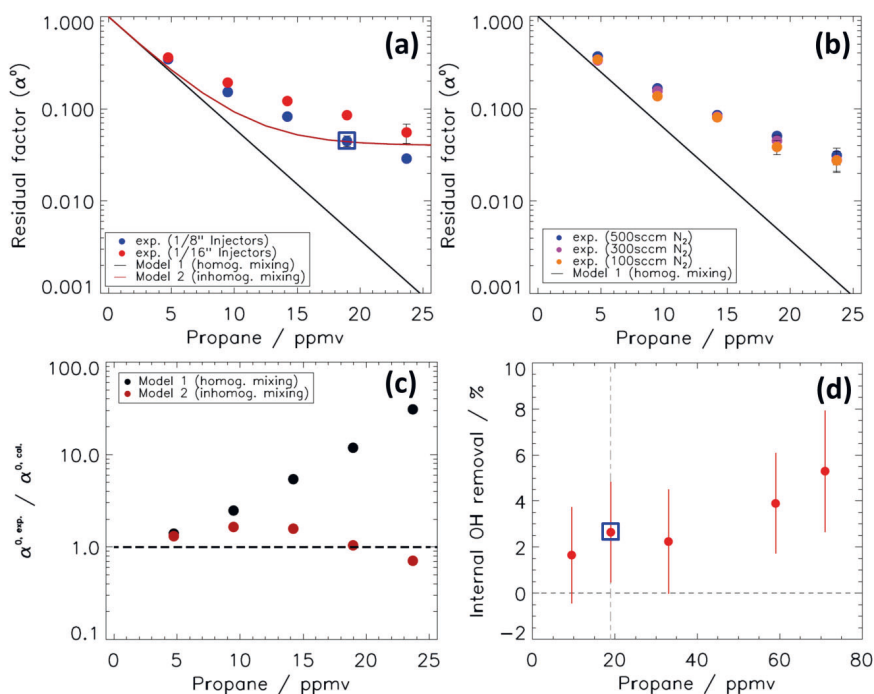


Figure 3. 8: a. Residual factor (α^0) of OH (= remaining fraction of OH) in the CMR for humidified synthetic air. The OH air mixture is provided by an OH radical source. α^0 is shown as a function of the calculated concentration of propane (at 298 K and 1 atm), which is injected as a scavenger together with 500 sccm N_2 into the CMR flow. The experimental α^0 values are shown for two types of injectors with different outer diameter (1/8" and 1/16"). The blue open squares indicate the condition used for standard operation of the CMR in this work. Measurements are compared to calculations assuming

either homogeneous or inhomogeneous mixing. b. Same as a., showing measured α^0 values for different injector flow rates. c. Ratio of experimental and modelled α^0 for the case with 1/8" injectors and 500 sccm N_2 injector flow. d. Measured removal of OH inside the OH detection cell by OH scavenging (see text).

Table 3. 4: Operational conditions of the CMR during the JULIAC campaigns.

	Winter (I)	Spring (II)	Summer (III) and Autumn (IV)
Period	14 Jan. – 11 Feb.	9 Apr. – 6 May	4 Aug. – 2 Sep. 28 Oct. – 24 Nov.
Injector type	1/8" injectors	1/16" injectors	1/8" injectors
Carrier flow	500 sccm	200 - 300 sccm	500 sccm
Propane concentration	15 ppmv	15 - 25 ppmv	19 ppmv
Scavenging efficiency ^{a,b}	91%	> 85%	96%
OH transmission ^{a,c}	64 %	75 %	64 %
Limit of detection ^d	$0.7 \times 10^6 \text{ cm}^{-3}$	$0.8 \times 10^6 \text{ cm}^{-3}$	$0.6 \times 10^6 \text{ cm}^{-3}$

^a Determined in clean synthetic air ($k_{OH} = 0$).

^b OH scavenging efficiency = $(1 - \alpha) \times 100\%$.

^c OH transmission (β_{N_2}) of the complete CMR.

^d Signal-to-noise ratio = 1, averaging time: 45s.

* From 01.02.2019 to 11.02.2019 the CMR was not mounted

Ideally, the remaining OH downstream of the CMR would be zero ($\alpha=0$), when the scavenger is applied. In this case, the OH signal in the scavenger mode would be exactly the interference signal from internally produced OH ($S_i = S_{OH}^{sc}$) and the ambient OH signal would be simply given by the difference of signals in both modes ($S_{OH} = S_{OH}^{N_2} - S_{OH}^{sc}$). Higher propane concentrations should result in smaller α values, but experiments shown in Figure 3.8a indicate that increase of the propane mixing ratio to higher values than 20 ppmv results in only small increases of α . If the propane concentration is further increased, however, there is the danger that also ambient OH is scavenged in the detection cell. This would lead to an underestimation of the interference signal. Therefore, a propane concentration in the CMR of 19 ppmv was chosen for routine operation in this work. It is worth noting that 19 ppmv is the mixing ratio that is expected, if the injected propane is homogeneously mixed in the air flowing through the CMR. With this flow of propane 96 % of OH is scavenged ($\alpha^0 = 0.042$) corresponding to an effective scavenging rate coefficient of $k_{sc}^{eff} = 283 \text{ s}^{-1}$ (Eq. 3.20). This value is a factor of 1.8 smaller than calculated for homogenous mixing of the scavenger ($k_{sc} = 513 \text{ s}^{-1}$).

A plausible explanation for the weaker than expected dependence of the residual factor α on the propane concentration is incomplete mixing of the injected scavenger. A minor fraction f of a few

percent of the total CMR flow containing little or no scavenger would explain the observed dependence of α^0 (Figure 3.8a). The part containing no scavenger ($k'_{sc} = 0$) can be imagined as gas filaments, in which OH radicals are completely transmitted ($\alpha_1(k'_{sc} = 0) = 1$). They would be embedded in the turbulent flow, in which the scavenger is present. This major part of the flow (fraction: $1-f$), would contain all the injected propane. Assuming good mixing the remaining OH is decreased to $\alpha_2(k''_{sc} = k_{OH+propane}[Propane]) < 1$). The average α^0 of the total CMR flow would then be the superposition of the two parts of the flow:

$$\begin{aligned}\alpha^0 &= (1-f) \alpha_2(k''_{sc}) + f \alpha_1(k'_{sc} = 0) \\ &= (1-f) \alpha_2(k''_{sc}) + f\end{aligned}\quad (\text{Eq. 3.21})$$

Using Eq. 3.20 and 3.21 gives

$$\alpha^0 = (1-f) \exp(k''_{sc} \Delta t_r) + f. \quad (\text{Eq. 3.22})$$

This simplified model describing inhomogeneous mixing can provide a better description of the observed dependence of the residual factor α on the propane concentration than Eq. 3.20 (Figure 3.8 a, c), if a small fraction of air without scavenger ($f=0.04$) is assumed. In this case, the calculated scavenger reactivity k''_{sc} is 534 s^{-1} , which is only slightly higher than the value expected for complete homogeneous mixing.

3.4.3 Scavenging of OH in the fluorescence detection cell

The concentration of propane is chosen, such that OH radicals are only scavenged in the CMR, but not in the detection cell. Calculations suggest that less than 1% of OH radicals are scavenged in the detection cell with a propane mixing ratio of 19 ppmv because the low pressure (4 hPa) reduces the scavenger concentration and the residence time in the detection cell is short (3ms).

Tests were performed to confirm that scavenging in the detection is not relevant. One test was proposed by Woodward-Massey et al. (2020) and was also done in this work. In this test, the radical source was operated as a pure HO₂ (Section 3.1). The CMR was mounted on the HO_x detection cell, which operated with 10 times higher NO concentration than during typical operation for ambient HO₂ concentration measurements by injecting 8 sccm of a 10% NO mixture in nitrogen (Linde). Therefore, a high efficiency of the HO₂ to OH radical conversion of 85 % is achieved. The HO₂ radical concentration provided by the radical source is not affected by the propane injection in the CMR, but the HO₂ is converted to OH in the detection cell. If a significant amount of OH radicals was scavenged by propane inside the detection cell, a difference between the measured signals with and without propane injection in the CMR would be expected. Different propane concentrations (10 to 75 ppmv) were tested (Figure 3.8d). A small amount of (3±2) % of internal OH was scavenged when 19 ppmv of propane was applied. An increase of internal removal up to a value of (5±3) % was observed for the highest propane mixing ratio (75 ppmv).

The internal scavenging value of (3 ± 2) % for the operation conditions of the CMR in this work applies to OH radicals, which are internally formed and have a similar residence time as OH produced from the HO₂ to OH conversion (ca. 2 ms) in the test experiment. OH that is for example produced photolytically in the center of the fluorescence cell, where the laser beam is located, has a much shorter residence time (ca. 0.1ms) before it is removed by the fast gas flow and will therefore be much less affected by internal scavenging. As discussed by Woodward-Massey et al. (2020), internally produced OH that is immediately formed after the sampled air has passed the inlet nozzle would have a longer residence time, which could be larger by up to a factor of two compared to the HO₂ conversion experiment. Even in this case, however, internal scavenging would have a small effect and is therefore considered to be negligible for the operation of the CMR in this work.

3.4.4 Performance of the LIF-CMR system in experiments with clean air in the SAPHIR chamber

The conversion of fluorescence signals S_{OH} to OH concentrations requires the experimental determination of the sensitivity, C_{OH} , and the OH transmission β_{N_2} (Section 3.3, Eq. 3.10). The combined detection sensitivity $C_{OH} \times \beta_{N_2}^0$ of the measurement system with the CMR can be determined with the radical source (Section 3.1). The superscript (0) in $\beta_{N_2}^0$ indicates that the calibration was done in synthetic air without other OH reactants ($k_{OH} = 0$).

The validity of the calibration was tested by comparing the OH concentrations with measurements by the OH DOAS instrument, which provides an absolute reference for OH concentrations in the SAPHIR chamber. In these experiments, the chamber was filled with humidified clean synthetic air. The chamber roof was opened allowing for the photolytic formation of OH radicals from nitrous acid (HONO), which is photochemically produced from the chamber walls (Rohrer et al., 2005) (Section 2.2).

Figure 3.9 shows the OH radical concentrations measured by the DOAS and LIF-CMR instruments. The difference between the measured time series is on average $(0.29 \pm 0.9) \times 10^6 \text{ cm}^{-3}$, which is less than 5% of the average measured OH concentrations between 08:30 and 12:00. Thus, measurements by both instruments agreed well within the combined 1σ accuracies of the LIF-CMR ($\pm 18\%$) and DOAS ($\pm 6.5\%$) measurements, which confirms the validity of the calibration of the LIF instrument. A linear regression, which considers the precision of measurements from both instruments, yields a slope of 0.97. The good agreement gives confidence in the applied chemical modulation technique under the operational conditions, and in the laboratory-determined parameters α^0 and $C_{OH} \times \beta_{N_2}^0$ used for data evaluation.

The implementation of the chemical modulation system in the FZJ-LIF instrument has specific disadvantages compared to the operation of the LIF OH detection without the CMR. It requires a longer measurement time, because half of the time is spent for the measurement of interferences in the scavenger mode. In this work, measurement of ambient OH (N₂ mode, 135 s) contains three on-off resonance cycles for the wavelength modulation, which yield three ambient OH data points (45 s). The subsequent scavenger mode (135 s) takes again three wavelength modulation cycles. Another

disadvantage of the CMR is the reduction of the OH detection sensitivity by a factor of 1.6 due to OH wall loss in the CMR, yielding a 1σ limit-of-detection (LOD) of $7 \times 10^5 \text{ cm}^{-3}$ at a time resolution of 45s.

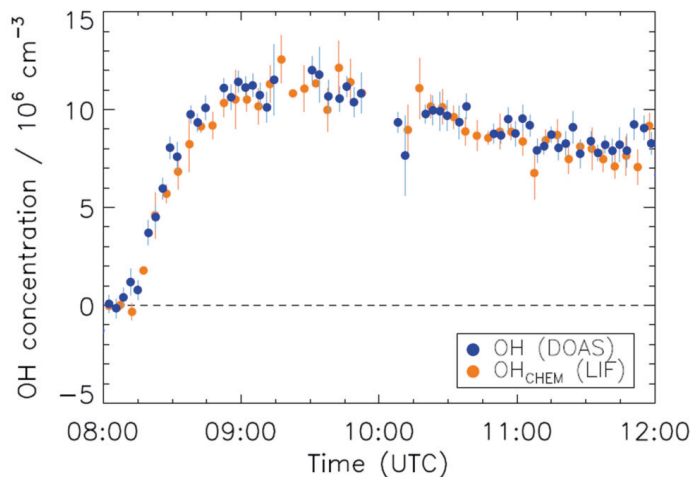


Figure 3. 9: Time series of OH concentrations measured by DOAS and LIF (with CMR) instruments in an experiment with humidified synthetic air in the SAPHIR chamber. The measured OH reactivity in the chamber air was less than 2 s^{-1} . The chamber was illuminated by solar radiation. OH was mainly produced by the photolysis of nitrous acid emitted from the chamber wall. All data are 300s average values.

Accuracy and precision of the OH measurements are generally worsened, if the CMR is used, compared to the OH measurement without the CMR, because OH concentrations determined from the chemical modulation, $[\text{OH}]_{\text{CHEM}}$, requires a higher number of experimental parameters (C_{OH} , α , β_{N_2}) for the evaluation than from the wavelength modulation $[\text{OH}]_{\text{WAVE}}$. In addition, several measurements from the different modes are required, each of which contributes additional noise. The 1σ accuracy of OH measurements depends on the accuracy of the calibration (10 %) and the reproducibility of the experimental determination of the parameters $C_{\text{OH}} \times \beta_{\text{N}_2}^0$ and α^0 . However, the influence of the accuracy of α^0 is small by definition (Eq. 3.8). Over the one-year long JULIAC campaign, the reproducibility was 15% and 10%, respectively, resulting in a total 1σ accuracy of $\pm 18\%$. Additional uncertainties arise when air pollutants influence the chemistry in the CMR (Section 3.5).

3.4.5 Test of the CMR for known interferences

The main purpose of the CMR system is to discriminate the signal from ambient OH radicals and signals interferences. Two types of known interferences (from ozone photolysis and NO₃ radicals) were re-investigated in this work by making use of the chemical modulation technique. These tests were done in synthetic air to avoid potential interferences from other sources.

3.4.5.1 Interference from ozone photolysis

It is well-known that internal OH can be produced by photolysis of O₃ in humid air by the 308 nm laser radiation applied for the excitation of OH in the LIF instrument (Holland et al., 2003). The magnitude of the interference is proportional to the concentrations of ozone and water vapor, and the laser power:

$$\text{OH}_{\text{Interference, O}_3+\text{H}_2\text{O}} \propto [\text{O}_3] \times [\text{H}_2\text{O}] \times \text{Laser Power} \quad (\text{Eq. 3.23})$$

OH concentrations measurements using the wavelength modulation, OH_{WAVE}, are routinely corrected for measurements by the FZJ-LIF instrument based on laboratory characterization experiments. Experiments were done in this work without and with the CMR for a range of conditions (Figure 3.10). Mixing ratios were varied with maximum values of 450 ppbv ozone and 1.8 % water vapor. The laser power was changed between 10 and 20 mW. Laboratory tests were performed by using the calibration source as a flow tube to overflow the inlet of the instrument with a total flow of 11 slpm, but without producing radicals. Ozone produced by a home-built ozone generator was added to the air and measured in the excess air with a UV photometer (Ansyco). Relative humidity was monitored by a humidity sensor (HMT 333, Vaisala). In two additional experiments in the SAPHIR chamber, water vapor and ozone were added in synthetic air in the dark (chamber roof closed). Their concentrations were measured by the instruments listed in Table 2.1 (Section 2.1).

The OH interferences observed in the laboratory and SAPHIR experiments scale linearly with the product of ozone and water vapor mixing ratios as expected (Eq. 3.23, Figure 3.10). Results from all three experiments with and without the CMR agree within 15 %. On average, the interference is equivalent to an OH concentration of $(3.4 \pm 0.3) \times 10^5 \text{ cm}^{-3}$ per 50 ppbv of O₃ and 1 % water mixing ratio, which is at the limit-of-detection for the LIF instrument without the CMR, and a factor of two below the limit-of-detection for the instrument with the CMR. The value of the interference agrees well with earlier determinations for the FZJ-LIF instrument that resulted in values of $(2.7 \pm 0.8) \times 10^5 \text{ cm}^{-3}$ (Holland et al., 1998) and $(3.2 \pm 0.8) \times 10^5 \text{ cm}^{-3}$ (Holland et al., 2003) for the same conditions.

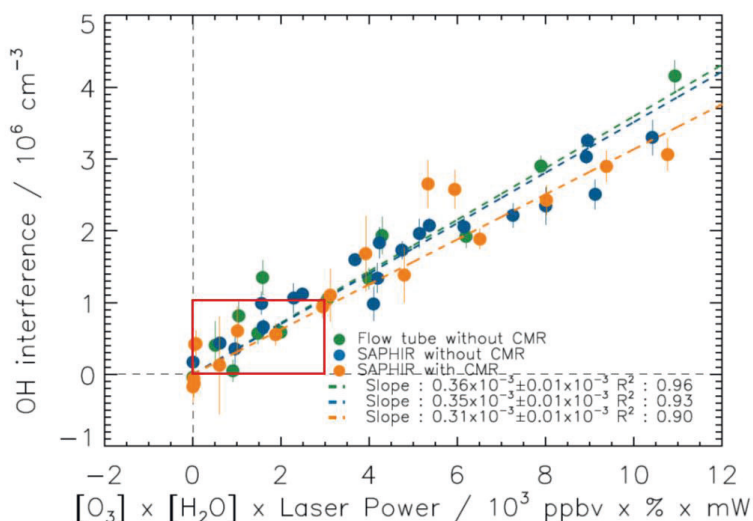


Figure 3. 10: OH interference signal expressed as equivalent ambient OH concentration from the laser photolysis of ozone in humidified synthetic air for a range of concentrations of ozone, water vapor and laser power. Tests were done with and without the CMR in experiments with a flow tube or in chamber experiments. Measurements were fitted to a linear function forced through the origin. The red box specifies the interference signals expected for concentrations of ozone and water vapor typically observed in the lower troposphere.

3.4.5.2 Interference from NO_3

Fuchs et al. (2016) have reported an OH interference from NO_3 radicals by an unknown mechanism producing OH in the FZJ-LIF instrument. The observed interference was independent of water vapor in the gas phase and independent of the laser power. The reported interference signal in the presence of 10 pptv NO_3 was equivalent to an atmospheric OH concentration of $1.1 \times 10^5 \text{ cm}^{-3}$.

In the present work, the interference from NO_3 was determined applying chemical modulation. The experiments were performed in the SAPHIR chamber. NO_3 radicals were injected by flowing air over a trap with N_2O_5 crystals, so that NO_3 is produced from thermal decomposition of N_2O_5 . This method has the advantage that there is no ozone present, which could add an additional artificial OH signal. Figure 3.11 shows a linear increase of the measured OH interference with increasing NO_3 concentrations, which was measured by a cavity ringdown instrument similar to the instrument described in Fuchs et al. (2009) and Wagner et al. (2011). A linear regression analysis yields a slope that is equivalent to an OH concentration of $5.8 \times 10^4 \text{ cm}^{-3}$ per 10 pptv NO_3 . The value is roughly 2 times smaller than the results reported in Fuchs et al. (2016). The reason for the discrepancy between the two tests is unclear. One reason could be NO_3 loss to the wall of the CMR. As the origin of the

NO₃ radical interference in the LIF instrument is unknown, it cannot be ruled out that other experimental conditions affected the interfering signal. In any case, the small interference from NO₃ is negligible for ambient OH measurements for the FZJ-LIF instrument, regardless of whether chemical modulation is used or not. A similar conclusion was drawn from experiments by Woodward-Massey et al. (2020) for the LIF instrument used by the University of Leeds (UK).

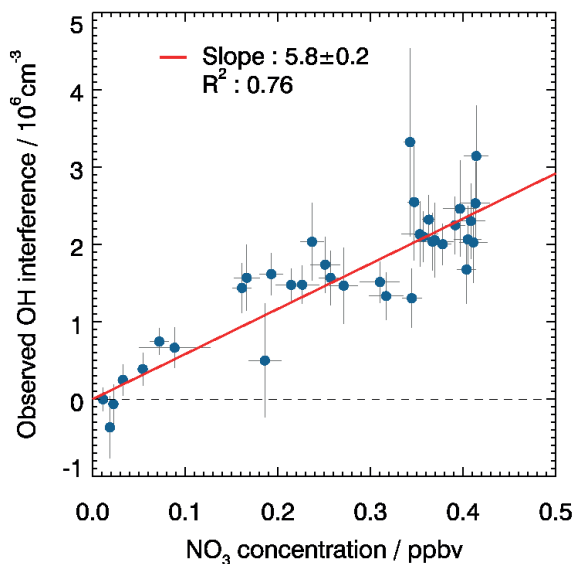


Figure 3. 11: Correlation between the measured OH interference expressed as equivalent ambient OH concentration determined by chemical modulation, and the NO₃ concentration measured during an experiment, when NO₃ (from thermal decomposition of frozen N₂O₃ crystals) was present in the chamber. Measurements are fitted to a linear function forced through the origin.

3.5 OH concentration measurements in ambient air applying chemical modulation

3.5.1 Sensitivity study of the influence of ambient conditions on the performance of the chemical modulation

3.5.1.1 Model description of the impact of ambient conditions on the OH transmission efficiency

When polluted air containing high OH reactivity (k_{OH}) is sampled by the CMR, the reaction of OH with atmospheric reactants competes with the OH loss by wall reactions and scavenging inside the CMR. Therefore, an influence of the OH reactivity on the OH transmission and scavenging efficiency is possible. In addition, OH radicals could be produced by chemical reactions in the CMR. A simple kinetic model is used to quantify these influences. In the atmosphere, the ambient concentration of short-lived OH radicals is in steady state and can be calculated from the total OH production rate and OH reactivity.

$$[OH]_a = \frac{P_{hv} + P_d}{k_{OH}} \quad (\text{Eq. 3.24})$$

Here, P_{hv} represents the photolytic OH production rate, which is dominated in the lower troposphere by the photolysis of O_3 and HONO (Reaction R1.1, R1.2, R1.5). P_d denotes non-photolytic (dark) OH production, which includes the reaction of HO_2 radicals with NO (Reaction R1.12), ozonolysis of alkenes and, for example, isomerization reactions of RO_2 leading directly to OH formation.

When the air enters the CMR, photolysis reactions stop, but chemical reactions of OH with atmospheric reactants and dark OH production continues, as long as the reactants that produce or destroy OH are not lost in the CMR tube. In many atmospheric environments, the reaction between HO_2 and NO (R3.12) with a reaction rate constant of $k_{HO_2+NO} = 8.1 \times 10^{-12} \text{ cm}^3 \text{ s}^{-1}$ at 298 K (Atkinson et al., 2004) is the dominant non-photolytic source of atmospheric OH. It can be assumed that the OH production from Reaction R3.12 continues inside the CMR at the same rate as in the ambient atmosphere, because concentrations of HO_2 and NO do not significantly change. HO_2 is relatively short-lived, but during the short transit time of 18 ms through the reactor, its conversion to OH is small for typical conditions. Even high ambient NO mixing ratios of 30 ppbv lead only to a conversion of HO_2 to OH of less than 10%. Furthermore, HO_2 loss is partly compensated by HO_2 production from the reaction of atmospheric RO_2 with NO. Also, the loss of HO_2 by wall reactions is small (18%) (Section 3.4.1). NO has an even longer chemical lifetime (on order of several minutes) than HO_2 , which is usually determined by the reaction of NO with O_3 and peroxy radicals (HO_2 and RO_2).

As a result of the ongoing chemical reactions, ambient OH concentrations relax in the CMR to a new steady state resulting in a concentration $[OH]'$ and having a chemical lifetime τ'_{OH} .

$$[OH]' = \frac{P_d}{k_{OH} + k_w + k_{sc}} \quad (\text{Eq. 3.25})$$

$$\tau'_{OH} = \frac{1}{k_{OH} + k_w + k_{sc}} \quad (\text{Eq. 3.26})$$

The relaxation follows first order kinetics and the reaction time t in the reactor determines the degree of relaxation. The general time law for such a transition from an initial concentration $[OH]_0$ ($t = 0$) to a final concentration $[OH]'$ is given by

$$[OH](t) = [OH]_0 + \{[OH]' - [OH]_0\} \left[1 - \exp\left(-\frac{t}{\tau'_{OH}}\right) \right] \quad (\text{Eq. 3.27})$$

Using this expression, an OH transmission β can be defined for a tube with the transit time Δt of the air.

$$\beta = \frac{[\text{OH}](\Delta t)}{[\text{OH}]_0} \quad (\text{Eq. 3.28})$$

The initial OH concentration ($[\text{OH}]_0$) is reduced compared to the ambient OH concentration by the factor c ($c [\text{OH}]_a$) with a value of the reduction factor of $c = 1.0$ for the entrance section and $c = \beta^e$ for the reaction section (Figure 3.6). Making use of the relationships in Eq. 3.24, 3.25 and 3.26, the transmission can be written as

$$\begin{aligned} \beta(c, k_{\text{OH}}, k_w, k_{\text{sc}}, \Delta t) \\ = 1 + \left\{ \frac{1}{c} \frac{P_d}{P_{\text{hv}} + P_d} \times \frac{k_{\text{OH}}}{k_{\text{OH}} + k_w + k_{\text{sc}}} - 1 \right\} [1 - \exp(-[k_{\text{OH}} + k_w + k_{\text{sc}}] \Delta t)] \end{aligned} \quad (\text{Eq. 3.29})$$

More specifically, the OH transmissions for the entrance and reaction sections in the modes with and without scavenger are obtained as:

$$\beta^e = \beta(c = 1, k_{\text{OH}}, k_w^e, k_{\text{sc}} = 0, \Delta t_e) \quad (\text{Eq. 3.30})$$

$$\beta_{\text{N}_2}^r = \beta(c = \beta^e, k_{\text{OH}}, k_w^r, k_{\text{sc}} = 0, \Delta t_r) \quad (\text{Eq. 3.31})$$

$$\beta_{\text{sc}}^r = \beta(c = \beta^e, k_{\text{OH}}, k_w^r, k_{\text{sc}}, \Delta t_r) \quad (\text{Eq. 3.32})$$

These formulas can be inserted in Eq. 3.12 and 3.13 to calculate the OH transmission β_{N_2} and residual factor α as functions of the OH reactivity. It is worth noting that in the case that no ambient OH reactants ($k_{\text{OH}} = 0$) are present, Eq. 3.30, 3.31 and 3.32 become identical to Eq. 3.14, 3.9 and 3.11, respectively.

3.5.1.2 Modelling the scavenging assuming homogeneous mixing of the scavenger

The kinetic model (Section 3.5.1.1) can be used to estimate the influence of the ambient OH reactivity and dark OH production on the determination of interferences and ambient OH concentrations. The OH wall loss rate coefficients, k_w^e and k_w^r , are taken from the characterization experiments (Table 3.3). The reaction times are $\Delta t_e = 6.6$ ms and $\Delta t_r = 11.2$ ms. Homogeneous mixing of the propane in the scavenging mode is assumed and an effective rate coefficient $k_{\text{sc}}^{\text{eff}} = 283 \text{ s}^{-1}$ is applied as calculated from the experimentally derived value for the residual factor $\alpha^0 = 0.042$ (Section 3.4.1).

The extraction of the ambient OH signal S_{OH} and the OH interference signal S_i from the measured OH signals in the scavenging and nitrogen modes (Eq. 3.8 and 3.9) requires the knowledge of the remaining fraction of ambient OH in the scavenging mode (α). Figure 3.12a presents modelled values of α as a function of atmospheric OH reactivity for different ratios of dark-to-total OH production rates $P_d/(P_{\text{hv}} + P_d)$. The dependence is shown for reactivities from 0 to 100 s^{-1} , a range that is typical

for the lower troposphere (e.g., Lou et al. (2010)), and for $P_d/(P_{hv}+P_d)$ ratios between 0 and 1. The parameter α shows a considerable variation for these conditions with the largest effect for high OH reactivities. For $k_{OH} = 100 \text{ s}^{-1}$, α varies from 0.042 to 0.3 for variations of the fraction of dark OH production ($P_d/(P_{hv}+P_d)$) from 0 to 1. The latter case with $P_d \gg P_{hv}$ is typical at nighttime. In the special case of only photolytic production of OH ($P_d = 0$) meaning no OH production inside the CMR, the residual factor α remains constant (same as the experimental value $\alpha^0 = 0.042$) and becomes independent of the OH reactivity. In this case, the OH reactivity from ambient OH reactants adds to the total first-order loss rates and cancels out in Eq. 3.19, yielding Eq. 3.20. Small non-photolytic OH production (P_d) would be expected, for example, in an environment with low NO mixing ratios, where the reaction of HO_2 with NO does not play a significant role. Under atmospheric conditions, when the production P_d exceeds the photolytic OH production, the remaining fraction of ambient OH reaching the nozzle increases due to the ongoing dark OH production in the CMR. Its sensitivity to the OH reactivity increases with increasing fraction of dark OH production and becomes largest at nighttime, when ambient OH is only produced by dark reactions.

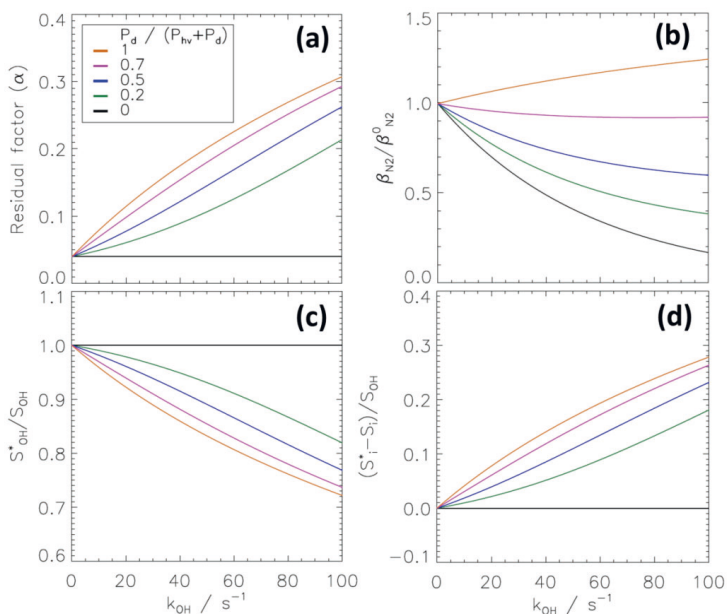


Figure 3. 12: Theoretical dependence of the residual factor α (a.) and normalized transmission $\beta_{N_2}/\beta_{N_2}^0$ (b.) on the OH reactivity in the sampled air. The applied model assumes homogeneous mixing. Parameters are taken from the characterization experiments of the CMR. The dependence is shown for different ratios of dark to total atmospheric OH production rates. A ratio of one corresponds to nighttime (without photolytic OH production), while a ratio of zero denotes a case without dark OH production. Panels c. and d. show the bias in the determination of the ambient OH signal (S_{OH}) and interference signal (S_i), if the k_{OH} dependence of α is not taken into account. The biased signals S_{OH}^* and S_i^* are calculated with the residual factor in the synthetic air sampling α^0 without the consideration of the chemical perturbations by the sampled air (see text).

The sensitivity of the calculated ambient OH signal S_{OH} (Eq. 3.8) and the OH interference signal S_i (Eq. 3.9) to variations of the residual factor α can also be seen in Figure 3.12. A biased signal S_{OH}^* would be obtained, if the influence of OH reactivity on the signal obtained from the chemical modulation was neglected.

$$\frac{S_{OH}^*}{S_{OH}} = \frac{1 - \alpha}{1 - \alpha^0} \quad (\text{Eq. 3.33})$$

The corresponding bias in the interference signal S_i^* is:

$$\frac{S_i^* - S_i}{S_{OH}} = 1 - \frac{S_{OH}^*}{S_{OH}} \quad (\text{Eq. 3.34})$$

Figure 3.12d demonstrates that the interference signal would be systematically overdetermined, while the ambient OH signal would be correspondingly underestimated (Figure 3.12c), if the chemistry in the CMR was not considered. This effect is largest at night, when up to 25% of the true ambient OH signal could be wrongly assigned as interference for high OH reactivity of $k_{OH} = 100 \text{ s}^{-1}$. The error remains generally small (< 5%) for all contributions of dark OH production ($P_d/(P_{hv}+P_d)$) in the range between 0 – 1), if OH reactivities stay below 10 s^{-1} . More generally, the influence of the OH reactivity on the residual factor α is small, when the OH reactivity is much lower than the scavenger reactivity (here 283 s^{-1}) and therefore introduces only a small perturbation of the CMR chemistry.

3.5.1.3 Modelling of the scavenging assuming inhomogeneous mixing of the scavenger

A reduced effective reactivity of $k_{sc}^{eff} = 283 \text{ s}^{-1}$ compared to the reactivity of the scavenger expected from homogeneous mixing is used in the analysis in the previous section (Figure 3.12). As an alternative approach, inhomogeneous mixing with different scavenger concentrations in two different parts (Eq. 3.21) can be applied to describe the observed scavenging efficiency (Section 3.4.2). A small fraction $f = 0.04$ of air would be required to contain little or no scavenger to explain observations. This part does not contribute to chemical modulation ($\alpha_1 = 1$). The main part (1-f) of the gas flow is assumed to contain well-mixed propane with a scavenger reactivity of $k_{sc}'' = 534 \text{ s}^{-1}$ as expected from the propane addition. Similar as in the model assuming homogeneous mixing, chemical perturbations in the CMR from the chemistry of ambient reactants (Eq. 3.20, 3.31 and 3.32) can then be applied to calculate the dependence of the residual factor α_2 on the OH reactivity of the sampled air (Eq. 3.21).

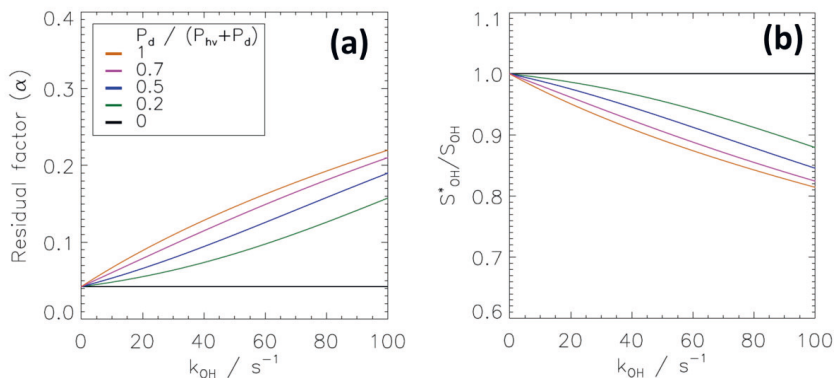


Figure 3.13: Calculated dependence of the residual factor α and ratio S_{OH}^* / S_{OH} on the OH reactivity in the sampled air using a model that takes inhomogeneous mixing of the scavenger into account. The dependence is shown for different ratios of dark to total atmospheric OH production rates. The coloured horizontal lines denote the same ratios of dark to total OH production rates as used in Figure 3.12.

The results presented in Figure 3.13a are very similar to the results obtained, if homogeneous mixing with reduced scavenger reactivity is assumed. Again, the residual factor α is constant (0.042) and independent of the OH reactivity, if there are only photolytic OH sources ($P_d = 0$). In this model, the constant offset of $f = 0.04$ in the Eq. 3.21 represents ambient OH that was not scavenged in the minor fraction of air with no scavenger. In the bulk flow, however, essentially all OH is depleted by the high scavenger reactivity of $534 s^{-1}$. If there is also dark OH production ($P_d > 0$), the residual factor α increases with increasing OH reactivity like in the case of assumed homogeneous mixing. The maximum sensitivity to OH reactivity is again obtained for a $P_d / (P_{hv} + P_d)$ ratio of 1, for example, for very high NO concentrations or for night time conditions ($P_d = 0$).

The main difference between the results assuming either homogeneous or inhomogeneous mixing is a slightly weaker sensitivity to the OH reactivity in the case of inhomogeneous mixing. This can be explained by the higher scavenging reactivity in the bulk flow. Thus, α varies from 0.042 to 0.22 at an OH reactivity of $k_{OH} = 100 s^{-1}$ for the model with inhomogeneous mixing, whereas the span is slightly larger reaching 0.3 in the model with homogeneous mixing. As the results for α are very similar, also the ratio S_{OH}^* / S_{OH} gives comparable results (Figure 3.12c and Figure 3.13b).

3.5.1.4 Model description of the OH transmission

The conversion of the signals S_{OH} from ambient OH and S_i from interferences to concentrations requires the knowledge of the transmission β_{N_2} (Eq. 3.10 and 3.11). As the calibration of the LIF-CMR instrument gives the combined sensitivity and OH transmission for OH in clean air $C_{OH} \times \beta_{N_2}^0$ (Section 3.4.4), the ambient concentration derived from the chemical modulation (Eq. 3.10) can be rewritten as

$$[\text{OH}]_{\text{CHEM}} = \frac{1}{C_{\text{OH}}\beta_{\text{N}_2}^0} \times \frac{\beta_{\text{N}_2}}{\beta_{\text{N}_2}^0} \times S_{\text{OH}} \quad (\text{Eq. 3.35})$$

Here, the normalized function $\beta_{\text{N}_2}/\beta_{\text{N}_2}^0$ contains the dependence of the OH transmission on the OH reactivity in the sampled air shown in Figure 3.12b. The value of the function $\beta_{\text{N}_2}/\beta_{\text{N}_2}^0$ is much more sensitive to the OH reactivity from OH reactants contained in the sampled air than the remaining fraction of OH in the scavenger mode, α . Without scavenger, the atmospheric OH reactivity competes only with wall loss, for which the rate is of similar magnitude as the loss rate due to ambient OH reactants (k_{OH}). In an environment with little NO, i.e. with no dark OH production $P_{\text{d}}/(P_{\text{hv}}+P_{\text{d}}) = 0$, the reactivity due to OH reactants has to be added to the wall loss rate. The normalized ratio $\beta_{\text{N}_2}/\beta_{\text{N}_2}^0$ decreases exponentially with $-k_{\text{OH}}(\Delta t_{\text{e}} + \Delta t_{\text{r}})$ in this case. Under this condition, the normalized transmission decreases by a factor of 6, when the OH reactivity k_{OH} reaches a value of 100 s^{-1} . Without taking this effect into account, the calculated ambient OH concentration would be extremely underestimated in an environment with very little NO. However, when the OH reactivity remains below 10 s^{-1} , the OH concentration is underestimated by less than 15%.

When the value of $P_{\text{d}}/(P_{\text{hv}}+P_{\text{d}})$ ratio exceeds 0.7, the dependence of the normalized transmission on OH reactivity becomes weak. In this case, the normalized transmission is around 1.0. It exceeds 100% transmission at $P_{\text{d}}/(P_{\text{hv}}+P_{\text{d}}) = 1$. This means that the loss of OH in ambient air during the transit in the CMR is smaller than expected from measurements in clean synthetic air. The condition $P_{\text{d}}/(P_{\text{hv}}+P_{\text{d}}) = 1$ implies that the total atmospheric OH production continues when the air enters the CMR. Inside the CMR, OH wall reactions compete with gas-phase reactions (k_{OH}). When k_{OH} is much larger than k_{w} , the expected steady-state of OH in the CMR is the same value as in outside air, which means that the transmission β_{N_2} becomes effectively 1.0, and $\beta_{\text{N}_2}/\beta_{\text{N}_2}^0 = 1/\beta_{\text{N}_2}^0$.

3.5.2 Atmospheric OH radical measurements with the FZJ-LIF-CMR instrument during the JULIAC campaign

The JULIAC campaign was designed to investigate tropospheric chemistry in a rural environment, which is influenced by biogenic and anthropogenic emissions. The one-year campaign made use of the SAPHIR infrastructure and instrumentation (Chapter 2). During the four intensive JULIAC periods in 2019 (Table 3.5 and 3.6), OH measurements were performed by the LIF instrument with the newly developed chemical modulation system. In addition, OH was measured by the DOAS instrument for some periods of the JULIAC campaign (winter, summer, and autumn periods). Besides studying atmospheric chemical processes, the campaign offered the opportunity to test the chemical modulation system under atmospheric conditions. The CMR was partly operated with different types of injectors and with different propane concentrations (Table 3.4). For a short time between 1 to 11 February 2019, OH detection was done without the CMR system to increase the OH detection sensitivity for measurements of low wintertime OH concentrations.

3.5.2.1 Influence of ambient conditions

The possible influence of ambient conditions on the chemical modulation results was investigated for the conditions of the JULIAC campaign. The ratio of the dark-to-total OH production, $P_d/(P_{hv}+P_d)$, was calculated from the reaction of HO₂ and NO (Reaction R1.12) and the photolysis of O₃ and HONO (Reaction R1.1, R1.2, R1.5). The ratio was between 0.7 and 1.0 most of the time during spring, summer, and autumn periods (Figure 3.14). Only in the winter season, the range of values was broader (0.4 - 1.0). The low values of the ratios are due to high NO_x concentrations in the morning, which suppressed the HO₂ concentration and the OH production by the reaction of HO₂ with NO, until NO_x concentrations decreased later in the day.

During all seasons, measured OH reactivities were relatively low ($< 15 \text{ s}^{-1}$) (Table 3.5) with few exceptions in the winter period where the OH reactivity reached 30 s^{-1} . In the JULIAC campaign, the predicted influence of the OH reactivity on the residual factor α and the OH transmission β_{N_2} remained small (Figure 3.15). The influence on the calculated ambient OH signal was mostly less than 5 % during the spring, summer, and autumn periods, and less than 12 % in the winter period (Figure 3.15c). For the encountered $P_d/(P_{hv}+P_d)$ ratios of 0.7 - 1.0, the normalized transmission of the CMR system, $\beta_{N_2}/\beta_{N_2}^0$, was only weakly dependent on the OH reactivity and the variability was less than $\pm 5\%$ in most cases (Figure 3.15b). When ambient OH concentrations were calculated (Eq. 3.10 and 3.11), the influences of the OH reactivity on the remaining OH, α , and the OH transmission, β_{N_2} , are included. The bias, when the influence of the OH reactivity on the calculated OH concentration is neglected, can be described by the ratio

$$\frac{[\text{OH}]^*}{[\text{OH}]} = \frac{S_{\text{OH}}^*}{S_{\text{OH}}} \times \frac{\beta_{N_2}}{\beta_{N_2}^0} \quad (\text{Eq. 3.31})$$

shown in Figure 3.15d. $[\text{OH}]^*$ represents the biased OH concentration that is evaluated without the consideration of the changes in residual OH after scavenging by propane injection and OH transmission (using α^0 and $\beta_{N_2}^0$), whereas the correct $[\text{OH}]$ takes the changes by using α (Eq. 3.33) and β_{N_2} (Eq. 3.35) into account. For $P_d/(P_d+P_{hv})$ ratios between 0.7 and 1.0, the biases in the evaluated OH concentrations ($[\text{OH}]^*/[\text{OH}]$) from the residual factor α and OH transmission β_{N_2} partly compensate each other due to the increase of the OH transmission β_{N_2} . For $P_d/(P_d+P_{hv})$ ratios smaller than 0.7, the biases add up and lead to an increasing underestimation of the ambient OH concentration, when the OH reactivity becomes larger.

Although during the winter season the influence of the OH reactivity on the calculated ambient OH signal could reach 12%, its combined influence on the calculated OH concentration is on average 2 % for the entire data set from the JULIAC campaign. If the corresponding corrections were applied, the number of OH radical data points would be reduced by 20 %, because not all data (e.g., HO₂, NO, HONO) needed for corrections were always available. For this reason, no additional corrections were applied to the calculations of the OH radical concentrations for the data set of the JULIAC campaign.

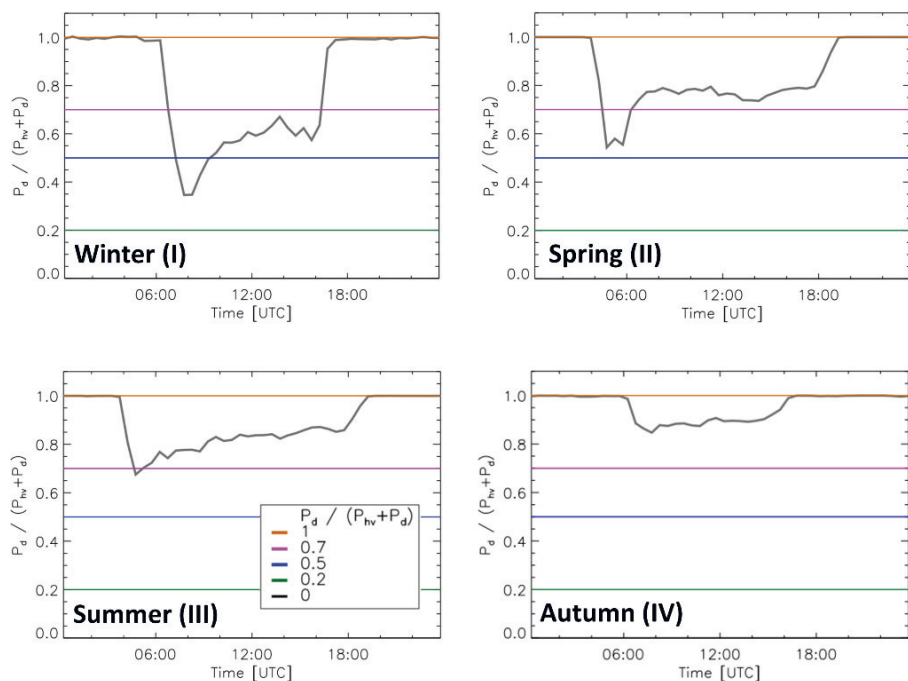


Figure 3. 14: The median ratio of dark to total atmospheric OH production rates during the four periods of the JULIAC campaign (grey lines). P_d is the calculated reaction rate of HO₂ with NO (Reaction R1.12), and P_{hv} is the OH production rate from the photolysis of ozone (Reaction R1.1, R1.2) and HONO (Reaction R1.5). For the calculations, measurements were averaged to 300s (Table 2.1). The coloured horizontal lines denote the same ratios of dark to total OH production rates as used in Figure 3.12 and 3.13.

Table 3. 5: Summary of meteorological conditions and trace gas concentrations during daytime of the JULIAC campaign (median values with 1 σ standard deviations of ambient variabilities).

	OH / 10 ⁶ cm ⁻³	NO / ppbv	O ₃ / ppbv	H ₂ O / % ^a	k _{OH} / s ⁻¹	k _{VOC} ^b / s ⁻¹	T / °C	j(O ¹ D) / 10 ⁻⁶ s ⁻¹	P _d / ppbv s ⁻¹	P _{hv} / ppbv s ⁻¹
14 Jan. – 11 Feb.	0.27	0.3	22.3	0.6	6.1	2.2	4.7	0.3	0.2	0.15
9 Apr. – 6 May	1.6	0.2	41.6	0.7	5.8	3.0	15.6	2.0	1.9	0.6
4 Aug. – 2 Sep.	3.0	0.2	38.5	1.4	6.3	3.2	26.6	3.6	1.9	0.4
28 Oct. – 24 Nov.	0.4	0.8	16.8	0.8	5.6	1.7	8.4	0.5	0.9	0.1

^a Volume mixing ratio

^b OH reactivity of non-methane VOCs, calculated as the difference between measured total OH reactivity and the sum of calculated reactivities of CH₄, CO, O₃, NO, and NO₂.

Table 3. 6: Summary of meteorological conditions and trace gas concentrations during nighttime of the JULIAC campaign (median values with 1σ standard deviations of ambient variabilities).

	OH / 10^6 cm^{-3}	NO / ppbv	O ₃ / ppbv	H ₂ O / % ^a	k _{OH} / s ⁻¹	k _{VOC} ^b / s ⁻¹	T / °C
14 Jan. – 11 Feb.			22.8	0.6	6.3	2.5	2.4
9 Apr. – 6 May			40.1	0.7	5.8	3.2	10.0
4 Aug. – 2 Sep.	N/A ^c	N/A ^c	31.4	1.4	6.0	3.8	17.7
28 Oct. – 24 Nov.			15.0	0.7	6.5	2.4	4.6

^a Volume mixing ratio

^b OH reactivity of non-methane VOCs, calculated as the difference between measured total k_{OH} and the sum of calculated reactivities of CH₄, CO, O₃, NO, and NO₂.

^c Below the limit of the detection.

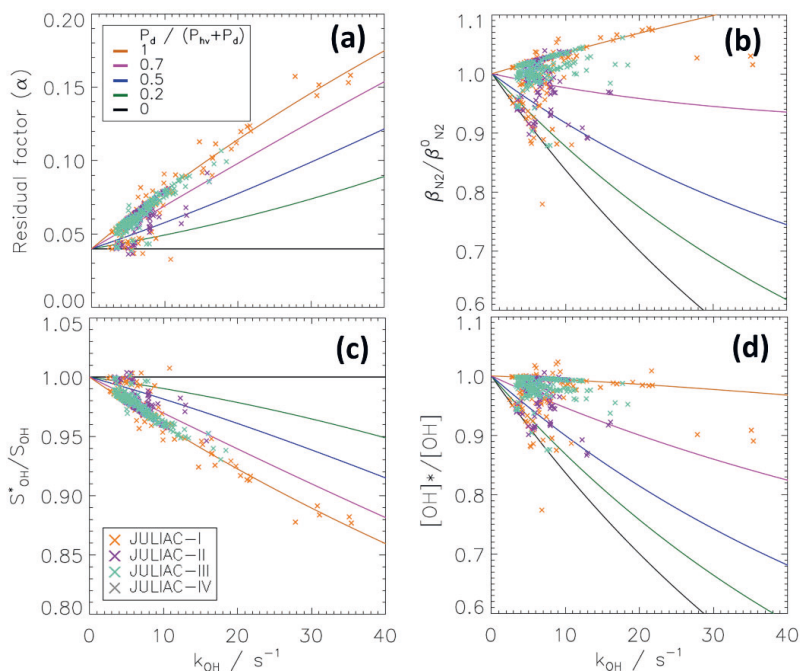


Figure 3. 15: Modelled dependence of the CMR properties on the OH reactivity for the chemical conditions during the different seasons 2019 in the JULIAC campaign. Here, the model for a homogeneously mixed scavenger was applied. Theoretical dependence of the residual factor α (a.) and normalized transmission $\beta_{\text{N}_2}/\beta_{\text{N}_2}^0$ (b.) on the OH reactivity in the sampled air. The applied model assumes homogeneous mixing. Parameters are taken from the characterization experiments of the CMR. The dependence is shown for different ratios of dark to total atmospheric OH production rates. A ratio of one corresponds to nighttime (without photolytic OH production), while a ratio of zero denotes a case without dark OH production. Panels c. shows the bias in the determination of the ambient OH signal (S_{OH}), if the dependence of α is not taken into account. Panel (d) shows the ratio of corrected to uncorrected ambient OH concentrations, if the dependence of the parameters α and β_{N_2} on the OH reactivity is taken into account.

3.5.2.2 Comparison of OH concentrations measured in the JULIAC campaign

The combined OH data set measured by the DOAS and the LIF-CMR instruments which accounts for the correction of the potential interference was used for an OH measurement comparison in ambient air. Only summertime (August) data are used, because OH concentrations measured in the other JULIAC periods were either close to the limit of detection of the instruments (winter and autumn) or the DOAS instrument was not operated (spring). In general, the measurements by LIF and DOAS instruments agree well within their combined 1σ accuracies of 18% and 6.5 %, respectively (Figure 3.16). An exception is the heat wave period between 22 and 26 August, when the floor beneath the

chamber was continuously heated by the strong solar radiation. In this period, the measurements by the LIF instrument were systematically higher by about 25% than those by the DOAS instrument. The reason for the discrepancy is not clear as no issue with either instrument was found.

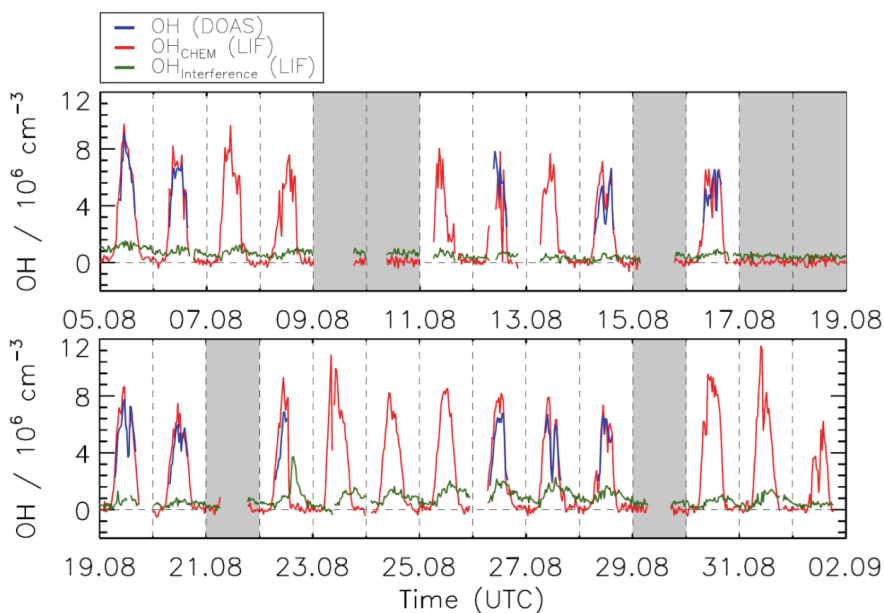


Figure 3. 16: Time series of OH concentrations measured by LIF-CMR (red line) and DOAS (blue line) instrument and the interference signal of the LIF instrument determined from the CMR measurement scheme during the summer period of the JULIAC campaign. All data points are 30 min averages. Vertical dashed lines denote midnight. Grey coloured areas indicate when the chamber roof was closed. Data gaps occurred when measurements were stopped for calibration measurements of instruments.

The scatter plot of the OH data and the results of a linear regression are shown in Figure 3.17. The linear regression is forced through the origin because of the small number of data points in nighttime, when OH concentrations from both of instruments are expected to be zero. The slope of the regression line is 1.11 ± 0.02 . The deviation of the slope from unity is well within the instrumental accuracies. This demonstrates that there were no significant systematic errors from the calibration of the instrument with the CMR system. The residual of the fit scatters symmetrically around zero without exhibiting any specific dependence, which implies that there is a linear relationship between the two OH measurements.

Similar good agreement was found in previous intercomparisons between OH concentration measurements by the DOAS and FZJ-LIF instruments, when the LIF instrument used wavelength modulation only and data were corrected for the known ozone interference. These intercomparisons were performed in photochemistry experiments in SAPHIR for a wide range of different VOCs and chemical conditions (Schlosser et al., 2007; Schlosser et al., 2009; Fuchs et al., 2012; Novelli et al.,

2018; Rolletter et al., 2019; Novelli et al., 2020), and in a field campaign in relatively clean air in North East Germany (Hofzumahaus et al., 1998).

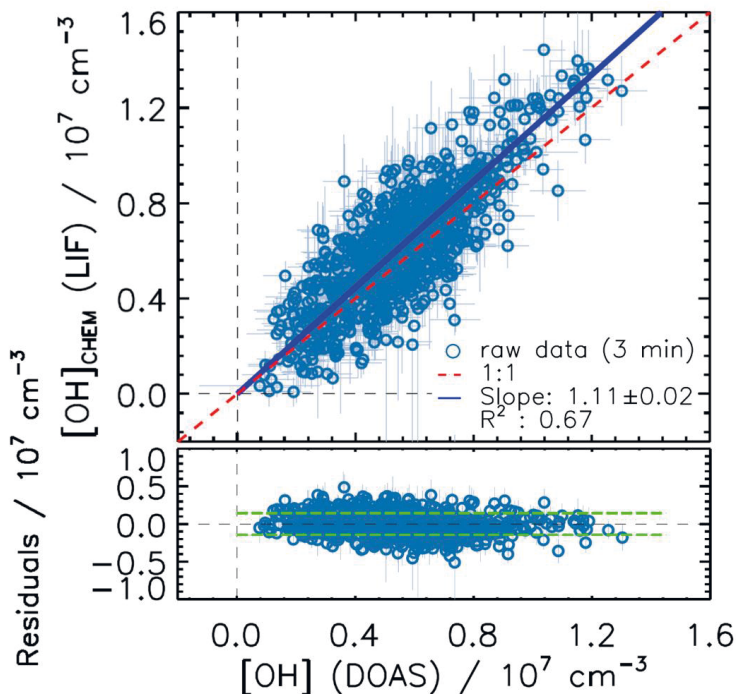


Figure 3.17: Correlation plot between OH concentrations measured by the FZJ-LIF-CMR and the DOAS instruments during the summer period of the JULIAC campaign. Data from the strong heat wave period between 22 and 26 August were excluded (see text). The blue line is a linear fit of 3-minute data set weighted with the statistical errors of both instruments and forced to the origin. Vertical and horizontal bars denote the 1σ precision of the measured data points. The below panel shows the residuals of the OH concentrations obtained from the difference between the OH concentrations measured by the FZJ-LIF-CMR instrument and the linear fit. Green dashed lines represent the value of the standard deviation of the residuals.

3.5.2.3 OH interferences determined by the CMR system during the JULIAC campaign

The time series of the OH interference in the OH concentration measurements that were determined by chemical modulation system during the summer period are presented in Figure 3.16. The interference signal shows diurnal variations with minimum values at night and maximum values around midday. Median values (5 Aug. to 1 Sep.) of the interference signal exhibit a diurnal variation with a maximum daytime value of $0.9 \times 10^6 \text{ cm}^{-3}$ and a minimum nighttime value of $0.4 \times$

10^6 cm^{-3} . The highest value of the interference signal of $2 \times 10^6 \text{ cm}^{-3}$ occurred during the heat wave from 22 – 29 August, when the daytime air temperature reached 40°C and ozone mixing ratios were 100 ppbv, respectively. At the same time, the total OH reactivity reached the highest values (19 s^{-1}) during the JULIAC summer campaign with a contribution of reactivity from organic compounds (k_{VOC}) of up to 14 s^{-1} . During the other seasons, interfering signals at daytime were lower with maximum values of $1 \times 10^6 \text{ cm}^{-3}$ (Figure 3.18).

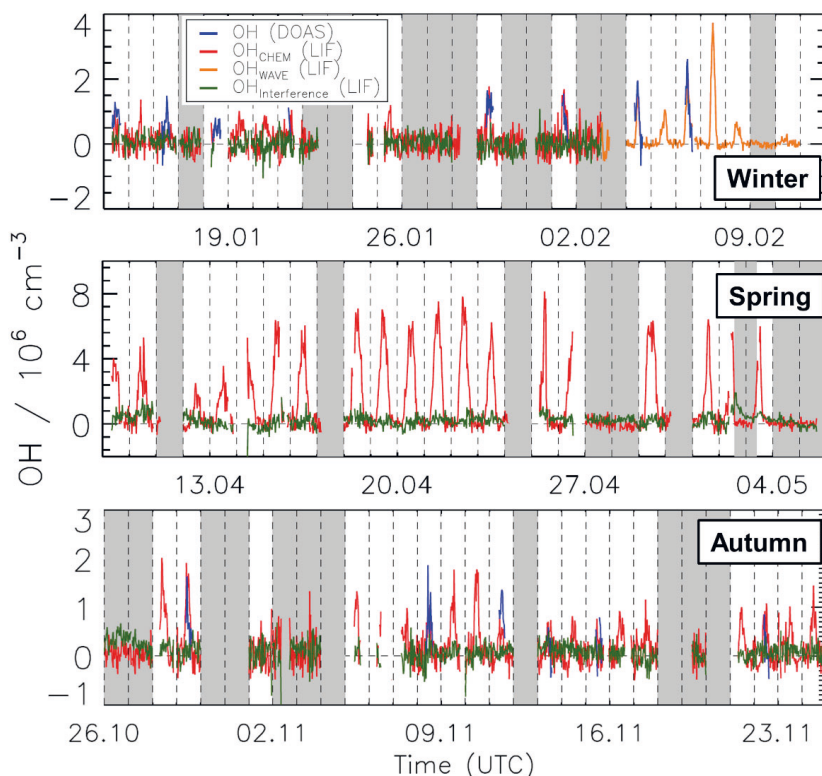


Figure 3.18: Measured OH concentrations and OH interference signals by the LIF instrument with the CMR system and DOAS instrument during the JULIAC campaign in the winter, spring and autumn periods. During the spring period, the DOAS instrument was not operated. All data are 30 min average values. Dashed lines denote midnights. Grey coloured areas indicate when the chamber roof was closed.

The OH interferences measured during all four periods of the JULIAC campaign are compared to the expected interferences from the laser photolysis of ozone (Figure 3.19). The expected ozone interference is calculated using the parameterization of the ozone interference signal (Eq. 3.23) resulting from the three different chamber and laboratory experiments (Figure 3.10). It is worth noting that there is a slight curvature in the parameterization of the ozone interference (Figure 3.19) because of the fluorescence quenching effect by water vapor in the detection cell (Holland et al.,

2003). This becomes visible in this data set due to the large range of the water vapor mixing ratios experienced in the JULIAC campaign.

The comparison demonstrates that the measured interference signals can be on average explained by the known ozone water interference within the uncertainty of the parametrization for the entire data set that includes a large range of atmospheric conditions. The maximum difference between the measured and the calculated ozone interferences is $(3.4 \pm 2.5) \times 10^5 \text{ cm}^{-3}$ for the highest ozone and water vapor concentrations. This difference is well below the limit of detection of the LIF-CMR technique ($7 \times 10^5 \text{ cm}^{-3}$). Thus, there is no evidence for a significant, unexplained OH interference for the atmospheric conditions in the JULIAC campaign (Table 3.5). It is worth noting that the potential contribution of NO_3 to the interfering signal was negligible for the entire campaign due to the low NO_3 concentrations that were maximum 10 pptv.

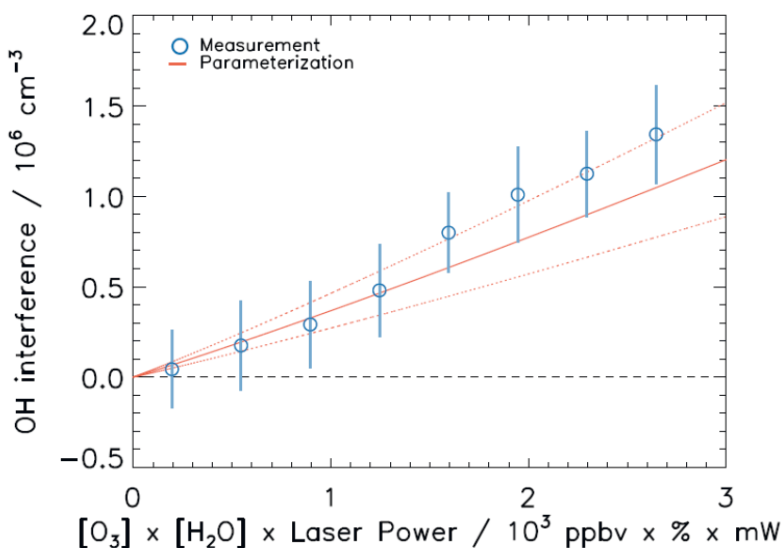


Figure 3. 19: Averaged OH interference measured during all periods of the JULIAC campaign (vertical bars are standard deviations of averaged data) compared to calculations of the expected ozone interference using the parameterization determined in laboratory experiments (Eq. 3.23, Section 3.4.5.1). The red dotted lines represent the uncertainty of the parameterization. Each data point includes more than 100 measurements.

3.6 Comparison of the CMR system of the FZJ-LIF instrument with systems of other LIF instruments and challenges of the application in specific environments

The tests of the CMR system performed in experiments with synthetic air (Section 3.4) and with ambient air during the JULIAC campaign (Section 3.5) demonstrate that the new chemical

modulation system of the FZJ-LIF instrument is suitable for measurements of interference-free ambient OH concentrations and for determining interferences from OH that is artificially produced inside the instrument. The theoretically expected dependence of the OH scavenging efficiency and OH transmission on ambient conditions could not be tested, because the effects for conditions experienced in the JULIAC campaign were too small to be clearly detected within the precision of the measurements. Thus, for atmospheric OH reactivities below 15 s^{-1} , it was sufficient to use the CMR parameters and calibration factors that were determined in synthetic air.

In other field campaigns with higher OH reactivities ($> 30 \text{ s}^{-1}$), for example in strongly polluted urban air or in forested environments, the accurate evaluation of OH measurement by the LIF instrument with the CMR could be more challenging. As shown in Figure 3.12a and 3.13a, the residual factor α could significantly increase at high OH reactivities. If not properly corrected, this leads to an overestimation of the calculated interference signal and therefore a systematic underestimation of ambient OH concentrations on the order of (15 - 25) % (Figure 3.15).

The sensitivity of the CMR parameters to the OH reactivity in the sampled air can be reduced by applying higher scavenger concentrations. Some other research groups use much higher scavenger concentrations in their chemical modulation systems (Table 3.1) with reactivities that are a factor of 5 to 100 higher than in the CMR system in this work (Mao et al., 2012; Novelli et al., 2014a; Rickly and Stevens, 2018; Woodward-Massey et al., 2020). For scavenger reactivities above $10,000 \text{ s}^{-1}$, the influence of atmospheric OH reactivity on the scavenging efficiency becomes negligible. However, this has the danger that also internally produced OH could be scavenged and therefore the determined interference signal too small. Differently from other groups, which did not observe such an effect in their instruments, the characterization experiments performed in this work indicate that up to 5 % of the internally produced OH could be scavenged, when the injected propane concentration is increased by a factor of 4 (Figure 3.8d). To avoid scavenging of internally produced OH, the scavenger concentration is kept low enough. Only one other group operating a chemical modulation method in their LIF instrument reported scavenging of internally produced OH with an efficiency of up to (5 - 10) %, but this was observed for an exceptionally high scavenger reactivity of $30,000 \text{ s}^{-1}$ (Woodward-Massey et al., 2020). Currently, it is not clear, why the FZJ instrument seems to be more sensitive to scavenging of internally produced OH than other instruments.

It can be very challenging to determine the change of the OH transmission of the CMR system with changing ambient conditions, when no scavenger is added. The value of this transmission (β_{N_2}) needs to be known in order to calculate the ambient OH concentration from the retrieved interference-free ambient OH signal (Eq. 3.10). The transmission in the N_2 mode depends on the wall loss rate, the atmospheric OH reactivity, and the transit time through the chemical modulation reactor (Figure 3.12b). While the impact for the ambient conditions in the JULIAC campaign was small (Section 3.5.2.1), a considerable impact would be expected, for example, in a pristine environment like in the Amazonian rain forest. Here, OH reactivities up to 70 s^{-1} were reported (Sinha et al., 2008), while the dark OH production from the reaction of HO_2 with NO can be small compared to the total OH production rate. Novelli et al. (2020) estimated the chemical regeneration of OH from the reaction of HO_2 with NO to be 10% in an isoprene rich forest, where NO mixing ratios were only 10 pptv, which according to the steady-state condition (Eq. 3.24) would correspond to a $P_{\text{d}}/(P_{\text{hv}}+P_{\text{d}})$ ratio of 0.1.

For such conditions, the kinetic model for the CMR predicts a decrease of the OH transmission by a factor of 2.5 - 3. A large correction would be required to account for this effect.

Novelli et al. (2020) also pointed out that additional OH regeneration occurs by isomerization of isoprene peroxy radicals, which increases the non-photolytic regeneration rate to about 50 % of the OH loss rate. Even if this increased the $P_d/(P_{hv}+P_d)$ ratio to 0.5, the predicted decrease of the CMR transmission would be still a factor of 1.5. Therefore, the chemical OH regeneration including processes like RO₂ isomerization needs to be known to calculate the CMR transmission, if the system is operated in environments, in which RO₂ isomerization contributes significantly to the OH production.

One possibility to reduce the sensitivity of the transmission with respect to the ambient OH reactivity is to shorten the transit time in the CMR system. The CMR system of the instrument of the group at Max-Planck-Institute for Chemistry in Mainz (Novelli et al., 2014a) uses a residence time which is a factor of 3 - 4 shorter than in the system in this work. A similar reduction in the FZJ system would lead to much smaller change of the OH transmission β_{N_2} (< 10%) at high OH reactivity values. The main disadvantage is the requirement to draw a large air flow on the order of 100 slpm through the CMR. Such a high flow rate has several problems. The radical source that is used for calibration in this work and that has been trusted for many years in the past provides a maximum air flow rate of 30 slpm and would therefore need to be newly designed. Second, delivering high flows of clean (synthetic) air for calibration and characterization is expensive. Third, the application in the SAPHIR chamber would not be possible because this high flow rate exceeds the total amount of air that can be sampled from the chamber during standard operation.

Another solution to quantify the impact of ambient conditions on the OH transmission is to measure the transmission in-situ in the field by taking measurements of OH with and without the CMR on top of the fluorescence cell in the same air. This directly provides the transmission for the prevailing conditions, but works only reasonably, if OH measurements are interference-free. With interference from internally produced OH, the transmission is overestimated. In order to track changes of the CMR transmission with changes of the ambient OH reactivity and of $P_d/(P_{hv}+P_d)$ over the course of a day, the transmission needs to be frequently determined. This complicates an automatic operation of the system, because the CMR needs to be regularly removed. A number of groups determined the CMR transmission in the field by this approach, but did not discuss the possible influence of ambient conditions on their results (Table 3.1). Mao et al. (2012) reported negligible OH loss in the CMR system in field tests, and Woodward-Massey et al. (2020) found less than 5 % sensitivity reduction in ambient air, if the CMR system is mounted. Both systems used transit times similar to the system in this work. Contrary, the MPI instrument reported lower transmissions of 73 % during tests in daytime for a much shorter residence time in their CMR system. Because of the sparse information about the characteristics of chemical modulation reactors in literature, it is not possible to perform more quantitative comparisons.

Different CMR prototypes built in Jülich were tested with the Peking University LIF instrument (PKU-LIF) in three field campaigns in China (Tan et al., 2017; Tan et al., 2018; Tan et al., 2019). The reactor diameter and total air flow were the same as in this work, but different reactor lengths, injector types, scavenger concentrations and injection flow rates were applied (Table 3.1). The tests were

performed under different ambient conditions in campaigns in summer 2014 in Wangdu south of Beijing (Tan et al., 2017), in autumn 2014 in Heshan in the Pearl River Delta in southern China (Tan et al., 2019), and in winter 2016 in Huairou north of Beijing (Tan et al., 2018). In each case, the CMR was occasionally mounted for a few hours on top of the OH cell of the LIF instrument to investigate possible OH interferences. The scavenging efficiency was determined in the field using an OH calibration source.

Similar to observations during the JULIAC campaign, no significant unknown OH interference signals were detected with the exception of the campaign in Wangdu (Tan et al., 2017) where high mixing ratios of isoprene (up to 3 ppbv) was present. In this campaign, unexplained interference signals equivalent to OH concentrations of $(0.5 - 1) \times 10^6 \text{ cm}^{-3}$ were found with an 1σ uncertainty of $0.5 \times 10^6 \text{ cm}^{-3}$. Around noontime, these signals were less than 10 % of the ambient OH signals. However, the magnitude of the interference was small compared to the interferences found in field observations with other LIF instruments in forested environments (Mao et al., 2012; Hens et al., 2014; Novelli et al., 2014a; Feiner et al., 2016; Lew et al., 2020).

The evaluation of the measurements with the CMR from the PKU-LIF instrument did not take into account the possible dependences of the sensitivity on ambient conditions. If corrections as discussed in Section 3.5 are applied, about half of the unknown interference could have been an artefact due to the unaccounted influence of the atmospheric OH reactivity on the scavenging efficiency at daytime with OH reactivities of about 15 s^{-1} . At nighttime, however, including corrections for the influence of OH reactivity does not make a difference. Tan et al. (2017) reported that the sensitivity loss of the OH detection with the CMR compared to the sensitivity of the fluorescence cell without CMR system was only 5 %. This result was derived from calibration measurements with and without the CMR system using an OH calibration source with a longer flow tube (Fuchs et al., 2012) compared to the one used in this work that does not provide a uniform OH concentration over the area of the flow tube, because the longer residence allows to establish a laminar flow, which has a radial flow velocity profile. A comparison of results for the OH transmission obtained with this radical source and with the plug-flow radical source used in this work (Section 3.4.1) shows that the transmission reported by Tan et al. (2017) needs to be corrected from 0.95 to 0.7. This value is in good agreement with the results for the CMR in the present work. A correction of the transmission as suggested, however, does not have any impact on the main findings of the study by Tan et al. (2017), because the CMR system was only applied for short periods. Tan et al. (2017) used OH concentrations derived from the wavelength modulation of the LIF instrument corrected for calculated ozone interferences for the interpretation of data.

Chapter 4. Measurements of radical and trace gas concentrations and experimental chemical budgets of OH, HO₂ and RO₂ radicals in the JULIAC campaign

4.1 Measurements of radical and trace gas concentrations during the JULIAC campaign

4.1.1 Meteorological and chemical conditions during the JULIAC campaign

Measurements of meteorological parameters, trace gas concentrations, and aerosol properties were performed in the chamber for one month in each season in 2019. A broad range of meteorological and chemical conditions was encountered. During the winter and autumn periods (Fig. 4.1 and 4.4), the overall temperature and solar UV radiation were low, and precipitation often occurred resulting in low photochemical activity. In contrast, during the spring and summer periods (Fig. 4.2 and 4.3), the temperature was high with a heat wave event, which occurred between 24 and 31 August, when the temperature reached up to 40°C.

Overall, relatively clean air was sampled during the whole JULIAC campaign with CO and NO mixing ratios below 0.3 ppmv and 2 ppbv, respectively. However, more polluted plumes with NO mixing ratios higher than 4 ppbv were occasionally observed, especially in winter and autumn. Overall, the concentrations of anthropogenic VOCs (e.g., benzene and toluene) were low with mixing ratios of less than 0.5 ppbv.

Even though the measurement site is surrounded by a deciduous forest, the concentration of biogenic organic compounds (isoprene and monoterpenes) was generally low compared to previously reported values of isoprene mixing ratios, which ranged between 0.5 to 4 ppbv in summer, on the campus of the Forschungszentrum Jülich (Komenda et al., 2003; Spirig et al., 2005; Kanaya et al., 2012). During summer 2019, the observed maximum isoprene and monoterpene mixing ratios reached 0.8 ppbv and 0.15 ppbv with median values of 0.15 ppbv and 0.03 ppbv, respectively. It is important to note that the sampling point for the JULIAC was approximately 20 m higher than the canopy level of the deciduous forest (height: ~ 30 m). In addition, severe droughts and heat waves in 2018 and 2019 caused widespread damage to trees as reported by the Federal Ministry of Food and Agriculture (BMEL, 2021). This may be one reason for the low concentrations of biogenic VOCs during the JULIAC campaign.

Nitrous acid (HONO) and formaldehyde (HCHO) concentrations in the chamber were affected by the light-driven emission from the film of the chamber resulting in peak concentrations (HONO: 0.5 – 0.8 ppbv and HCHO: 2 – 6 ppbv) in the morning when the chamber was illuminated, and these species started to be released by the chamber film.

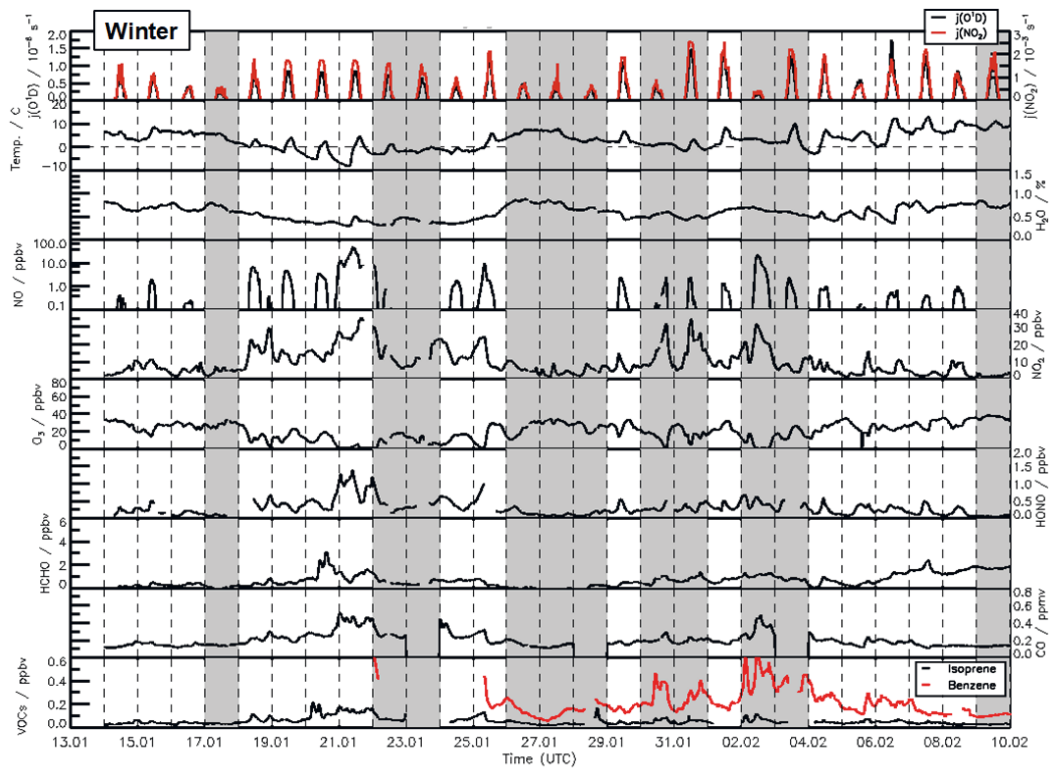


Figure 4. 1: Time series of temperature and trace gas concentrations during the winter period of the JULIAC campaign. Vertical dashed lines denote midnight. Grey shaded areas indicate calibration days or days when the chamber roof was closed.

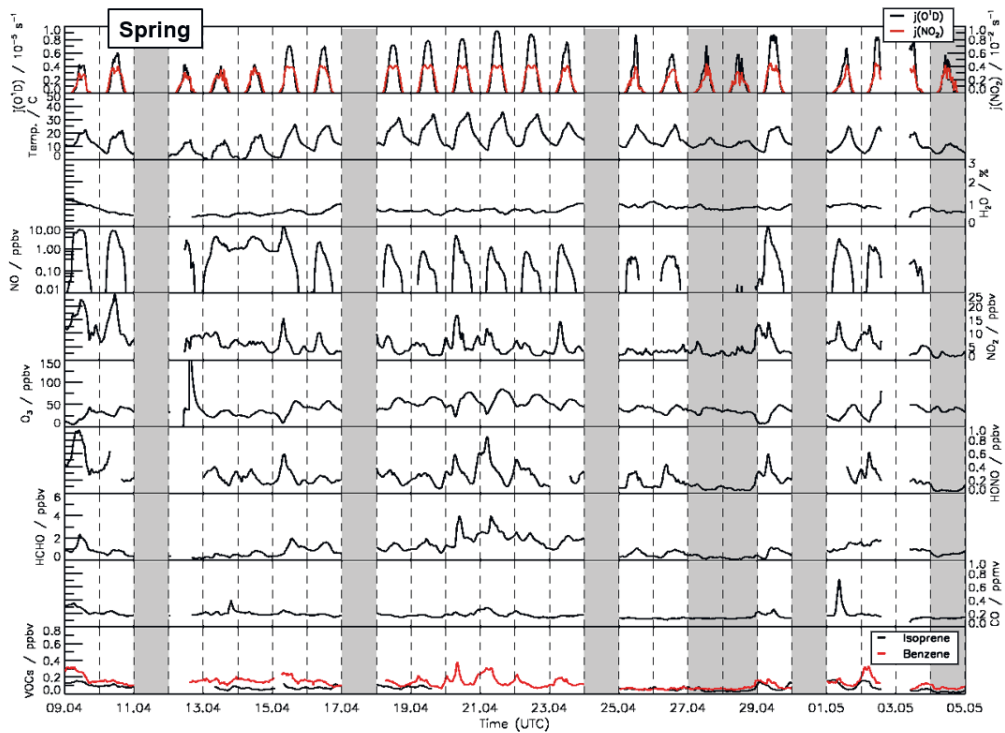


Figure 4. 2: Time series of temperature and trace gas concentrations during the spring period of the JULIAC campaign. Vertical dashed lines denote midnight. Grey shaded areas indicate calibration days or days when the chamber roof was closed.

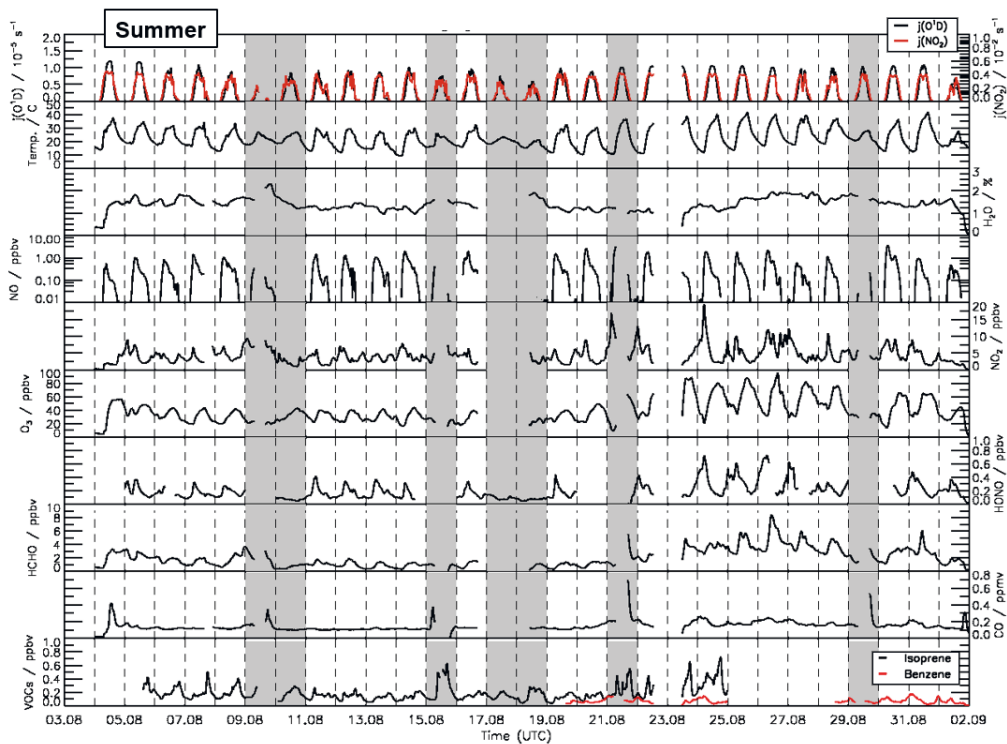


Figure 4. 3: Time series of temperature and trace gas concentrations during the summer period of the JULIAC campaign. Vertical dashed lines denote midnight. Grey areas indicate calibration days or days when the chamber roof was closed.

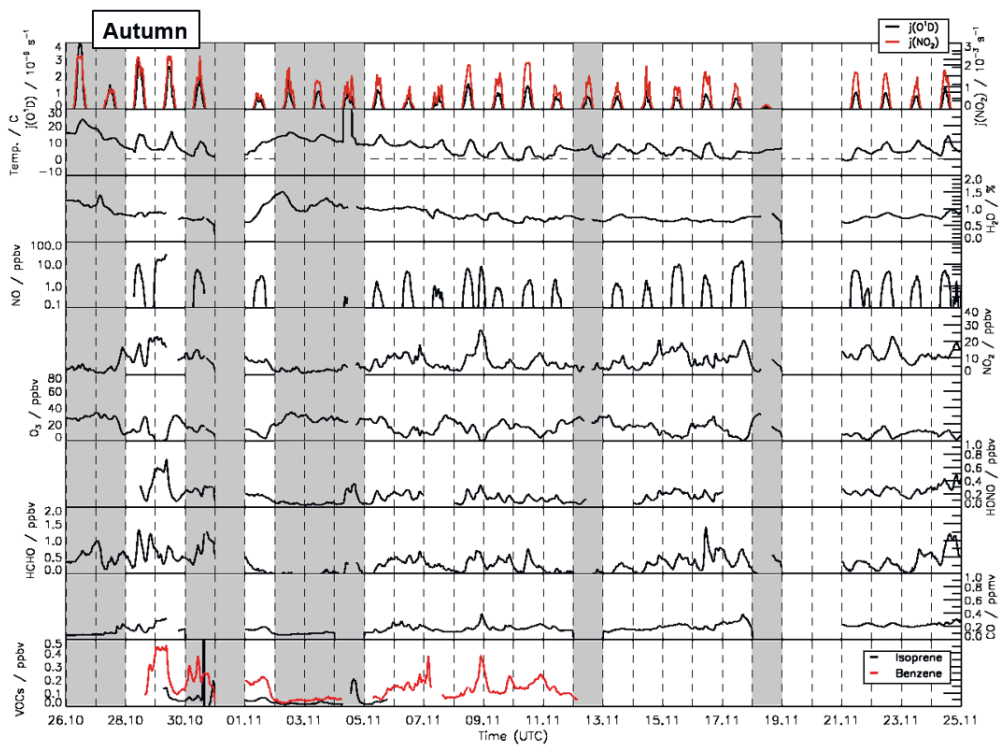


Figure 4. 4: Time series of temperature and trace gas concentrations during the autumn period of the JULIAC campaign. Vertical dashed lines denote midnight. Grey areas indicate calibration days or days when the chamber roof was closed.

4.1.2 OH, HO₂, and RO₂ radical concentrations and OH reactivity during the JULIAC campaign

Time series and median diurnal profiles of measured OH, HO₂, and RO₂ radical concentrations and OH reactivity are shown in Fig. 4.5 – 4.8 and Fig. 4.9 and 4.10, respectively, for each season.

During winter and autumn (Fig. 4.1, 4.4 and 4.10), median daytime OH concentrations were below $1 \times 10^6 \text{ cm}^{-3}$, more than a factor of five smaller compared to values in spring (Fig. 4.6) and summer (Fig. 4.7) due to the low primary radical production at low solar UV radiation, even lower than previously reported wintertime OH concentrations in other field campaigns (Heard et al., 2004; Ren et al., 2006; Kanaya et al., 2007; Tan et al., 2018; Ma et al., 2019). The low wintertime OH concentrations in the JULIAC campaign are partly due to the low photolysis frequencies in the chamber, which were up to 40 % lower than values outside of the chamber.

During spring and summer (Fig. 4.6, 4.7 and 4.9), median OH concentrations were up to $6 - 8 \times 10^6 \text{ cm}^{-3}$, which is within the range of values that have been observed in other field studies in summertime in urban and suburban areas (Tan et al., 2001; Ren et al., 2003; Kanaya et al., 2007; Mao et al., 2010; Lu et al., 2013; Brune et al., 2016; Tan et al., 2017; Whalley et al., 2018; Tan et al., 2019). The photolysis frequency of ozone was also reduced in the JULIAC campaign due to the transmission of the chamber film like in winter and autumn. However, the photolysis of HONO emitted from the chamber wall significantly contributed to the primary OH production, so that a high OH production rate was achieved. The highest OH concentrations ($1.2 \times 10^7 \text{ cm}^{-3}$) occurred during the summer heat wave period.

The diurnal OH concentration profile shows a high correlation with the ozone photolysis rate ($j_{\text{O}^1\text{D}}$) as expected because ozone photolysis is often the most important primary OH source. However, in the JULIAC campaign, the photolysis of HONO gain the most importance due to the emission of HONO from the chamber (Section 2.2). A linear regression analysis (Fig. 4.11) between the OH radical concentrations and $j_{\text{O}^1\text{D}}$ yields a slope of $8.0 \times 10^{11} \text{ cm}^{-3} \text{ s}^{-1}$ with an insignificant intercept of $3.0 \times 10^4 \text{ cm}^{-3}$. A significant intercept would indicate OH concentrations above the limit of detection of the instrument ($\sim 5.0 \times 10^5 \text{ cm}^{-3}$) in the night, when photolysis frequencies are essentially zero. No nighttime OH was also observed in other field campaigns in Germany (Ehhalt and Rohrer, 2000; Handisides et al., 2003; Holland et al., 2003), but was found in field campaigns in China with concentrations of up to $2.4 \times 10^6 \text{ cm}^{-3}$ (Lu et al., 2014; Rohrer et al., 2014; Tan et al., 2017; Tan et al., 2018; Whalley et al., 2021). The slope of the correlation in the JULIAC campaign is 2 – 3 times higher than found in other field campaigns in similar environments (Ehhalt and Rohrer, 2000; Handisides et al., 2003; Holland et al., 2003; Tan et al., 2017). The high value of the slope is likely due to the additional OH production by the photolysis of HONO (Reaction R4.1, Table 4.1) which is emitted from the chamber wall in the presence of light.

Due to the low photochemical activity observed in winter and autumn (Fig. 4.5 and 4.8), also peroxy radical (HO₂ and RO₂) concentrations during these periods were approximately a factor 10 lower than concentrations in spring and summer (Fig. 4.6 and 4.7). The maximum HO₂ and RO₂ concentrations were observed with values of $8.0 \times 10^8 \text{ cm}^{-3}$ and $7.0 \times 10^8 \text{ cm}^{-3}$, respectively, during the heat wave period in August.

In spring and summer, peroxy radical concentrations show a similar diurnal pattern as often observed in rural areas (Sillman et al., 2002; Holland et al., 2003; Ren et al., 2005; Hofzumahaus et al., 2009; Tan et al., 2017). Both, HO₂ and RO₂ radical concentrations, were suppressed in the early morning (between 05:00 and 07:00) due to the reaction with NO, which peaked with concentrations of up to 1.5 ppbv at that time. Peroxy radical concentrations were usually highest in the afternoon (~14:00), when NO concentrations were low. At the same time, O₃ concentrations were maximum due to efficient ozone production by the reaction of peroxy radicals with NO (Reaction R4.9 and R4.10, Table 4.1).

During winter and autumn, HO₂ and RO₂ radical concentrations show different diurnal profiles. HO₂ concentrations built-up together with NO and reached peak concentrations at noon. In contrast, daytime RO₂ concentrations were suppressed by high NO leading to a fast loss of RO₂ by the reaction with NO. In these seasons, the low radical concentrations led to slow inter-radical conversions by the reactions with NO, but, for OH and HO₂, other radical production pathways such as the reaction of HCHO and OH and the photolysis of HONO and HCHO sustained radical concentrations during daytime. In addition, the RO₂ production from the reaction of OH and VOCs (Reaction R4.8) was low, so that RO₂ concentrations were close to the instrument's limit of detection ($< 2 \times 10^7 \text{ cm}^{-3}$). RO₂ concentrations increased after sunset, when NO concentrations were essentially zero, because NO production by the photolysis of NO₂ stopped and NO rapidly reacted with ozone, while RO₂ production from the reactions of VOC with NO and O₃ still exists. Maximum RO₂ concentrations were reached at midnight.

The measured OH reactivity (k_{OH}) ranged between 4 and 33 s⁻¹ during the campaign. The highest value was observed on 21 January, when a highly polluted plume containing 50 ppbv of NO was sampled.

The measured OH reactivity can be compared to calculated OH reactivity obtained from summing up the product between measured OH reactant concentrations and their reaction rate coefficients with the OH radical. On average, 2.5 s⁻¹ (40 %) of the measured OH reactivity could not be explained by the calculated OH reactivity during the spring and summer periods (Fig. 4.9). NO_x, CH₄, CO, and VOCs contributed approximately 18, 5, 14 and 20 %, respectively, to the measured OH reactivity. Reactivity from isoprene had the largest contribution among the VOCs with values of up to 5 % of the measured OH reactivity. During winter and autumn (Fig. 4.10), the average measured OH reactivity was approximately 20 % (1.4 s⁻¹) higher than the calculated OH reactivity. NO_x (52%), CO (24%), and the sum of the measured VOCs (17%) contributed most to the entire reactivity. Unfortunately, the number of detected VOC species was small (Table 2.3). It is likely that the unaccounted OH reactivity is due to unmeasured VOCs. This, however, does not impact the analyze performed in this study as the measured OH reactivity is used to determine the loss rate of OH radicals.

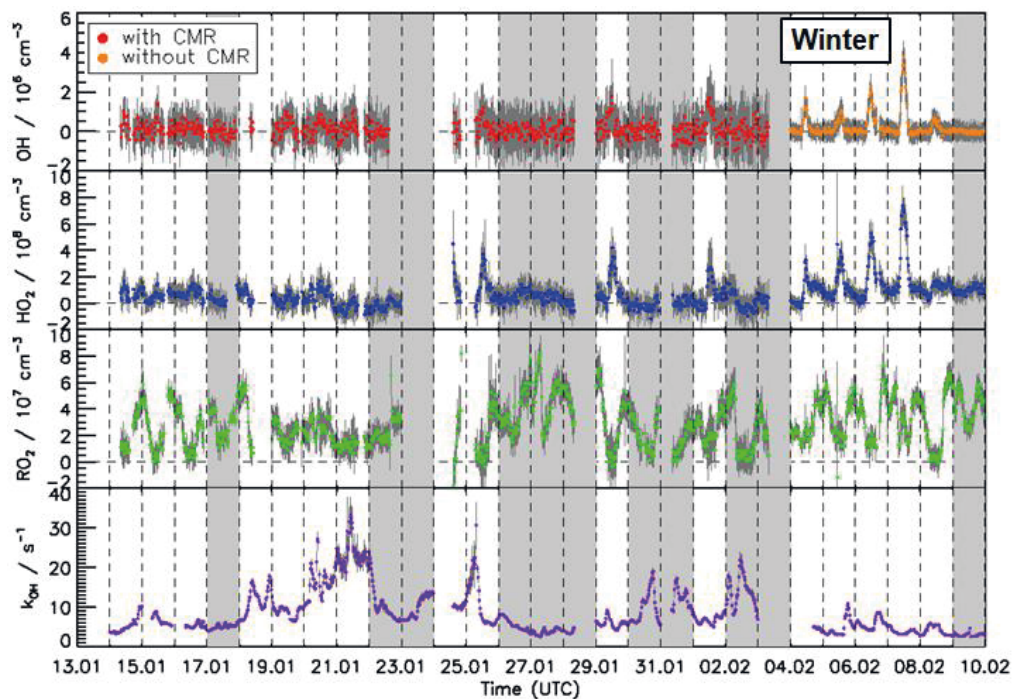


Figure 4. 5: Time series of OH, HO₂, and RO₂ concentration measured by the FZJ-LIF-CMR instrument and OH reactivity (k_{OH}) measured by the FZJ-LP-LIF instrument during the winter period of the JULIAC. Vertical dashed lines denote midnight. Grey shaded areas indicate calibration days or days when the chamber roof was closed.

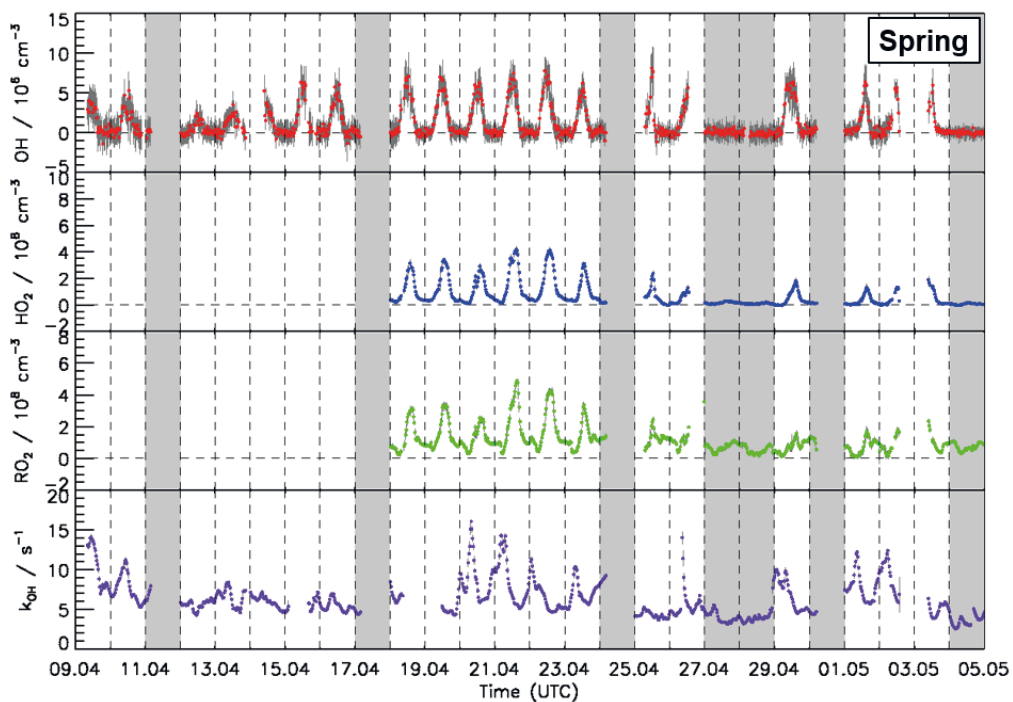


Figure 4. 6: Time series of OH, HO₂, and RO₂ concentration measured by the FZJ-LIF-CMR instrument and OH reactivity (k_{OH}) measured by the FZJ-LP-LIF instrument during the spring period of the JULIAC campaign. Vertical dashed lines denote midnight. Grey shaded areas indicate calibration days or days when the chamber roof was closed.

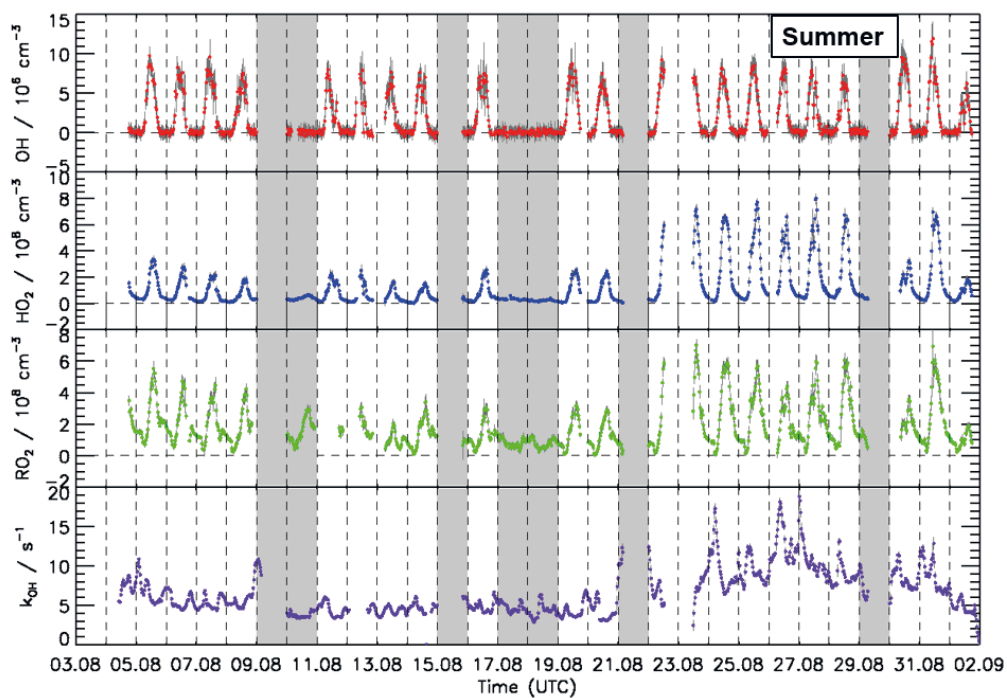


Figure 4. 7: Time series of OH, HO₂, and RO₂ concentration measured by the FZJ-LIF-CMR instrument and OH reactivity (k_{OH}) measured by the FZJ-LP-LIF instrument during the summer period of the JULIAC campaign. Vertical dashed lines denote midnight. Grey areas indicate calibration days or days when the chamber roof was closed.

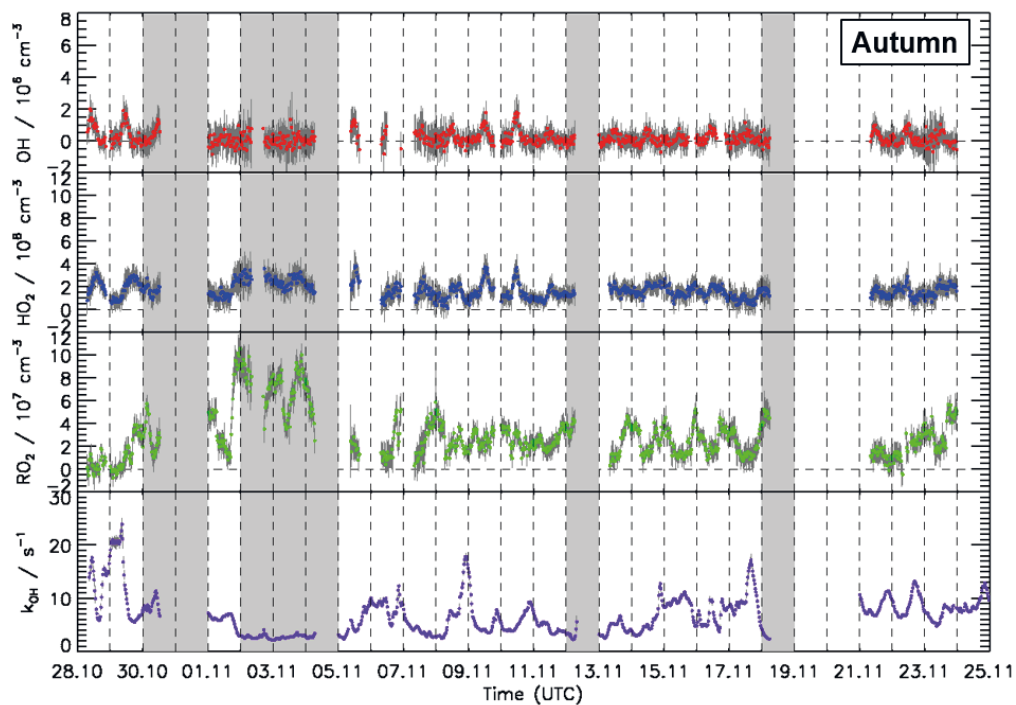


Figure 4. 8: Time series of OH, HO₂, and RO₂ concentration measured by the FZJ-LIF-CMR instrument and OH reactivity (k_{OH}) measured by the FZJ-LP-LIF instrument during the autumn period of the JULIAC campaign. Vertical dashed lines denote midnight. Grey areas indicate calibration days or days when the chamber roof was closed.

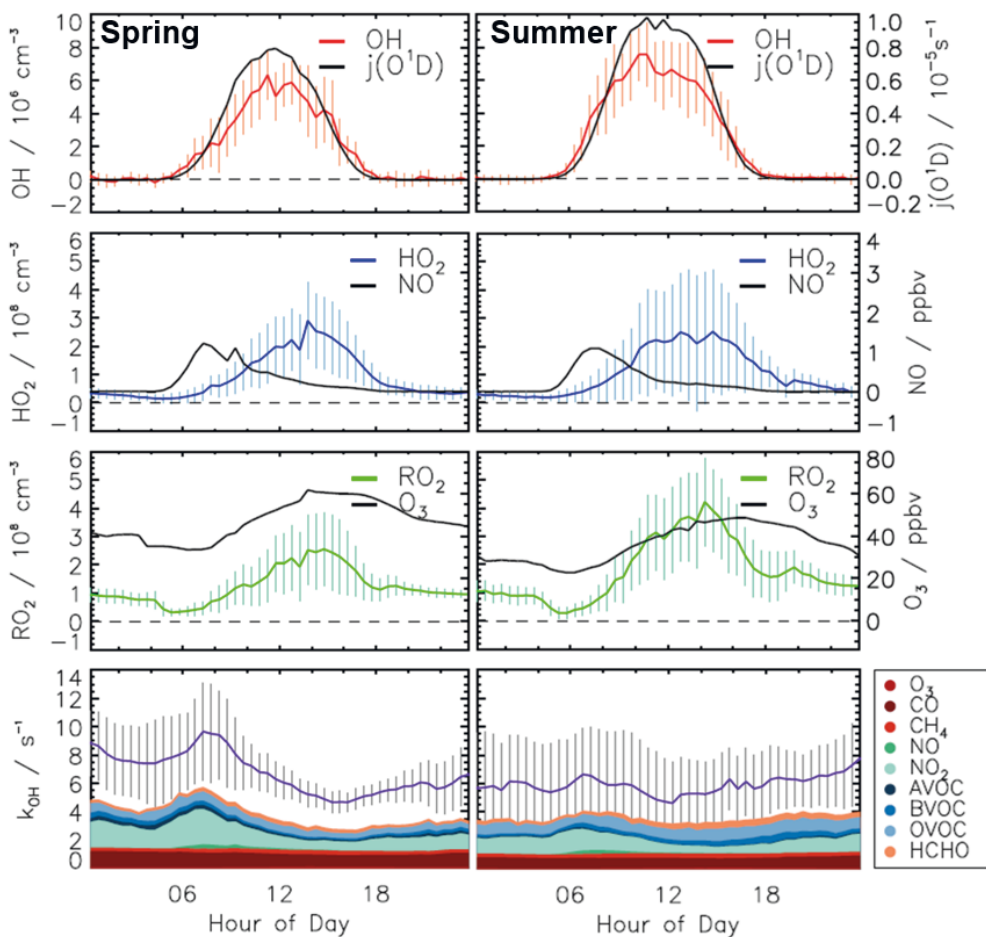


Figure 4. 9: Median values of the diurnal profiles of OH, HO₂, RO₂, concentrations, OH reactivity, $j(\text{O}^1\text{D})$, NO, O₃ mixing ratios measured during spring and summer periods of the JULIAC campaign. Coloured areas represent the contributions of measured reactants to the OH reactivity. Vertical lines show the standard deviation of the distributions.

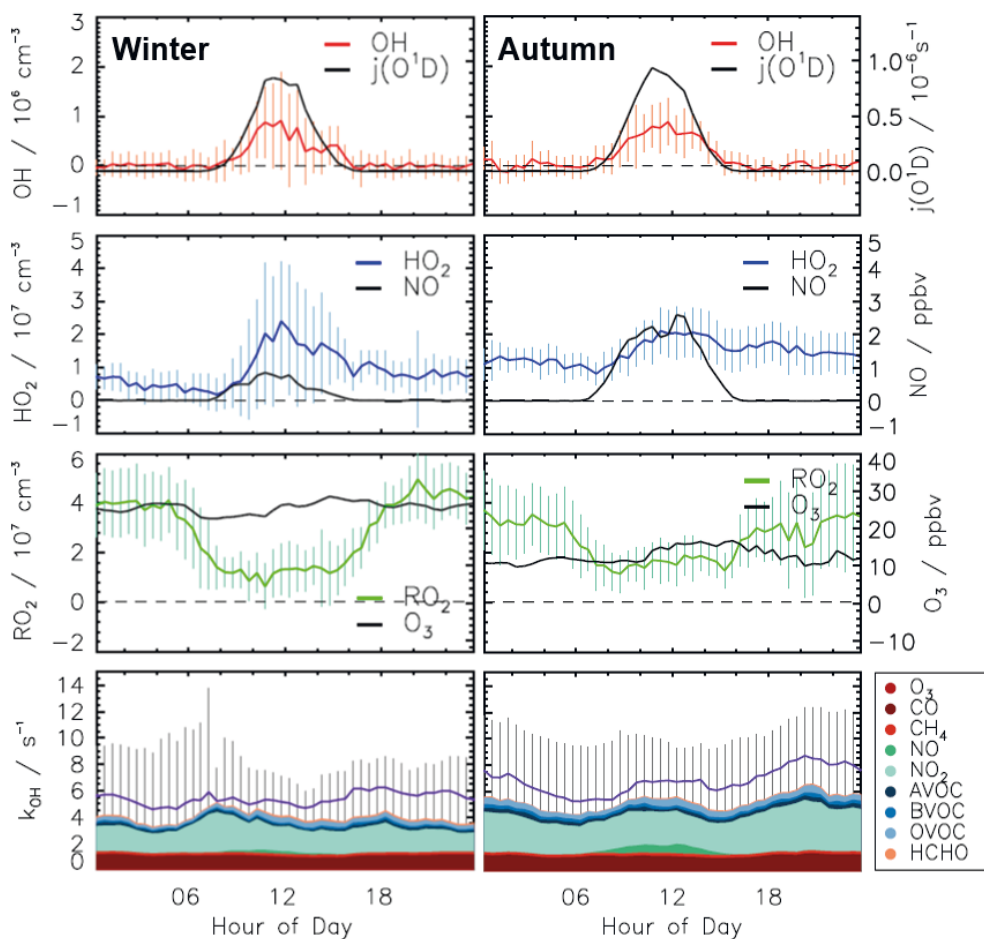


Figure 4. 10: Median values of the diurnal profiles of OH, HO₂, RO₂ concentrations, OH reactivity, $j(O^1D)$, NO, O₃ mixing ratios measured during winter and autumn periods of the JULIAC campaign. Coloured areas represent the contributions from measured reactants to the OH reactivity. Vertical lines show the standard deviation of the distributions.

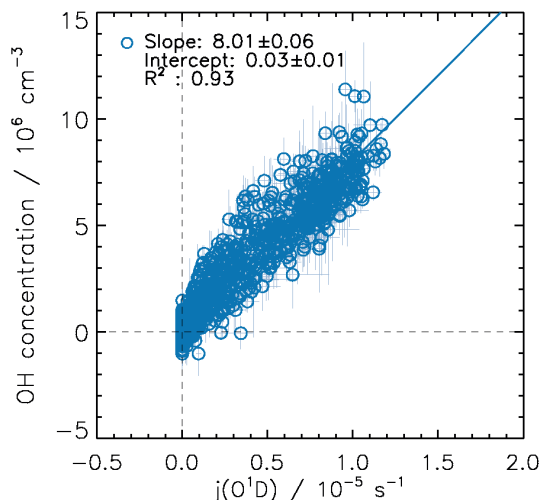


Figure 4. 11: Correlation plot between OH concentrations measured by the FZJ-LIF-CMR instrument and the photolysis frequency of ozone leading to $O(^1D)$ during the JULIAC campaign. The blue line is a linear fit of 3-minute data set weighted with the statistical errors of both instruments. Vertical and horizontal bars denote the 1σ precision of the measured data points.

4.1.3 Nighttime observation of OH concentrations during the JULIAC

During all JULIAC periods, nighttime (solar zenith angle $> 90^\circ$) OH concentrations were very low with a mean value of $(2.0 \pm 0.7) \times 10^4 \text{ cm}^{-3}$, which is below the limit of detection of OH measurements with the FZJ-CMR-LIF instrument ($0.7 \times 10^6 \text{ cm}^{-3}$) (Fig. 4.9 and 4.10). The nighttime mean value of the measured interference in the OH signal was equivalent to an OH concentration of $(0.2 \pm 0.3) \times 10^6 \text{ cm}^{-3}$, of which more than 90% originated from the well-characterized interference from ozone photolysis (Chapter 3). Together with the overall low VOC reactivity around 4 s^{-1} , this indicates that there was no substantial OH source at nighttime.

This result is consistent with observations in other field campaigns performed in Germany (Ehhalt and Rohrer, 2000; Handisides et al., 2003; Holland et al., 2003), for which nighttime OH concentrations of less than $1 \times 10^5 \text{ cm}^{-3}$ were reported. However, in several other field studies conducted in urban areas, nighttime OH concentrations in the range of 0.2 to $3 \times 10^6 \text{ cm}^{-3}$ were found, for example in campaigns in China (Lu et al., 2014; Rohrer et al., 2014; Tan et al., 2017; Tan et al., 2018; Ma et al., 2019; Tan et al., 2019; Wang et al., 2019; Whalley et al., 2021), in the US (Martinez et al., 2003; Brune et al., 2016; Griffith et al., 2016), and in the UK (Ren et al., 2003; Vaughan et al., 2012). In these studies, the nighttime OH concentrations could not be explained by the model-predicted values and raised questions about the presence of interferences in the OH signal that were measured by LIF instruments (Mao et al., 2010; Lu et al., 2014).

In some of the campaigns, the chemical modulation method was applied, and a large fraction of the observed nighttime OH concentrations (OH_{CHEM}) could be attributed to interferences. After correcting for these interferences, OH measurements agreed with model predictions in some cases (Mao et al., 2012; Novelli et al., 2014a; Brune et al., 2016; Tan et al., 2018; Ma et al., 2019; Whalley et al., 2021). However, significant nighttime OH concentrations (OH_{CHEM}) above the detection limit that were higher than model predictions were observed in campaigns in the US (Griffith et al., 2016) and in China (Tan et al. (2017); (2019)). The reason of the model-measurement discrepancies of OH concentrations is unclear.

Overall, results from previous campaigns and this study strongly suggests the necessity of the OH interference correction by the chemical modulation method to study nighttime OH chemistry.

4.1.4 Data quality check of radical measurements

OH concentrations were measured by both the FZJ-LIF-CMR and the DOAS instruments (Chapter 3). Unfortunately, the DOAS instrument was not operated in spring due to technical problems. OH concentrations measured by both instruments agreed well within the measurement uncertainties during the summer period (linear regression slope: 1.11 ± 0.02) except for the heat wave, when the OH concentrations measured by the LIF instrument were systematically higher by 25% than concentrations measured by the DOAS instrument (Section 3.5.2.2). Therefore, the OH concentration measured by the DOAS instrument was used for the analysis of the radical budgets for this period. The overall good agreement between the two OH data sets gives confidence that OH radical concentrations were not affected by artefacts or calibration errors. In addition, the observed OH interferences in measurements by the FZJ-LIF-CMR instrument could be well explained by the well-understood and characterized interference from ozone photolysis by the exciting laser beam at 308nm.

The quality of peroxy radical concentration measurements could be assessed by the consistency of ozone production rates calculated from either peroxy radical concentration in the chamber or from ozone and NO_2 concentration measurements in the chamber and in the air flowed into the chamber (Section 2.2). The detailed mathematical description of the determination of the O_x production rate is shown in Chapter 5. In addition, the odd oxygen (O_x) production rate can be calculated from the NO_2 production from the reaction of peroxy radicals (HO_2 and RO_2) with NO and NO_2 destruction in the reaction of OH. An overall good agreement within 15% between both methods to calculate ozone production rates is found in the JULIAC campaign during spring and summer periods, when ozone production rates were higher than the precision of the calculations for most of the time. The consistency of both methods indicates that peroxy radical measurements are accurate within 40 %. More details about the comparison are shown in Chapter 5.

4.2 Chemical budget calculations

A chemical budget analysis was done for OH, HO₂, RO₂ radicals and the sum of all three radicals (RO_x) using the data set collected during the JULIAC campaign (Chapter 2) following the chemical mechanism in Figure 1.1 and Table 4.1. Rate coefficients and their uncertainties were mainly taken from IUPAC recommendations (Atkinson et al., 2004; Atkinson et al., 2006; Cox et al., 2020) or from more recent studies (Table 4.1). If not otherwise specified, radical production and destruction rates are calculated using only measured quantities.

4.2.1 OH radical chemical budget

The production rate of OH radicals includes primary production reactions (Reaction R 4.1, R 4.2, and R 4.5, Table 4.1) and radical interconversion reactions (Reaction R 4.10 and R 4.11, Table 4.1):

$$P_{\text{OH}} = j_{\text{HONO}}[\text{HONO}] + \varphi_{\text{OH}}j_{\text{O}^1\text{D}}[\text{O}_3] + k_{\text{R4.10}}[\text{NO}][\text{HO}_2] + k_{\text{R4.11}}[\text{O}_3][\text{HO}_2] + \sum\{\varphi_{\text{OH}}^i k_{\text{R4.5}}^i [\text{alkene}]^i [\text{O}_3]\} + P_{\text{OH,Isop.}} \quad (\text{Eq. 4.1})$$

In Eq. 4.1, φ_{OH} is the effective OH yield of the ozone photolysis reaction including the subsequent reaction of O(¹D) with H₂O, which produces 2 OH radicals. φ_{OH}^i are the OH yields of the ozonolysis reactions of alkenes (i), and k_i represents the reaction rate coefficients of the corresponding reactions (Table 4.1).

In addition, as introduced in Section 1.3, regeneration of OH radicals from unimolecular reactions (1,6-hydrogen shifts) of isoprene-RO₂ radicals (Z- δ -RO₂-I and II) are included ($P_{\text{OH,Isop}}$) in the calculations of OH production rates in this work. The nomenclature for the RO₂ isomers and the calculation of concentrations and reaction rates follows Peeters et al. (2014). Because there was no measurement of specific RO₂ radicals, the RO₂(isop.) radical concentration from isoprene is estimated from steady state conditions considering production from the reaction of isoprene with OH and destruction in bi-molecular (k_{bi}) and unimolecular ($k_{\text{bulk 1,6-H}}$) reactions:

$$[\text{RO}_2(\text{isop.})]_{\text{SS}} = \frac{k_{\text{R4.18}}[\text{Isoprene}][\text{OH}]}{k_{\text{bi}} + k_{\text{bulk 1,6-H}}} \quad (\text{Eq. 4.2})$$

$$k_{\text{bi}} = (k_{\text{R4.9}} + k_{\text{R4.14}})[\text{NO}] + k_{\text{R4.15}}[\text{RO}_2] + k_{\text{R4.16}}[\text{HO}_2] \quad (\text{Eq. 4.2a})$$

Here, k_{bi} is the RO₂ removal rate due to bi-molecular reactions with NO (Reaction R4.9 and R4.14), RO₂ (Reaction R4.15) and HO₂ (Reaction R4.16). $k_{\text{bulk 1,6-H}}$ is the bulk 1,6-H shift isomerization reaction rate constant that can be applied to the sum of all RO₂ isomers formed in the reaction of isoprene with OH as introduced by Peeters et al. (2014) can be calculated by:

$$k_{\text{bulk 1,6-H}} = 0.62 \times k_{1,6\text{-H (I)}} + 0.31 \times k_{1,6\text{-H (II)}} \quad (\text{Eq. 4.3})$$

Table 4. 1: Chemical reactions with rate constants and their uncertainty used for the chemical radical budget analysis. Rate constants are listed for standard conditions (T=25 °C, P=1atm). The radical budget analysis in this study uses the actual measured air temperature and pressure.

No.	Reaction	k (25 °C, 1 atm) / cm ³ s ⁻¹	Uncertainty ^a	Reference
Radical initiation reactions				
R 4.1	HONO+hν → OH + NO	j(HONO) ^b		
R 4.2	O ₃ +hν → O(¹ D)+O ₂	j(O ¹ D) ^b		
R 4.2a	O(¹ D)+H ₂ O → 2OH	2.1×10 ⁻¹⁰	±13%	IUPAC
R 4.3	HCHO+hν → 2HO ₂ + CO	j(HCHO) ^b		
R 4.4	CH ₃ CHO+hν → CH ₃ O ₂ +HO ₂ + CO	j(CH ₃ CHO) ^b		
R 4.5	Alkenes+O ₃ →OH, HO ₂ , RO ₂ +Products			
	Propene+O ₃ → Products ^c	1.0×10 ⁻¹⁷	±20%	IUPAC
	cis-But-2-ene+O ₃ → Products ^d	1.3×10 ⁻¹⁶	±12%	IUPAC
	1-Pentene+O ₃ → Products ^e	1.0×10 ⁻¹⁷	±20%	Saunders et al. (2003)
	2-Hexene+O ₃ → Products ^f	1.1×10 ⁻¹⁷	±20%	Saunders et al. (2003)
	Isoprene+O ₃ → Products ^g	1.3×10 ⁻¹⁷	±13%	IUPAC
	α-pinene+O ₃ → Products ^h	9.6×10 ⁻¹⁷	±20%	IUPAC
Radical interconversion reactions				
R 4.6	HCHO+OH+O ₂ →CO+H ₂ O+HO ₂	8.5×10 ⁻¹²	±10%	IUPAC
R 4.7	CO+OH+O ₂ →CO ₂ +HO ₂	2.3×10 ⁻¹³	±6%	IUPAC
R 4.8	VOC+OH+O ₂ → RO ₂ +H ₂ O ⁱ			
R 4.9	RO ₂ +NO→RO+NO ₂ ^j	(1-α) × 9.0×10 ⁻¹²	±20%	Jenkin et al. (2019)
R 4.10	HO ₂ +NO→OH+NO ₂	8.5×10 ⁻¹²	±13%	IUPAC
R 4.11	HO ₂ +O ₃ →OH+2O ₂	2.0×10 ⁻¹⁵	±29%	IUPAC
Radical termination reactions				
R 4.12	NO ₂ +OH→HNO ₂	1.0×10 ⁻¹¹	±30%	IUPAC
R 4.13	NO+OH→HONO	9.7×10 ⁻¹²	±13%	IUPAC
R 4.14	RO ₂ +NO→RONO ₂ ^j	α × 9.0 × 10 ⁻¹²	±20%	Jenkin et al. (2019)
R 4.15	RO ₂ +RO ₂ →Products ^k	3.5×10 ⁻¹³	±50%	Jenkin et al. (2019)
R 4.16	RO ₂ +HO ₂ →ROOH+O ₂ ^l	2.2×10 ⁻¹¹	±50%	Jenkin et al. (2019)
R 4.17	HO ₂ +HO ₂ →H ₂ O ₂ +O ₂ ^m	4.5×10 ⁻¹²	±20%	IUPAC
Cl reactions				
R 4.21	ClNO ₂ +hν→Cl+NO ₂	j(ClNO ₂) ^b		
R 4.23	Cl+VOCs→RO ₂ ⁿ			

^a 1σ uncertainty

^b Measured photolysis frequencies are used (Table 2.1).

^c Yield for OH: 0.36, HO₂: 0.10, RO₂: 0.42 from Novelli et al. (2021).

^d Yield for OH: 0.36, HO₂: 0.15, RO₂: 0.51 from Novelli et al. (2021).

^e Yield for OH: 0.32, HO₂: 0.09, RO₂: 0.37 from Novelli et al. (2021).

^f Yield for OH: 0.48, HO₂: 0.11, RO₂: 0.59 from Novelli et al. (2021).

^g Yield for OH: 0.26, HO₂: 0.26 from Malkin et al. (2010).

^h Yield for OH: 0.8 from Cox et al. (2020).

ⁱ The turnover rate of this reaction is calculated from measured OH reactivity from VOCs and OH concentrations.

^j Rate constant for the class of alkyl (≥ C2) + oxygenated RO₂ species (Jenkin et al., 2019). The assumed 20% uncertainty covers the range of published values including the low value for CH₃O₂ (7.7×10⁻¹² cm³ s⁻¹) but excludes values for acyl peroxy radicals (2.0×10⁻¹¹ cm³ s⁻¹). The applied value for the branching ratio α is 0.05.

^k Rate constant for the CH₃O₂ + CH₃O₂ reaction. Self- and cross-reactions of RO₂ species have strongly structure-dependent rate constants that can be as high as reaction rate constants of RO₂+HO₂ reactions (R4.16) (Jenkin et al., 2019).

^l Published rate constants vary between 0.5×10⁻¹¹ cm³ s⁻¹ and 2.2×10⁻¹¹ cm³ s⁻¹ depending on the chemical structure of the RO₂ species (Jenkin et al., 2019). Here, the upper limit value is applied.

^m At 1% water vapor mixing ratio.

ⁿ For the calculation of the RO₂ production rate, it is assumed that the rate limiting step is the production of Cl from the photolysis of ClNO₂.

In Eq. 4.3, the factors 0.62 and 0.31 are the branching ratios of the OH addition to the specific position of isoprene which can form the Z- δ -RO₂ isomers. $k_{1,6-H(I)}$ and $k_{1,6-H(II)}$ are the product of the isomer-specific reaction rate coefficient and the fraction of the Z- δ -RO₂-I and II radicals that can isomerize. The values of the rate constants are parameterized as functions of temperature and the bimolecular loss rate of RO₂ (k_{bi} , Eq. 4.2a) in (Peeters et al., 2014):

$$k_{1,6-H(I)} = 9.50 \times 10^7 \text{ s}^{-1} \times \exp\left(-\frac{7009}{T}\right) + 1.79 \times 10^{-7} \exp\left(\frac{3722.5}{T}\right) \times k_{bi} \quad (\text{Eq. 4.3a})$$

$$k_{1,6-H(II)} = 3.80 \times 10^{13} \text{ s}^{-1} \times \exp\left(-\frac{10745}{T}\right) + 5.82 \times 10^{-2} \exp\left(\frac{476.3}{T}\right) \times k_{bi} \quad (\text{Eq. 4.3b})$$

To account for the OH production from isomerization reactions, it is assumed that the isomerization produces only one OH radical per Z- δ -RO₂-I and II molecule from the photolysis of HPALD (Section 1.1) resulting in a radical production that is equal to the loss rate of the bulk RO₂ from isoprene, $D_{Z-\delta-RO_2,Isop}$:

$$P_{OH,Isop} = D_{Z-\delta-RO_2,Isop} = k_{bulk,1,6-H} [RO_2(isop.)]_{SS} \quad (\text{Eq. 4.4})$$

The loss rate of OH radicals is determined by the product of the total OH reactivity (k_{OH}) and the OH radical concentration:

$$D_{OH} = k_{OH}[OH] \quad (\text{Eq. 4.5})$$

4.2.2 HO₂ radical chemical budget

The production rate of HO₂ radicals includes primary production (Reaction R 4.3, R 4.4, R 4.5, Table 4.1) and interconversion of radicals (Reaction R 4.6, R 4.7, R 4.9, Table 4.1):

$$P_{HO_2} = 2j_{HCHO}[HCHO] + k_{R4.6}[HCHO][OH] + k_{R4.7}[CO][OH] + k_{R4.9}[NO][RO_2] + \Sigma\{\varphi_{HO_2}^i k_{R4.5}^i [alkene]^i [O_3]\} \quad (\text{Eq. 4.6})$$

Here, the photolysis frequency of HCHO includes only radical generating pathways. The reaction rate constant $k_{R4.9}$ includes the yield of HO₂ from the reaction of NO with RO₂ (Reaction R 4.9) competing with the formation of organic nitrates (Reaction 4.14). Because there are no measurements of specific RO₂ radicals, a yield of 5 % for the formation of organic nitrates is assumed for all RO₂. The influence of the variability of the organic nitrate yield on the results is discussed in Section 4.3.1. $\varphi_{HO_2}^i$ is the HO₂ yield from the ozonolysis of alkenes (i). The reactions of OH with H₂ and O₃ are not considered due to their negligible contributions to the total HO₂ production.

The loss rate of HO₂ radicals is determined by HO₂ reactions with NO (Reaction R 4.10), O₃ (Reaction R 4.11), RO₂ (Reaction R 4.16), and HO₂ (Reaction R 4.17) and potentially aerosol uptake:

$$D_{HO_2} = (k_{R4.10}[NO] + k_{R4.11}[O_3] + k_{R4.16}[RO_2] + 2k_{R4.17}[HO_2] + k_{het.})[HO_2] \quad (\text{Eq. 4.7})$$

The reaction of HO₂ radicals with NO₂ is not included as the thermal equilibrium between HO₂NO₂ and HO₂ radicals and NO₂ can be assumed for the temperature observed during JULIAC.

The first order loss rate from heterogeneous uptake of HO₂ radicals on aerosol (k_{het}) can be described as:

$$k_{\text{het}} = \frac{\gamma_{\text{eff}} \cdot v_{\text{HO}_2} \cdot [\text{AS}]}{4} \quad (\text{Eq. 4.8})$$

v_{HO_2} is the mean molecular velocity of HO₂ ($4.44 \times 10^5 \text{ cm s}^{-1}$ at 298K) and [AS] is the aerosol surface area concentration and γ_{eff} the effective uptake coefficient. Previous laboratory showed a large variability for the uptake coefficient γ_{eff} , giving values ranging from 0.08 to 0.6 depending on the aerosol chemical composition and its physical state (George et al., 2007; Taketani et al., 2008, 2009; George et al., 2013; Lakey et al., 2015; Song et al., 2020; Tan et al., 2020). In the JULIAC campaign, measurements of aerosol properties did not allow to determine an HO₂ uptake coefficient. In order to estimate, if aerosol uptake could have been of relevance, an upper limit of the uptake coefficient of 0.2 was used in the calculations. This high value was determined from a field measurement, in which the HO₂ uptake coefficient was measured on aerosol sampled in the North China Plain (Taketani et al., 2012).

4.2.3 RO₂ radical chemical budget

Primary sources of RO₂ radicals include all oxidation reactions of VOCs with OH, Cl, NO₃ radicals and O₃. Because the number of measured VOC species in this study was limited (Table 2.3) and because it is generally difficult to capture the entire spectrum of atmospheric VOCs (Goldstein and Galbally, 2007; Lou et al., 2010), the measured total OH reactivity (k_{OH}) is used to calculate the RO₂ radicals production from the reactions of VOCs with OH. First, the contributions from CO, NO, NO₂, HCHO, and O₃ is removed from the measured OH reactivity as these species do not form RO₂ radicals upon reaction with OH radical. This value is then defined as the VOC reactivity (k_{VOC}). By using this methodology, it is assumed that any observed OH reactivity that cannot be attributed to measured OH reactants is caused by unmeasured VOCs. RO₂ production from ozonolysis and Cl oxidation are included from only the reaction of measured organic compounds.

The impact of the oxidation of VOCs by the NO₃ radical on the RO₂ production rate is generally negligible during daytime due to the fast NO₃ destruction by photolysis and reaction with NO. Because the analysis focuses on daytime NO₃ reactions are not considered.

Cl concentrations were not measured in the JULIAC campaign, but the pre-cursor species nitryl chloride (ClNO₂) was measured for part of the campaign. ClNO₂ can accumulate during nighttime, but it is rapidly photolyzed after sunrise yielding NO₂ and Cl atoms (Reaction R 4.20). Therefore, the potential impact of RO₂ production from the oxidation of VOC by Cl radicals produced from the photolysis of ClNO₂ can be investigated. The Cl atom can react with organic compounds and produce RO₂ radicals. The RO₂ production rate from Cl radicals can be calculated as:

$$P_{RO_2,Cl} = j_{ClNO_2}[ClNO_2] \quad (\text{Eq. 4.9})$$

This can be considered as an upper limit for RO₂ radical production from this process as it is assumed that one RO₂ radical is formed from the reaction of each Cl atom produced by the photolysis of ClNO₂. This is justified as most of Cl atom is expected to react with VOCs due to its fast reaction rate with VOCs (Tanaka et al., 2003). Consequently, the RO₂ production rate is calculated as:

$$P_{RO_2} = k_{VOC}[OH] + \Sigma\{\varphi_{RO_2}^i k_{R4.5}^i [alkene]^i [O_3]\} + P_{RO_2,Cl} \quad (\text{Eq. 4.10})$$

Here, $\varphi_{RO_2}^i$ is the RO₂ yield from the ozonolysis of alkenes (i) (Table 4.1).

The destruction rate of RO₂ includes its reaction with NO, HO₂, and RO₂ and the loss rate of specific isoprene-RO₂ radicals, $D_{Z-\delta-RO_2,Isop}$, due to unimolecular reactions (Eq. 4.4):

$$D_{RO_2} = \{(k_{R4.9} + k_{R4.14})[NO] + 2k_{R4.15}[RO_2] + k_{R4.16}[HO_2]\}[RO_2] + D_{Z-\delta-RO_2,Isop} \quad (\text{Eq. 4.11})$$

4.2.4 RO_x radical chemical budget

In the chemical budget of the sum of OH, HO₂ and RO₂, inter-radical conversion reactions cancel out and only initiation and termination reactions are included. Therefore, the RO_x radical budget analysis allows to investigate whether there are missing primary radical sources or termination processes.

The production rate of the RO_x radical is given by the sum of rates from radical initiation reactions (Reaction R 4.1 – R 4.5 and R 4.21 – 4.23, Table 4.1):

$$P_{RO_x} = j_{HONO}[HONO] + \varphi_{OH} j_{O^1D}[O_3] + 2j_{HCHO}[HCHO] + \Sigma(\varphi_{OH}^i + \varphi_{HO_2}^i + \varphi_{RO_2}^i) k_{R4.5}^i [alkene]^i [O_3] + P_{RO_2,Cl} \quad (\text{Eq. 4.12})$$

The loss rate of the RO_x radical is calculated by the sum of rates from radical termination reactions (Reaction R13-R17):

$$D_{RO_x} = (k_{R4.12}[NO_2] + k_{R4.13}[NO])[OH] + k_{R4.14}[NO][RO_2] + 2k_{R4.15}[RO_2]^2 + 2k_{R4.16}[HO_2][RO_2] + 2k_{R4.17}[HO_2]^2 \quad (\text{Eq. 4.13})$$

Radicals can be additionally produced from the photolysis of other oxygenated organic compounds not included in Eq. 4.12. Unfortunately, only acetaldehyde (CH₃CHO), methyl vinyl ketone (MVK), methacrolein (MACR), and methyl glyoxal were detected during part of the campaign. Calculations show that the radical production rate from the photolysis of these species was less than 0.1 ppbv h⁻¹, so that it can be expected that photolysis of other OVOCs overall played a minor role for conditions of this campaign.

4.2.5 Uncertainty of the calculated production and destruction rates

The uncertainty of each production rate or loss rate is calculated by the Gaussian summation of 1 σ accuracies of measured quantities (Table 2.1) and reaction rate coefficients (Table 4.1).

For reactions of RO₂ with NO (Reaction R 4.9), HO₂ (Reaction R 4.16), and RO₂ (Reaction R 4.15), generic reaction rate coefficients are applied for the sum measurement of RO₂ radical concentrations (Table 4.1, Jenkin et al. (2019)). Depending on RO₂ species, rate coefficients of the NO reaction with RO₂ (Reaction R 4.9) range from $7.7 \times 10^{-12} \text{ cm}^3 \text{ s}^{-1}$ (for CH₃O₂) to $1.1 \times 10^{-11} \text{ cm}^3 \text{ s}^{-1}$ (for *c*-C₅H₉O₂) (Jenkin et al., 2019). The uncertainty of the rate coefficients varies from 6 to 30 % (1 σ uncertainty). In the calculations here, the upper limit value of the uncertainty of 30 % is applied.

The reaction rate constants for reactions of RO₂ with HO₂ and with RO₂ vary by more than an order of magnitude. In the calculations in this work, 50% uncertainty is used for the reaction rate constant of RO₂ with HO₂ reactions.

The highest contribution in the uncertainty of the peroxy radical measurements is due to the uncertainties in the background signal of the measurements with values of up to $1.0 \times 10^7 \text{ cm}^{-3}$ for HO₂ and $2.8 \times 10^7 \text{ cm}^{-3}$ for RO₂ (Section 3.2.4).

4.3 Results of the OH, HO₂, RO₂ and RO_x radical chemical budgets

Due to the very low photochemical activity observed in autumn and winter, which resulted in radical concentrations close to the detection limit of the instrument, a chemical budget analysis is performed only for the campaigns in spring and summer and focusses on daytime (solar zenith angle (SZA) < 90).

Time series of the OH, HO₂, RO₂ and RO_x radical turnover rates for spring and summer periods are presented in Figures 4.12 and 4.13, respectively. All radical production and destruction rates showed diurnal variations with maximum values in the afternoon and minimum values at night. The highest OH turnover rates of up to 17 ppbv hr⁻¹ were observed on 31 August, when the air temperature reached 40°C. Highest turnover rates for HO₂, RO₂, and RO_x radicals occurred on 29 April with values of 14 ppbv hr⁻¹, 15 ppbv hr⁻¹, and 4 ppbv hr⁻¹, respectively, when the NO mixing ratio exceeded 9 ppbv.

It is expected that radical production and destruction rates are balanced. A balanced chemical OH budget was indeed observed on 16 and 29 April and 16 August to 2 September. However, the daily peak in the diurnal profiles of the OH production rates was often lower than the maximum destruction rates (on average, 2 ppbv hr⁻¹) in April (Section 4.3.1) except on 16 and 29 April and in the first week of August (Section 4.3.2).

In the spring period, the production and destruction rates of peroxy radicals (HO₂ and RO₂) were generally balanced. If there is an imbalance between the production and destruction rates, it indicates

a missing radical production or destruction process. Significant discrepancies larger than 4 ppbv hr⁻¹ are only found on 21 and 29 April, when high NO mixing ratios above 2 ppbv were observed. Details of the radical budgets in these periods are described in Section 4.2.4. In contrast, in the summer period, HO₂ destruction rates were higher than production rates (on average 2 ppbv hr⁻¹) from 4 August to 20 August. Destruction and production rates were balanced from 22 August to 2 September (details are shown in Section 4.3.3). The RO₂ production rate was slightly (on average 1 ppbv hr⁻¹) higher than the destruction rate from 14 August to 25 August, but, on other days, agreement between RO₂ production and destruction rates was observed.

RO_x radical production and destruction rates were 2 to 4 times smaller than those of OH, HO₂ and RO₂ due to the cancelation of inter-radical conversion reactions. Overall, RO_x radical production and destruction rates were balanced during both periods, spring and summer. A higher RO_x radical destruction than production rate, however, was found on 29 April and the RO_x destruction rate was 0.5 to 1 ppbv hr⁻¹ lower than the production rate during the heat wave period in August.

Three different cases differing in the chemical and meteorological conditions (Table 4.2, Fig. 4.12 and 4.13) are described in the following sections. Firstly, in Case #1 (Section 4.3.1), changes in the chemical radical budgets due to varying NO mixing ratios from 9 to 0.01 ppbv on different days between 20 to 22 April and 29 April are shown. In the second case, Case #2 from 5 to 8 August (Section 4.3.2), significant imbalances in the OH and HO₂ budgets are continuously observed. Lastly, Case #3 during the period of heatwave from 22 to 31 August (Section 4.3.3), the results of radical budgets are shown, when there was high photochemical activity. Reasons for observed discrepancies between radical production and destruction rates are discussed in Section 4.4.1.

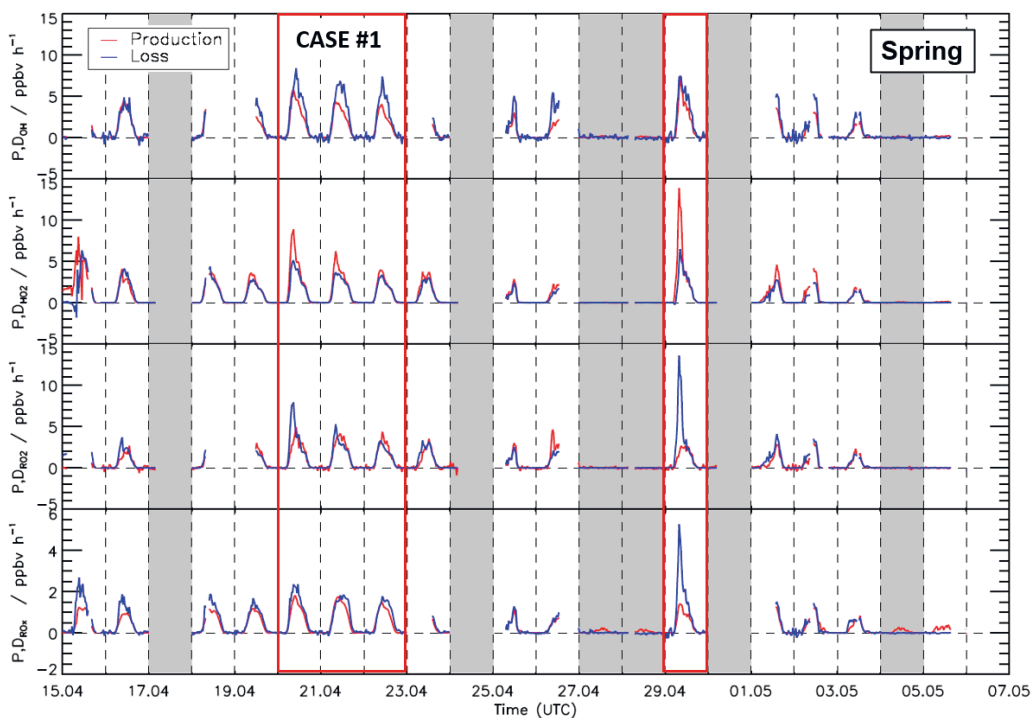


Figure 4. 12: Time series of total production and destruction rates of OH, HO₂, RO₂, and RO_x radicals during the spring period of the JULIAC campaign. Vertical dashed lines denote midnight. Grey areas indicate calibration days or days when the chamber roof was closed. The red boxed areas denote the selected period for the case study (Case #1).

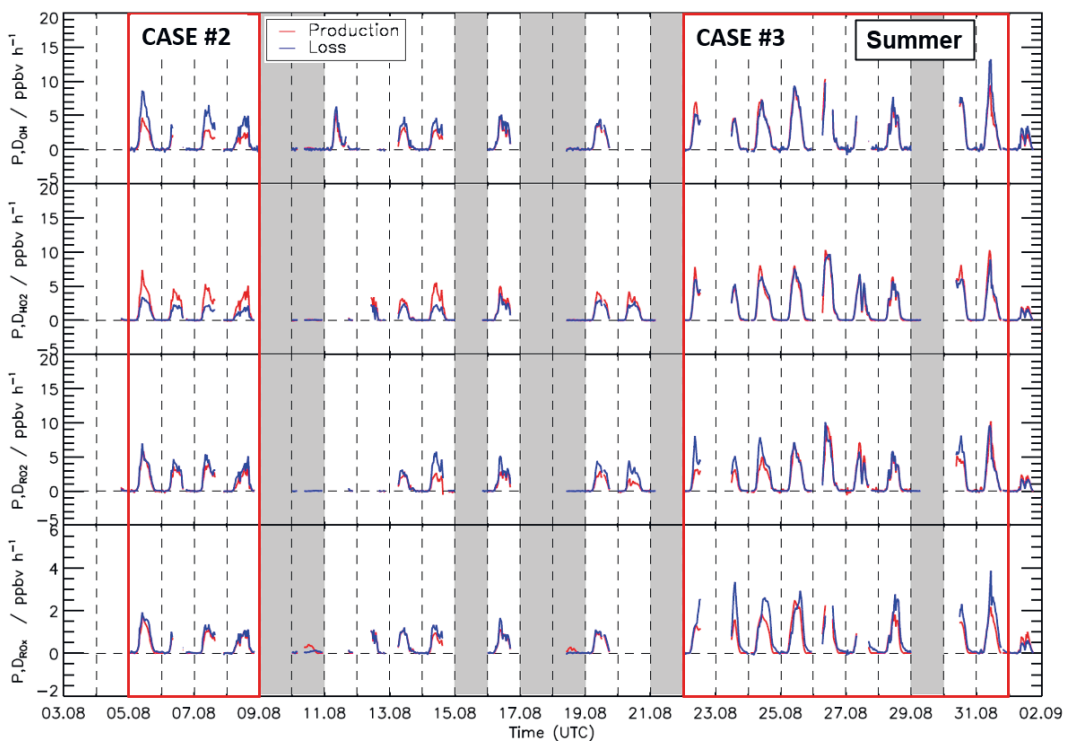


Figure 4. 13: Time series of total production and destruction rates of OH, HO₂, RO₂, and RO_x during the summer period of the JULIAC campaign. Vertical dashed lines denote midnight. Grey areas indicate calibration days or days when the chamber roof was closed. The red boxed areas denote the selected periods for the case studies (Case #2 and #3).

Table 4. 2: Summary of trace gas concentrations and temperatures for each case study given as daytime mean values with 1σ standard deviations. For Case #1, daily averaged values are shown. For Case #2 and #3, the daytime mean values are averaged over the period.

	Period	NO / ppbv	O ₃ / ppbv	k _{OH} / s ⁻¹	T / °C
Case #1	20 Apr. 2019	0.6	56.5	8.8	20.6
	21 Apr. 2019	0.2	61.7	8.5	20.1
	22 Apr. 2019	0.1	58.1	6.6	20.7
	29 Apr. 2019	1.3	29.0	6.8	15.3
Case #2	05 Aug. 2019 – 08 Aug. 2019	0.2	33.0	5.9	23.0
Case #3	22 Aug. 2019 – 31 Aug. 2019	0.3	50.6	8.8	25.2

4.3.1 Results of Case #1: Chemical radical budgets for conditions with different NO mixing ratios

Radical concentrations and radical production and destruction rates highly depend on the NO concentration as the reaction of peroxy radicals with NO dominates the overall turnover of radicals (Reaction R 4.9 and R 4.10) at high NO mixing ratios (> 1 ppbv). During the period from 20 April to 22 April and 29 April, high peaks of the NO mixing ratios were observed in the morning (06:00 – 10:00 UTC), which sharply decreased in the afternoon. The highest NO mixing ratio of 9 ppbv was observed on 29 April, and daily peak mixing ratios of NO decreased from 4 to 0.8 ppbv (Fig. 4.14) from 20 April to 22 April. The data set during this period allows to investigate the sensitivity of the OH, HO₂, RO₂ and RO_x radical budgets for very different NO levels (Fig. 4.14 and 15). Other chemical and meteorological conditions in this period are shown in Table 4.2.

As shown in Figure 4.14, the reaction of HO₂ with NO (Reaction R4.10) was the dominant OH radical production pathway contributing more than 70 % to the total OH production rate on all days in this period. The peak value of the calculated production rate was highest on 29 April as 7 ppbv hr⁻¹, and lowest on 22 April with a value of 4 ppbv hr⁻¹, while the peak of OH destruction rates did not significantly change. On each day, a maximum of the total OH production rate was observed in the morning slightly after the peak of the NO concentration followed by a gradual decrease of values till nighttime. The photolysis of HONO (Reaction R4.1) was the most important primary OH source during daytime contributing approximately 20 % to the total OH production. The reaction of HO₂ with ozone (Reaction R4.11), the photolysis of ozone (Reaction R4.2), and the ozonolysis of alkenes (Reaction R4.5) contributed less than 3 % to the total OH production. In addition, regeneration of OH

from unimolecular reactions of isoprene-RO₂ radicals (Eq. 4.3 and Reaction R4.18 and R4.19) contributed only 1% of the total OH production due to the low isoprene concentration (< 0.2 ppbv) and the competition of unimolecular reactions with the bimolecular reaction of RO₂ with NO. The OH production and destruction rates were balanced on 29 April for the entire day and in the early morning (before 08:00 UTC) on 20 – 22 April, when NO mixing ratios were higher than 1 ppbv. A discrepancy of up to 3.5 ppbv h⁻¹ (47 % of the total OH destruction rate) between production and destruction rates was found for low NO mixing ratios (<1 ppbv). This is larger than the uncertainty of the calculation.

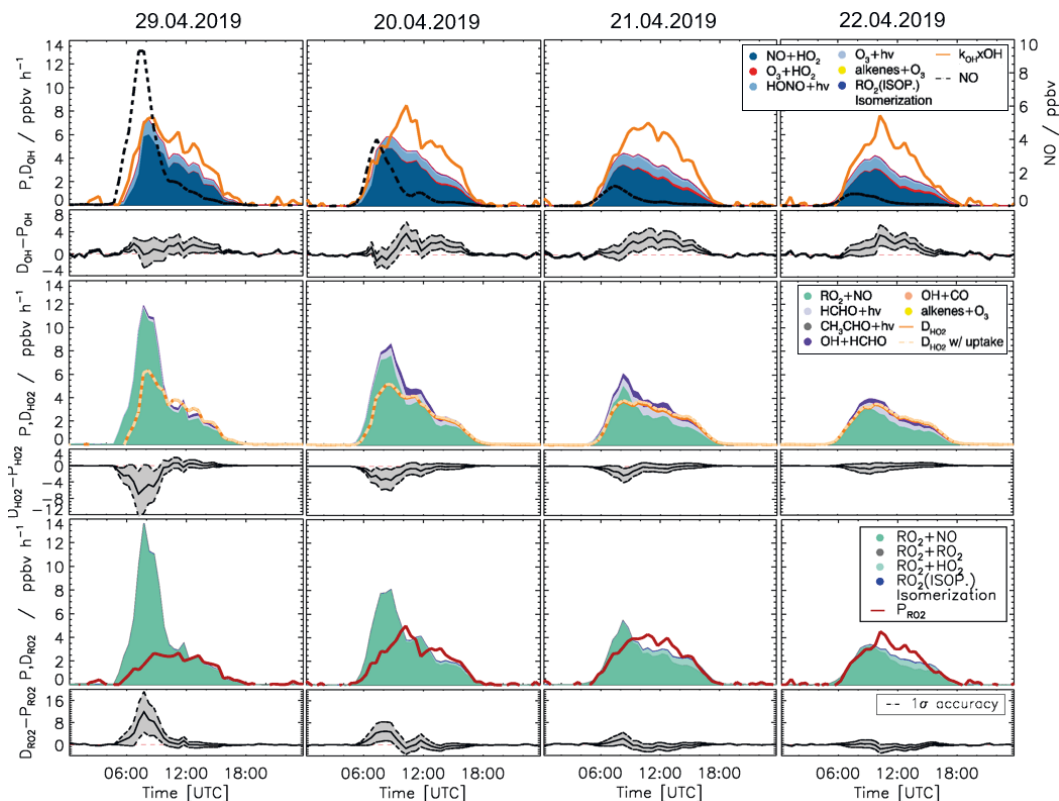


Figure 4. 14: Production and destruction rates of OH, HO₂, and RO₂ radicals for the period of Case #1. In addition, the differences between the destruction and production rates are shown. Grey areas and black dashed lines indicate the uncertainty from the experimental errors of the measured quantities (Table 2.1) and the reaction rate coefficients (Table 4.1).

The HO₂ production could mostly be attributed to the reaction of RO₂ with NO (Reaction R4.9), which contributes up to 90 % of the total production rate on 29 April and 78% from 20 to 22 April. The remaining part of the HO₂ radical production was due to the photolysis of formaldehyde (6 – 16 %) and the reaction of formaldehyde with OH (5 – 12 %). Other HO₂ production reactions played only a minor role (< 0.5 %). The HO₂ destruction was mostly governed by the reaction of HO₂ with

NO (Reaction R4.10, contribution on average 87%) and to less extent by the reaction of HO₂ with RO₂ radicals (Reaction R4.16, contribution on average 8%). The HO₂ destruction and production rates showed good agreement within the uncertainty of calculations during the entire day on 21 and 22 April and in the late afternoon on 20 and 29 April, when the NO mixing ratio was lower than 2 ppbv. Large imbalances were observed in the morning on 20 and 29 April with values of up to 6 ppbv h⁻¹ (50 % of the total HO₂ production rate). However, the uncertainty of the calculations for conditions of high NO mixing ratios was high due to the high uncertainties in HO₂ and RO₂ background signals. Therefore, the imbalances were closed within the uncertainty limits.

The reaction of RO₂ with NO (Reaction R4.9) dominated the RO₂ destruction rate contributing to the total loss rate more than 85 %. When the NO mixing ratio was low, < 1.5 ppbv, (21 and 22 April), the RO₂ termination reaction with HO₂ gained in importance with contributions of more than 10 %. Like for the OH radical chemical budget, unimolecular decomposition reactions of isoprene-RO₂ radicals were negligible with a contribution to the RO₂ destruction rate of less than 1 %. The daily maximum RO₂ destruction rate appeared in the morning together with the peak of the NO concentration and decreased shortly before noontime, while the NO concentration was decreasing. In contrast, the RO₂ production rate reached maximum values at noon and showed much less variability compared to the destruction rate. This imbalance between the production and destruction rates was most significant in the morning on 29 and 20 April with values of up to 12 ppbv h⁻¹ (86 % of the total RO₂ destruction rate). Similar to the HO₂ budget, the uncertainties from the NO background signals were high, so that the imbalances were closed to the uncertainty limits.

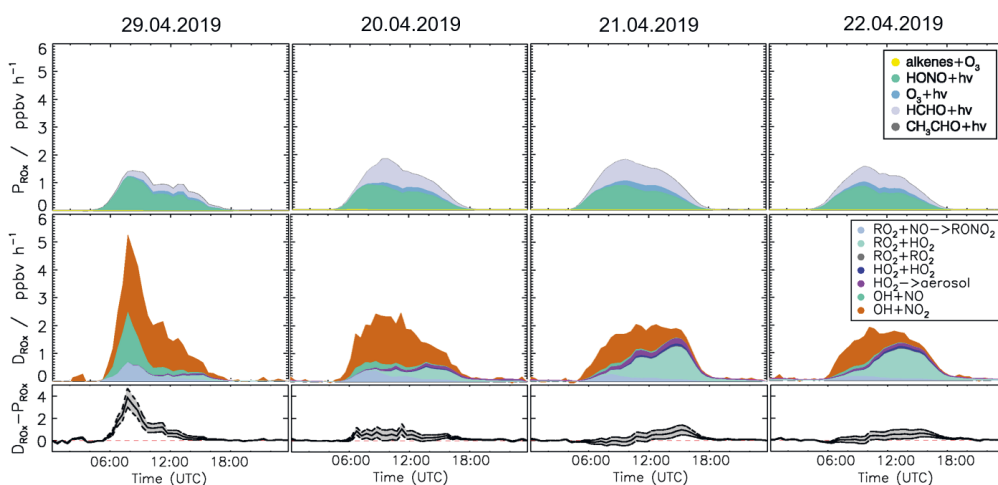


Figure 4. 15: Production and destruction rates of RO_X radicals for the period of Case #1. In addition, the differences between the destruction and production rates are shown. Grey areas and black dashed lines indicate the uncertainty from experimental errors of the measured quantities (Table 2.1) and the reaction rate coefficients (Table 4.1).

Figure 4.15 shows the calculated RO_X production and destruction rates. The photolysis of HONO (Reaction R4.1) and HCHO (Reaction R4.3) were the dominating radical initiation processes contributing to the total production rate on average 56 % and 41 %, respectively, on 20 – 22 April,

and 88 % and 10 % on 29 April. In the morning on 29 and 20 April, when NO mixing ratios were high with values above 2 ppbv, the reaction of OH with NO₂ (Reaction R4.12) was the most important radical termination process contributing up to 53 % to the total RO_x destruction rate. At these times, the reaction of OH with NO contributed to the RO_x loss rate 34 % and 11 %, respectively. In the afternoon on 21 and 22 April, radical self-reactions (Reaction R4.15 – 4.17), and, in particular, the reaction of RO₂ with HO₂ (Reaction R4.16), dominated the RO_x destruction due to the low NO mixing ratios. On 20 April, a slight imbalance between the RO_x production and destruction rates of up to 1 ppbv h⁻¹ (45 % of total RO_x destruction rate) was observed during daytime, while, on 21 and 22 April, the budget was closed in the morning and it started to deviate around noon until sunset (up to 1 ppbv h⁻¹, 58 % of the total RO_x turnover rate). A significant discrepancy of up to 3 ppbv h⁻¹ (70 % of total RO_x turnover) was observed from 06:00 to 12:00 on 29 April.

4.3.2 Results of Case #2: Chemical radical budgets for conditions with low NO mixing ratios and medium temperature

For the period between 5 and 8 August, the chemical budget analysis was performed. During this period NO mixing ratios were low with a median value of 0.2 ppbv. The temperature was typical for summer with a median value of 27°C (Table 4.2). Figure 4.16 shows the median diurnal experimental production and destruction rates for OH, HO₂, and RO₂ radicals in this period.

Similar to Case #1, the OH production was dominated by the reaction of HO₂ with NO (Reaction R4.10) and the photolysis of HONO (Reaction R4.1). A significant imbalance between OH production and destruction rates of up to 3 ppbv h⁻¹ (53 % of the total OH destruction rate) was found, which cannot be explained by the combined uncertainty of the calculations.

Concerning the HO₂ chemical budget, the major contribution to the HO₂ production was due to the reaction of RO₂ with NO (Reaction R4.9), while the HO₂ destruction was dominated by the reaction of HO₂ with NO (Reaction R4.10). The total HO₂ production rate was significantly (2.5 ppbv h⁻¹) higher than the destruction rate (40 % of the total HO₂ production rate), which cannot be explained by the uncertainty of the calculations.

The RO₂ production and destruction rates were well balanced. The reaction of RO₂ with NO dominated the overall RO₂ production and radical self-reactions played a minor role. In addition, the availability of ClNO₂ data during this period allowed to assess the potential impact of the reaction of VOCs with Cl (Eq. 4.9) on the RO₂ radical production. Due to the low mixing ratio of ClNO₂ of less than 0.4 ppbv, the RO₂ production from Cl was insignificant (<0.1 ppbv h⁻¹) and much lower than the RO₂ production from the reaction of OH with VOCs.

Rates of the RO_x initiation and termination reactions are shown in Figure 4.17. Similar as in the period between 20 to 22 April, the maximum difference between RO_x production and destruction rates was small (0.5 ppbv h⁻¹). The OH regeneration from isoprene-RO₂, the potential HO₂ uptake on aerosol, and radical production from Cl reactions had no significant impact on the radical chemical budget in this period.

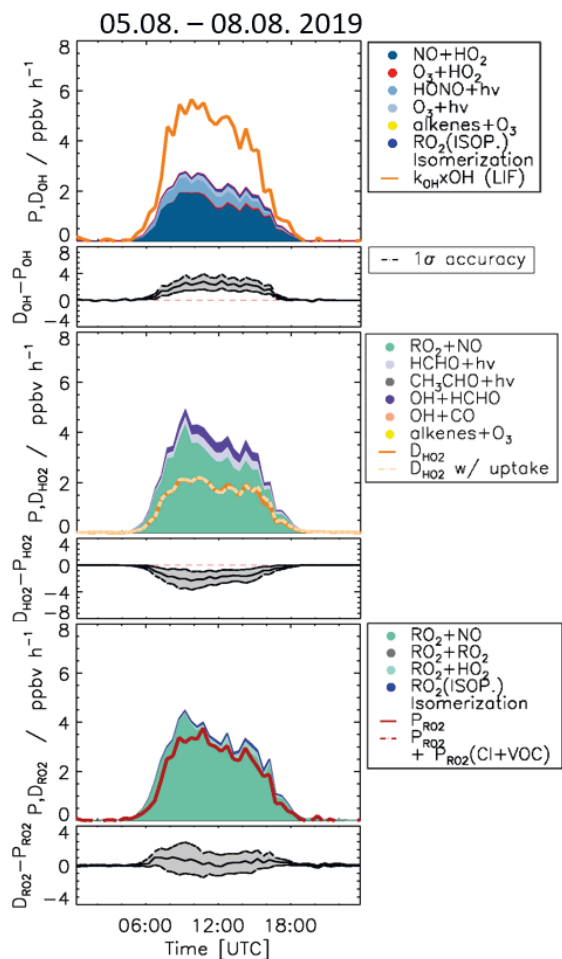


Figure 4. 16: Median values of production and destruction rates of OH, HO₂, and RO₂ radicals for the period of Case #2. In addition, the differences between the destruction and production rates are shown. Grey areas and black dashed lines indicate the uncertainty from experimental errors of the measured quantities (Table 2.1) and the reaction rate coefficients (Table 4.1).

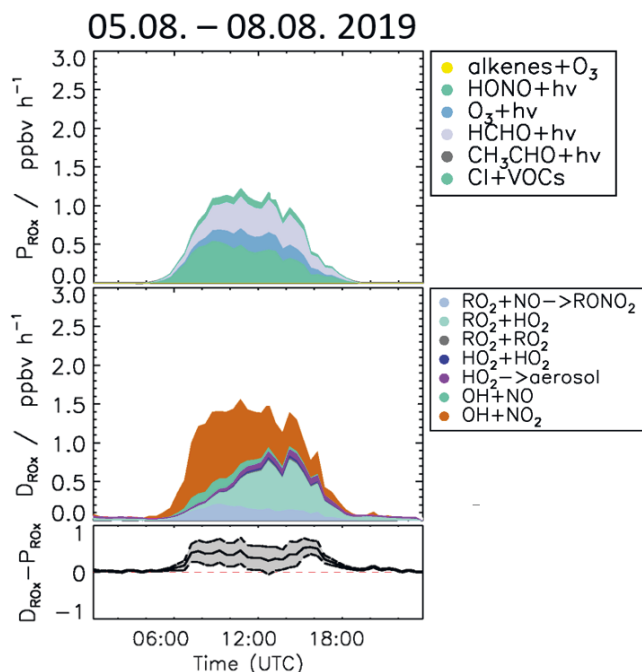


Figure 4. 17: Median values of production and destruction rates of RO_x radicals for the period of Case #2. In addition, the difference between the destruction and production rates is shown. Grey areas and black dashed lines indicate the uncertainty from experimental errors of the measured quantities (Table 2.1) and the reaction rate coefficients (Table 4.1).

4.3.3 Results of Case #3: Chemical radical budgets for conditions with low NO mixing ratios and high temperature

During the heat wave from 22 to 31 August, the temperature was high (maximum: 42°C) and air masses were stagnant (wind speed at 50 m: < 4 m/s). No precipitation occurred. Ozone mixing ratios reached maximum values of 100 ppbv and daytime NO mixing ratios were relatively low with average values of 0.3 ppbv. (Table 4.2). Radical production and destruction rates for this period are shown in Figure 4.18 and 4.19. During this period, the OH concentration measured by the LIF instrument was 25 % higher than values measured by the DOAS instrument. Therefore, the OH concentration measured by the DOAS instrument was used for the analysis of the radical budgets for this period.

The OH destruction rates were up to 2.0 ppbv h^{-1} (23 % of the total OH destruction rate) higher than the total production rate, which was dominated by the reaction of HO_2 with NO (Reaction R4.10). However, this discrepancy was smaller than the total uncertainty of the analysis. The impact of OH regeneration from unimolecular reaction of isoprene derived RO_2 was larger than for the other

cases (on average, 4%) consistent with the high isoprene concentration (~ 0.8 ppbv) and high temperature that favors emissions from plants (Vilà-Guerau de Arellano et al., 2009; Sarkar et al., 2020).

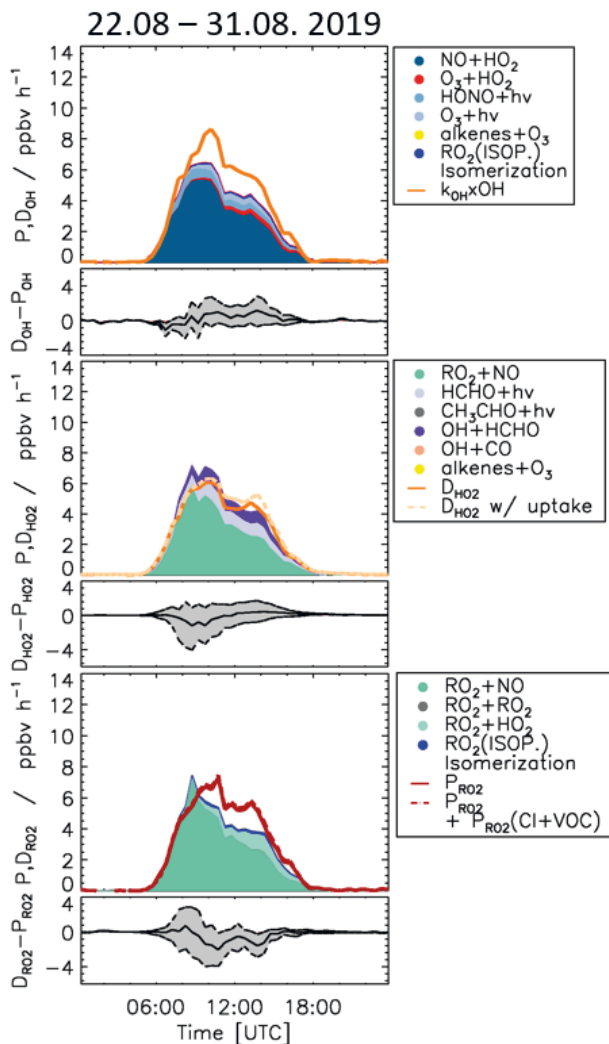


Figure 4. 18: Median values of production and destruction rates of OH, HO₂, and RO₂ radicals for the period of Case #3. In addition, the differences between the destruction and production rates are shown. Grey shaded areas and black dashed lines indicate the uncertainty from experimental errors of the measured quantities (Table 2.1) and the reaction rate coefficients (Table 4.1).

The HO₂ production and destruction rates showed a good agreement throughout daytime. Once again, the major HO₂ radical sink was the reaction of HO₂ with NO (Reaction R4.10). The major source of HO₂ radicals was the reaction of RO₂ with NO (Reaction R4.9). The contributions from the photolysis of HCHO and the reaction of HCHO with OH to the HO₂ production rates were larger compared to other cases contributing to the total production rate up to 15% and 13%, respectively, due to higher HCHO mixing ratios of up to 8 ppbv (Fig. 4.3).

Given the uncertainty of the calculation, the RO₂ production and destruction rates were overall well balanced. Again, most of the RO₂ destruction was due to the reaction of RO₂ with NO (Reaction R4.9). Although the destruction and production rates were balanced for the single radicals within the uncertainty of the calculations, the rates of radical initiation and termination reactions showed a significant imbalance. The total radical termination rate was up to 1.4 ppbv h⁻¹ higher than its production rate throughout daytime. The maximum difference cannot be explained by the uncertainty of the calculations at noontime when the difference was highest.

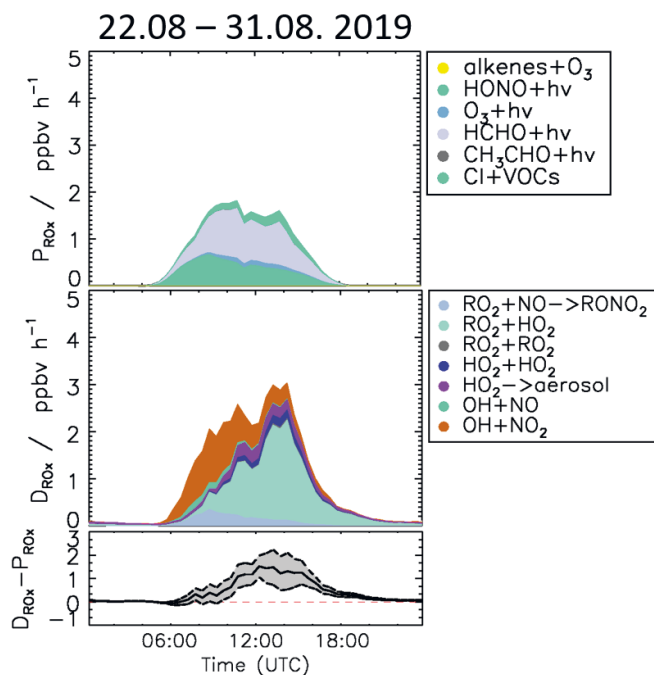


Figure 4. 19: Median values of production and destruction rates of RO_x radicals for the period of Case #3. In addition, the difference between the destruction and production rates is shown. Grey shaded areas and black dashed lines indicate the uncertainty from experimental errors of the measured quantities (Table 2.1) and the reaction rate coefficients (Table 4.1).

4.4 Discussion of the chemical budget analysis

4.4.1 Discussion of discrepancies in the radical budgets

In all cases described in Section 4.3, discrepancies of up to 3.5 ppbv h^{-1} between OH production and destruction rates are found for NO mixing ratios below 2 ppbv, indicating a missing OH production process with rates that range from 25 % (Case #3) to 53 % (Case #2) of total OH destruction rates. As the measured OH reactivity (k_{OH}) absolutely quantifies the chemical loss rate of OH including all OH reactants, the calculation of the OH destruction rate (Eq. 4.5) carries a small error. In addition, the measurement of OH concentrations by the LIF instrument is interference-corrected using the CMR system and is checked against OH measurements by the DOAS instrument (Chapter 3) and therefore has also a high accuracy. For these reasons, the calculated OH destruction rate has only an uncertainty of 25 %.

HO₂ and RO₂ radical measurements are also highly reliable as the calculated O_x production rates using the measured HO₂ and RO₂ concentrations are consistent with the O_x production rate determined from O₃ and NO₂ measurements (Section 4.1.4 and Chapter 5). Because the reaction of HO₂ with NO (Reaction R4.10) accounts for more than 70 % of the total OH production rate (Section 4.3), and other OH sources (e.g., the photolysis of HONO and O₃) play a minor role, the observed discrepancy between the OH production and destruction rates are unlikely affected by unaccounted systematic errors.

Furthermore, previous analysis of the OH budget during photochemical experiments in the SAPHIR chamber showed no evidence for a missing OH source originating from chamber wall effects (Kaminski et al., 2017; Fuchs et al., 2018; Novelli et al., 2018; Rolletter et al., 2019; Rolletter et al., 2020). For all these reasons, the most plausible explanation for the discrepancy between production and destruction rates of OH radicals observed in the JULIAC campaign is an unaccounted process of producing OH radicals.

In all cases described in the previous sections, a small imbalance in the RO_x budget of up to 1.4 ppbv h^{-1} is found and this implies the presence of unaccounted primary OH sources. One possible explanation for this discrepancy could be the lack of measured alkenes that can produce radicals in their ozonolysis reactions. The contributions of ozonolysis of measured alkenes to the radical production were very small with values in range of 0.005 to 0.03 ppb h^{-1} . To test the possible impact of the ozonolysis of unmeasured alkenes on the radical production, the OH reactivity that cannot be explained by measured OH reactants (on average, 2.5 s^{-1}) is assumed to originate from 1.5 ppbv propene and 1.0 ppbv cis-2-butene. Both species were not measured during the campaign but are commonly found in forested environments (Goldstein et al., 1996; Rhew et al., 2017). Especially, cis-2-butene reacts with O₃ with an exceptionally fast reaction rate constant (Table 4.1). Including these additional VOCs could increase the radical production rate by more than an order of magnitude for all cases (Fig. A.1 – A.3). This increase in the RO_x production rate would close the budget within the uncertainties for the periods in Case #1 (except for 29 April, Fig. A.1) and Case #2 (Fig. A.2), but it cannot explain the missing RO_x sources found on 29 April (Fig. A.1) and for the Case #3 (Fig. A.3) due to small unaccounted OH reactivities and too high discrepancies.

Therefore, the unaccounted primary OH source alone would not be sufficient to explain the discrepancy in the OH radical budgets. The additional missing OH source seems to be related to missing RO₂ or HO₂ loss reactions. This is suggested by a RO₂ destruction rate that is up to 1.5 ppbv h⁻¹ higher than the RO₂ production rate in the period of Case #1 (Section 4.3.1) and a missing HO₂ loss reaction with a rate of up to 2.5 ppbv h⁻¹ in the period of Case #2 (Section 4.3.2). Although there are large uncertainties in the difference between production and destruction rates for single radical species, values of the differences consistently indicate an unaccounted RO₂ or HO₂ to OH propagation pathway together with a missing primary OH source.

As a direct RO₂ to OH regeneration reaction, the OH production from the isomerization of the isoprene-RO₂ (Eq. 4.3) is included, but its contributions to the total OH production in all cases are minor. Therefore, the inferred missing OH source at low NO mixing ratios is likely caused by the combination of missing primary radical sources and inter-radical conversion reactions.

For NO mixing ratios higher than 2 ppbv, OH production and destruction rates are balanced while significant imbalances between production and destruction rates are observed for production and destruction rates of HO₂, RO₂ and RO_x radicals. A missing HO₂ sink with a rate of up to 6 ppbv h⁻¹, a missing RO₂ source with a rate of up to 12 ppbv h⁻¹ and a missing RO_x source with a rate of up to 3 ppbv h⁻¹ is needed to explain the discrepancies. As discussed in Section 3.2.4, the uncertainties in the turnover rates of HO₂ and RO₂ reactions with NO for such high NO concentrations is high due to the high uncertainties in the HO₂ and RO₂ background signals. As a sensitivity study, the production and destruction rates using the upper limits for HO₂ and RO₂ background signals are shown for the entire Case #1 period in Figure A.4 (Appendix). In this case, the imbalances in the HO₂ and RO₂ production and destruction rates are significantly decreased, and the budgets are closed within the large uncertainties.

Because RO_x production and destruction rates are much less affected (less than 3%) by the uncertainty from the HO₂ and RO₂ background signals than the individual HO₂ and RO₂ budgets, the imbalance in the RO_x budget is still significant and indicates that a radical source is needed. As the OH budget is balanced and the HO₂ budget does not require an additional HO₂ source, a missing RO_x source can partly explain the missing RO₂ source (Figure A.4). A missing RO₂ source could originate from the VOC oxidation by Cl radicals. Although oxidation of organic compounds by Cl produced from ClNO₂ does not have a significant effect on the RO₂ production in the summer period, a possible impact from Cl chemistry on the RO₂ production and therefore also on the RO_x production on 29 and 20 April cannot be ruled out, because the instrument detecting ClNO₂ was not available during the spring period of the campaign.

As described in Section 4.2.5, the same rate coefficients for the reaction of all RO₂ species with NO (Reaction R4.9), RO₂ (Reaction R4.15), and HO₂ (Reaction R4.16) are used in the calculations taking values from structure activity relationship by Jenkin et al. (2019). The reactions of RO₂ with RO₂ and HO₂ play a minor role for the destruction of RO₂ and HO₂ radicals. However, the rate coefficient of the reaction of RO₂ and NO has a large impact on both the HO₂ and RO₂ budgets as this reaction is the major production pathway for HO₂ and the main loss pathway for RO₂ radicals. A high limit for this rate coefficient would assume that all RO₂ would behave like c-C₅H₉O₂ having a rate constant of $1.1 \times 10^{-11} \text{ cm}^3 \text{ s}^{-1}$ (at 298 K), which is approximately 20 % higher than the rate

coefficient used in the calculations. If this value is applied for the period between 21 and 22 April as a sensitivity study (Fig. A.5), the observed discrepancies in the RO₂ budgets can be closed during times when the RO₂ production rate was higher than the destruction rate and NO mixing ratios were low. However, although the use of the high limit rate coefficient reduces the discrepancies in the RO₂ budgets, changes are smaller than the uncertainty limits.

In another sensitivity study, a low limit for the rate coefficient of the reaction of RO₂ with NO assuming that all RO₂ behaves like CH₃O₂ having a rate constant in the reaction with NO of $7.7 \times 10^{-12} \text{ cm}^3 \text{ s}^{-1}$ (at 298 K), which is approximately 17 % lower than the used rate coefficient, is applied. However, this cannot explain the observed discrepancy in the period of Case #2 (Fig. A.6), when the RO₂ production rate was lower than the destruction rate. To close the HO₂ budget, a 56 % smaller rate coefficient ($5.0 \times 10^{-12} \text{ cm}^3 \text{ s}^{-1}$) would be needed. However, this is much lower than reported rate coefficients for the reaction of RO₂ and NO. In addition, the use of such a low-rate coefficient would make a significant imbalance in RO₂ chemical budget.

Furthermore, an additional uncertainty in the HO₂ production rate comes from using a fixed, small organic nitrate yield of 0.05 for all RO₂ species in the reaction of RO₂ with NO. A sensitivity test varying the organic nitrate yield from 5 % to 20 % is performed. The use of a higher yield decreases the discrepancy in the RO₂ budgets only from 2 to 1.5 ppbv h⁻¹. It is worth noting that the organic nitrate yield generally increases for larger hydrocarbons, for which also the rate coefficient of the reaction of their RO₂ with NO is faster compared to small VOCs. Therefore, the presence of unmeasured large hydrocarbons is unlikely the reason for the imbalance in the HO₂ budget, because the high nitrate yield and the fast reaction rate coefficient are expected to partly compensate the effects on the HO₂ production rate.

The potential impact of heterogeneous uptake of HO₂ on aerosol surface (Eq. 4.8) is overall insignificant in all cases, even if an already high effective uptake coefficient of 0.2 is assumed (Section 4.2.2). In the period of Case #3, the HO₂ loss rate due to uptake on aerosol surface would be up to 0.15 ppbv h⁻¹, when the aerosol surface area was high with values of up to $3.0 \times 10^2 \text{ } \mu\text{m}^2 \text{ cm}^{-3}$. The contribution to the total loss rate, however, would be still very small (<4%). HO₂ uptake has also a high uncertainty, because the uptake coefficient highly depends on the aerosol properties. Measurements in this campaign did not allow to determine the uptake coefficient. However, even using an exceptionally high effective uptake coefficient of 0.5 that was determined in a campaign in China (Taketani et al., 2008) would increase the HO₂ loss to the aerosol surface up to 0.32 ppbv h⁻¹ (13% of the observed discrepancy). Therefore, no matter what the value of the effective uptake coefficient would be, the heterogeneous uptake of HO₂ on aerosol surface was insignificant during the JULIAC campaign.

4.4.2 Comparisons with other field campaigns investigating the radical budgets

Similar studies of the chemical budgets for OH, HO₂, RO₂, and RO_x radicals like in this work were performed for measurements in campaigns in a suburban area in the Pearl River Delta (PRD), China,

in autumn 2014 (Tan et al., 2019), and in central Beijing, China, (Whalley et al., 2021) in summer 2017.

Tan et al. (2019) observed median rates of propagation reactions for OH, HO₂ and RO₂ radicals ranging from 10 to 15 ppbv h⁻¹, while rates for RO_x initiation and termination reactions were on the order of 3 to 4 ppbv h⁻¹ during daytime for chemical conditions characterized by anthropogenic pollution. From the comparison between the radical production and destruction rates, up to 7 ppbv h⁻¹ (45 % of the total OH turnover) of a missing OH source and a missing RO₂ sink with a similar rate were found at low NO mixing ratios (< 1 ppbv), while HO₂ production and destruction rates were balanced. The authors suggested that an additional chemical mechanism that efficiently converts RO₂ to OH without NO is required. Tan et al. (2019) proposed that HO_x radicals could have been formed by auto-oxidation of specific RO₂ species which include multifunctional groups such as -OH, -OOH, or -CHO. Assuming such a mechanism could reasonably explain the missing RO₂ loss pathway and the missing primary OH source. Tan et al. (2019) also showed that a hypothetical radical propagation mechanism by an unknown reactant, which would convert RO₂ to HO₂ and, subsequently, HO₂ to OH as proposed by Hofzumahaus et al. (2009) could describe the missing OH source and RO₂ sink. The mixing ratio of such a reactant can be expressed as an NO equivalent that reacts with peroxy radicals. For the conditions of the campaign in Tan et al. (2019) the NO equivalent was 0.4 ppbv.

The OH budget for the JULIAC campaign showed a missing OH source with a rate ranging between 2 and 4 ppbv h⁻¹ (50 % of the total OH destruction rate) for low NO mixing ratios. The rate of the missing OH source in this study is smaller compared to that reported in Tan et al. (2019). However, considering that the overall OH radical turnover rates in the JULIAC campaign are about twice as small, the relative importance of the missing chemical pathways on the OH production is similar like in the campaign in the Pearl-River-Delta 2014.

The mechanism suggested by Tan et al. (2019) is likely not the only explanation for discrepancies in the radical budgets observed in this work. Although, a small missing RO₂ sink with a rate of up to 1.5 ppbv h⁻¹ was found together with a missing OH source on 21 and 22 April (Section 4.3.1), which fits the auto-oxidation pathway suggested by Tan et al. (2019), there are also other cases, where missing HO₂ and RO_x sinks were observed, and missing OH sources that are likely not only originate from RO₂ to OH conversion reactions, but also from HO₂ to OH conversion and primary OH production. This indicates that the origin of missing OH sources observed in field campaigns could differ depending on the chemical conditions, even if NO mixing ratios are similar.

Whalley et al. (2021) analyzed the chemical budgets for radicals over a wide range of NO mixing ratios (0.1 to 104 ppbv) for measurements performed in central Beijing, China. Compared to the results in Tan et al. (2019) and to results in this study, the rates of RO_x initiation and termination reactions were 2 to 4 times higher and the rates of radical propagation reactions for OH, HO₂ and RO₂ were 5 to 10 times higher due to fast inter-radical conversion reactions in the presence of high NO concentrations. Similar as in this study, a significant missing OH source with a rate of up to 15 ppbv h⁻¹ (50 % of the total OH destruction) was found for conditions of low NO mixing ratios. The value of the missing OH source was more than 3 times higher than in the JULIAC campaign and in the campaign reported by Tan et al. (2019). The HO₂ production rate observed in Beijing by Whalley et al. (2021) largely exceeded the destruction rate by a factor of 3 – 5 for conditions of low NO mixing

ratios. In contrast, production and destruction rates of RO_2 and RO_x radicals were well balanced. This was also the case for OH at high NO mixing ratios, when very high imbalances of up to 50 ppbv h^{-1} were observed for HO_2 and RO_2 budgets.

In Whalley et al. (2021), reducing the rate of radical propagation reactions from RO_2 to HO_2 by a factor of 10 would close the observed gaps between production and destruction rates. This suggests the presence of a significant fraction of large and multifunctional VOCs (e.g., monoterpenes and long-chain alkanes), which undergo multiple RO_2 to RO_2 conversion by unimolecular isomerization of alkoxy radicals formed in the reaction RO_2 with NO instead of producing HO_2 by O_2 abstraction. Such a RO_2 radical reaction chain would be similar to an increased chemical lifetime of RO_2 radicals, if RO_2 species cannot be distinguished by instruments like in the RO_2 sum measurements performed by the LIF radical instruments. Whalley et al. (2021) showed that RO_2 production by the isomerization reaction of RO in the oxidation of α -pinene would largely reconcile discrepancies between modelled and measured RO_2 concentrations (the observation-to-model ratio decreases from 6.2 to 1.8), if the OH reactivity from unmeasured OH reactants was attributed to α -pinene.

Applying a reduced rate constant for RO_2 to HO_2 propagation reactions as suggested in Whalley et al. (2021) to the calculations in this work could close the observed large discrepancy between HO_2 and RO_2 production and destruction rates for high NO mixing ratios on 29 April. In this case, a reduction by a factor of 2 would be required. As discussed in Section 4.3.1 and 4.4.1, reduced reaction rate constants of the RO_2 +NO reaction could be expected for RO_2 from large VOCs. However, the reduction would need to apply to all RO_2 , most of which are not derived from large VOCs, even if OH reactivity that is not explained by measured OH reactants is attributed to them. Therefore, it seems unlikely that the mechanism suggested by Whalley et al. (2021) affected results in this work. In addition, it cannot be excluded that observed imbalance in HO_2 and RO_2 budgets in the JULIAC campaign were caused by the instrumental artifacts due to the high uncertainty of the RO_2 background signal.

Chapter 5. Investigation of tropospheric ozone formation in a rural area in West-Germany in the JULIAC 2019 campaign

5.1 Determination of the net odd oxygen (O_x) production rate from ozone and NO_2 concentration measurements

One goal of the JULIAC campaign was to determine the net ozone production rate in ambient air. Because of the photochemical equilibrium between ozone and nitrogen dioxide, it is useful to investigate the sum of both called odd oxygen (O_x). The O_x production can be interpreted as ozone production potential (Chapter 1). The assumption is, however, that there are no direct emissions of NO_2 , which is fulfilled inside the SAPHIR chamber.

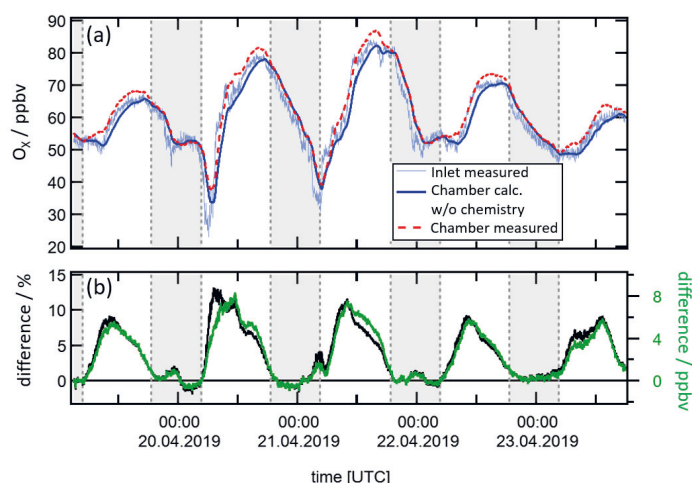


Figure 5. 1: (a) Concentrations of O_x (sum of NO_2 and O_3) in the inlet and in the chamber and expected in the chamber, if there was no chemical production and destruction (Chamber calc.). Grey areas indicate nighttime (solar zenith angle $> 90^\circ$). (b) Relative and absolute differences between measured concentrations and calculated concentrations expected without chemical production and destruction in the chamber.

The net O_x production during the JULIAC campaign can be calculated from measured ozone and NO_2 concentrations, both of which were simultaneously detected in the inlet and in the chamber by different instruments (Figure 5.1) using Equation 2.5 ($P_{O_x, NO_2 \& O_3}$). Because the O_x concentration that is produced on the time scale of the residence time of air in the chamber is small compared to the total O_x concentration, calibrations and offsets of the instruments are crucial to be accurately and precisely determined.

The precision of the net O_x production rate can be determined from the experiments when the roof of the SAPHIR chamber was closed, i.e., the photolysis rates within the chamber were zero. For

these dark conditions, no significant O_x production is expected in the chamber, so that the concentrations inside the chamber are only determined by the concentrations in the inflowing air similar (Section 2.5) and the precision can be calculated from the comparison of these values. For two of the three intervals of measurements in the dark (9 to 10 Feb. and 27 to 28 April), a 1σ precision of the O_x production rate of 0.3 ppb hr^{-1} was achieved. For the third interval of measurements in the dark (2 to 3 Nov.), the precision was 0.5 ppb hr^{-1} . In these periods, there was continuous precipitation and trace gas concentrations were very low (measured OH reactivity: $< 4 \text{ s}^{-1}$). Therefore, also O_x destruction processes can be assumed to be negligible.

The 1σ accuracy of the net O_x production rate is calculated to be 8 % from the gaussian summation of the accuracy of the instrument's calibration factors (Table 2.1) and the uncertainty of the residence time (1 %) in the chamber (Eq. 2.2).

For the calculation of the net O_x production rate, it is of particular importance that the instrumental offsets between instruments do not differ, because only differences between measurements are used (Eq. 2.5). However, the offset of a specific instrument may also drift over time. This can introduce an additional systematic error of the O_x production rate. In order to examine the stability of the offset, instruments measuring at the inlet switched periodically every 20 to 30 minutes to sampling air from inside the chamber during some periods of the campaign. This was done every 2 to 3 days for the entire day from 5 August to 23 August. 1σ variabilities of the offsets in the measurements of the NO_2 and O_3 instruments were 0.4 ppbv and 0.5 ppbv , respectively. These offsets drifted during the summer period of the campaign adding 0.5 ppbv hr^{-1} to the uncertainty of the O_x production rate. For the other periods of the JULIAC campaign, the same additional uncertainty is taken into account.

5.2 Calculation of the net odd oxygen (O_x) production rate from turnover rates of single reactions

Measurements of radical and trace gas concentrations in the JULIAC campaign allowed to calculate the net O_x production rate by another approach, in which the turnover rates of reactions contributing to the production or destruction of NO_2 and O_3 are summed up.

For conditions of the JULIAC campaign, the ozone is produced from the photolysis of NO_2 formed in the reaction of peroxy radicals (HO_2 and RO_2) with NO (Reaction R5.3 and R5.4). The most important destruction of O_x is expected to be the loss of NO_2 in the reaction with OH radicals (Reaction R5.7) (Finlayson-Pitts, 2000). Therefore, the net O_x production rate can be approximated by the turnover rates of these reactions:

$$P_{O_x, \text{base}} = k_{R5.3}[\text{NO}][\text{HO}_2] + k_{R5.4}[\text{NO}][\text{RO}_2] - k_{R5.7}[\text{NO}_2][\text{OH}] \quad (\text{Eq. 5.1})$$

Here, k_i are the rate coefficients for the specific reactions (Table 5.1). A yield of 5 % of organic nitrates formed in the reaction of RO_2 with NO is assumed as it is expected that the majority of organic peroxy radicals originate from small organic species, which typically have a low nitrate yield

(Chapter 4). For the rate coefficient of the reaction of RO₂ with NO (Reaction R5.4), an average rate coefficient is applied for the sum measurement of RO₂ radicals (Jenkin et al., 2019).

Equation 5.1 only includes the most important odd oxygen production and loss reactions. This approach can be extended by including additional reactions which have minor contributions, such as the reaction of nitrous acid with OH, photolysis of nitril chloride and ozone, reactions of ozone with OH, HO₂, NO₂ and alkenes:

$$P_{O_x, \text{extend}} = P_{O_x, \text{base}} + k_{R5.5}[\text{HONO}][\text{OH}] + j_{\text{ClNO}_2}[\text{ClNO}_2] - k_{R5.8}[\text{HO}_2][\text{O}_3] - k_{R5.9}[\text{OH}][\text{O}_3] - \varphi \cdot j_{\text{O}^1\text{D}}[\text{O}_3] - 2(1 - \beta)k_{R5.11}[\text{NO}_2][\text{O}_3] - \Sigma k_{R5.12i}[\text{alkene}]_i[\text{O}_3] \quad (\text{Eq. 5.2})$$

Here, j_i are photolysis frequencies for the specific species, and φ is the fraction of O(¹D) reacting with H₂O. The factor β takes into account that only a fraction of NO₃ formed in the reaction of NO₂ with O₃ leads to an effective O_x loss due to the rapid reformation of NO₂ mainly during daytime (see below for details). All quantities required to calculate the ozone production rate using Eq. 5.2 were measured in the JULIAC campaign.

In the atmosphere, O_x production from the reaction of nitrous acid (HONO) with OH radicals (Reaction 5.5) and the photolysis of nitril chloride (ClNO₂) (Reaction 5.6) may not be regarded as net odd oxygen production on a long-time scale but rather as O_x reservoir species, because both are produced from heterogeneous reactions of NO₂. Concerning HONO, this is complicated, because the sources of HONO in the troposphere are not well known (Stemmler et al., 2006; Stemmler et al., 2007; Su et al., 2011; Li et al., 2014). In the JULIAC campaign, a significant fraction of the HONO in the chamber was released by the chamber film (Chapter 2). For calculations of the odd oxygen net production in the JULIAC campaign, the reaction of HONO with OH and the photolysis of ClNO₂ need to be considered as odd oxygen sources, because they are not formed by for example heterogeneous conversion of NO₂ to HONO or ClNO₂ on the time scale of residence time of air in the chamber, so that there is no corresponding consumption of O_x. The additional O_x production and destruction by chlorine radicals (e.g., the reaction of Cl with O₃), which can be produced from the photolysis of ClNO₂ is not taken into account. The possible role of Cl radicals is further discussed in Section 5.4.2.

The extended calculation of the O_x production rate (Eq. 5.2) also includes the production of nitrate radicals (NO₃) from the reaction of NO₂ with O₃ (Reaction R5.10) meaning the loss of two O_x molecules. NO₃ and its reservoir species N₂O₅ formed by its reaction with NO₂ (Reaction R5.14) can act as odd oxygen reservoir, because NO₂ can be reformed by NO₃ photolysis (Reaction 5.17a, b) or reaction with NO (Reaction R5.13). However, they can also be permanent sinks, if NO₃ reacts with VOCs (Reaction R5.16) or N₂O₅ is taken up on particles.

Table 5. 1: Chemical reactions with rate constants and their uncertainties used for the calculation of O_X ($NO_2 + O_3$) production rates. Rate constants are listed for standard conditions (25 °C, 1atm). For the calculation of the O_X production rate, the actual measured air temperature and pressure are used.

No.	Reaction	k (25 °C, 1atm) / $cm^3 s^{-1}$	Uncertainty ^a	Reference
O_X production reactions				
R5.3	$HO_2+NO \rightarrow OH+NO_2$	8.5×10^{-12}	$\pm 13\%$	IUPAC
R5.4	$RO_2+NO \rightarrow RO+NO_2^c$	$(1-\alpha) \times 9.0 \times 10^{-12}$	$\pm 20\%$	Jenkin et al. (2019)
R5.5	$HONO+OH \rightarrow NO_2+H_2O$	6.0×10^{-12}	$\pm 20\%$	IUPAC
R5.6	$ClNO_2+ hv \rightarrow NO_2+Cl$	$j(ClNO_2)^b$	^b	
O_X destruction reactions				
R5.7	$NO_2+OH \rightarrow HNO_3$	1.0×10^{-11}	$\pm 30\%$	IUPAC
R5.8	$HO_2+O_3 \rightarrow OH+2O_2$	2.0×10^{-15}	$\pm 29\%$	IUPAC
R5.9	$OH+O_3 \rightarrow HO_2+O_2$	7.3×10^{-14}	$\pm 20\%$	IUPAC
R5.10	$O_3+h\nu+H_2O \rightarrow 2OH+O_2$	$\varphi \times j(O^1D)^{b,d}$	^b	
R5.11	$NO_2+O_3 \rightarrow NO_3+O_2$	3.5×10^{-17}	$\pm 7\%$	IUPAC
R5.12	$Alkenes+O_3 \rightarrow Products^c$			
NO_3 reactions				
R5.13	$NO_3+NO \rightarrow 2NO_2$	2.6×10^{-11}	$\pm 13\%$	IUPAC
R5.14	$NO_3+NO_2 \rightarrow N_2O_5$	1.2×10^{-12}	$\pm 20\%$	IUPAC
R5.15	$N_2O_5 \rightarrow NO_3+NO_2$	4.5×10^{-2}	$\pm 50\%$	IUPAC
R5.16	$NO_3+VOC \rightarrow RO_2$	^f	^f	
R5.17a	$NO_3+ hv \rightarrow NO_2+O_3$	$j(NO_3, M)^b$	^b	
R5.17b	$NO_3+ hv \rightarrow NO+O_2$	$j(NO_3, R)^b$	^b	

^a 1σ uncertainty.

^b Measured photolysis frequencies (Table 2.1).

^c Rate constant for the class of alkyl ($\geq C2$) + oxygenated RO_2 species (Jenkin et al., 2019). The assumed 20% uncertainty covers the range of published values including the low value for CH_3O_2 ($7.7 \times 10^{-12} cm^3 s^{-1}$) but excludes values for acyl peroxy radicals ($2.0 \times 10^{-11} cm^3 s^{-1}$). The assumed value for the branching ratio α is 0.05 (see discussion in text).

^d The major fraction of the $O(^1D)$ formed from the photolysis of O_3 reforms O_3 . The net O_3 loss is due to the subsequent reaction of $O(^1D)$ with H_2O . Therefore, the branching ratio φ is multiplied in addition to the photolysis frequency.

^e See Table 4.1.

^f Variable.

Rapid NO_2 regeneration from the photolysis of NO_3 and the NO_3 reaction with NO , both of which are mainly relevant during daytime, is accounted for in Eq. 5.8 by including the fraction of O_X that is regenerated in these reactions. Odd oxygen is only lost in these reactions due to the small yield of NO (approximately 13%) in the photolysis of NO_3 (Reaction R5.17b):

$$\beta = \frac{j_{NO_3, R5.17a} + k_{R5.13}[NO]}{j_{NO_3, R5.17a} + j_{NO_3, R5.17b} + k_{R5.13}[NO]} \quad (\text{Eq. 5.3})$$

During nighttime, further reactions of NO_3 with NO_2 and VOCs are of importance because of the absence of light and the rapid reaction of NO with ozone ($\beta = 0$). The reaction of NO_3 with NO_2 produces dinitrogen pentoxide (N_2O_5), which concentration is in a thermal equilibrium with NO_3 . On

the time scale of the residence time of air in the chamber during the JULIAC campaign, no reformation of odd oxygen is expected once NO_3 is produced in the night.

Another reaction involving NO_2 is the reaction of peroxy radicals with NO_2 and NO_2 production from the thermal decomposition of the products (e.g., HO_2NO_2 , PAN). Because thermal equilibrium is reached within less than 1 min., there is no net effect on the NO_2 concentration for conditions of the JULIAC campaign.

For experiments in chambers, O_3 and NO_2 loss on the wall could be significant. However, tests in the SAPHIR chamber demonstrated that these are negligible specifically for the short residence time of air during operation in the JULIAC campaign.

The uncertainties of the O_x production rates using Equation 5.7 or 5.8 were calculated by the Gaussian summation of the 1σ accuracies of the measured quantities (Table 2.1) and of the reaction rate coefficients (Table 5.1). The reaction rate constant of the RO_2 reaction with NO (Reaction R5.4) as well as the nitrate yield carry a higher uncertainty because averaged values are used, because the sum measurement of RO_2 does not give the speciation of these radicals. Generally, the use of the higher limit reaction rate constant and nitrate yield does not make significant changes (less than 10 %) in the O_x production rate calculations. The detailed discussion of the errors of all quantities can be found in the context of the discussion of the chemical radical budget that makes use of the same quantities (Chapter 4).

5.3 Results of the calculations of the net odd oxygen (O_x) production for measurements in the JULIAC campaign

Due to the very low photochemical activity during winter and autumn periods, the net O_x production rates were below 3 ppbv h^{-1} with daytime mean value of 0.2 ppbv h^{-1} . These values are close to 1σ accuracy of the methods used for the calculation. Therefore, only results from the spring and summer periods of the JULIAC campaign are further discussed similar to the analysis of the radical chemical budgets (Chapter 4).

Time series of the O_x production rate calculated from NO_2 and O_3 measurements in the incoming air and in the chamber are shown in Fig. 5.2 for the spring period in Fig. 5.3 for the summer period.

In the morning, ozone production raised fast, reaching often peak values around noon, before values decreased slowly during the afternoon. Values around sunset were close to zero. For typical conditions in spring and summer, O_x production rates were between 5 to 10 ppbv h^{-1} during the day. Highest values of up to 17 ppbv h^{-1} were observed during the heatwave period (21 to 31 August).

Small destruction of O_x with a rate of less than 0.6 ppbv h^{-1} were observed during some nights in the spring period, but these values are not significant, considering the uncertainty of the calculation. In contrast, on some days during the summer period (Fig. 5.3), O_x destruction rates of up to 2 ppbv h^{-1} are observed, higher than the uncertainty of the calculation.

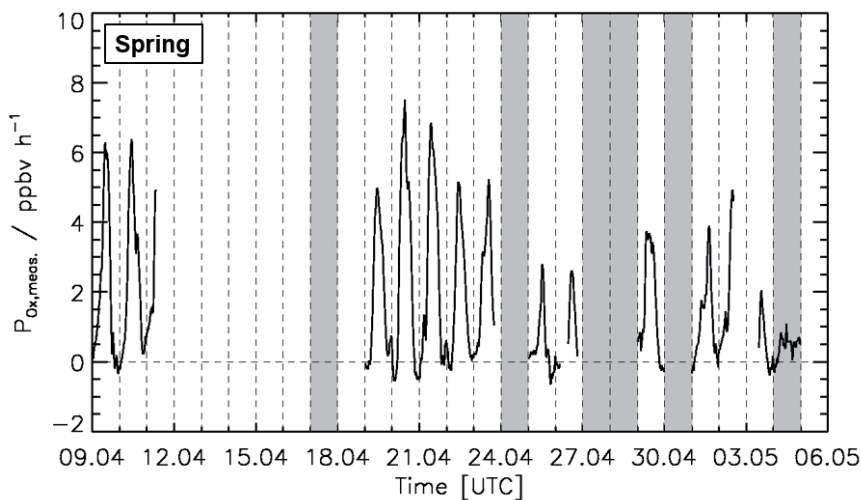


Figure 5. 2: Time series of O_X production rates calculated from NO_2 and O_3 measurements in the incoming air and in the chamber during the spring period of the JULIAC campaign. Vertical dashed lines denote midnight. Grey shaded areas indicate calibration days or days when the chamber roof was closed. All data points are 30 min averages.

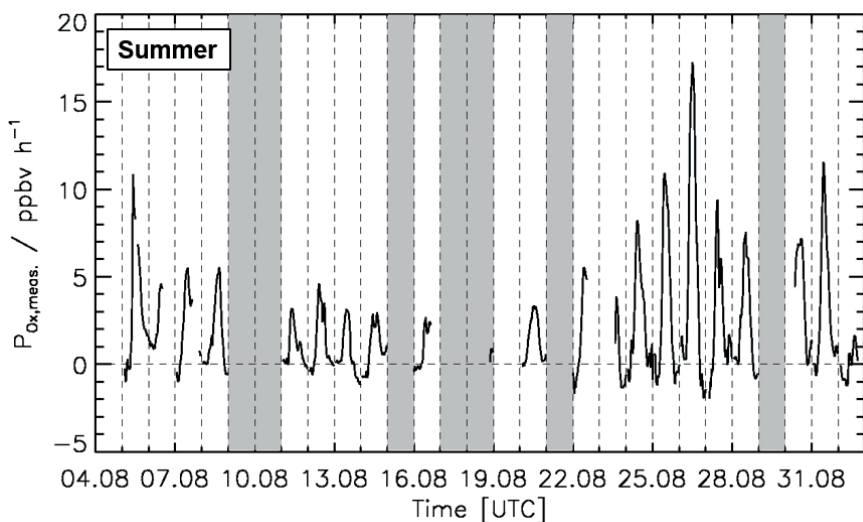


Figure 5. 3: Time series of O_X production rates calculated from NO_2 and O_3 measurements in the incoming air and in the chamber during the summer period of the JULIAC campaign. Vertical dashed lines denote midnight. Grey shaded areas indicate calibration days or days when the chamber roof was closed. All data points are 30 min averages.

Figure 5.4 shows the median diel values of turnover rates contributing to the O_x production and destruction for the spring and summer periods of the JULIAC campaign. As highlighted in Section 5.2, only measured concentrations are used for these calculations.

For the spring period, the O_x production was dominated by the reaction of HO_2 and RO_2 radicals with NO , which contributed similarly to the entire O_x production rate with contributions of 49 % and 50 %, respectively. During the summer period, the contribution of the RO_2 reaction with NO to the total O_x production was slightly higher (57 %) than the contribution of the reaction of HO_2 with NO (42 %). The other O_x production pathways considered in Eq. 5.2 were negligible in both periods. The overall calculated daytime O_x destruction was dominated by the reaction of NO_2 with OH (78 %) followed by the photolysis of O_3 (13%) during both seasons. The contributions of other O_x loss pathways were less than 5%.

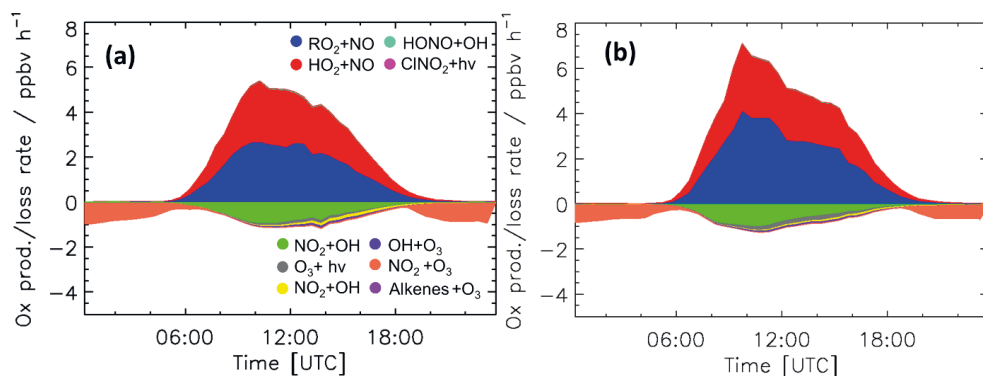


Figure 5. 4: Median diel profiles of turnover rates of reactions contributing to the O_x production and destruction for (a) the spring period and (b) the summer period of the JULIAC campaign.

During the day, the difference between the sum of turnover rates of the O_x production and destruction reactions, if either only the reaction of peroxy radicals with NO and the reaction of OH with NO_2 (Eq. 5.1) or additional reactions (Eq. 5.2) are considered, is less than 1 %. The additional reactions contributed only up to 0.5 ppbv h^{-1} to the net production rate. During the night, O_x destruction due to the reaction of NO_2 with O_3 that is only included in the extended calculation (Eq. 5.2) was significant with a rate up to 1 ppbv h^{-1} .

5.4 Discussion of the net odd oxygen production for measurements in the JULIAC campaign

5.4.1 Comparison of results from the different methods for determining the net O_X production rate

Figure 5.5 shows the comparisons between the O_X production rates calculated from NO_2 and O_3 measurements and from turnover rates of production and destruction reactions considering either few reactions (Eq. 5.1) or extended chemistry (Eq. 5.2) during 5 days in the spring and summer periods of JULIAC campaign. Results are representative for the entire campaign. The full timeseries are shown in Figure A7 in the Appendix.

Net O_X production rates calculated by using the base or extend chemistry agree well with calculations using NO_2 and O_3 measurements within their uncertainties. Small discrepancies are observed in the mornings on 20 and 23 April and in the afternoons of all days from 19 to 23 April, when the ozone production rate calculated from NO_2 and O_3 measurements is higher than rates from chemistry-based calculations. However, considering the uncertainties of the methods, the discrepancies are not significant. O_X losses at night are driven by the reaction of NO_2 with O_3 (Reaction R5.11) in the extended chemistry-based calculation, but calculations using NO_2 and O_3 measurements do not result in negative values during the spring campaign. Only in some nights (on 23, 25 and 26 August) during the summer campaign, the net O_X production rate calculated from NO_2 and O_3 measurements reflects the expected loss. The nighttime O_X loss is further discussed in Section 5.4.2.

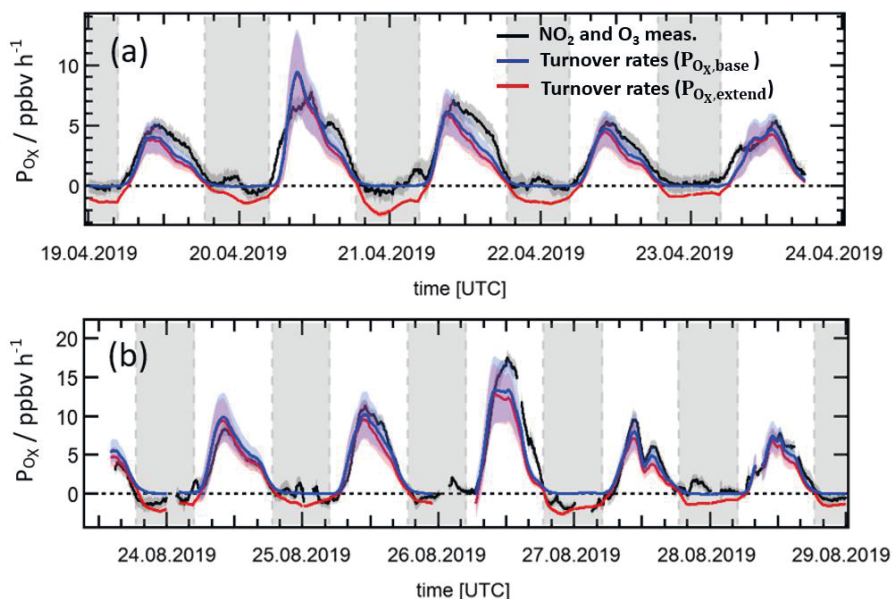


Figure 5.5: Time series of the net O_X production rate calculated from either NO_2 and O_3 measurements or turnover rates of reactions (base and extended chemistry, Eq. 5.1, Eq. 5.2) (a) from 19 April to 24 April and (b) from 23 August to 29 August. Coloured areas indicate the uncertainties of the O_X production rates. Grey areas indicate nighttime. All data points are 30 min averages. Periods shown here are representative for the entire spring and summer periods of the JULIAC campaign.

Diel median profiles and correlation scatter plots of O_X production rates calculated using either NO_2 and O_3 measurements or turnover rates of reactions during the spring and summer periods are shown in Figure 5.6. Results of all methods well agree with a tendency that calculations using turnover rates of reactions give slightly higher values around noon and slightly lower values in the afternoon compared to calculations using NO_2 and O_3 measurements.

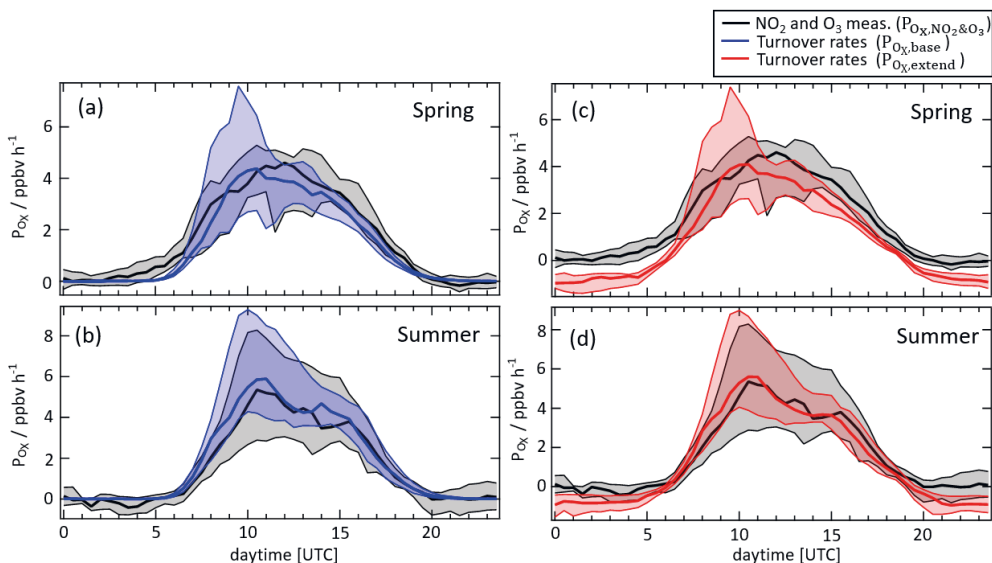


Figure 5. 6: Median diel profiles of the net O_x production rates calculated from either NO_2 and O_3 measurements or turnover rates of reactions using (a and b) the base chemistry (Eq. 5.1) or (c and d) the extended chemistry (Eq. 5.2) during the spring (a and c) and summer (b and d) periods of the JULIAC campaign. Coloured areas indicate the 25th and 75th percentiles of the O_x production rates.

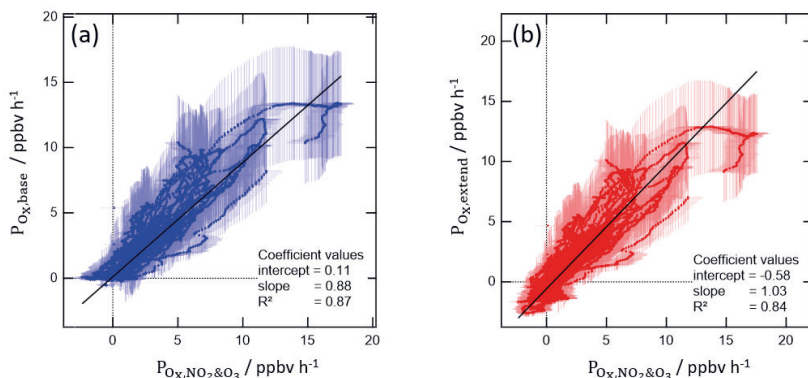


Figure 5. 7: Correlations between the net O_x production rates calculated from either NO_2 and O_3 measurements or turnover rates of reactions using the base chemistry ((a), Eq. 5.1) or the extended chemistry ((b), Eq. 5.2) during the spring and summer periods of the JULIAC campaign. Vertical and horizontal bars denote the errors of the measured data points. Data points in the correlation plots are 1 min average values.

The correlations (Fig. 5.7) between the results of the different methods to calculate the net O_x production rates are excellent with R^2 values of 0.87 and 0.84, respectively. The linear regression

analysis results in a slope of 0.88 indicating that O_X production rates calculated from NO_2 and O_3 measurements are 12% higher than calculations using turnover rates of few reactions (base case chemistry). The linear regression gives a small positive intercept of 0.11 ppbv h^{-1} that is smaller than the accuracy of the calculations.

If the extended chemistry is used to calculate the net O_X production rate, the correlation of these values and the net O_X production rates calculated using NO_2 and O_3 measurements further improves compared to the base chemistry. The slope of the regression line is close to unity (1.03). The negative intercept of $-0.58 \text{ ppbv h}^{-1}$ is mainly caused by the small differences in the results of both methods at night. Calculations of turnover rates using the extended chemistry give on average a net O_X destruction of 0.58 ppbv h^{-1} lower than calculations using NO_2 and O_3 measurements. If nighttime data is excluded from the regression, the slope (0.89) is similar to the slope achieved in the regression with the calculations using a small number of reactions. This again emphasizes that the daytime tropospheric ozone production is mostly explained by peroxy radical reactions with NO_X (Reaction R5.3, R5.4 and R5.7), while the investigation of the nighttime O_X loss needs a more detailed analysis (Section 5.4.2). The good agreement between calculations using turnover rates of reactions or NO_2 and O_3 measurements also highlights the reliability of measured HO_2 and RO_2 radical concentrations by the LIF instrument.

5.4.2 Potential impact of additional O_X production or destruction reactions on the net O_X production rate

Although the overall agreement between the different methods to calculate the net O_X production rates is excellent during the spring and summer periods of the JULIAC campaign, there are specific times, when the calculated O_X production rates based on the turnover rates of reactions give higher values of up to 3 ppbv h^{-1} than then calculations based on NO_2 and O_3 measurements. This is the case in the early morning on several days (Fig. 5.5 and Fig. 5.6). An additional O_X destruction reaction would be needed to reconcile this discrepancy.

Although O_X destruction by the reaction of O_3 with alkenes was included in the calculations using the extended chemistry (Eq. 5.2), the number of the measured alkene species was limited to hexene, pentene, isoprene and monoterpene species during the JULIAC campaign. Therefore, unmeasured alkenes could have additionally contributed to the ozone destruction. As described in the RO_X radical budget analysis (Section 4.4.1), 1.5 ppbv of propene and 1.0 ppbv of cis-but-2-ene could account for the observed OH reactivity (on average, 2.5 s^{-1}) that is not explained by measured OH reactant concentrations. As a sensitivity test, additional O_X loss due the ozonolysis of these alkene species is included in the calculations of the net O_X production rate (Fig. 5.8). This increases the O_X loss rate from the ozonolysis of alkenes from 0.02 ppbv h^{-1} to 0.4 ppbv h^{-1} , reducing the observed differences in the morning, for example, from 3 ppbv h^{-1} to 2.5 ppbv h^{-1} on 29 April, but worsening the agreement between the methods in the afternoon. Although this change is an upper limit, because it is unlikely that all unmeasured OH reactants were alkene species, the sensitivity test cannot explain the observed discrepancy on 29 April.

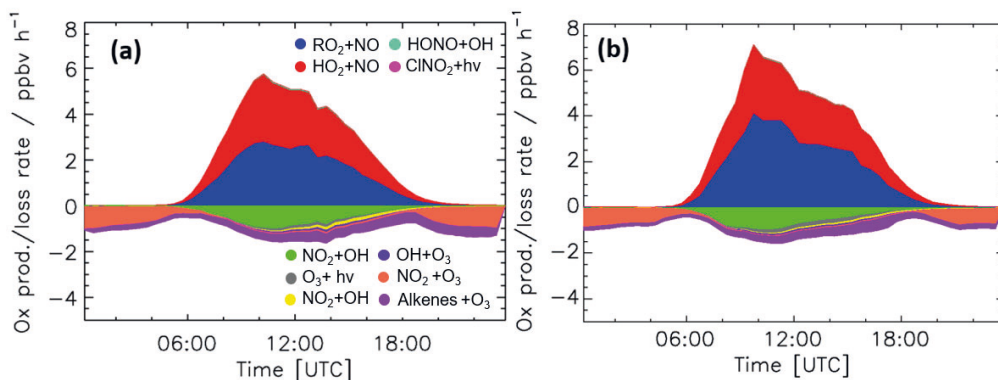


Figure 5. 8: Median diel profiles of turnover rates of reactions contributing to the O_X production and destruction for (a) the spring period and (b) the summer period of the JULIAC campaign like in Figure 5.4. Here, the O_X loss due to the ozonolysis of alkenes is calculated using an upper limit of their concentration by attributing OH reactivity that is not explained by measured OH reactants to alkene species.

The impact of the chlorine radical (Cl) release from the photolysis of $ClNO_2$ on the O_X production was not considered in Eq. 5.2 (Section 5.2). However, if a significant fraction of Cl reacted with O_3 and NO_2 , an additional O_X destruction would be observed. To investigate the potential impact of chlorine chemistry on the net O_X production rate, the Cl reactivity due to the reaction with O_3 , NO_X , CO and VOCs is first calculated using reaction rate coefficients in Table 5.2. Results are shown in Figure 5.9 for the period when measurements of both instruments detecting organic compounds (GC-FID and VOCUS) were available (5 to 8 August). The loss of chlorine atoms was dominated by the reactions with O_3 (47 %), alkane species (27%, mainly CH_4) and biogenic organic compounds (16 %, mainly isoprene).

The reaction of Cl with O_3 (Reaction R5.18) would lead to an additional O_X destruction,



but O_X is regenerated in the decomposition process of ClO in the presence of NO (Reaction R5.19):



Therefore, Cl from the photolysis of $ClNO_2$, which reacts with ozone, does not effectively destroy O_X molecules.

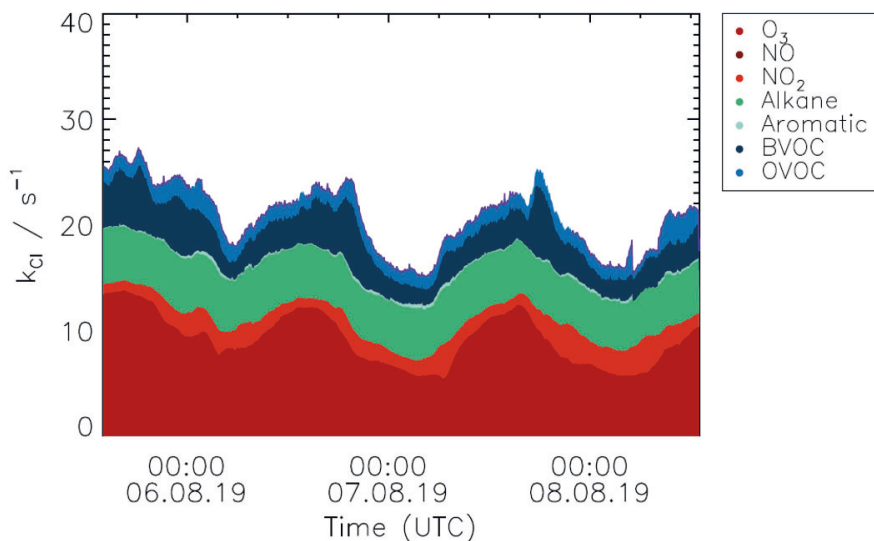


Figure 5. 9: Chlorine radical reactivity calculated from measured reactant concentrations for the period from 5 August to 8 August of the JULIAC campaign.

Cl atoms also potentially reacted with unmeasured VOCs, which would be part of the OH reactivity that was not explained by measured OH reactants. Considering that the reaction rate constants of reaction of saturated VOCs with Cl atoms are a few orders of magnitude higher compared to the reactions with OH (Young et al., 2014), unmeasured VOCs may have had a large contribution to the total Cl reactivity (approximately 25 to 250 s^{-1}). It is worth noting that the O_x production from the reaction of peroxy radicals with NO (Reaction R5.3 and R5.4) is included in the calculations regardless, if RO_2 is produced from OH or Cl reactions with organic compounds. Therefore, it can be assumed that most of the Cl atoms released from the photolysis of $ClNO_2$ were consumed by VOCs and therefore the contribution of the reaction of Cl atoms with O_3 and NO_2 would be negligible.

During nighttime, a significant discrepancy of approximately 1 ppbv h^{-1} between the methods for calculating the net O_x production rates is observed in the median diel profiles (Section 5.3). Calculations using O_3 and NO_2 measurements do not reflect net ozone destruction as expected from the consumption of O_3 and NO_2 in the production of nitrate radicals. This discrepancy could be explained, if the nitrate radical regenerated O_3 or NO_2 instead of acting as a permanent O_x loss. O_x could be regenerated from the reaction of NO_3 with nitrated- RO_2 radicals by yielding an alkoxy radical, RO, and NO_2 . If VOC species forming nitrated- RO_2 radicals from the reaction with NO_3 are short alkenes (e.g., cis-2-butene and 2,3-dimethyl-2-butene) or isoprene, the formed nitrated-RO may lead to an additional NO_2 molecule by decomposition of the nitrated-RO (Novelli et al., 2021; Vereecken et al., 2021). However, these species would need to be the dominant VOCs in the JULIAC campaign to significantly impact the net odd oxygen production rate. In order to explain why there is no O_x destruction observed from calculations using O_3 and NO_2 measurements, essentially every NO_3 radical would need to regenerate NO_2 from the reaction of nitrated- RO_2 radical with NO_3 . This is

unlikely the case due to the competition with other reaction pathways in the night (RO_2+RO_2 and RO_2+HO_2 recombination reactions; oxygen addition to the alkoxy radical instead of decomposition). It is worth noting that this mechanism would not be important during daytime, because the calculated NO_3 loss is dominated by its photolysis and the reaction with NO .

Table 5. 2: Rate constants of the reaction of organic compounds with chlorine used for the calculation of the Cl reactivity. Rate constants are listed for standard conditions (25 °C, 1atm). For the calculation of the O_X production rate, the actual measured air temperature is used.

Compound	Measurement technique	k (25 °C, 1atm) / $\text{cm}^3 \text{s}^{-1}$	Reference	
Alkanes	Methane	CRDS ^a	1.0×10^{-13}	JPL 2020
	i-Pentane	GC-FID ^b	1.93×10^{-13}	Anderson et al. (2007)
	Hexane	GC-FID ^b	3.2×10^{-10}	Anderson et al. (2007)
	Nonane	GC-FID ^b	4.28×10^{-10}	Aschmann and Atkinson (1995)
	Decane	GC-FID ^b	4.87×10^{-10}	Aschmann and Atkinson (1995)
Aromatics	Benzene	GC-FID ^b	1.3×10^{-15}	Shi and Bernhard (1997)
	Ethylbenzene	GC-FID ^b	1.0×10^{-10}	Shi and Bernhard (1997)
	Toluene	GC-FID ^b	6.2×10^{-11}	Wang et al. (2005)
	Xylene	GC-FID ^b	1.5×10^{-10}	Shi and Bernhard (1997)
BVOCs	Isoprene	VOCUS ^c	4.3×10^{-10}	Orlando et al. (2003)
	Monoterpene	VOCUS ^c	5.3×10^{-10}	Finlayson-Pitts et al. (1999)
	MVK	VOCUS ^c	2.2×10^{-10}	Orlando et al. (2003)
OVOCs	Acetaldehyde	VOCUS ^c	8.0×10^{-11}	IUPAC
	Acetone	VOCUS ^c	2.1×10^{-11}	IUPAC
	Benzaldehyde	VOCUS ^c	9.6×10^{-11}	(Noziere et al., 1994)
	Butanone	VOCUS ^c	4.0×10^{-11}	IUPAC
	Ethanol	VOCUS ^c	1.0×10^{-10}	IUPAC
	Propanal	VOCUS ^c	1.3×10^{-10}	IUPAC
	Propanol	VOCUS ^c	8.6×10^{-11}	IUPAC
Inorganics	O_3	UV photometry	1.2×10^{-11}	JPL 2020
	NO_2	CLD ^d	2.0×10^{-11}	JPL 2020
	NO	CLD ^d	1.9×10^{-12}	JPL 2020

^a Cavity ring-down spectroscopy

^b Gas chromatography – flame ionization detection

^c VOCUS proton-transfer-reaction time-of-flight mass spectrometer

^d Chemiluminescence detector

5.4.3 Potential simplification of the calculation of the net O_X production rate by using peroxy radical production rates determined from the measured OH reactivity

The calculation of the net ozone production rate based on turnover rates of reactions (Eq. 5.1, 5.2) discussed so far takes advantage of the measurement of peroxy radical concentrations. If they were not available, but OH reactivity and OH concentrations were measured, the production rate of peroxy radicals can be calculated. Assuming that peroxy radicals exclusively react with NO, so that ozone is subsequently formed, the peroxy radical production rate can be used to approximate the ozone production rate. In the following, it is discussed, how this simplification compares to the calculations using detailed chemistry.

In this approach, the reactions of peroxy radicals with NO in Eq. 5.1 is replaced by the RO₂ production rate obtained from the product of the OH reactivity from organic compounds (k_{VOC} , Section 4.2.3) and the OH concentration. The number of ozone molecules produced from each reaction of OH is 2 because of the subsequent reactions of the organic peroxy radical and of the hydroperoxyl radical with NO (Reaction 5.3, 5.4):

$$P_{\text{O}_X, k_{\text{VOC}}} = 2k_{\text{VOC}}[\text{OH}] - k_{\text{R5.7}}[\text{NO}_2][\text{OH}] \quad (\text{Eq 5.4})$$

The comparison between the calculated O_X production rates using the VOC reactivity and the O_X production rate calculated from O₃ and NO₂ measurements during the spring and summer periods is shown in Figure 5.10 and 5.11. For both periods, spring and summer, calculations using VOC reactivity are 20 – 60 % higher compared to the calculations using O₃ and NO₂ measurements. A linear regression analysis of results from both methods demonstrates a high correlation with an R² values of 0.87. As expected from the comparison of the time series, the slope of the linear fit is 1.41.

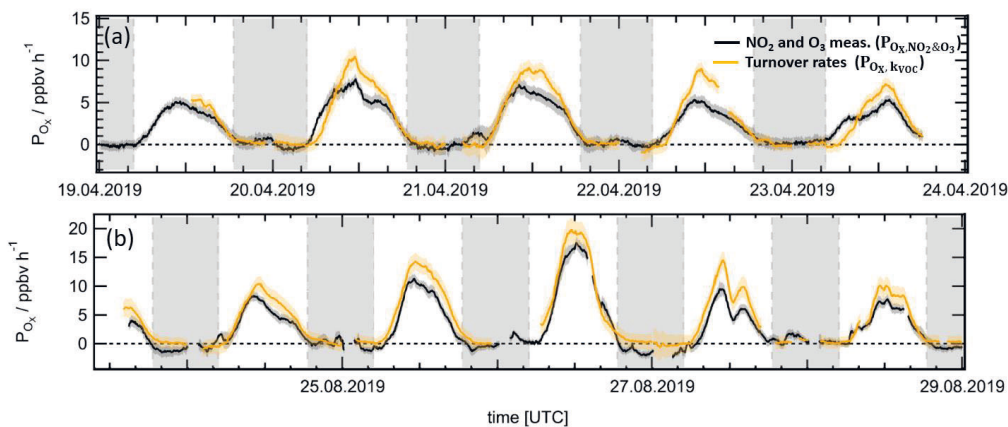


Figure 5. 10: Time series of O_X production rates either calculated from NO₂ and O₃ measurements ($P_{\text{O}_X, \text{NO}_2 \& \text{O}_3}$) or from turnover rates of reactions using peroxy radical production rates calculated from OH reactivity measurements ($P_{\text{O}_X, k_{\text{VOC}}}$) for the period (a) from 19 April to 24 April and (b) from 23 August to 29 August of the JULIAC campaign.

Coloured areas indicate the uncertainties of the O_x production rates. Grey areas indicate nighttime. All data points are 30 min averages.

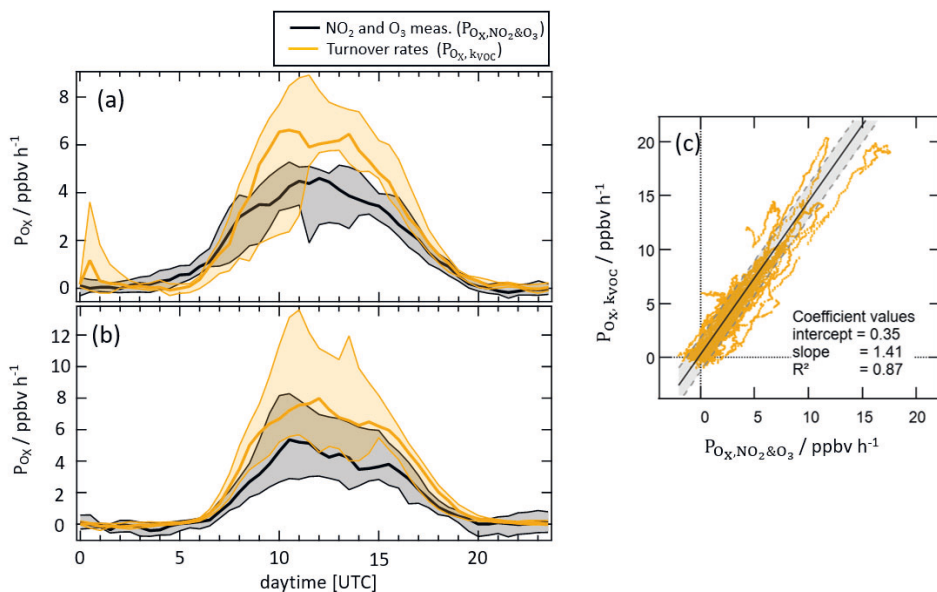


Figure 5. 11: Median diel profiles of the net O_x production rate calculated from either NO_2 and O_3 measurements or turnover rates of reactions using peroxy radical production rates calculated from OH reactivity measurements for the spring (a) and summer (b) periods of the JULIAC campaign. Coloured areas indicate the 25th and 27th percentiles of the O_x production rates. Correlations (c) between results from the different methods are in addition shown. The black line is the result of a weighted linear fit. The grey area is the prediction band, where 95% of experimental values are expected. Data points in the correlation plots are 1 min average values.

The higher values of the O_x production rate using the VOC reactivity compared to the calculations using O_3 and NO_2 measurements can be expected, because an ozone yield of 2 is assumed for each OH reaction with an organic compound. This method therefore neglects reactions that compete with the reaction of peroxy radicals with NO such as peroxy radical recombination reactions, organic nitrate formation and unaccounted peroxy radical sinks which do not produce O_x .

In the analysis of the chemical radical budget for conditions of low NO mixing ratios (Chapter 4), results from the Case #1 indicates that a small missing RO_2 sink with a rate of up to 1.5 ppbv h^{-1} is required to balance the RO_2 production and destruction rates. In Case #2, an additional HO_2 sink with a rate of up to 2.5 ppbv h^{-1} is required to explain the imbalance in chemical HO_2 radical budget. These radical destruction processes which do not produce O_x are neglected in the O_x production calculation using OH reactivity and could contribute to the higher values for the O_x production rate than obtained in the other calculations.

Another reason for differences in the O_x production rate values could be that reactions that produce peroxy radicals primarily, for example, HO_2 productions from HCHO, ozonolysis of OVOCs and unaccounted other primary radical sources are neglected. In the analysis of the chemical radical budget (Chapter 4), a missing primary RO_x radical sources with a rate of 3 ppbv h^{-1} and 1.4 ppbv h^{-1} are observed in the Case #1 and Case #3 periods, respectively. Neglecting these reactions leads to an underestimation of the O_x production rate calculations using OH reactivity. In general, unaccounted O_x production and destruction processes can partly compensate each other, but they increase the uncertainty of the calculations.

Previous studies calculated the net ozone production efficiency by using the calculated VOC reactivity from the product of the sum of the observed VOCs with their rate coefficient with the OH radical (Kleinman et al., 2002; Murphy et al., 2007; Farmer et al., 2011; Fitzky et al., 2019; Romer Present et al., 2020; Zavala et al., 2020). In these studies, the VOC reactivity was used as a proxy for the reaction of peroxy radicals with NO by assuming that the peroxy radical chain propagation by NO dominates the ozone production and that other loss processes for peroxy radicals were negligible, similar as Eq 5.4. In addition, Yang et al. (2017) showed the role of the unmeasured VOCs on the ozone production by comparing ozone production efficiencies calculated from the sum of the measured VOCs and the ozone production from the VOC reactivity obtained by subtracting the inorganic reactivity from the measured total OH reactivity. In two different locations (Beijing and Heshan) in China, the ozone production efficiencies constrained by the measured OH reactivity were significantly higher, on average 21 % and 30 %, respectively (Yang et al., 2017). Therefore, deriving the VOC reactivity from the OH reactivity measurement can help to approximate the ozone production, but peroxy radical measurements are necessary for an accurate calculation.

5.4.4 NO dependency of the net O_x production rates

Figure 5.12 shows the median O_x production rates calculated from either NO_2 and O_3 measurements or from turnover rates of reactions using the different sets of reactions depending on the NO mixing ratios observed in spring and summer. As discussed in the previous sections (Section 5.4.1, 5.4.3), all calculations well agree within their uncertainties over the range of NO except for the calculation using the VOC reactivity. The O_x production rates derived from the various methods show an increasing trend to values of 4 ppbv h^{-1} with increasing NO mixing ratios up to NO mixing ratios of 0.3 ppbv . For NO mixing ratio higher than 0.3 ppbv in summer, the O_x production rates remain at similar values. In summer, the O_x production rates show a slight decreasing trend as NO increase, but the range of NO mixing ratios are limited in relatively low less than 4 ppbv .

Other previous field studies have also calculated the O_x production rate based on the turnover rates of reaction of NO with peroxy radicals similar to Equation 5.1 and 5.2 (Ren et al., 2013; Brune et al., 2016; Tan et al., 2017; Whalley et al., 2018; Whalley et al., 2021) from the observed and modelled peroxy radical concentrations (Section 1.5). The calculations using the observed peroxy radical often showed an increasing O_x production with increasing NO mixing ratios similar to the results in the JULIAC campaign. In contrast, calculations using modelled peroxy radical

concentrations were often much lower in environments with high NO mixing ratios (>2ppbv), because peroxy radical concentrations were underestimated by model calculations.

The agreement of the O_X production rate calculations from NO_2 and O_3 measurements and the turnover rates of radical reactions during the JULIAC strongly supports that the reaction of peroxy radicals with NO is the main contributor to the net O_X formation. Therefore, in order to predict surface O_3 concentrations and in order to establish an efficient ozone control policy, it is essential to achieve accurate predictions of peroxy radical concentrations by model calculations.

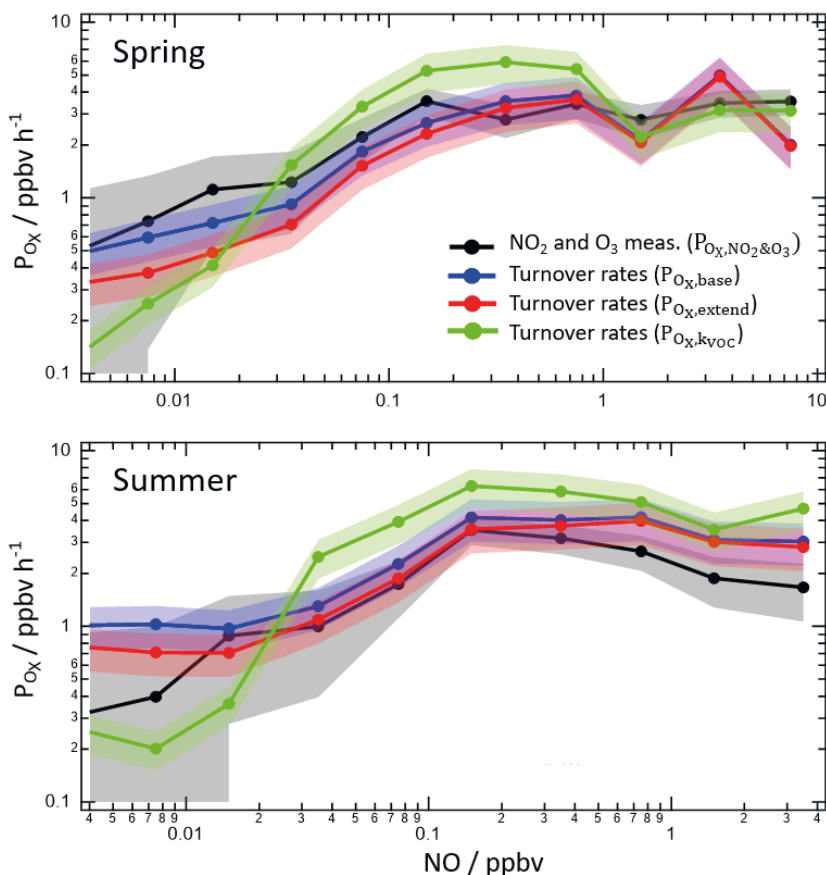


Figure 5. 12: NO dependence of median O_X production rates derived from the different methods during the spring and summer periods of the JULIAC campaign. Coloured areas represent the uncertainties.

Chapter 6. Summary and conclusions

The goal of this work was to investigate the chemistry of atmospheric hydroxyl (OH) and peroxy (HO_2 and RO_2) radicals and their role in tropospheric ozone (O_3) formation during the Jülich Atmospheric Chemistry project (JULIAC) campaign. Ambient measurements of atmospheric radicals, trace gases, and aerosol properties were performed during JULIAC using the atmospheric simulation chamber SAPHIR at Forschungszentrum Jülich, Germany. Ambient air was continuously flowed at a high rate through the chamber sampling from a 50m high inlet line for one month in each season throughout 2019. Tests with unreactive trace gases such as methane and carbon monoxide demonstrate that the JULIAC-SAPHIR flow system is well characterized, and trace gases are well mixed. Their concentrations in the chamber can be calculated from their concentrations in the air flowing into the chamber and the residence time of air in the chamber.

OH, HO_2 and RO_2 radical concentrations were measured as part of this work in the campaign. A chemical modulation reactor (CMR) was implemented and characterized for the measurement of interference-free OH radical concentrations in this work. Results were published in the journal *Atmos. Meas. Techn.* (Cho et al., 2021).

In order to optimize the operational parameters of the CMR system, several laboratory tests were conducted by using an OH calibration source to provide a continuous and stable OH radicals concentration. The flow rate in the reactor was found to be optimum at 21.1 slpm to minimize OH losses on the walls of the CMR. This resulted in an OH transmission of 64 %. In addition, it was found that a concentration of 19 ppmv of propane that was injected together with a carrier gas of 500 sccm N_2 provided an efficient mixing of the scavenger in the CMR flow tube. A scavenging efficiency of about 96% was achieved without any significant removal of radicals in the low-pressure detection cell (less than 3 %).

Characterization experiments performed in the SAPHIR chamber with humidified synthetic air showed a very good agreement within 10% between the OH concentrations from the FZJ-LIF-CMR and the Differential Optical Absorption Spectroscopy (DOAS) instruments demonstrating that the CMR system accurately accounts for potential interferences. Interferences from laser photolysis of ozone in humid air and from NO_3 reactions in the detection cell known from previous studies with the FZJ-LIF instrument were investigated. The photolytic ozone-water interference was found to be equivalent to an OH concentration of $3.4 \times 10^5 \text{ cm}^{-3}$ for 50 ppbv O_3 and 1% water vapor mixing ratio. These values are within the range of values previously determined in laboratory characterization experiments (Holland et al., 1998; Holland et al., 2003). The observed interference in the presence of ambient levels of NO_3 was negligible in the experiments in this work similar to finding in previous investigations (Fuchs et al., 2016).

The FZJ-CMR-LIF instruments was deployed in four campaigns in different seasons while ambient air was flowed through the SAPHIR chamber (JULIAC campaign). The comparison of OH measurements by the FZJ- LIF-CMR and DOAS instruments in the summer period showed good agreement within the uncertainties of measurements. Values of the LIF instrument were on average

only 11 % higher than measurements by the DOAS instrument, which is in agreement with the humidified synthetic air experiment. The interferences measured in the summer had a median diurnal variation with a maximum value equivalent to an OH concentration of $0.9 \times 10^6 \text{ cm}^{-3}$ during daytime and a minimum value of $0.4 \times 10^6 \text{ cm}^{-3}$ at night. The highest interference equivalent to an OH concentration of $2 \times 10^6 \text{ cm}^{-3}$ occurred in a period with high temperature (up to $40 \text{ }^\circ\text{C}$) from 22 to 29 August, when also the ozone mixing ratio increased to 100 ppbv. Interference observed in the JULIAC campaign could be fully explained by the well-characterized ozone interference. No additional interferences were observed.

A simple kinetic model was developed in this work to estimate possible perturbations of the OH transmission and scavenging efficiency in the CMR caused by reactants in ambient air for different atmospheric chemical conditions. It was found that, for the air composition encountered in the JULIAC campaign, the impact on the evaluated OH concentration was small (2 %). However, in other environments, in particular those with high VOC reactivity and low NO_x concentrations, OH loss reactions with atmospheric constituents inside the CMR system could cause significant changes of the transmission and the scavenging efficiency. For example, for air containing OH reactants equivalent to an OH reactivity of more than 40 s^{-1} , ambient OH can be depleted in the CMR by more than a factor of 2 in the reaction with these compounds for residence times of air in the CMR system of 20 ms like in the system used in this work. This effect could be reduced, if a very high sampling flow rate was used.

For the future applications of the CMR system for OH measurements by the LIF instrument, such perturbations need to be considered for the specific chemical conditions of a field campaign, in order to evaluate if corrections need to be applied. This means, that although the chemical modulation method was developed to eliminate interferences in ambient OH measurements, its application requires careful considerations. In addition, the OH detection sensitivity, precision as well as the time resolution are worse compared to the system without the CMR. So far, for experiments in the SAPHIR chamber, OH radical measurements by the FZJ-LIF have exhibited good agreement with measurements by DOAS demonstrating interference-free measurements without the need of the chemical modulation method (Schlosser et al., 2007; Schlosser et al., 2009; Fuchs et al., 2012; Novelli et al., 2018; Rolletter et al., 2019; Novelli et al., 2020). However, it is not possible to exclude the presence of an unknown interference for all the possible environments. Therefore, the application of chemical modulation will remain an important tool for the detection of ambient OH by LIF instruments.

Ambient measurements of OH, HO_2 , and RO_2 radical concentrations as well as OH reactivity and concentrations of other trace gases were measured during the JULIAC campaign. The reliability of the radical measurements by the FZJ-CMR-LIF instrument was assessed by either simultaneous detection by independent instruments for the OH radical or by the comparison of the measured and calculated O_x production rates for HO_2 and RO_2 radicals. These comparisons give a high confidence in the radical concentrations measured in the JULIAC campaign.

In the spring and summer periods, median OH concentrations reached up to $7 \times 10^6 \text{ cm}^{-3}$ at noon. HO_2 and RO_2 showed their maximum concentrations with values of $3 \times 10^6 \text{ cm}^{-3}$ and $4 \times 10^6 \text{ cm}^{-3}$, respectively, in the afternoon. In the autumn and winter periods, different diurnal patterns were

observed with median OH and HO₂ concentrations that were significantly lower compared to the other seasons with values of $0.8 \times 10^6 \text{ cm}^{-3}$ and $2.2 \times 10^7 \text{ cm}^{-3}$, respectively. Maximum values occurred at noon. Daytime median RO₂ concentrations were close to the limit of the detection ($0.8 \times 10^7 \text{ cm}^{-3}$) with maximum values occurring at midnight in autumn and winter periods.

Overall, the concentrations of OH reactants were relatively low resulting in a median value of the OH reactivity of 6 s^{-1} in spring and summer. The highest reactivity of up to 33 s^{-1} was observed on 21 January, when a highly polluted plume containing 50 ppbv NO was sampled. In spring and summer, inorganic compounds (NO_x, CH₄, CO, and O₃) contributed on average 40 % to the total measured OH reactivity, while 20 % could be explained by measured organic compounds. A significant fraction (40 %, 2.5 s^{-1}) of the OH reactivity remained unexplained and is likely due to unmeasured VOCs. In winter and autumn, the contribution of VOCs and the unaccounted OH reactivity were 14 % and 23 %, respectively. These values are smaller than in the other seasons due to the increased contributions of inorganic compounds (63 %) to the total OH reactivity.

Chemical budget analyses of OH, HO₂, RO₂, and RO_x radicals were performed in this work for the campaigns in spring and summer. For most conditions, the high concentrations of radicals were sustained by the regeneration of OH via reactions of HO₂ and RO₂ radicals with nitric oxide (NO). In the budget of the sum of all radicals (RO_x), the photolysis of HONO and HCHO contributed most to the primary radical production. The reactions of OH with NO₂ and RO₂ with HO₂ dominated the radical termination processes. On average, daytime radical turnover rates in spring and summer ranged between 3 to 5 ppbv h⁻¹ and 5 to 6 ppbv h⁻¹, respectively, for OH, HO₂ and RO₂ while total rates of RO_x initiation and termination reactions were below 2.0 ppbv h⁻¹. The maximum OH radical turnover rate of 17 ppbv h⁻¹ was observed during a heat wave period in August, while the highest HO₂, RO₂ and RO_x turnover rates were 11.7, 13.5 and 4.8 ppbv h⁻¹, respectively, observed in the spring period when NO concentrations exceeded 9 ppbv.

For NO mixing ratios higher than 2 ppbv, OH production and destruction rates were balanced. In contrast, an additional HO₂ loss reaction and an additional RO₂ production pathway with rates of 6 ppbv h⁻¹ and 12 ppbv h⁻¹, respectively, were required to balance production and destruction rates. However, the discrepancies found in individual radical budgets had large uncertainties due to uncertainties of the background signal in the measured HO₂ and RO₂ concentrations for high NO and low RO₂ concentrations. For the same conditions a primary RO_x source with a rate of 3 ppbv h⁻¹ was needed to balance the RO_x destruction rate. Because only RO₂ budget is required an additional source, the missing primary RO_x source indicates that the part of missing RO₂ source likely attributed to missing primary RO₂ source. Unfortunately, in this period, the potential impact of chlorine chemistry could not be examined due to ClNO₂ measurement was not available. Therefore, more investigation of radical budget for the high NO environment with the consideration of Cl chemistry would be beneficial to identify the missing RO₂ source.

On the other hand, for NO mixing ratios below 2 ppbv, an accounted OH source with a rate of 3.5 ppbv h⁻¹ was commonly needed to balance the OH destruction rate in spring and summer. This OH source could be a combination of a missing primary radical source ($0.5 \sim 1.4 \text{ ppbv h}^{-1}$) and an unaccounted inter-radical conversion reaction of HO₂ to OH (rate of 2 ppbv h⁻¹) or RO₂ to OH (rate of 1.5 ppbv h⁻¹).

The potential impact of OH regeneration from RO₂ isomerization reactions from isoprene-RO₂, HO₂ loss due to uptake on aerosol and radical production from chlorine chemistry initiated by the photolysis of ClNO₂ was examined in this work. However, their impact on the radical budgets was negligible for conditions of the JULIAC campaign.

In order to see if the discrepancies in radical budgets can be explained by the changes of the assumptions made in the budget calculations, for example, the inclusion of unmeasured alkenes to the radical production from their ozonolysis reactions and uses of the lower and higher limits of the reaction rate constants for the reaction of RO₂ with NO, sensitivity tests were performed, but generally, they could not explain whole discrepancies. For chemical conditions, when the contribution from the HO₂ and NO reaction to the OH production reduces in importance, competing radical pathways such as isomerization reactions of RO₂ radicals, OH formation from ozonolysis of alkenes or photolysis of multifunctional organic compounds could gain in importance and need to be properly accounted for. These processes remain relatively poorly constrained and investigated and the lack of direct measurements (e.g., multifunctional VOC) limits our understanding.

The missing OH source at low NO mixing ratios observed in this work is consistent with findings in other field campaigns (Tan et al., 2017; Tan et al., 2019; Whalley et al., 2021). The high reliability of radical data in this study gives further confidence that the discrepancies arise from unaccounted chemical processes rather than from instrumental artefacts.

The photochemical net ozone production rate was determined for the measurements in the JULIAC campaign as one goal of this work. A direct measurement of the net O_x (sum of NO₂ and O₃) production rate in the SAPHIR chamber was obtained from the difference between NO₂ and O₃ concentrations measured in the chamber and in the air that is flowed into the chamber. Daytime net O_x production rates in the spring and summer periods were on average 3.2 and 4.1 ppbv h⁻¹, respectively. The highest O_x production rates were observed during a heat wave in August with rates of 17 ppbv h⁻¹.

The net O_x production rates calculated from NO₂ and O₃ measurements were compared to O_x production rates calculated from turnover rates of radical reactions contributing to the production or destruction of NO₂ and O₃ using the measured radical and trace gas concentrations. O_x production rates calculated using a limited set of reactions (base case) considered the atmospherically most important O_x production process from the reaction of peroxy radicals (RO₂ and HO₂) with NO and the major O_x destruction reaction by the reaction of OH radicals with NO₂. Calculations considering an extended set of reactions included other minor O_x production and destruction reactions such as the photolysis of ClNO₂ and O₃ and the reactions of O₃ with NO₂ and HO₂. During daytime, both calculations using the turnover rates of radical reactions agreed well with the net O_x production rates calculated from NO₂ and O₃ measurements. This demonstrates that the reactions of peroxy radicals with NO is the main contributor to the net O_x formation and the reaction of OH with NO₂ is the main O_x loss in a rural environment as expected.

During nighttime, the calculation based on the extended chemistry including O_x loss by the reaction of NO₂ and O₃ results in a negative net O_x production rate (up to 2 ppbv h⁻¹), whereas calculations using NO₂ and O₃ measurements were nearly zero except for some days during the summer period. Possible explanations for this discrepancy could be nighttime NO₂ production from

NO₃ oxidation processes of specific VOCs such as short alkenes (cis-2-butene and 2,3-dimethyl-2-butene) and isoprene.

Another approach to calculate the O_x production rate makes use of the VOC reactivity obtained from the measured OH reactivity after subtracting the contributions from CO, NO, NO₂, HCHO, and O₃. The production of peroxy radicals is calculated from the turnover rate of the reaction of VOCs with OH assuming that every peroxy radical leads to the production of 2 ozone molecules in the reaction with NO. However, this method neglects other peroxy radical production and termination processes. O_x production rates calculated by this approach are significantly higher (on average 41 %) than values from the other O_x production rate calculations applied in this work. This indicates that HO₂ and RO₂ radical termination processes need to be taken into account for an accurate calculation of the ozone production rate.

This investigation of the ozone formation for the comprehensive measurements in the JULIAC campaign including radical and NO₂ and O₃ measurements confirms the current chemical understanding of tropospheric ozone production from the reaction of peroxy radicals with NO. Therefore, results demonstrate that accurate predictions of radical concentrations in atmospheric models are crucial in order to accurately predict the formation of secondary pollutants such as ozone.

Chemical conditions in the JULIAC campaign were representative for conditions in a rural environment. Further investigations of the tropospheric ozone formation in more polluted environments with similar methods as applied in this work would be beneficial. This could be achieved by performing chamber experiments like in the JULIAC campaign, but adding additional reactants such as NO_x and VOCs to the chamber air to simulate polluted environments. Results can be used to develop ozone pollution control policies in urban areas.

Appendix

Table A 1: Specification of the FZJ-LIF-CMR instrument used in this study.

Symbol	Definition	Equation number	Value	Unit
S_{OH}	Ambient OH signal obtained from chemical modulation	Eq. 3.6 and 3.5	^a	Counts $mW^{-1} s^{-1}$
S_{OH}^*	Ambient OH signal obtained from chemical modulation when the influence of k_{OH} on the chemical modulation is neglected.	Eq. 3.33	^a	Counts $mW^{-1} s^{-1}$
S_i	Interference signal obtained from the chemical modulation	Eq. 3.6 and 3.9	^a	Counts $mW^{-1} s^{-1}$
S_i^*	Interference signal obtained from chemical modulation when the influence of k_{OH} on the chemical modulation is neglected.	Eq. 3.34	^a	Counts $mW^{-1} s^{-1}$
$S_{OH}^{N_2}$	OH fluorescence signal obtained from the N_2 mode	Eq. 3.6	^a	Counts $mW^{-1} s^{-1}$
S_{OH}^{SC}	OH fluorescence signal obtained from the scavenger mode	Eq. 3.7	^a	Counts $mW^{-1} s^{-1}$
$[OH]_{CHEM}$	OH concentration measured by chemical modulation	Eq. 3.10	^a	cm^{-3}
$[OH]_i$	OH interference measured by chemical modulation	Eq. 3.11	^a	cm^{-3}
$[OH]_a$	Steady state ambient OH concentration	Eq. 3.24	^a	cm^{-3}
$[OH]'$	Steady state OH concentration in the CMR	Eq. 3.25	^a	cm^{-3}
C_{OH}	OH detection sensitivity obtained from calibration	Eq. 3.1	^a	$cm^3 \text{ Counts}^{-1} s$

α	Residual factor representing the fraction of ambient OH that is not scavenged by propane in the reactor	Eq. 3.19	a	b
α^0	The residual factor when clean synthetic air is carrier gas for OH	Eq. 3.20	0.042	b
β	General function to calculate the OH transmission of a tube section of the CMR	Eq. 3.28	a	b
β_{tube}^0	OH transmission of the CMR tube without built-in injectors when clean synthetic air is carrier gas for OH	Eq. 3.13	0.81	b
β_{N_2}	OH transmission of the CMR for the N ₂ mode	Eq. 3.10	a	b
$\beta_{\text{N}_2}^0$	OH transmission of the CMR for the N ₂ mode when clean synthetic air is used as carrier gas for OH	Eq. 3.12	0.64	b
β^e	OH transmission in the entrance section	Eq. 3.12	a	b
$\beta^{e,0}$	OH transmission in the entrance section when clean synthetic air is carrier gas for OH	Eq. 3.14	0.92	b
$\beta_{\text{N}_2}^r$	OH transmission in the reaction section (N ₂ mode)	Eq. 3.12	a	b
$\beta_{\text{N}_2}^{r,0}$	OH transmission in the reaction section (N ₂ mode) when clean synthetic air is carrier gas for OH	Eq. 3.16	0.69	b
β_{SC}^r	OH transmission in the reaction reactor section (scavenger mode)	Eq. 3.32	a	b
$\beta_{\text{SC}}^{r,0}$	OH transmission in the reaction section (scavenger mode) when clean synthetic air is carrier gas for OH	Eq. 3.15	0.03	b
f	Fraction of the total CMR flow which does not contain scavenger	Eq. 3.21	0.04	b
k_w	OH wall loss rate coefficient in the CMR tube without built-in injectors	Eq. 3.13	11.8	s ⁻¹
k_w^e	OH wall loss rate coefficient in the entrance section of the CMR tube	Eq. 3.14	12.3	s ⁻¹
k_w^r	OH wall loss rate coefficient in the reactor section of the CMR tube	Eq. 3.16	33	s ⁻¹
k_{SC}	Scavenging rate coefficient of OH by propane in complete homogenous mixing case	Eq. 3.18	513	s ⁻¹

k_{SC}^{eff}	Effective scavenging rate coefficient of OH by propane obtained from scavenging efficiency tests		283	s^{-1}
k'_{SC}	Scavenging rate coefficient of OH by propane in the fraction containing no propane in case of inhomogeneous mixing		0	s^{-1}
k''_{SC}	Scavenging rate coefficient of OH by propane in the fraction containing propane in case of inhomogeneous mixing	Eq. 3.21	534	s^{-1}
Δt	The transit time through the CMR tube	Eq. 3.13	17.8	ms
Δt_r	The transit time through the reactor section	Eq. 3.17	11.2	ms
Δt_e	The transit time through the entrance section	Eq. 3.14	6.6	ms

^a Variable

^b Dimensionless

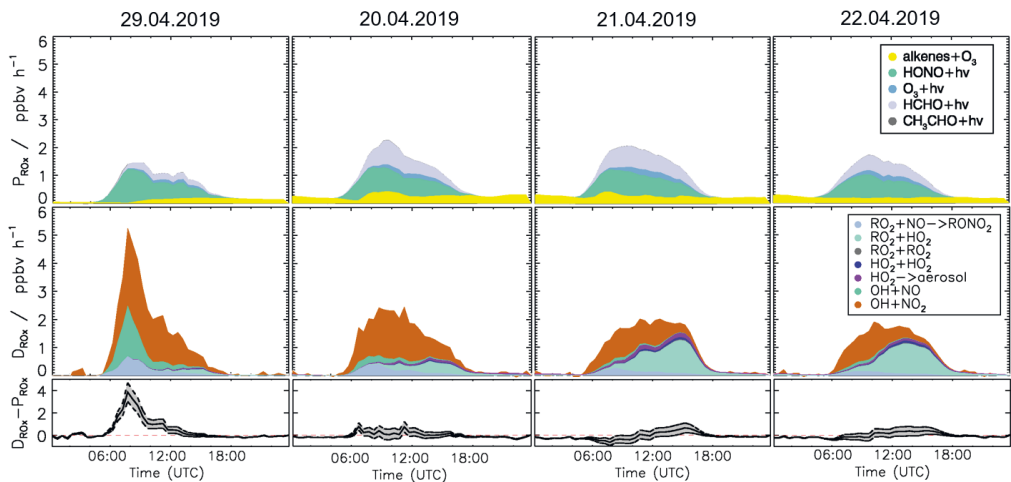


Figure A. 1: Chemical budgets for OH, HO₂, and RO₂ radicals similar to Figure 4.15 (Case #1 period), but using the high limits for the concentration of alkene species that contribute to radical production by ozonolysis reactions (Section 4.4.1).

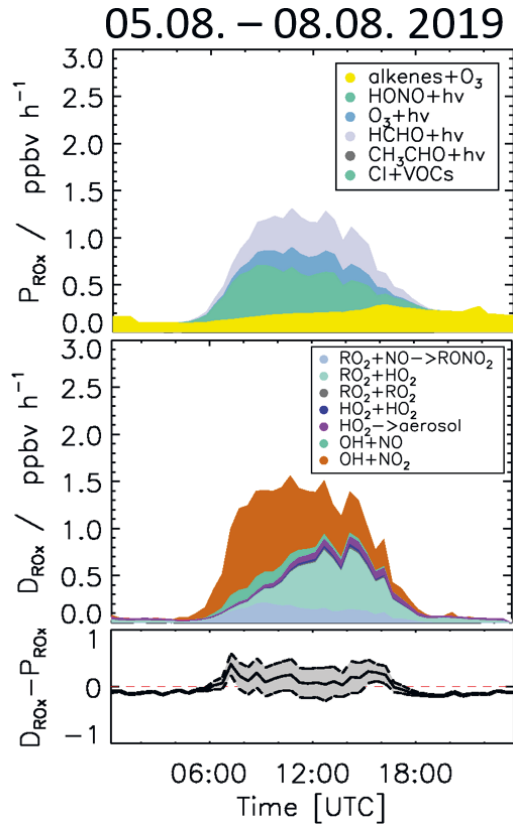


Figure A. 2: Chemical budget for the sum of OH, HO₂, and RO₂ radicals similar to Figure 4.17 (Case #2 period), but using the high limits of alkene concentrations contributing to radical production by ozonolysis reactions (Section 4.4.1).

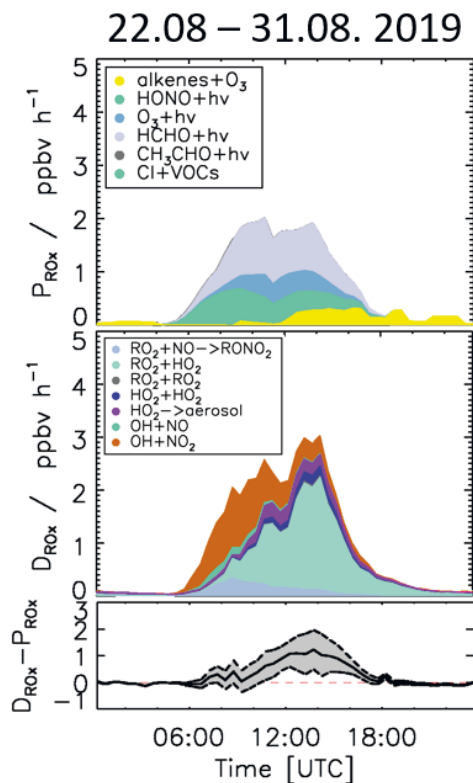


Figure A. 3: Chemical budget for the sum of OH, HO₂, and RO₂ radicals similar to Figure 4.19 (Case #3 period), but using the high limit of alkene concentrations contributing to radical production by ozonolysis reactions (Section 4.4.1).

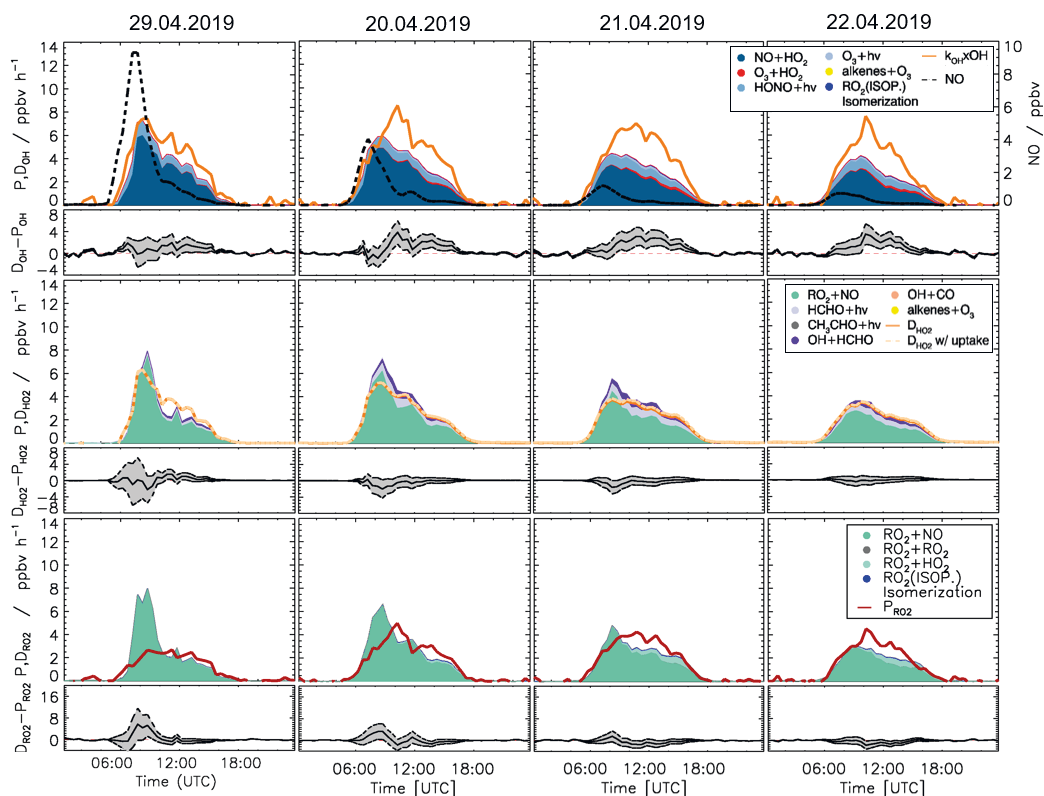


Figure A. 4: Chemical budgets for OH, HO₂, and RO₂ radicals similar to Figure 4.14, but RO₂ radical concentrations were calculated using the upper limit of the RO₂ background signal of the measurements (Table 3.2).

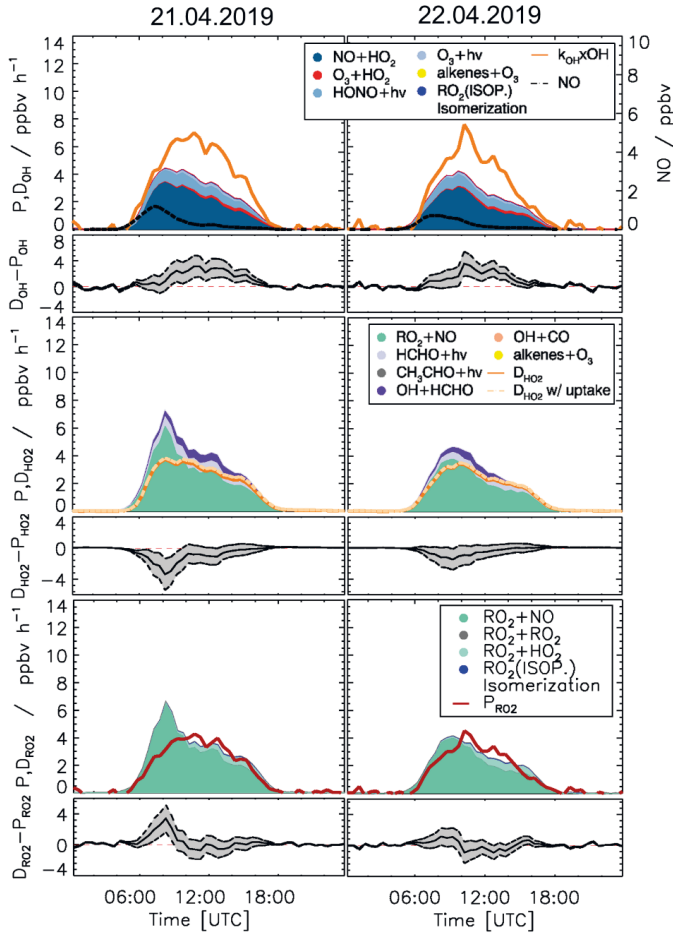


Figure A. 5: Chemical budgets for OH, HO₂, and RO₂ radicals similar to Figure 4.14 for 2 days in the spring period, when NO concentrations were low, but using the low limit of the reaction rate coefficient of the reaction of RO₂ with NO, $1.1 \times 10^{-12} \text{ cm}^3 \text{ s}^{-1}$ (at 298 K for c-C₅H₉O₂) to calculate the turnover rate of this reaction.

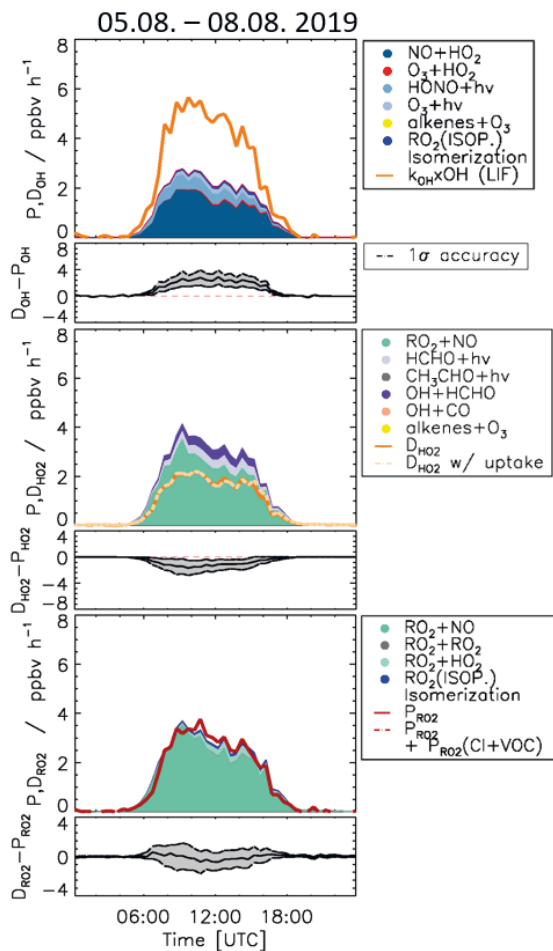


Figure A. 6: Chemical budgets for OH, HO₂, and RO₂ radicals similar to Figure 4.16 (Case #2 period), but using the low limit of the reaction rate coefficient of the reaction of RO₂ with NO, $7.7 \times 10^{-12} \text{ cm}^3 \text{ s}^{-1}$ (at 298 K for CH₃O₂) to calculate the turnover rate of this reaction.

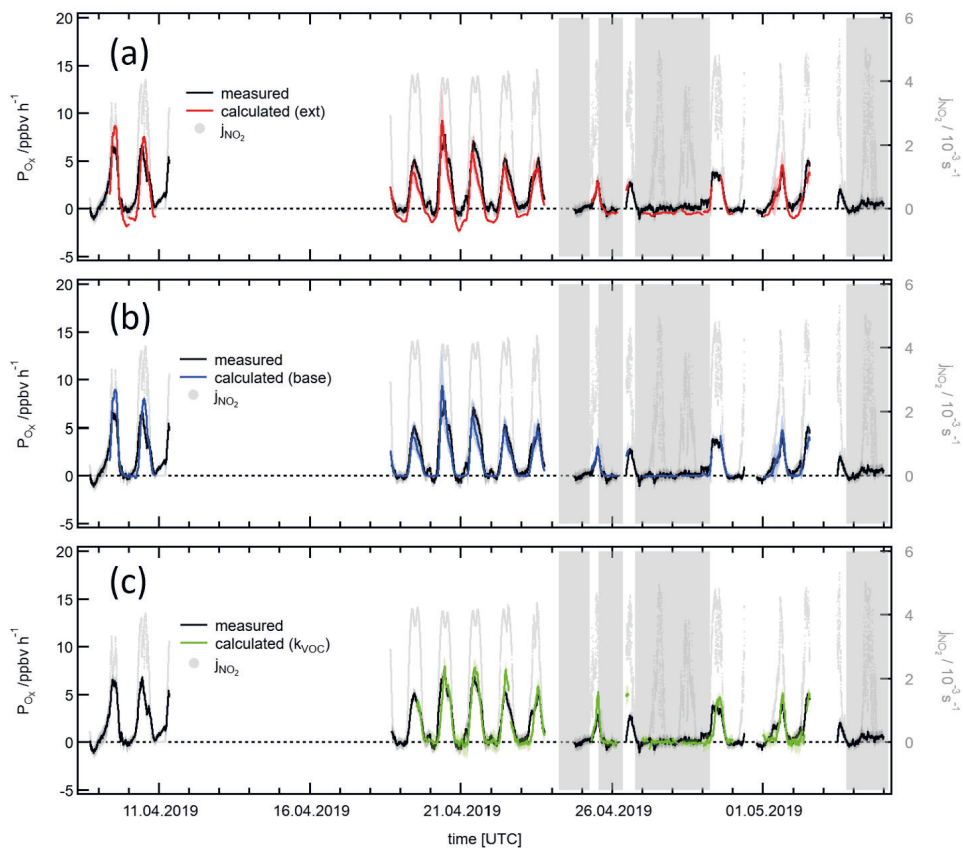


Figure A. 7: Timeseries of calculated O_X production rates using different methods. Calculations using measured O_3 and NO_2 concentrations in the chamber and in the air flowing into the chamber (“measured”) are compared to (a) calculations of turnover rates of reactions using only the major reactions ($\text{P}_{\text{O}_X,\text{base}}$), (b) calculations of turnover rates of reactions using an extended set of reactions ($\text{P}_{\text{O}_X,\text{extend}}$), and (c) calculations using OH reactivity from organic compounds to calculate the production rate of peroxy radicals ($\text{P}_{\text{O}_X,\text{kVOC}}$) in the spring (a-c) and summer (d-f) periods of the JULIAC campaign. Details of the different calculation methods are explained in Chapter 5. Grey areas indicate times when the chamber roof was closed. The intensity of solar radiation indicating photochemical activity is shown as ozone photolysis frequency outside the chamber.

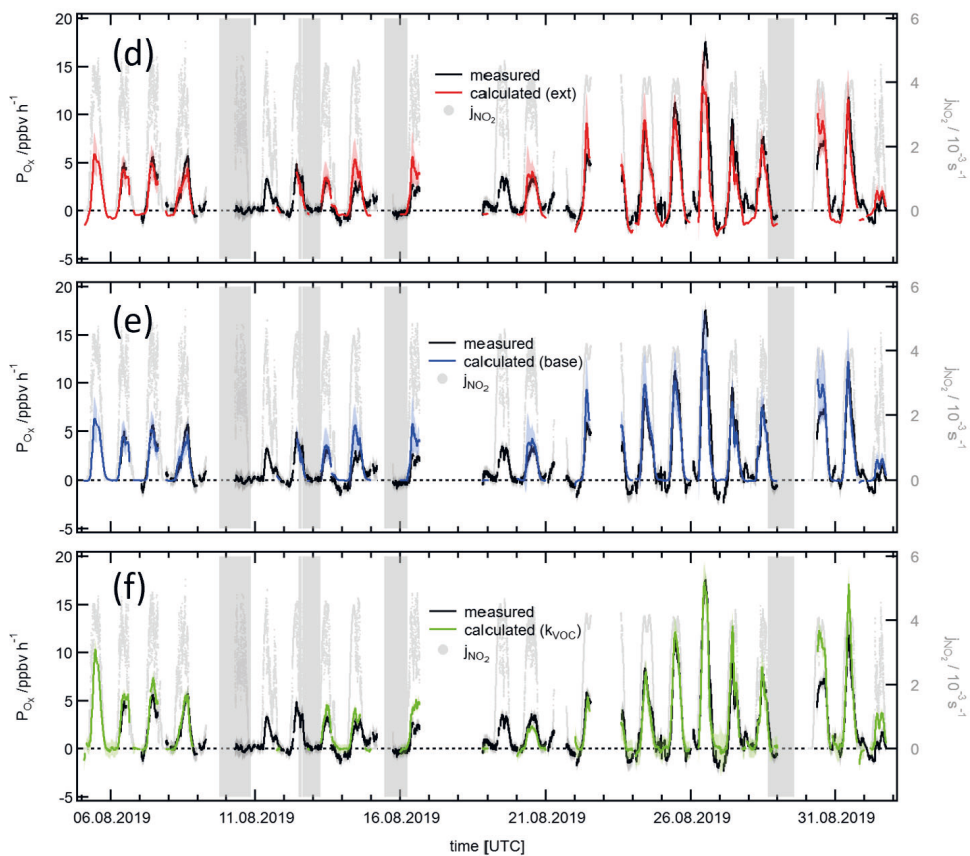


Figure A7: Continued.

Bibliography

- Ainsworth, E. A., Yendrek, C. R., Sitch, S., Collins, W. J., and Emberson, L. D.: The Effects of Tropospheric Ozone on Net Primary Productivity and Implications for Climate Change, *Annu. Rev. Plant Biol.*, 63, 637-661, doi:10.1146/annurev-arplant-042110-103829, 2012.
- Albrecht, S. R., Novelli, A., Hofzumahaus, A., Kang, S., Baker, Y., Mentel, T., Wahner, A., and Fuchs, H.: Measurements of hydroperoxy radicals (HO_2) at atmospheric concentrations using bromide chemical ionisation mass spectrometry, *Atmos. Meas. Tech.*, 12, 891-902, doi:10.5194/amt-12-891-2019, 2019.
- Alicke, B., Geyer, A., Hofzumahaus, A., Holland, F., Konrad, S., Pätz, H. W., Schäfer, J., Stutz, J., Volz-Thomas, A., and Platt, U.: OH formation by HONO photolysis during the BERLIOZ experiment, *J. Geophys. Res.: Atmos.*, 108, PHO 3-1-PHO 3-17, doi:10.1029/2001JD000579, 2003.
- Anderson, R. S., Huang, L., Iannone, R., and Rudolph, J.: Measurements of the $^{12}\text{C}/^{13}\text{C}$ Kinetic Isotope Effects in the Gas-Phase Reactions of Light Alkanes with Chlorine Atoms, *J. Phys. Chem. A*, 111, 495-504, doi:10.1021/jp064634p, 2007.
- Aschmann, S. M., and Atkinson, R.: Rate constants for the gas-phase reactions of alkanes with Cl atoms at 296 ± 2 K, *Int. J. Chem. Kinet.*, 27, 613-622, doi:10.1002/kin.550270611, 1995.
- Atkinson, R., Baulch, D. L., Cox, R. A., Crowley, J. N., Hampson, R. F., Hynes, R. G., Jenkin, M. E., Rossi, M. J., and Troe, J.: Evaluated kinetic and photochemical data for atmospheric chemistry: Volume I - gas phase reactions of O_x , HO_x , NO_x and SO_x species, *Atmos. Chem. Phys.*, 4, 1461-1738, doi:10.5194/acp-4-1461-2004, 2004.
- Atkinson, R., Baulch, D. L., Cox, R. A., Crowley, J. N., Hampson, R. F., Hynes, R. G., Jenkin, M. E., Rossi, M. J., Troe, J., and Subcommittee, I.: Evaluated kinetic and photochemical data for atmospheric chemistry: Volume II - gas phase reactions of organic species, *Atmos. Chem. Phys.*, 6, 3625-4055, doi:10.5194/acp-6-3625-2006, 2006.
- Baardsen, E. L., and Terhune, R. W.: Detection of OH in the atmosphere using a dye laser, *Appl. Phys. Lett.*, 21, 209-211, doi:10.1063/1.1654347, 1972.
- Baier, B. C., Brune, W. H., Lefer, B. L., Miller, D. O., and Martins, D. K.: Direct ozone production rate measurements and their use in assessing ozone source and receptor regions for Houston in 2013, *Atmos. Environ.*, 114, 83-91, doi:10.1016/j.atmosenv.2015.05.033, 2015.
- Bannan, T. J., Booth, A. M., Bacak, A., Muller, J. B. A., Leather, K. E., Le Breton, M., Jones, B., Young, D., Coe, H., Allan, J., Visser, S., Slowik, J. G., Furger, M., Prévôt, A. S. H., Lee, J., Dunmore, R. E., Hopkins, J. R., Hamilton, J. F., Lewis, A. C., Whalley, L. K., Sharp, T., Stone, D., Heard, D. E., Fleming, Z. L., Leigh, R., Shallcross, D. E., and Percival, C. J.: The first UK measurements of nitryl chloride using a chemical ionization mass spectrometer in central London in the summer of 2012, and an investigation of the role of Cl atom oxidation, *J. Geophys. Res.: Atmos.*, 120, 5638-5657, doi:10.1002/2014JD022629, 2015.
- Berndt, T.: Formation of carbonyls and hydroperoxyenals (HPALDs) from the OH radical reaction of isoprene for low- NO_x conditions: influence of temperature and water vapour content, *J. Atmos. Chem.*, 69, 253-272, doi:10.1007/s10874-012-9245-2, 2012.

- Berresheim, H., Elste, T., Plass-Dülmer, C., Eiseleb, F. L., and Tannerb, D. J.: Chemical ionization mass spectrometer for long-term measurements of atmospheric OH and H₂SO₄, *Int. J. Mass Spectrom.*, 202, 91-109, doi:10.1016/S1387-3806(00)00233-5, 2000.
- Bisbis, M. B., Gruda, N., and Blanke, M.: Potential impacts of climate change on vegetable production and product quality – A review, *J. Clean. Prod.*, 170, 1602-1620, doi:10.1016/j.jclepro.2017.09.224, 2018.
- BMEL: Ergebnisse der Waldzustandserhebung 2020
Bonn, Germany, 2021.
- Bohn, B., Rohrer, F., Brauers, T., and Wahner, A.: Actinometric measurements of NO₂ photolysis frequencies in the atmosphere simulation chamber SAPHIR, *Atmos. Chem. Phys.*, 5, 493-503, doi:10.5194/acp-5-493-2005, 2005.
- Bohn, B., and Zilken, H.: Model-aided radiometric determination of photolysis frequencies in a sunlit atmosphere simulation chamber, *Atmos. Chem. Phys.*, 5, 191-206, doi:10.5194/acp-5-191-2005, 2005.
- Broch, S.: Ein neues LIF-Instrument für flugzeug- und bodengebundene Messungen von OH- und HO₂-Radikalen in der Troposphäre, Ph.D. Thesis, Bergischen Universität Wuppertal, Forschungszentrum Jülich GmbH, 2011.
- Brune, W. H., Baier, B. C., Thomas, J., Ren, X., Cohen, R. C., Pusede, S. E., Browne, E. C., Goldstein, A. H., Gentner, D. R., Keutsch, F. N., Thornton, J. A., Harrold, S., Lopez-Hilfiker, F. D., and Wennberg, P. O.: Ozone production chemistry in the presence of urban plumes, *Faraday Discuss.*, 189, 169-189, doi:10.1039/C5FD00204D, 2016.
- Burkholder, J. B., Sander, S. P., Abbatt, J., Barker, J., Huie, R., Kolb, C. E., Kurylo, M., Orkin, V., Wilmouth, D. M., and Wine, P.: Chemical Kinetics and Photochemical Data for Use in Atmospheric Studies, Evaluation Number 18, 2015.
- Cantrell, C. A., Zimmer, A., and Tyndall, G. S.: Absorption cross sections for water vapor from 183 to 193 nm, *Geophys. Res. Lett.*, 24, 2195-2198, doi:10.1029/97GL02100, 1997.
- Cantrell, C. A., Edwards, G. D., Stephens, S., Mauldin, L., Kosciuch, E., Zondlo, M., and Eisele, F.: Peroxy radical observations using chemical ionization mass spectrometry during TOPSE, *J. Geophys. Res.: Atmos.*, 108, doi:10.1029/2002JD002715, 2003.
- Cazorla, M., and Brune, W. H.: Measurement of Ozone Production Sensor, *Atmos. Meas. Tech.*, 3, 545-555, doi:10.5194/amt-3-545-2010, 2010.
- Cazorla, M., Brune, W. H., Ren, X., and Lefer, B.: Direct measurement of ozone production rates in Houston in 2009 and comparison with two estimation methods, *Atmos. Chem. Phys.*, 12, 1203-1212, doi:10.5194/acp-12-1203-2012, 2012.
- Chen, D., Huey, L. G., Tanner, D. J., Li, J., Ng, N. L., and Wang, Y.: Derivation of Hydroperoxyl Radical Levels at an Urban Site via Measurement of Pernitric Acid by Iodide Chemical Ionization Mass Spectrometry, *Environ. Sci. Technol.*, 51, 3355-3363, doi:10.1021/acs.est.6b05169, 2017.

- Chen, S., Ren, X., Mao, J., Chen, Z., Brune, W. H., Lefer, B., Rappenglück, B., Flynn, J., Olson, J., and Crawford, J. H.: A comparison of chemical mechanisms based on TRAMP-2006 field data, *Atmos. Environ.*, 44, 4116-4125, doi:10.1016/j.atmosenv.2009.05.027, 2010.
- Cho, C., Hofzumahaus, A., Fuchs, H., Dorn, H. P., Glowania, M., Holland, F., Rohrer, F., Vardhan, V., Kiendler-Scharr, A., Wahner, A., and Novelli, A.: Characterization of a chemical modulation reactor (CMR) for the measurement of atmospheric concentrations of hydroxyl radicals with a laser-induced fluorescence instrument, *Atmos. Meas. Tech.*, 14, 1851-1877, doi:10.5194/amt-14-1851-2021, 2021.
- Cohen, A. J., Brauer, M., Burnett, R., Anderson, H. R., Frostad, J., Estep, K., Balakrishnan, K., Brunekreef, B., Dandona, L., Dandona, R., Feigin, V., Freedman, G., Hubbell, B., Jobling, A., Kan, H., Knibbs, L., Liu, Y., Martin, R., Morawska, L., Pope, C. A., Shin, H., Straif, K., Shaddick, G., Thomas, M., van Dingenen, R., van Donkelaar, A., Vos, T., Murray, C. J. L., and Forouzanfar, M. H.: Estimates and 25-year trends of the global burden of disease attributable to ambient air pollution: an analysis of data from the Global Burden of Diseases Study 2015, *The Lancet*, 389, 1907-1918, doi:10.1016/S0140-6736(17)30505-6, 2017.
- Cox, R. A., Ammann, M., Crowley, J. N., Herrmann, H., Jenkin, M. E., McNeill, V. F., Mellouki, A., Troe, J., and Wallington, T. J.: Evaluated kinetic and photochemical data for atmospheric chemistry: Volume VII – Criegee intermediates, *Atmos. Chem. Phys.*, 20, 13497-13519, doi:10.5194/acp-20-13497-2020, 2020.
- Creasey, D. J., Heard, D. E., and Lee, J. D.: Absorption cross-section measurements of water vapour and oxygen at 185 nm. Implications for the calibration of field instruments to measure OH, HO₂ and RO₂ radicals, *Geophys. Res. Lett.*, 27, 1651-1654, doi:10.1029/1999GL011014, 2000.
- Creasey, D. J., Evans, G. E., Heard, D. E., and Lee, J. D.: Measurements of OH and HO₂ concentrations in the Southern Ocean marine boundary layer, *J. Geophys. Res.: Atmos.*, 108, doi:10.1029/2002jd003206, 2003.
- Crouse, J. D., Paulot, F., Kjaergaard, H. G., and Wennberg, P. O.: Peroxy radical isomerization in the oxidation of isoprene, *Phys. Chem. Chem. Phys.*, 13, 13607-13613, doi:10.1039/C1CP21330J, 2011.
- Crouse, J. D., Knap, H. C., Ørnsø, K. B., Jørgensen, S., Paulot, F., Kjaergaard, H. G., and Wennberg, P. O.: Atmospheric Fate of Methacrolein. 1. Peroxy Radical Isomerization Following Addition of OH and O₂, *J. Phys. Chem. A*, 116, 5756-5762, doi:10.1021/jp211560u, 2012.
- da Silva, G., Graham, C., and Wang, Z.-F.: Unimolecular β-hydroxyperoxy radical decomposition with OH recycling in the photochemical oxidation of isoprene, *Environ. Sci. Technol.*, 44, 250-256, doi:10.1021/es900924d, 2010.
- Dorn, H.-P., Brandenburger, U., Brauers, T., Hausmann, M., and Ehhalt, D. H.: In-situ detection of tropospheric OH radicals by folded long-path laser absorption. Results from the POPCORN Field Campaign in August 1994, *J. Geophys. Res.*, 23, 2537-2540, doi:10.1029/96GL02206, 1996.
- Dubey, M. K., Hanisco, T. F., Wennberg, P. O., and Anderson, J. G.: Monitoring potential photochemical interference in laser-induced fluorescence measurements of atmospheric OH, *Geophys. Res. Lett.*, 23, 3215-3218, doi:10.1029/96gl03008, 1996.

- Dusanter, S., Vimal, D., Stevens, P. S., Volkamer, R., Molina, L. T., Baker, A., Meinardi, S., Blake, D., Sheehy, P., Merten, A., Zhang, R., Zheng, J., Fortner, E. C., Junkermann, W., Dubey, M., Rahn, T., Eichinger, B., Lewandowski, P., Prueger, J., and Holder, H.: Measurements of OH and HO₂ concentrations during the MCMA-2006 field campaign – Part 2: Model comparison and radical budget, *Atmos. Chem. Phys.*, 9, 6655-6675, doi:10.5194/acp-9-6655-2009, 2009.
- Edwards, G. D., Cantrell, C. A., Stephens, S., Hill, B., Goyea, O., Shetter, R. E., Mauldin, R. L., Kosciuch, E., Tanner, D. J., and Eisele, F. L.: Chemical Ionization Mass Spectrometer Instrument for the Measurement of Tropospheric HO₂ and RO₂, *Anal. Chem.*, 75, 5317-5327, doi:10.1021/ac034402b, 2003.
- Ehhalt, D. H., and Rohrer, F.: Dependence of the OH concentration on solar UV, *J. Geophys. Res.: Atmos.*, 105, 3565-3571, doi:10.1029/1999jd901070, 2000.
- Eisele, F. L., and Tanner, D. J.: Ion-assisted tropospheric OH measurements, *J. Geophys. Res.: Atmos.*, 96, 9295-9308, doi:10.1029/91JD00198, 1991.
- Engel, V., Staemmler, V., Vander Wal, R. L., Crim, F. F., Sension, R. J., Hudson, B., Andresen, P., Hennig, S., Weide, K., and Schinke, R.: Photodissociation of water in the first absorption band: a prototype for dissociation on a repulsive potential energy surface, *J. Phys. Chem.*, 96, 3201-3213, doi:10.1021/j100187a007, 1992.
- Faloona, I. C., Tan, D., Leshner, R. L., Hazen, N. L., Frame, C. L., Simpas, J. B., Harder, H., Martinez, M., Di Carlo, P., Ren, X., and Brune, W. H.: A Laser-induced Fluorescence Instrument for Detecting Tropospheric OH and HO₂: Characteristics and Calibration, *J. Atmos. Chem.*, 47, 139-167, doi:10.1023/B:JOCH.0000021036.53185.0e, 2004.
- Farmer, D. K., Perring, A. E., Wooldridge, P. J., Blake, D. R., Baker, A., Meinardi, S., Huey, L. G., Tanner, D., Vargas, O., and Cohen, R. C.: Impact of organic nitrates on urban ozone production, *Atmos. Chem. Phys.*, 11, 4085-4094, doi:10.5194/acp-11-4085-2011, 2011.
- Feiner, P. A., Brune, W. H., Miller, D. O., Zhang, L., Cohen, R. C., Romer, P. S., Goldstein, A. H., Keutsch, F. N., Skog, K. M., Wennberg, P. O., Nguyen, T. B., Teng, A. P., DeGouw, J., Koss, A., Wild, R. J., Brown, S. S., Guenther, A., Edgerton, E., Baumann, K., and Fry, J. L.: Testing atmospheric oxidation in an Alabama forest, *J. Atmos. Sci.*, 73, 4699-4710, doi:10.1175/jas-d-16-0044.1, 2016.
- Finlayson-Pitts, B. J., Keoshian, C. J., Buehler, B., and Ezell, A. A.: Kinetics of reaction of chlorine atoms with some biogenic organics, *Int. J. Chem. Kinet.*, 31, 491-499, doi:10.1002/(SICI)1097-4601(1999)31:7<491::AID-KIN4>3.0.CO;2-E, 1999.
- Finlayson-Pitts, B. J. a. P. J., J. N.: *Chemistry of the upper and lower atmosphere*, Academic Press, San Diego, 2000.
- Fitzky, A. C., Sandén, H., Karl, T., Fares, S., Calfapietra, C., Grote, R., Saunier, A., and Rewald, B.: The Interplay Between Ozone and Urban Vegetation—BVOC Emissions, Ozone Deposition, and Tree Ecophysiology, *Front. for. glob. change*, 2, doi:10.3389/ffgc.2019.00050, 2019.
- Fuchs, H.: *Measurement of Peroxy Radicals using Laser-Induced Fluorescence Technique*, Ph.D. Thesis, Mathematisch-Naturwissenschaftlichen Fakultät I der Humboldt-Universität zu Berlin, 2007.

- Fuchs, H., Holland, F., and Hofzumahaus, A.: Measurement of tropospheric RO₂ and HO₂ radicals by a laser-induced fluorescence instrument, *Rev. Sci. Instrum.*, 79, 084104, doi:10.1063/1.2968712, 2008.
- Fuchs, H., Dubé, W. P., Lerner, B. M., Wagner, N. L., Williams, E. J., and Brown, S. S.: A Sensitive and Versatile Detector for Atmospheric NO₂ and NO_x Based on Blue Diode Laser Cavity Ring-Down Spectroscopy, *Environ. Sci. Technol.*, 43, 7831-7836, doi:10.1021/es902067h, 2009.
- Fuchs, H., Bohn, B., Hofzumahaus, A., Holland, F., Lu, K. D., Nehr, S., Rohrer, F., and Wahner, A.: Detection of HO₂ by laser-induced fluorescence: calibration and interferences from RO₂ radicals, *Atmos. Meas. Tech.*, 4, 1209-1225, doi:10.5194/amt-4-1209-2011, 2011.
- Fuchs, H., Dorn, H. P., Bachner, M., Bohn, B., Brauers, T., Gomm, S., Hofzumahaus, A., Holland, F., Nehr, S., Rohrer, F., Tillmann, R., and Wahner, A.: Comparison of OH concentration measurements by DOAS and LIF during SAPHIR chamber experiments at high OH reactivity and low NO concentration, *Atmos. Meas. Tech.*, 5, 1611-1626, doi:10.5194/amt-5-1611-2012, 2012.
- Fuchs, H., Hofzumahaus, A., Rohrer, F., Bohn, B., Brauers, T., Dorn, H. P., Häsel, R., Holland, F., Kaminski, M., Li, X., Lu, K., Nehr, S., Tillmann, R., Wegener, R., and Wahner, A.: Experimental evidence for efficient hydroxyl radical regeneration in isoprene oxidation, *Nat. Geosci.*, 6, 1023-1026, doi:10.1038/ngeo1964, 2013.
- Fuchs, H., Acir, I. H., Bohn, B., Brauers, T., Dorn, H. P., Häsel, R., Hofzumahaus, A., Holland, F., Kaminski, M., Li, X., Lu, K., Lutz, A., Nehr, S., Rohrer, F., Tillmann, R., Wegener, R., and Wahner, A.: OH regeneration from methacrolein oxidation investigated in the atmosphere simulation chamber SAPHIR, *Atmos. Chem. Phys.*, 14, 7895-7908, doi:10.5194/acp-14-7895-2014, 2014.
- Fuchs, H., Tan, Z., Hofzumahaus, A., Broch, S., Dorn, H. P., Holland, F., Künstler, C., Gomm, S., Rohrer, F., Schrade, S., Tillmann, R., and Wahner, A.: Investigation of potential interferences in the detection of atmospheric RO_x radicals by laser-induced fluorescence under dark conditions, *Atmos. Meas. Tech.*, 9, 1431-1447, doi:10.5194/amt-9-1431-2016, 2016.
- Fuchs, H., Novelli, A., Rolletter, M., Hofzumahaus, A., Pfannerstill, E. Y., Kessel, S., Edtbauer, A., Williams, J., Michoud, V., Dusanter, S., Locoge, N., Zannoni, N., Gros, V., Truong, F., Sarda-Esteve, R., Cryer, D. R., Brumby, C. A., Whalley, L. K., Stone, D., Seakins, P. W., Heard, D. E., Schoemaeker, C., Blocquet, M., Coudert, S., Batut, S., Fittschen, C., Thames, A. B., Brune, W. H., Ernest, C., Harder, H., Müller, J. B. A., Elste, T., Kubistin, D., Andres, S., Bohn, B., Hohaus, T., Holland, F., Li, X., Rohrer, F., Kiendler-Scharr, A., Tillmann, R., Wegener, R., Yu, Z., Zou, Q., and Wahner, A.: Comparison of OH reactivity measurements in the atmospheric simulation chamber SAPHIR, *Atmos. Meas. Tech.*, 10, 4023-4053, doi:10.5194/amt-10-4023-2017, 2017.
- Fuchs, H., Albrecht, S., Acir, I., Bohn, B., Breitenlechner, M., Dorn, H. P., Gkatzelis, G. I., Hofzumahaus, A., Holland, F., Kaminski, M., Keutsch, F. N., Novelli, A., Reimer, D., Rohrer, F., Tillmann, R., Vereecken, L., Wegener, R., Zaytsev, A., Kiendler-Scharr, A., and Wahner, A.: Investigation of the oxidation of methyl vinyl ketone (MVK) by OH radicals in the atmospheric simulation chamber SAPHIR, *Atmos. Chem. Phys.*, 18, 8001-8016, doi:10.5194/acp-18-8001-2018, 2018.

- George, I. J., Vlasenko, A., Slowik, J. G., Broekhuizen, K., and Abbatt, J. P. D.: Heterogeneous oxidation of saturated organic aerosols by hydroxyl radicals: uptake kinetics, condensed-phase products, and particle size change, *Atmos. Chem. Phys.*, 7, 4187-4201, doi:10.5194/acp-7-4187-2007, 2007.
- George, I. J., Matthews, P. S. J., Whalley, L. K., Brooks, B., Goddard, A., Baeza-Romero, M. T., and Heard, D. E.: Measurements of uptake coefficients for heterogeneous loss of HO₂ onto submicron inorganic salt aerosols, *Phys. Chem. Chem. Phys.*, 15, 12829-12845, doi:10.1039/C3CP51831K, 2013.
- Goldstein, A. H., Fan, S. M., Goulden, M. L., Munger, J. W., and Wofsy, S. C.: Emissions of ethene, propene, and 1-butene by a midlatitude forest, *Journal of Geophysical Research: Atmospheres*, 101, 9149-9157, doi:10.1029/96JD00334, 1996.
- Goldstein, A. H., and Galbally, I. E.: Known and Unexplored Organic Constituents in the Earth's Atmosphere, *Environmental Science & Technology*, 41, 1514-1521, doi:10.1021/es072476p, 2007.
- Green, T. J., Reeves, C. E., Fleming, Z. L., Brough, N., Rickard, A. R., Bandy, B. J., Monks, P. S., and Penkett, S. A.: An improved dual channel PERCA instrument for atmospheric measurements of peroxy radicals, *J. Environ. Monitor.*, 8, 530-536, doi:10.1039/B514630E, 2006.
- Griffith, S. M., Hansen, R. F., Dusanter, S., Michoud, V., Gilman, J. B., Kuster, W. C., Veres, P. R., Graus, M., de Gouw, J. A., Roberts, J., Young, C., Washenfelder, R., Brown, S. S., Thalman, R., Waxman, E., Volkamer, R., Tsai, C., Stutz, J., Flynn, J. H., Grossberg, N., Lefer, B., Alvarez, S. L., Rappenglueck, B., Mielke, L. H., Osthoff, H. D., and Stevens, P. S.: Measurements of hydroxyl and hydroperoxy radicals during CalNex-LA: Model comparisons and radical budgets, *J. Geophys. Res.: Atmos.*, 121, 4211-4232, doi:10.1002/2015jd024358, 2016.
- Handisides, G. M., Plass-Dülmer, C., Gilge, S., Bingemer, H., and Berresheim, H.: Hohenpeissenberg Photochemical Experiment (HOPE 2000): Measurements and photostationary state calculations of OH and peroxy radicals, *Atmos. Chem. Phys.*, 3, 1565-1588, doi:10.5194/acp-3-1565-2003, 2003.
- Hard, T. M., O'Brien, R. J., Chan, C. Y., and Mehrabzadeh, A. A.: Tropospheric free radical determination by fluorescence assay with gas expansion, *Environ. Sci. Technol.*, 18, 768-777, doi:10.1021/es00128a009, 1984.
- Hard, T. M., George, L. A., and O'Brien, R. J.: An Absolute Calibration for Gas-Phase Hydroxyl Measurements, *Environ. Sci. Technol.*, 36, 1783-1790, doi:10.1021/es0156461, 2002.
- Hausmann, M., Brandenburger, U., Brauers, T., and Dorn, H.-P.: Detection of tropospheric OH radicals by long-path differential optical-absorption spectroscopy: Experimental setup, accuracy, and precision, *J. Geophys. Res.*, 102, 16011-16022, 1997.
- Heard, D. E., and Pilling, M. J.: Measurement of OH and HO₂ in the Troposphere, *Chemical Reviews*, 103, 5163-5198, doi:10.1021/cr020522s, 2003.
- Heard, D. E., Carpenter, L. J., Creasey, D. J., Hopkins, J. R., Lee, J. D., Lewis, A. C., Pilling, M. J., Seakins, P. W., Carslaw, N., and Emmerson, K. M.: High levels of the hydroxyl radical in the winter urban troposphere, *J. Geophys. Res.*, 31, doi:10.1029/2004GL020544, 2004.

- Hens, K., Novelli, A., Martinez, M., Auld, J., Axinte, R., Bohn, B., Fischer, H., Keronen, P., Kubistin, D., Nölscher, A. C., Oswald, R., Paasonen, P., Petäjä, T., Regelin, E., Sander, R., Sinha, V., Sipilä, M., Taraborrelli, D., Tatum Ernest, C., Williams, J., Lelieveld, J., and Harder, H.: Observation and modelling of HO_x radicals in a boreal forest, *Atmos. Chem. Phys.*, 14, 8723-8747, doi:10.5194/acp-14-8723-2014, 2014.
- Hernández, M. D. A., Burkert, J., Reichert, L., Stöbener, D., Meyer-Arneke, J., Burrows, J. P., Dickerson, R. R., and Doddridge, B. G.: Marine boundary layer peroxy radical chemistry during the AEROSOLS99 campaign: Measurements and analysis, *J. Geophys. Res.: Atmos.*, 106, 20833-20846, doi:10.1029/2001JD900113, 2001.
- Hofzumahaus, A., Aschmutat, U., Heßling, M., Holland, F., and Ehhalt, D. H.: The measurement of tropospheric OH radicals by laser-induced fluorescence spectroscopy during the POPCORN Field Campaign, *Geophys. Res. Lett.*, 23, 2541-2544, doi:10.1029/96gl02205, 1996.
- Hofzumahaus, A., Aschmutat, U., Brandenburger, U., Brauers, T., Dorn, H. P., Hausmann, M., Heßling, M., Holland, F., Plass-Dülmer, C., and Ehhalt, D. H.: Intercomparison of Tropospheric OH Measurements by Different Laser Techniques during the POPCORN Campaign 1994, *J. Atmos. Chem.*, 31, 227-246, doi:10.1023/A:1006014707617, 1998.
- Hofzumahaus, A., Rohrer, F., Lu, K., Bohn, B., Brauers, T., Chang, C.-C., Fuchs, H., Holland, F., Kita, K., Kondo, Y., Li, X., Lou, S., Shao, M., Zeng, L., Wahner, A., and Zhang, Y.: Amplified trace gas removal in the troposphere, *Science*, 324, 1702-1704, doi:10.1126/science.1164566, 2009.
- Hofzumahaus, A., and Heard, D. H.: Assessment of local HO_x and RO_x measurement techniques: achievements, challenges, and future directions - Outcomes of the 2015 international HO_x workshop, Forschungszentrum Jülich, Jülich, 20-21, 2016.
- Holland, F., Hessling, M., and Hofzumahaus, A.: In Situ Measurement of Tropospheric OH Radicals by Laser-Induced Fluorescence—A Description of the KFA Instrument, *J. Atmos. Sci.*, 52, 3393-3401, doi:10.1175/1520-0469(1995)052<3393:ismoto>2.0.Co;2, 1995.
- Holland, F., Aschmutat, U., Heßling, M., Hofzumahaus, A., and Ehhalt, D. H.: Highly Time Resolved Measurements of OH during POPCORN Using Laser-Induced Fluorescence Spectroscopy, in: *Atmospheric Measurements during POPCORN — Characterisation of the Photochemistry over a Rural Area*, edited by: Rudolph, J., and Koppmann, R., Springer Netherlands, Dordrecht, 205-225, 1998.
- Holland, F., Hofzumahaus, A., Schäfer, J., Kraus, A., and Pätz, H.-W.: Measurements of OH and HO₂ radical concentrations and photolysis frequencies during BERLIOZ, *J. Geophys. Res.: Atmos.*, 108, 8246, doi:10.1029/2001jd001393, 2003.
- Hornbrook, R. S., Crawford, J. H., Edwards, G. D., Goyea, O., Mauldin Iii, R. L., Olson, J. S., and Cantrell, C. A.: Measurements of tropospheric HO₂ and RO₂ by oxygen dilution modulation and chemical ionization mass spectrometry, *Atmos. Meas. Tech.*, 4, 735-756, doi:10.5194/amt-4-735-2011, 2011.
- J. Creasey, D., A. Halford-Maw, P., E. Heard, D., J. Pilling, M., and J. Whitaker, B.: Implementation and initial deployment of a field instrument for measurement of OH and HO₂ in the

- troposphere by laser-induced fluorescence, *J. Chem. Soc., Faraday Transac.*, 93, 2907-2913, doi:10.1039/A701469D, 1997.
- Jenkin, M. E., Valorso, R., Aumont, B., and Rickard, A. R.: Estimation of rate coefficients and branching ratios for reactions of organic peroxy radicals for use in automated mechanism construction, *Atmos. Chem. Phys.*, 19, 7691-7717, doi:10.5194/acp-19-7691-2019, 2019.
- Jordan, A., Haidacher, S., Hanel, G., Hartungen, E., Märk, L., Seehauser, H., Schottkowsky, R., Sulzer, P., and Märk, T. D.: A high resolution and high sensitivity proton-transfer-reaction time-of-flight mass spectrometer (PTR-TOF-MS), *Int. J. Mass Spectrom.*, 286, 122-128, doi:10.1016/j.ijms.2009.07.005, 2009.
- Kaminski, M., Fuchs, H., Acir, I. H., Bohn, B., Brauers, T., Dorn, H. P., Häsel, R., Hofzumahaus, A., Li, X., Lutz, A., Nehr, S., Rohrer, F., Tillmann, R., Vereecken, L., Wegener, R., and Wahner, A.: Investigation of the β -pinene photooxidation by OH in the atmosphere simulation chamber SAPHIR, *Atmos. Chem. Phys.*, 17, 6631-6650, doi:10.5194/acp-17-6631-2017, 2017.
- Kanaya, Y., Sadanaga, Y., Hirokawa, J., Kajii, Y., and Akimoto, H.: Development of a Ground-Based LIF Instrument for Measuring HO_x Radicals: Instrumentation and Calibrations, *J. Atmos. Chem.*, 38, 73-110, doi:10.1023/A:1026559321911, 2001.
- Kanaya, Y., Cao, R., Akimoto, H., Fukuda, M., Komazaki, Y., Yokouchi, Y., Koike, M., Tanimoto, H., Takegawa, N., and Kondo, Y.: Urban photochemistry in central Tokyo: 1. Observed and modeled OH and HO₂ radical concentrations during the winter and summer of 2004, *J. Geophys. Res.: Atmos.*, 112, doi:10.1029/2007jd008670, 2007.
- Kanaya, Y., Hofzumahaus, A., Dorn, H. P., Brauers, T., Fuchs, H., Holland, F., Rohrer, F., Bohn, B., Tillmann, R., Wegener, R., Wahner, A., Kajii, Y., Miyamoto, K., Nishida, S., Watanabe, K., Yoshino, A., Kubistin, D., Martinez, M., Rudolf, M., Harder, H., Berresheim, H., Elste, T., Plass-Dülmer, C., Stange, G., Kleffmann, J., Elshorbany, Y., and Schurath, U.: Comparisons of observed and modeled OH and HO₂ concentrations during the ambient measurement period of the HO_xComp field campaign, *Atmos. Chem. Phys.*, 12, 2567-2585, doi:10.5194/acp-12-2567-2012, 2012.
- Karl, M., Brauers, T., Dorn, H.-P., Holland, F., Komenda, M., Poppe, D., Rohrer, F., Rupp, L., Schaub, A., and Wahner, A.: Kinetic Study of the OH-isoprene and O₃-isoprene reaction in the atmosphere simulation chamber, SAPHIR, *Geophys. Res. Lett.*, 31, doi:10.1029/2003GL019189, 2004.
- Kim, S., Wolfe, G. M., Mauldin, L., Cantrell, C., Guenther, A., Karl, T., Turnipseed, A., Greenberg, J., Hall, S. R., Ullmann, K., Apel, E., Hornbrook, R., Kajii, Y., Nakashima, Y., Keutsch, F. N., DiGangi, J. P., Henry, S. B., Kaser, L., Schnitzhofer, R., Graus, M., Hansel, A., Zheng, W., and Flocke, F. F.: Evaluation of HO_x sources and cycling using measurement-constrained model calculations in a 2-methyl-3-butene-2-ol (MBO) and monoterpene (MT) dominated ecosystem, *Atmos. Chem. Phys.*, 13, 2031-2044, doi:10.5194/acp-13-2031-2013, 2013.
- Kleffmann, J., Gavriloaiei, T., Hofzumahaus, A., Holland, F., Koppmann, R., Rupp, L., Schlosser, E., Siese, M., and Wahner, A.: Daytime formation of nitrous acid: A major source of OH radicals in a forest, *Geophys. Res. Lett.*, 32, doi:10.1029/2005GL022524, 2005.

- Kleffmann, J., Lörzer, J. C., Wiesen, P., Kern, C., Trick, S., Volkamer, R., Rodenas, M., and Wirtz, K.: Intercomparison of the DOAS and LOPAP techniques for the detection of nitrous acid (HONO), *Atmos. Environ.*, 40, 3640-3652, doi:10.1016/j.atmosenv.2006.03.027, 2006.
- Kleinman, L. I., Daum, P. H., Lee, Y.-N., Nunnermacker, L. J., Springston, S. R., Weinstein-Lloyd, J., and Rudolph, J.: Ozone production efficiency in an urban area, *J. Geophys. Res.: Atmos.*, 107, ACH 23-21-ACH 23-12, doi:10.1029/2002JD002529, 2002.
- Komenda, M., Schaub, A., and Koppmann, R.: Description and characterization of an on-line system for long-term measurements of isoprene, methyl vinyl ketone, and methacrolein in ambient air, *Journal of Chromatography A*, 995, 185-201, doi:10.1016/S0021-9673(03)00518-1, 2003.
- Konrad, S., Schmitz, T., Buers, H.-J., Houben, N., Mannschreck, K., Mihelcic, D., Müsgen, P., Pätz, H.-W., Holland, F., Hofzumahaus, A., Schäfer, H.-J., Schröder, S., Volz-Thomas, A., Bächmann, K., Schlomski, S., Moortgat, G., and Großmann, D.: Hydrocarbon measurements at Pabstthum during the BERLIOZ campaign and modeling of free radicals, *J. Geophys. Res.: Atmos.*, 108, doi:10.1029/2001JD000866, 2003.
- Kubistin, D., Harder, H., Martinez, M., Rudolf, M., Sander, R., Bozem, H., Eerdeken, G., Fischer, H., Gurk, C., Klüpfel, T., Königstedt, R., Parchatka, U., Schiller, C. L., Stickler, A., Taraborrelli, D., Williams, J., and Lelieveld, J.: Hydroxyl radicals in the tropical troposphere over the Suriname rainforest: comparison of measurements with the box model MECCA, *Atmos. Chem. Phys.*, 10, 9705-9728, doi:10.5194/acp-10-9705-2010, 2010.
- Künstler, C.: Measurements of Atmospheric OH and HO₂ Radicals by Laser-Induced Fluorescence on the HALO Aircraft during the OMO-ASIA 2015 Campaign, Ph.D. Thesis, Universität zu Köln, 2020.
- Lahib, A.: Analytical Developments for Measuring Atmospheric Peroxy Radicals, Ph.D. Thesis, EcolenationalesupérieureMines-TélécomLilleDouai, 2019.
- Lakey, P. S. J., George, I. J., Whalley, L. K., Baeza-Romero, M. T., and Heard, D. E.: Measurements of the HO₂ Uptake Coefficients onto Single Component Organic Aerosols, *Environ. Sci. Technol.*, 49, 4878-4885, doi:10.1021/acs.est.5b00948, 2015.
- Le Breton, M., Hallquist, Å. M., Pathak, R. K., Simpson, D., Wang, Y., Johansson, J., Zheng, J., Yang, Y., Shang, D., Wang, H., Liu, Q., Chan, C., Wang, T., Bannan, T. J., Priestley, M., Percival, C. J., Shallcross, D. E., Lu, K., Guo, S., Hu, M., and Hallquist, M.: Chlorine oxidation of VOCs at a semi-rural site in Beijing: significant chlorine liberation from ClNO₂ and subsequent gas- and particle-phase Cl-VOC production, *Atmos. Chem. Phys.*, 18, 13013-13030, doi:10.5194/acp-18-13013-2018, 2018.
- Lelieveld, J., Butler, T. M., Crowley, J. N., Dillon, T. J., Fischer, H., Ganzeveld, L., Harder, H., Lawrence, M. G., Martinez, M., Taraborrelli, D., and Williams, J.: Atmospheric oxidation capacity sustained by a tropical forest, *Nature*, 452, 737, doi:10.1038/nature06870, 2008.
- Lew, M. M., Dusanter, S., and Stevens, P. S.: Measurement of interferences associated with the detection of the hydroperoxy radical in the atmosphere using laser-induced fluorescence, *Atmos. Meas. Tech.*, 11, 95-109, doi:10.5194/amt-11-95-2018, 2018.
- Lew, M. M., Rickly, P. S., Bottorff, B. P., Reidy, E., Sklaveniti, S., Léonardis, T., Locoge, N., Dusanter, S., Kundu, S., Wood, E., and Stevens, P. S.: OH and HO₂ radical chemistry in a

- midlatitude forest: measurements and model comparisons, *Atmos. Chem. Phys.*, 20, 9209-9230, doi:10.5194/acp-20-9209-2020, 2020.
- Li, X., Rohrer, F., Hofzumahaus, A., Brauers, T., Häsel, R., Bohn, B., Broch, S., Fuchs, H., Gomm, S., Holland, F., Jäger, J., Kaiser, J., Keutsch, F. N., Lohse, I., Lu, K., Tillmann, R., Wegener, R., Wolfe, G. M., Mentel, T. F., Kiendler-Scharr, A., and Wahner, A.: Missing gas-phase source of HONO Inferred from zeppelin measurements in the troposphere, *Science*, 344, 292-296, doi:10.1126/science.1248999, 2014.
- Liu, Y., and Zhang, J.: Atmospheric Peroxy Radical Measurements Using Dual-Channel Chemical Amplification Cavity Ringdown Spectroscopy, *Anal. Chem.*, 86, 5391-5398, doi:10.1021/ac5004689, 2014.
- Liu, Z., Nguyen, V. S., Harvey, J., Müller, J.-F., and Peeters, J.: Theoretically derived mechanisms of HPALD photolysis in isoprene oxidation, *Phys. Chem. Chem. Phys.*, 19, 9096-9106, doi:10.1039/C7CP00288B, 2017.
- Lou, S., Holland, F., Rohrer, F., Lu, K., Bohn, B., Brauers, T., Chang, C. C., Fuchs, H., Häsel, R., Kita, K., Kondo, Y., Li, X., Shao, M., Zeng, L., Wahner, A., Zhang, Y., Wang, W., and Hofzumahaus, A.: Atmospheric OH reactivities in the Pearl River Delta – China in summer 2006: measurement and model results, *Atmos. Chem. Phys.*, 10, 11243-11260, doi:10.5194/acp-10-11243-2010, 2010.
- Lu, K. D., Rohrer, F., Holland, F., Fuchs, H., Bohn, B., Brauers, T., Chang, C. C., Häsel, R., Hu, M., Kita, K., Kondo, Y., Li, X., Lou, S. R., Nehr, S., Shao, M., Zeng, L. M., Wahner, A., Zhang, Y. H., and Hofzumahaus, A.: Observation and modelling of OH and HO₂ concentrations in the Pearl River Delta 2006: a missing OH source in a VOC rich atmosphere, *Atmos. Chem. Phys.*, 12, 1541-1569, doi:10.5194/acp-12-1541-2012, 2012.
- Lu, K. D., Hofzumahaus, A., Holland, F., Bohn, B., Brauers, T., Fuchs, H., Hu, M., Häsel, R., Kita, K., Kondo, Y., Li, X., Lou, S. R., Oebel, A., Shao, M., Zeng, L. M., Wahner, A., Zhu, T., Zhang, Y. H., and Rohrer, F.: Missing OH source in a suburban environment near Beijing: observed and modelled OH and HO₂ concentrations in summer 2006, *Atmos. Chem. Phys.*, 13, 1057-1080, doi:10.5194/acp-13-1057-2013, 2013.
- Lu, K. D., Rohrer, F., Holland, F., Fuchs, H., Brauers, T., Oebel, A., Dlugi, R., Hu, M., Li, X., Lou, S. R., Shao, M., Zhu, T., Wahner, A., Zhang, Y. H., and Hofzumahaus, A.: Nighttime observation and chemistry of HO_x in the Pearl River Delta and Beijing in summer 2006, *Atmos. Chem. Phys.*, 14, 4979-4999, doi:10.5194/acp-14-4979-2014, 2014.
- Ma, X., Tan, Z., Lu, K., Yang, X., Liu, Y., Li, S., Li, X., Chen, S., Novelli, A., Cho, C., Zeng, L., Wahner, A., and Zhang, Y.: Winter photochemistry in Beijing: Observation and model simulation of OH and HO₂ radicals at an urban site, *Sci. Tot. Environ.*, 685, 85-95, doi:10.1016/j.scitotenv.2019.05.329, 2019.
- Malkin, T. L., Goddard, A., Heard, D. E., and Seakins, P. W.: Measurements of OH and HO₂ yields from the gas phase ozonolysis of isoprene, *Atmos. Chem. Phys.*, 10, 1441-1459, doi:10.5194/acp-10-1441-2010, 2010.
- Mallik, C., Tomsche, L., Bourtsoukidis, E., Crowley, J. N., Derstroff, B., Fischer, H., Hafemann, S., Hüser, I., Javed, U., Keßel, S., Lelieveld, J., Martinez, M., Meusel, H., Novelli, A., Phillips, G. J., Pozzer, A., Reiffs, A., Sander, R., Taraborrelli, D., Sauvage, C., Schuladen, J., Su, H., Williams, J., and Harder, H.: Oxidation processes in the eastern Mediterranean atmosphere:

- evidence from the modelling of HO_x measurements over Cyprus, *Atmos. Chem. Phys.*, 18, 10825-10847, doi:10.5194/acp-18-10825-2018, 2018.
- Mao, J., Ren, X., Chen, S., Brune, W. H., Chen, Z., Martinez, M., Harder, H., Lefer, B., Rappenglück, B., Flynn, J., and Leuchner, M.: Atmospheric oxidation capacity in the summer of Houston 2006: Comparison with summer measurements in other metropolitan studies, *Atmos. Environ.*, 44, 4107-4115, doi:doi.org/10.1016/j.atmosenv.2009.01.013, 2010.
- Mao, J., Ren, X., Zhang, L., Van Duin, D. M., Cohen, R. C., Park, J. H., Goldstein, A. H., Paulot, F., Beaver, M. R., Crounse, J. D., Wennberg, P. O., DiGangi, J. P., Henry, S. B., Keutsch, F. N., Park, C., Schade, G. W., Wolfe, G. M., Thornton, J. A., and Brune, W. H.: Insights into hydroxyl measurements and atmospheric oxidation in a California forest, *Atmos. Chem. Phys.*, 12, 8009-8020, doi:10.5194/acp-12-8009-2012, 2012.
- Martinez, M., Harder, H., Kovacs, T. A., Simpas, J. B., Bassis, J., Leshner, R., Brune, W. H., Frost, G. J., Williams, E. J., Stroud, C. A., Jobson, B. T., Roberts, J. M., Hall, S. R., Shetter, R. E., Wert, B., Fried, A., Alicke, B., Stutz, J., Young, V. L., White, A. B., and Zamora, R. J.: OH and HO₂ concentrations, sources, and loss rates during the Southern Oxidants Study in Nashville, Tennessee, summer 1999, *J. Geophys. Res.: Atmos.*, 108, doi:10.1029/2003JD003551, 2003.
- Mihelcic, D., Müsgen, P., and Ehhalt, D. H.: An improved method of measuring tropospheric NO₂ and RO₂ by matrix isolation and electron spin resonance, *J. Atmos. Chem.*, 3, 341-361, doi:10.1007/BF00122523, 1985.
- Mihelcic, D., Volz-Thomas, A., Pätz, H. W., Kley, D., and Mihelcic, M.: Numerical analysis of ESR spectra from atmospheric samples, *J. Atmos. Chem.*, 11, 271-297, doi:10.1007/BF00118353, 1990.
- Mihelcic, D., Holland, F., Hofzumahaus, A., Hoppe, L., Konrad, S., Müsgen, P., Pätz, H.-W., Schäfer, H.-J., Schmitz, T., Volz-Thomas, A., Bächmann, K., Schlomski, S., Platt, U., Geyer, A., Alicke, B., and Moortgat, G. K.: Peroxy radicals during BERLIOZ at Pabstthum: Measurements, radical budgets and ozone production, *J. Geophys. Res.: Atmos.*, 108, doi:10.1029/2001JD001014, 2003.
- Mills, G., Sharps, K., Simpson, D., Pleijel, H., Broberg, M., Uddling, J., Jaramillo, F., Davies, W. J., Dentener, F., Van den Berg, M., Agrawal, M., Agrawal, Shahibhushan B., Ainsworth, E. A., Büker, P., Emberson, L., Feng, Z., Harmens, H., Hayes, F., Kobayashi, K., Paoletti, E., and Van Dingenen, R.: Ozone pollution will compromise efforts to increase global wheat production, *Glob. Change Biol.*, 24, 3560-3574, doi:10.1111/gcb.14157, 2018.
- Møller, K. H., Otkjær, R. V., Chen, J., and Kjaergaard, H. G.: Double Bonds Are Key to Fast Unimolecular Reactivity in First-Generation Monoterpene Hydroxy Peroxy Radicals, *J. Phys. Chem. A*, 124, 2885-2896, doi:10.1021/acs.jpca.0c01079, 2020.
- Murphy, J. G., Day, D. A., Cleary, P. A., Wooldridge, P. J., Millet, D. B., Goldstein, A. H., and Cohen, R. C.: The weekend effect within and downwind of Sacramento – Part 1: Observations of ozone, nitrogen oxides, and VOC reactivity, *Atmos. Chem. Phys.*, 7, 5327-5339, doi:10.5194/acp-7-5327-2007, 2007.
- Novelli, A., Hens, K., Tatum Ernest, C., Kubistin, D., Regelin, E., Elste, T., Plass-Dülmer, C., Martinez, M., Lelieveld, J., and Harder, H.: Characterisation of an inlet pre-injector laser-

- induced fluorescence instrument for the measurement of atmospheric hydroxyl radicals, *Atmos. Meas. Tech.*, 7, 3413-3430, doi:10.5194/amt-7-3413-2014, 2014a.
- Novelli, A., Vereecken, L., Lelieveld, J., and Harder, H.: Direct observation of OH formation from stabilised Criegee intermediates, *Phys. Chem. Chem. Phys.*, 16, 19941-19951, doi:10.1039/C4CP02719A, 2014b.
- Novelli, A., Hens, K., Tatum Ernest, C., Martinez, M., Nölscher, A. C., Sinha, V., Paasonen, P., Petäjä, T., Sipilä, M., Elste, T., Plass-Dülmer, C., Phillips, G. J., Kubistin, D., Williams, J., Vereecken, L., Lelieveld, J., and Harder, H.: Estimating the atmospheric concentration of Criegee intermediates and their possible interference in a FAGE-LIF instrument, *Atmos. Chem. Phys.*, 17, 7807-7826, doi:10.5194/acp-17-7807-2017, 2017.
- Novelli, A., Kaminski, M., Rolletter, M., Acir, I. H., Bohn, B., Dorn, H. P., Li, X., Lutz, A., Nehr, S., Rohrer, F., Tillmann, R., Wegener, R., Holland, F., Hofzumahaus, A., Kiendler-Scharr, A., Wahner, A., and Fuchs, H.: Evaluation of OH and HO₂ concentrations and their budgets during photooxidation of 2-methyl-3-butene-2-ol (MBO) in the atmospheric simulation chamber SAPHIR, *Atmos. Chem. Phys.*, 18, 11409-11422, doi:10.5194/acp-18-11409-2018, 2018.
- Novelli, A., Vereecken, L., Bohn, B., Dorn, H. P., Gkatzelis, G. I., Hofzumahaus, A., Holland, F., Reimer, D., Rohrer, F., Rosanka, S., Taraborrelli, D., Tillmann, R., Wegener, R., Yu, Z., Kiendler-Scharr, A., Wahner, A., and Fuchs, H.: Importance of isomerization reactions for OH radical regeneration from the photo-oxidation of isoprene investigated in the atmospheric simulation chamber SAPHIR, *Atmos. Chem. Phys.*, 20, 3333-3355, doi:10.5194/acp-20-3333-2020, 2020.
- Novelli, A., Cho, C., Fuchs, H., Hofzumahaus, A., Rohrer, F., Tillmann, R., Kiendler-Scharr, A., Wahner, A., and Vereecken, L.: Experimental and theoretical study on the impact of a nitrate group on the chemistry of alkoxy radicals, *Phys. Chem. Chem. Phys.*, 23, 5474-5495, doi:10.1039/d0cp05555g, 2021.
- Noziere, B., Lesclaux, R., Hurley, M. D., Dearth, M. A., and Wallington, T. J.: A Kinetic and Mechanistic Study of the Self-Reaction and Reaction with HO₂ of the Benzylperoxy Radical, *J. Phys. Chem.*, 98, 2864-2873, doi:10.1021/j100062a023, 1994.
- Orlando, J. J., Tyndall, G. S., Apel, E. C., Riemer, D. D., and Paulson, S. E.: Rate coefficients and mechanisms of the reaction of Cl-atoms with a series of unsaturated hydrocarbons under atmospheric conditions, *Int. J. Chem. Kinet.*, 35, 334-353, doi:10.1002/kin.10135, 2003.
- Peeters, J., Nguyen, T., and Vereecken, L.: HO_x radical regeneration in the oxidation of isoprene, *Phys. Chem. Chem. Phys.*, 11, 5935-5939, doi:10.1039/b908511d, 2009.
- Peeters, J., and Müller, J.-F.: HO_x radical regeneration in isoprene oxidation via peroxy radical isomerisations. II: experimental evidence and global impact, *Phys. Chem. Chem. Phys.*, 12, 14227-14235, doi:10.1039/C0CP00811G, 2010.
- Peeters, J., Müller, J. F., Stavrou, T., and Vinh Son, N.: Hydroxyl radical recycling in isoprene oxidation driven by hydrogen bonding and hydrogen tunneling: The upgraded LIM1 mechanism, *J. Phys. Chem. A*, 118, doi:10.1021/jp5033146, 2014.
- Ren, X., Harder, H., Martinez, M., Leshner, R. L., Oligier, A., Simpas, J. B., Brune, W. H., Schwab, J. J., Demerjian, K. L., He, Y., Zhou, X., and Gao, H.: OH and HO₂ Chemistry in the urban

- atmosphere of New York City, *Atmos. Environ.*, 37, 3639-3651, doi:10.1016/S1352-2310(03)00459-X, 2003.
- Ren, X., Harder, H., Martinez, M., Faloona, I. C., Tan, D., Leshner, R. L., Di Carlo, P., Simpas, J. B., and Brune, W. H.: Interference testing for atmospheric HO_x measurements by laser-induced fluorescence, *J. Atmos. Chem.*, 47, 169-190, doi:10.1023/b:Joch.0000021037.46866.81, 2004.
- Ren, X., Brune, W. H., Cantrell, C. A., Edwards, G. D., Shirley, T., Metcalf, A. R., and Leshner, R. L.: Hydroxyl and Peroxy Radical Chemistry in a Rural Area of Central Pennsylvania: Observations and Model Comparisons, *J. Atmos. Chem.*, 52, 231-257, doi:10.1007/s10874-005-3651-7, 2005.
- Ren, X., Brune, W. H., Mao, J., Mitchell, M. J., Leshner, R. L., Simpas, J. B., Metcalf, A. R., Schwab, J. J., Cai, C., Li, Y., Demerjian, K. L., Felton, H. D., Boynton, G., Adams, A., Perry, J., He, Y., Zhou, X., and Hou, J.: Behavior of OH and HO₂ in the winter atmosphere in New York City, *Atmos. Environ.*, 40, 252-263, doi:10.1016/j.atmosenv.2005.11.073, 2006.
- Ren, X., van Duin, D., Cazorla, M., Chen, S., Mao, J., Zhang, L., Brune, W. H., Flynn, J. H., Grossberg, N., Lefer, B. L., Rappenglück, B., Wong, K. W., Tsai, C., Stutz, J., Dibb, J. E., Thomas Jobson, B., Luke, W. T., and Kelley, P.: Atmospheric oxidation chemistry and ozone production: Results from SHARP 2009 in Houston, Texas, *J. Geophys. Res.: Atmos.*, 118, 5770-5780, doi:10.1002/jgrd.50342, 2013.
- Requia, W. J., Adams, M. D., Arain, A., Papatheodorou, S., Koutrakis, P., and Mahmoud, M.: Global Association of Air Pollution and Cardiorespiratory Diseases: A Systematic Review, Meta-Analysis, and Investigation of Modifier Variables, *Am. J. Public Health*, 108, S123-S130, doi:10.2105/AJPH.2017.303839, 2017.
- Rhew, R. C., Deventer, M. J., Turnipseed, A. A., Warneke, C., Ortega, J., Shen, S., Martinez, L., Koss, A., Lerner, B. M., Gilman, J. B., Smith, J. N., Guenther, A. B., and de Gouw, J. A.: Ethene, propene, butene and isoprene emissions from a ponderosa pine forest measured by relaxed eddy accumulation, *Atmos. Chem. Phys.*, 17, 13417-13438, doi:10.5194/acp-17-13417-2017, 2017.
- Rickly, P., and Stevens, P. S.: Measurements of a potential interference with laser-induced fluorescence measurements of ambient OH from the ozonolysis of biogenic alkenes, *Atmos. Meas. Tech.*, 11, 1-16, doi:10.5194/amt-11-1-2018, 2018.
- Rohrer, F., Bohn, B., Brauers, T., Brüning, D., Johnen, F. J., Wahner, A., and Kleffmann, J.: Characterisation of the photolytic HONO-source in the atmosphere simulation chamber SAPHIR, *Atmos. Chem. Phys.*, 5, 2189-2201, doi:10.5194/acp-5-2189-2005, 2005.
- Rohrer, F., Lu, K., Hofzumahaus, A., Bohn, B., Brauers, T., Chang, C.-C., Fuchs, H., Häseler, R., Holland, F., Hu, M., Kita, K., Kondo, Y., Li, X., Lou, S., Oebel, A., Shao, M., Zeng, L., Zhu, T., Zhang, Y., and Wahner, A.: Maximum efficiency in the hydroxyl-radical-based self-cleansing of the troposphere, *Nat. Geosci.*, 7, 559, doi:10.1038/ngeo2199, 2014.
- Rolletter, M., Kaminski, M., Acir, I. H., Bohn, B., Dorn, H. P., Li, X., Lutz, A., Nehr, S., Rohrer, F., Tillmann, R., Wegener, R., Hofzumahaus, A., Kiendler-Scharr, A., Wahner, A., and Fuchs, H.: Investigation of the α -pinene photooxidation by OH in the atmospheric simulation chamber SAPHIR, *Atmos. Chem. Phys.*, 19, 11635-11649, doi:10.5194/acp-19-11635-2019, 2019.

- Rolletter, M., Blocquet, M., Kaminski, M., Bohn, B., Dorn, H. P., Hofzumahaus, A., Holland, F., Li, X., Rohrer, F., Tillmann, R., Wegener, R., Kiendler-Scharr, A., Wahner, A., and Fuchs, H.: Photooxidation of pinonaldehyde at ambient conditions investigated in the atmospheric simulation chamber SAPHIR, *Atmos. Chem. Phys.*, 20, 13701-13719, doi:10.5194/acp-20-13701-2020, 2020.
- Romer Present, P. S., Zare, A., and Cohen, R. C.: The changing role of organic nitrates in the removal and transport of NO_x, *Atmos. Chem. Phys.*, 20, 267-279, doi:10.5194/acp-20-267-2020, 2020.
- Rozhenshtein, V. B., Gershenzon, Y. M., Il'in, S. D., and Kishkovich, O. P.: Study of reactions of HO₂ radicals by means of combined ESR/LMR spectrometer. Destruction on surface, *Kinet. Catal.*, 26:3,PT.1, 1985.
- Sadanaga, Y., Matsumoto, J., Sakurai, K.-i., Isozaki, R., Kato, S., Nomaguchi, T., Bandow, H., and Kajii, Y.: Development of a measurement system of peroxy radicals using a chemical amplification/laser-induced fluorescence technique, *Rev. Sci. Instrum.*, 75, 864-872, doi:10.1063/1.1666985, 2004.
- Sadanaga, Y., Kawasaki, S., Tanaka, Y., Kajii, Y., and Bandow, H.: New System for Measuring the Photochemical Ozone Production Rate in the Atmosphere, *Environ. Sci. Technol.*, 51, 2871-2878, doi:10.1021/acs.est.6b04639, 2017.
- Sanchez, D., Jeong, D., Seco, R., Wrangham, I., Park, J.-H., Brune, W. H., Koss, A., Gilman, J., de Gouw, J., Misztal, P., Goldstein, A., Baumann, K., Wennberg, P. O., Keutsch, F. N., Guenther, A., and Kim, S.: Intercomparison of OH and OH reactivity measurements in a high isoprene and low NO environment during the Southern Oxidant and Aerosol Study (SOAS), *Atmos. Environ.*, 174, 227-236, doi:10.1016/j.atmosenv.2017.10.056, 2018.
- Sanchez, J., Tanner, D. J., Chen, D., Huey, L. G., and Ng, N. L.: A new technique for the direct detection of HO₂ radicals using bromide chemical ionization mass spectrometry (Br-CIMS): initial characterization, *Atmos. Meas. Tech.*, 9, 3851-3861, doi:10.5194/amt-9-3851-2016, 2016.
- Sarkar, C., Guenther, A. B., Park, J. H., Seco, R., Alves, E., Batalha, S., Santana, R., Kim, S., Smith, J., Tóta, J., and Vega, O.: PTR-TOF-MS eddy covariance measurements of isoprene and monoterpene fluxes from an eastern Amazonian rainforest, *Atmos. Chem. Phys.*, 20, 7179-7191, doi:10.5194/acp-20-7179-2020, 2020.
- Saunders, S. M., Jenkin, M. E., Derwent, R. G., and Pilling, M. J.: Protocol for the development of the Master Chemical Mechanism, MCM v3 (Part A): tropospheric degradation of non-aromatic volatile organic compounds, *Atmos. Chem. Phys.*, 3, 161-180, doi:10.5194/acp-3-161-2003, 2003.
- Schlosser, E., Bohn, B., Brauers, T., Dorn, H.-P., Fuchs, H., Häsel, R., Hofzumahaus, A., Holland, F., Rohrer, F., Rupp, L. O., Siese, M., Tillmann, R., and Wahner, A.: Intercomparison of two hydroxyl radical measurement techniques at the atmosphere simulation chamber SAPHIR, *J. Atmos. Chem.*, 56, 187-205, doi:10.1007/s10874-006-9049-3, 2007.
- Schlosser, E., Brauers, T., Dorn, H. P., Fuchs, H., Häsel, R., Hofzumahaus, A., Holland, F., Wahner, A., Kanaya, Y., Kajii, Y., Miyamoto, K., Nishida, S., Watanabe, K., Yoshino, A., Kubistin, D., Martinez, M., Rudolf, M., Harder, H., Berresheim, H., Elste, T., Plass-Dülmer, C., Stange, G., and Schurath, U.: Technical Note: Formal blind intercomparison of OH measurements:

- results from the international campaign HOxComp, *Atmos. Chem. Phys.*, 9, 7923-7948, doi:10.5194/acp-9-7923-2009, 2009.
- Schraufnagel, D. E., Balmes, J. R., Cowl, C. T., De Matteis, S., Jung, S.-H., Mortimer, K., Perez-Padilla, R., Rice, M. B., Riojas-Rodriguez, H., Sood, A., Thurston, G. D., To, T., Vanker, A., and Wuebbles, D. J.: Air Pollution and Noncommunicable Diseases: A Review by the Forum of International Respiratory Societies' Environmental Committee, Part 1: The Damaging Effects of Air Pollution, *Chest*, 155, 409-416, doi:10.1016/j.chest.2018.10.042, 2019.
- Sedlacek, M.: Messung der Hydroxylradikal-Konzentration in der marinen Troposphäre mittel laserinduzierter Fluoreszenz., Universität Bonn, 2001.
- Shi, J., and Bernhard, M. J.: Kinetic studies of Cl-atom reactions with selected aromatic compounds using the photochemical reactor-FTIR spectroscopy technique, *Int. J. Chem. Kinet.*, 29, 349-358, doi:10.1002/(SICI)1097-4601(1997)29:5<349::AID-KIN5>3.0.CO;2-U, 1997.
- Sillman, S., Carroll, M. A., Thornberry, T., Lamb, B. K., Westberg, H., Brune, W. H., Faloona, I., Tan, D., Shepson, P. B., Sumner, A. L., Hastie, D. R., Mihele, C. M., Apel, E. C., Riemer, D. D., and Zika, R. G.: Loss of isoprene and sources of nighttime OH radicals at a rural site in the United States: Results from photochemical models, *J. Geophys. Resear. Atmos.*, 107, ACH 2-1-ACH 2-14, doi:10.1029/2001JD000449, 2002.
- Simpson, D., Arneth, A., Mills, G., Solberg, S., and Uddling, J.: Ozone — the persistent menace: interactions with the N cycle and climate change, *Curr. Opin. Environ. Sustain.*, 9-10, 9-19, doi:10.1016/j.cosust.2014.07.008, 2014.
- Sinha, V., Williams, J., Crowley, J. N., and Lelieveld, J.: The Comparative Reactivity Method; a new tool to measure total OH Reactivity in ambient air, *Atmos. Chem. Phys.*, 8, 2213-2227, doi:10.5194/acp-8-2213-2008, 2008.
- Sklaveniti, S., Locoge, N., Stevens, P. S., Wood, E., Kundu, S., and Dusanter, S.: Development of an instrument for direct ozone production rate measurements: measurement reliability and current limitations, *Atmos. Meas. Tech.*, 11, 741-761, doi:10.5194/amt-11-741-2018, 2018.
- Slater, E. J., Whalley, L. K., Woodward-Massey, R., Ye, C., Lee, J. D., Squires, F., Hopkins, J. R., Dunmore, R. E., Shaw, M., Hamilton, J. F., Lewis, A. C., Crilley, L. R., Kramer, L., Bloss, W., Vu, T., Sun, Y., Xu, W., Yue, S., Ren, L., Acton, W. J. F., Hewitt, C. N., Wang, X., Fu, P., and Heard, D. E.: Elevated levels of OH observed in haze events during wintertime in central Beijing, *Atmos. Chem. Phys. Discuss.*, 2020, 1-43, doi:10.5194/acp-2020-362, 2020.
- Smith, G. P., and Crosley, D. R.: A photochemical model of ozone interference effects in laser detection of tropospheric OH, *J. Geophys. Resear. Atmos.*, 95, 16427-16442, doi:10.1029/JD095iD10p16427, 1990.
- Sommariva, R., Crilley, L. R., Ball, S. M., Cordell, R. L., Hollis, L. D. J., Bloss, W. J., and Monks, P. S.: Enhanced wintertime oxidation of VOCs via sustained radical sources in the urban atmosphere, *Environ. Pollut.*, 274, 116563, doi:10.1016/j.envpol.2021.116563, 2021.
- Song, H., Chen, X., Lu, K., Zou, Q., Tan, Z., Fuchs, H., Wiedensohler, A., Moon, D. R., Heard, D. E., Baeza-Romero, M. T., Zheng, M., Wahner, A., Kiendler-Scharr, A., and Zhang, Y.: Influence of aerosol copper on HO₂ uptake: a novel parameterized equation, *Atmos. Chem. Phys.*, 20, 15835-15850, doi:10.5194/acp-20-15835-2020, 2020.

- Spirig, C., Neftel, A., Ammann, C., Dommen, J., Grabmer, W., Thielmann, A., Schaub, A., Beauchamp, J., Wisthaler, A., and Hansel, A.: Eddy covariance flux measurements of biogenic VOCs during ECHO 2003 using proton transfer reaction mass spectrometry, *Atmos. Chem. Phys.*, 5, 465-481, doi:10.5194/acp-5-465-2005, 2005.
- Stemmler, K., Ammann, M., Donders, C., Kleffmann, J., and George, C.: Photosensitized reduction of nitrogen dioxide on humic acid as a source of nitrous acid, *Nature*, 440, 195-198, doi:10.1038/nature04603, 2006.
- Stemmler, K., Ndour, M., Elshorbany, Y., Kleffmann, J., D'Anna, B., George, C., Bohn, B., and Ammann, M.: Light induced conversion of nitrogen dioxide into nitrous acid on submicron humic acid aerosol, *Atmos. Chem. Phys.*, 7, 4237-4248, doi:10.5194/acp-7-4237-2007, 2007.
- Stevens, P. S., Mather, J. H., and Brune, W. H.: Measurement of tropospheric OH and HO₂ by laser-induced fluorescence at low pressure, *J. Geophys. Resear. Atmos.*, 99, 3543-3557, doi:10.1029/93JD03342, 1994.
- Stone, D., Evans, M. J., Walker, H., Ingham, T., Vaughan, S., Ouyang, B., Kennedy, O. J., McLeod, M. W., Jones, R. L., Hopkins, J., Punjabi, S., Lidster, R., Hamilton, J. F., Lee, J. D., Lewis, A. C., Carpenter, L. J., Forster, G., Oram, D. E., Reeves, C. E., Bauguitte, S., Morgan, W., Coe, H., Aruffo, E., Dari-Salisburgo, C., Giammaria, F., Di Carlo, P., and Heard, D. E.: Radical chemistry at night: comparisons between observed and modelled HO_x, NO₃ and N₂O₅ during the RONOCO project, *Atmos. Chem. Phys.*, 14, 1299-1321, doi:10.5194/acp-14-1299-2014, 2014.
- Su, H., Cheng, Y., Oswald, R., Behrendt, T., Trebs, I., Meixner, F. X., Andreae, M. O., Cheng, P., Zhang, Y., and Pöschl, U.: Soil Nitrite as a Source of Atmospheric HONO and OH Radicals, *Science*, 333, 1616-1618, doi:10.1126/science.1207687, 2011.
- Takahashi, K., Hayashi, S., Matsumi, Y., Taniguchi, N., and Hayashida, S.: Quantum yields of O(1D) formation in the photolysis of ozone between 230 and 308 nm, *J. Geophys. Resear. Atmos.*, 107, ACH 11-11-ACH 11-18, doi:10.1029/2001JD002048, 2002.
- Taketani, F., Kanaya, Y., and Akimoto, H.: Kinetics of Heterogeneous Reactions of HO₂ Radical at Ambient Concentration Levels with (NH₄)₂SO₄ and NaCl Aerosol Particles, *J. Phys. Chem. A*, 112, 2370-2377, doi:10.1021/jp0769936, 2008.
- Taketani, F., Kanaya, Y., and Akimoto, H.: Heterogeneous loss of HO₂ by KCl, synthetic sea salt, and natural seawater aerosol particles, *Atmos. Environ.*, 43, 1660-1665, doi:10.1016/j.atmosenv.2008.12.010, 2009.
- Taketani, F., Kanaya, Y., Pochanart, P., Liu, Y., Li, J., Okuzawa, K., Kawamura, K., Wang, Z., and Akimoto, H.: Measurement of overall uptake coefficients for HO₂ radicals by aerosol particles sampled from ambient air at Mts. Tai and Mang (China), *Atmos. Chem. Phys.*, 12, 11907-11916, doi:10.5194/acp-12-11907-2012, 2012.
- Tan, D., Faloon, I., Simpas, J. B., Brune, W., Shepson, P. B., Couch, T. L., Sumner, A. L., Carroll, M. A., Thornberry, T., Apel, E., Riemer, D., and Stockwell, W.: HO_x budgets in a deciduous forest: Results from the PROPHET summer 1998 campaign, *J. Geophys. Res.: Atmos.*, 106, 24407-24427, doi:10.1029/2001jd900016, 2001.

- Tan, Z., Fuchs, H., Lu, K., Hofzumahaus, A., Bohn, B., Broch, S., Dong, H., Gomm, S., Häsel, R., He, L., Holland, F., Li, X., Liu, Y., Lu, S., Rohrer, F., Shao, M., Wang, B., Wang, M., Wu, Y., Zeng, L., Zhang, Y., Wahner, A., and Zhang, Y.: Radical chemistry at a rural site (Wangdu) in the North China Plain: observation and model calculations of OH, HO₂ and RO₂ radicals, *Atmos. Chem. Phys.*, 17, 663-690, doi:10.5194/acp-17-663-2017, 2017.
- Tan, Z., Rohrer, F., Lu, K., Ma, X., Bohn, B., Broch, S., Dong, H., Fuchs, H., Gkatzelis, G. I., Hofzumahaus, A., Holland, F., Li, X., Liu, Y., Liu, Y., Novelli, A., Shao, M., Wang, H., Wu, Y., Zeng, L., Hu, M., Kiendler-Scharr, A., Wahner, A., and Zhang, Y.: Wintertime photochemistry in Beijing: observations of RO_x radical concentrations in the North China Plain during the BEST-ONE campaign, *Atmos. Chem. Phys.*, 18, 12391-12411, doi:10.5194/acp-18-12391-2018, 2018.
- Tan, Z., Lu, K., Hofzumahaus, A., Fuchs, H., Bohn, B., Holland, F., Liu, Y., Rohrer, F., Shao, M., Sun, K., Wu, Y., Zeng, L., Zhang, Y., Zou, Q., Kiendler-Scharr, A., Wahner, A., and Zhang, Y.: Experimental budgets of OH, HO₂, and RO₂ radicals and implications for ozone formation in the Pearl River Delta in China 2014, *Atmos. Chem. Phys.*, 19, 7129-7150, doi:10.5194/acp-19-7129-2019, 2019.
- Tan, Z., Hofzumahaus, A., Lu, K., Brown, S. S., Holland, F., Huey, L. G., Kiendler-Scharr, A., Li, X., Liu, X., Ma, N., Min, K.-E., Rohrer, F., Shao, M., Wahner, A., Wang, Y., Wiedensohler, A., Wu, Y., Wu, Z., Zeng, L., Zhang, Y., and Fuchs, H.: No Evidence for a Significant Impact of Heterogeneous Chemistry on Radical Concentrations in the North China Plain in Summer 2014, *Environ. Sci. Technol.*, 54, 5973-5979, doi:10.1021/acs.est.0c00525, 2020.
- Tanaka, P. L., Riemer, D. D., Chang, S., Yarwood, G., McDonald-Buller, E. C., Apel, E. C., Orlando, J. J., Silva, P. J., Jimenez, J. L., Canagaratna, M. R., Neece, J. D., Mullins, C. B., and Allen, D. T.: Direct evidence for chlorine-enhanced urban ozone formation in Houston, Texas, *Atmos. Environ.*, 37, 1393-1400, doi:10.1016/S1352-2310(02)01007-5, 2003.
- Tanner, D. J., Jefferson, A., and Eisele, F. L.: Selected ion chemical ionization mass spectrometric measurement of OH, *J. Geophys. Res.: Atmos.*, 102, 6415-6425, doi:10.1029/96jd03919, 1997.
- Teng, A. P., Crounse, J. D., and Wennberg, P. O.: Isoprene peroxy radical dynamics, *J. Am. Chem. Soc.*, 139, 5367-5377, doi:10.1021/jacs.6b12838, 2017.
- Vaughan, S., Ingham, T., Whalley, L. K., Stone, D., Evans, M. J., Read, K. A., Lee, J. D., Moller, S. J., Carpenter, L. J., Lewis, A. C., Fleming, Z. L., and Heard, D. E.: Seasonal observations of OH and HO₂ in the remote tropical marine boundary layer, *Atmos. Chem. Phys.*, 12, 2149-2172, doi:10.5194/acp-12-2149-2012, 2012.
- Vereecken, L., Müller, J. F., and Peeters, J.: Low-volatility poly-oxygenates in the OH-initiated atmospheric oxidation of α -pinene: impact of non-traditional peroxy radical chemistry, *Phys. Chem. Chem. Phys.*, 9, 5241-5248, doi:10.1039/B708023A, 2007.
- Vereecken, L., and Peeters, J.: A theoretical study of the OH-initiated gas-phase oxidation mechanism of β -pinene (C₁₀H₁₆): first generation products, *Phys. Chem. Chem. Phys.*, 14, 3802-3815, doi:10.1039/C2CP23711C, 2012.
- Vereecken, L., and Nozière, B.: H migration in peroxy radicals under atmospheric conditions, *Atmos. Chem. Phys.*, 20, 7429-7458, doi:10.5194/acp-20-7429-2020, 2020.

- Vereecken, L., Carlsson, P. T. M., Novelli, A., Bernard, F., Brown, S. S., Cho, C., Crowley, J. N., Fuchs, H., Mellouki, W., Reimer, D., Shenolikar, J., Tillmann, R., Zhou, L., Kiendler-Scharr, A., and Wahner, A.: Theoretical and experimental study of peroxy and alkoxy radicals in the NO₃-initiated oxidation of isoprene, *Phys. Chem. Chem. Phys.*, 23, 5496-5515, doi:10.1039/D0CP06267G, 2021.
- Vilà-Guerau de Arellano, J., van den Dries, K., and Pino, D.: On inferring isoprene emission surface flux from atmospheric boundary layer concentration measurements, *Atmos. Chem. Phys.*, 9, 3629-3640, doi:10.5194/acp-9-3629-2009, 2009.
- Wagner, N. L., Dubé, W. P., Washenfelder, R. A., Young, C. J., Pollack, I. B., Ryerson, T. B., and Brown, S. S.: Diode laser-based cavity ring-down instrument for NO₃, N₂O₅, NO, NO₂ and O₃ from aircraft, *Atmos. Meas. Tech.*, 4, 1227-1240, doi:10.5194/amt-4-1227-2011, 2011.
- Wang, C. C., and Davis, L. I.: Measurement of Hydroxyl Concentrations in Air Using a Tunable uv Laser Beam, *Phys. Rev. Lett.*, 32, 349-352, doi:10.1103/PhysRevLett.32.349, 1974.
- Wang, F., Hu, R., Chen, H., Xie, P., Wang, Y., Li, Z., Jin, H., Liu, J., and Liu, W.: Development of a field system for measurement of tropospheric OH radical using laser-induced fluorescence technique, *Optics Express*, 27, A419-A435, doi:10.1364/OE.27.00A419, 2019.
- Wang, L., Arey, J., and Atkinson, R.: Reactions of Chlorine Atoms with a Series of Aromatic Hydrocarbons, *Environ. Sci. Technol.*, 39, 5302-5310, doi:10.1021/es0479437, 2005.
- Wang, S., Riva, M., Yan, C., Ehn, M., and Wang, L.: Primary formation of highly oxidized multifunctional products in the OH-initiated oxidation of isoprene: A combined theoretical and experimental study, *Environ. Sci. Technol.*, 52, 12255-12264, doi:10.1021/acs.est.8b02783, 2018.
- Whalley, L. K., Edwards, P. M., Furneaux, K. L., Goddard, A., Ingham, T., Evans, M. J., Stone, D., Hopkins, J. R., Jones, C. E., Karunaharan, A., Lee, J. D., Lewis, A. C., Monks, P. S., Moller, S. J., and Heard, D. E.: Quantifying the magnitude of a missing hydroxyl radical source in a tropical rainforest, *Atmos. Chem. Phys.*, 11, 7223-7233, doi:10.5194/acp-11-7223-2011, 2011.
- Whalley, L. K., Blitz, M. A., Desservettaz, M., Seakins, P. W., and Heard, D. E.: Reporting the sensitivity of laser-induced fluorescence instruments used for HO₂ detection to an interference from RO₂ radicals and introducing a novel approach that enables HO₂ and certain RO₂ types to be selectively measured, *Atmos. Meas. Tech.*, 6, 3425-3440, doi:10.5194/amt-6-3425-2013, 2013.
- Whalley, L. K., Stone, D., Dunmore, R., Hamilton, J., Hopkins, J. R., Lee, J. D., Lewis, A. C., Williams, P., Kleffmann, J., Laufs, S., Woodward-Massey, R., and Heard, D. E.: Understanding in situ ozone production in the summertime through radical observations and modelling studies during the Clean air for London project (ClearfLo), *Atmos. Chem. Phys.*, 18, 2547-2571, doi:10.5194/acp-18-2547-2018, 2018.
- Whalley, L. K., Slater, E. J., Woodward-Massey, R., Ye, C., Lee, J. D., Squires, F., Hopkins, J. R., Dunmore, R. E., Shaw, M., Hamilton, J. F., Lewis, A. C., Mehra, A., Worrall, S. D., Bacak, A., Bannan, T. J., Coe, H., Ouyang, B., Jones, R. L., Crilley, L. R., Kramer, L. J., Bloss, W. J., Vu, T., Kotthaus, S., Grimmond, S., Sun, Y., Xu, W., Yue, S., Ren, L., Acton, W. J. F.,

- Hewitt, C. N., Wang, X., Fu, P., and Heard, D. E.: Evaluating the sensitivity of radical chemistry and ozone formation to ambient VOCs and NO_x in Beijing, *Atmos. Chem. Phys. Discuss.*, 2020, 1-41, doi:10.5194/acp-2020-785, 2020.
- Whalley, L. K., Slater, E. J., Woodward-Massey, R., Ye, C., Lee, J. D., Squires, F., Hopkins, J. R., Dunmore, R. E., Shaw, M., Hamilton, J. F., Lewis, A. C., Mehra, A., Worrall, S. D., Bacak, A., Bannan, T. J., Coe, H., Percival, C. J., Ouyang, B., Jones, R. L., Crilley, L. R., Kramer, L. J., Bloss, W. J., Vu, T., Kotthaus, S., Grimmond, S., Sun, Y., Xu, W., Yue, S., Ren, L., Acton, W. J. F., Hewitt, C. N., Wang, X., Fu, P., and Heard, D. E.: Evaluating the sensitivity of radical chemistry and ozone formation to ambient VOCs and NO_x in Beijing, *Atmos. Chem. Phys.*, 21, 2125-2147, doi:10.5194/acp-21-2125-2021, 2021.
- WHO: WHO releases country estimates on air pollution exposure and health impact, 2016.
- WHO: More than 90% of the world's children breathe toxic air every day., 2018.
- Wolfe, G. M., Thornton, J. A., Bouvier-Brown, N. C., Goldstein, A. H., Park, J. H., McKay, M., Matross, D. M., Mao, J., Brune, W. H., LaFranchi, B. W., Browne, E. C., Min, K. E., Wooldridge, P. J., Cohen, R. C., Crouse, J. D., Faloona, I. C., Gilman, J. B., Kuster, W. C., de Gouw, J. A., Huisman, A., and Keutsch, F. N.: The Chemistry of Atmosphere-Forest Exchange (CAFE) Model – Part 2: Application to BEARPEX-2007 observations, *Atmos. Chem. Phys.*, 11, 1269-1294, doi:10.5194/acp-11-1269-2011, 2011.
- Wolfe, G. M., Crouse, J. D., Parrish, J. D., St. Clair, J. M., Beaver, M. R., Paulot, F., Yoon, T. P., Wennberg, P. O., and Keutsch, F. N.: Photolysis, OH reactivity and ozone reactivity of a proxy for isoprene-derived hydroperoxyenals (HPALDs), *Phys. Chem. Chem. Phys.*, 14, 7276-7286, doi:10.1039/C2CP40388A, 2012.
- Wolfe, G. M., Cantrell, C., Kim, S., Mauldin Iii, R. L., Karl, T., Harley, P., Turnipseed, A., Zheng, W., Flocke, F., Apel, E. C., Hornbrook, R. S., Hall, S. R., Ullmann, K., Henry, S. B., DiGangi, J. P., Boyle, E. S., Kaser, L., Schnitzhofer, R., Hansel, A., Graus, M., Nakashima, Y., Kajii, Y., Guenther, A., and Keutsch, F. N.: Missing peroxy radical sources within a summertime ponderosa pine forest, *Atmos. Chem. Phys.*, 14, 4715-4732, doi:10.5194/acp-14-4715-2014, 2014.
- Woodward-Massey, R., Slater, E. J., Alen, J., Ingham, T., Cryer, D. R., Stimpson, L. M., Ye, C., Seakins, P. W., Whalley, L. K., and Heard, D. E.: Implementation of a chemical background method for atmospheric OH measurements by laser-induced fluorescence: characterisation and observations from the UK and China, *Atmos. Meas. Tech.*, 13, 3119-3146, doi:10.5194/amt-13-3119-2020, 2020.
- Yang, Y., Shao, M., Keßel, S., Li, Y., Lu, K., Lu, S., Williams, J., Zhang, Y., Zeng, L., Nölscher, A. C., Wu, Y., Wang, X., and Zheng, J.: How the OH reactivity affects the ozone production efficiency: case studies in Beijing and Heshan, China, *Atmos. Chem. Phys.*, 17, 7127-7142, doi:10.5194/acp-17-7127-2017, 2017.
- Young, C. J., Washenfelder, R. A., Edwards, P. M., Parrish, D. D., Gilman, J. B., Kuster, W. C., Mielke, L. H., Osthoff, H. D., Tsai, C., Pikelnaya, O., Stutz, J., Veres, P. R., Roberts, J. M., Griffith, S., Dusanter, S., Stevens, P. S., Flynn, J., Grossberg, N., Lefer, B., Holloway, J. S., Peischl, J., Ryerson, T. B., Atlas, E. L., Blake, D. R., and Brown, S. S.: Chlorine as a primary radical: evaluation of methods to understand its role in initiation of oxidative cycles, *Atmos. Chem. Phys.*, 14, 3427-3440, doi:10.5194/acp-14-3427-2014, 2014.

Zasytkin, A. Y., Grigor'eva, V. M., Korchak, V. N., and Gershenson, Y. M.: A formula for summing of kinetic resistances for mobile and stationary media: I. Cylindrical reactor, *Kinet. Catal.*, 38, 772-781, 1997.

Zavala, M., Brune, W. H., Velasco, E., Retama, A., Cruz-Alavez, L. A., and Molina, L. T.: Changes in ozone production and VOC reactivity in the atmosphere of the Mexico City Metropolitan Area, *Atmos. Environ.*, 238, 117747, doi:10.1016/j.atmosenv.2020.117747, 2020.

Band / Volume 561

Introduction Strategies for Hydrogen Infrastructure

S. Cerniauskas (2021), viii, 179 pp

ISBN: 978-3-95806-602-1

Band / Volume 562

Noble Metal Coated Porous Transport Layers for Polymer Electrolyte Membrane Water Electrolysis

C. Liu (2021), 139 pp

ISBN: 978-3-95806-603-8

Band / Volume 563

Modeling and Diagnosis of the Stratospheric Circulation

E. J. Charlesworth (2021), v, 103, A2 pp

ISBN: 978-3-95806-605-2

Band / Volume 564

Potentialfeldmessungen zur Qualitätsbewertung von Bipolarplatten

M. Sietmann (2021), ix, 160 pp

ISBN: 978-3-95806-606-9

Band / Volume 565

Sequential and coupled inversion of time-lapse borehole GPR measurements for vadose zone model parameterization

Y. Yu (2022), XX, 121 pp

ISBN: 978-3-95806-607-6

Band / Volume 566

Cirrus clouds in the extratropical tropopause and lowermost stratosphere region

I. Bartolomé García (2022), iii, 155 pp

ISBN: 978-3-95806-610-6

Band / Volume 567

Stationary and Transient Behaviour of Polymer Electrolyte Fuel Cells

Y. Shi (2022), viii, 172 pp

ISBN: 978-3-95806-611-3

Band / Volume 568

14th Carolus Magnus Summer School on Plasma and Fusion Energy Physics

D. Reiser (Ed.), (2022), 207 pp

ISBN: 978-3-95806-613-7

Band / Volume 569

Spectral induced polarization of calcite precipitation in porous media

S. Izumoto (2022), xviii, 106 pp

ISBN: 978-3-95806-614-4

Band / Volume 570

Technische und ökonomische Bewertung der Polymer-Elektrolyt-Membran Elektrolyse

S. M. Saba (2022), IV, 263 pp

ISBN: 978-3-95806-615-1

Band / Volume 571

Advanced Sintering of Garnet-Based Ceramic Composite Cathodes for All-Solid-State Lithium Batteries

M. Ihrig (2022), VIII, 160 pp

ISBN: 978-3-95806-616-8

Band / Volume 572

Developing an integrated value-based institutional framework for analyzing nexus governance challenges – the case study of Germany

C. Märker (2022), 290 pp

ISBN: 978-3-95806-617-5

Band / Volume 573

Ecological sanitation via thermophilic co-composting of humanure and biochar as an approach to climate-smart agriculture

D. Castro Herrera (2022), XVIII, 127 pp

ISBN: 978-3-95806-622-9

Band / Volume 574

Towards 3D crosshole GPR full-waveform inversion

A. Mozaffari (2022), viii, 122 pp

ISBN: 978-3-95806-623-6

Band / Volume 575

Investigations of the atmospheric OH, HO₂ and RO₂ radical chemical budgets and their impact on tropospheric ozone formation in a rural area in West-Germany in the JULIAC 2019 campaign

C. Cho (2022), 182 pp

ISBN: 978-3-95806-625-0

Weitere **Schriften des Verlags im Forschungszentrum Jülich** unter
<http://www.zb1.fz-juelich.de/verlagextern1/index.asp>

Energie & Umwelt / Energy & Environment
Band / Volume 575
ISBN 978-3-95806-625-0